The Dissertation Committee for Elizabeth A. Costner Certifies that this is the approved version of the following dissertation:

The Refractive Index and Absorbance of Aqueous and Organic Fluids for Immersion Lithography

Committee:

C. Grant Willson, Supervisor

Roger T. Bonnecaze

Allen Bowling

Alan Campion

Benny D. Freeman

The Refractive Index and Absorbance of Aqueous and Organic Fluids for Immersion Lithography

by

Elizabeth A. Costner, B.S.; M.S.

Dissertation

Presented to the Faculty of the Graduate School of
The University of Texas at Austin
in Partial Fulfillment
of the Requirements
for the Degree of

Doctor of Philosophy

The University of Texas at Austin
May 2009

Dedication

To My Parents

Acknowledgements

An undertaking of this magnitude certainly cannot be completed alone, and I would like to thank everyone who has made the completion of this dissertation possible. I want to thank my family for their love and support. I cannot begin to express my gratitude to my parents for all that they have done for me; they have always been my most unwavering supporters. I would also like to thank my brothers, Douglas, Andy, and Michael, for their unfailing ability to find humor in any situation. My boyfriend, Michael, has also been tirelessly patient and supportive throughout this process, and I cannot thank him enough.

I also want to thank the entire Willson Group, past and present. I would like to thank Chris Taylor, who started the immersion lithography project and helped to get me started so that I could continue the project after he graduated. Thank you to Brian Long, Kazuya Matsumoto, and Jeff Strahan for teaching me chemistry and helping with my frequent questions. Bob Leseur helped me learn the electrochemical method to measure diffusion coefficients in a hydrogel. I also acknowledge the assistance of a few talented undergraduate students: Sumarlin Goh, Scott North, and Carlos Navar. I was privileged to start the Willson Group with Saul Lee, Mikey Lin, and Kane Jen. Their friendship and support during classes in the early years has meant a lot to me. I also want to express my effusive thanks to Kathleen Sparks. She is an invaluable member of the Willson Group and is always ready to lend a sympathetic ear and to make sure everything is running smoothly. Last, but certainly not least, I cannot thank Dr. Willson enough for taking me into his group. I have learned so much from him and cannot envision a better advisor.

I have been privileged to receive support through a Semiconductor Research Corporation (SRC) fellowship sponsored by Texas Instruments. I would like to thank

everyone at the SRC and TI for their generous offer of this fellowship and to TI for also funding my research project. Dr. Allen Bowling at TI has been a great friend and support to me throughout my graduate work. I also received a scholarship from the Philanthropic Educational Organization (P.E.O.) and would like to thank the ladies in the Austin chapter for honoring me with a nomination for this scholarship.

I have also received research support from a variety of sources. I would like to thank Georgia Rich, Alvina Williams, and Tom Beasley for their help with the Acton VUV Spectrophotometer at SEMATECH. Emil Piscani, also at SEMATECH, has helped me with the fluid imaging. I would also like to thank James Park, Jianming Zhou, and Dr. Bruce Smith at RIT for their help in imaging with the salt solutions. Mark Stasney, Dean Dewulf, and Bill Wojtczak at SACHEM, Inc helped to develop some of the salt solutions. I would like to thank Dr. Steffen Jockusch, Dr. Xeugong Lei, and Dr. Nicholas Turro at Columbia for their help with some of the absorbance measurements and purification of the hydrocarbon fluids. Derek Bassett and Dr. Roger Bonnecaze developed a "drag-a-drop" test stand and kindly let me complete some experiments with it. I would like to thank Will Conley at Freescale Semiconductor for the pizza lunches and support over the years. I would also like to acknowledge Dr. Paul Zimmerman with Intel/SEMATECH for his help, friendship, and support of the high index fluids project.

Finally, thank you to my committee members: Dr. Roger Bonnecaze, Dr. Allen Bowling, Dr. Alan Campion, and Dr. Benny Freeman. I appreciate your time in serving on my committee and your helpful comments and criticisms. Special thanks to Dr. Campion for the generous donation of his time and knowledge of spectroscopy in helping me evaluate the trends in the saturated hydrocarbon absorbance data. Finally, thank you again to Dr. Willson for teaching me so much and making this experience so enjoyable.

The Refractive Index and Absorbance of Aqueous and Organic Fluids for Immersion Lithography

Publication No._____________

Elizabeth A. Costner, Ph.D.
The University of Texas at Austin, 2009

Supervisor: C. Grant Willson

The semiconductor industry is continually challenged to maintain the trend identified in 1965 by Gordon Moore of increasing the density of transistors on an integrated circuit. These advances have been achieved by increasing the resolution that can be printed with photolithography, traditionally by decreasing the exposure wavelength. Decreasing the exposure wavelength from 193 nm, the current state of the art, presents significant technical challenges. To circumvent these challenges, resolution can be increased by enabling increases in numerical aperture (without changing the exposure wavelength), using immersion lithography. In immersion lithography, the air gap between the photoresist-coated wafer and lens is replaced with a high refractive index fluid. Immersion lithography has been demonstrated with water as the immersion fluid. With water immersion lithography at 193 nm, the maximum resolution that can be printed can be decreased from 65 nm to 45 nm. To enable further resolution increases, immersion fluids with a higher index than water are needed. The requirements for next

generation high index fluids are: an index of refraction higher than water, high transparency, and physical properties similar to water.

A variety of methods to identify a high index fluid were completed. First, the optical properties of aqueous solutions of metal cations with varying anions were tested. A series of linear, cyclic, and polycyclic alkanes were also studied, since saturated systems have electronic transitions at wavelengths less than 200 nm, to provide the necessary transparency at 193 nm. Large alkane groups were also incorporated into either the cation or anion of a salt to develop an aqueous solution with the optical properties of a saturated hydrocarbon. In addition to these empirical surveys, a modeling approach was used to develop "designer" absorbance spectra that would correspond to fluids with a high index and low absorbance at 193 nm.

Additionally, in Appendix D, the results of an electrochemical study of the diffusion coefficient of ferrocene methanol in poly(ethylene glycol) diacrylate hydrogels of varying molecular weight and water content will be presented. The results of these mass transport studies can be used to qualitatively understand the mass transport characteristics of additional species in the hydrogel.

Table of Contents

List of Tables

List of Figures

List of Schemes

Chapter 1: Introduction to Immersion Lithography

Photolithography is the process used to define patterns in a semiconductor substrate, such as silicon, using light. These patterns are printed in multiple layers on the silicon wafer to make the complex integrated circuits used in the electronics industry. The semiconductor industry is continually driven to improve device performance and decrease cost through increasing the resolution of the patterning process and thereby create ever smaller circuit elements. Immersion lithography is a variant of photolithography in which a fluid, such as water, is introduced in place of air in the gap between the final lens element and the substrate. The high index of refraction of this fluid enables the transmission of greater angles of light to the photoresist so that higher resolution patterns can be printed. Research and development of immersion lithography is needed to provide hope that this technology can be used to continue to increase the resolution of the integrated circuit elements.

1.1 IMMERSION MICROSCOPY

Optical immersion imaging techniques were first applied in microscopy to increase the resolution and quality of the image. In 1679 Robert Hooke proposed the concept of an "index-matched" microscope to improve imaging "clearness and brightness."[1] When light passes through a component interface, some of the light is reflected and some is transmitted. In an index-matched microscope, the index of refraction of each component through which the light travels (sample, cover slip, lens, etc) is approximately the same. By increasing the similarity in the index of refraction of these components, less light will be reflected and more will be transmitted through index-matching.[2] Since in microscopy the transmitted light contains the information necessary for producing an image, reducing reflected light increases transmitted light and improves imaging contrast. Hooke suggested adding an immersion oil with an index of refraction similar to the lens and cover slip to the imaging system to improve imaging.[1]

An immersion microscope was not actually designed until the late 1840s, when Giovanni Battista Amici demonstrated imaging through a fluid layer. He proved Hooke's concept by inserting an index-matched immersion oil in the space between a microscope lens and the cover glass. This space was previously filled by air, which has a significantly different index than the lens and cover glass. The index-matching between the oil, lens, and cover glass reduced reflections and enhanced the image contrast.[1]

In about 1880 Ernest Abbe expanded the understanding of immersion imaging techniques by showing how these immersion techniques increase the light-accepting power of the lens. He called this light-accepting power the numerical aperture (NA).[1] NA is defined by

$$NA = n\sin\theta \tag{1.1}$$

where n is the index of refraction of the lens and θ is the angle the light makes with the normal within the lens. Higher lens NA values increase imaging resolution. To increase NA without changing the index of the lens material, the angle of transmitted light in the lens must be increased. The value of this angle depends on the behavior of the light as it passes through each layer prior to reaching the lens. In a microscope, the light passes through a slide, sample, cover glass, air (or immersion oil), and finally a lens. An $n\sin\theta$ term can be defined for each of these layers, where n is the index of refraction of the layer and θ is the angle the light makes with the normal within the layer. According to Snell's Law, which will be discussed in more detail in Section 1.3.2, the $n\sin\theta$ term across the light path is constant, or invariant. The layer with the minimum index of refraction thus limits the maximum $n \sin \theta$ value that can be obtained in the light path and, thus, the maximum possible angle of light in the lens.

In microscopes of Abbe's day, the sample was mounted in oil (Canada balsam) and placed under a cover glass to form the sample stack. The lens and sample stack were separated by a layer of air such that the light would travel first through the sample stack, then air, and finally the lens. This configuration is shown in Figure 1.1a. The index of refraction of the lens and sample stack is approximately 1.5 while the index of air is 1. Since air has the minimum index of the layers, the air layer limits $n \sin \theta$ in the light path to a value no greater than 1. If the air layer was replaced with a higher index layer, greater $n \sin \theta$ values would be possible and would enable greater angles of light to propagate to the lens, increasing resolution.

Abbe realized that replacing the low-index air layer with a high-index immersion oil would enable increases in the light-accepting power (NA) of the lens. With the high-index immersion oil, larger angles of light would be able to propagate to the lens and a greater NA lens could be used. A high NA immersion microscope, with an angle of light in the lens greater than the dry microscope, is shown in Figure 1.1b. In addition to increasing resolution the index-matching, due to replacing the air layer, decreases reflections between the layers, enhancing image contrast. Abbe called this microscopy technique "homogeneous immersion" since each layer has approximately the same index.[1, 3, 4] In 1889, Abbe designed his masterpiece, an immersion lens with an NA of 1.6. By increasing the resolution of the microscope, Abbe enabled research on microorganisms in the fields of biology and bacteriology that would not otherwise have been possible.[5]

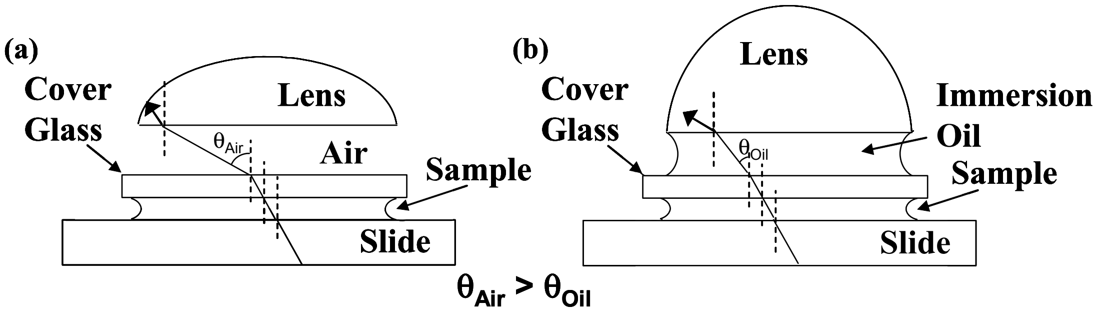

Figure 1.1: Dry (a) and immersion (b) microscopes

1.2 PHOTOLITHOGRAPHY

Photolithography is the process used to generate complex patterns on silicon wafers for semiconductor device manufacturing. An outline of the projection photolithography process is shown in Figure 1.2. A silicon wafer is first coated with a light sensitive, etch resistant organic film called a photoresist, or resist.[6, 7] The resist is exposed to light passed through a chromium-on-glass photomask fabricated such that only selected areas, corresponding to the desired circuit pattern, will be exposed in the resist. The light travels first through the mask and then through a configuration of lenses to form an image of the photomask in the resist. The configuration of lenses in a modern photostepper used in semiconductor manufacturing is composed of over thirty simple lens elements that can weigh more than 1000 pounds and is designed to produce an optical image of the mask in the photoresist that is reduced by a demagnification factor of 4.[8] Exposure to light initiates a photochemical reaction in the resist that changes the solubility of the resist in a developer solution. Development produces a three dimensional relief image of the mask pattern, which can be either positive or negative in tone, depending upon whether exposure enhances or inhibits solubility. The resist relief image then acts as an etch mask so that the pattern can be transferred into the wafer.

Finally, the remaining resist is stripped from the substrate. This photolithographic process is repeated multiple times to build device structures on the substrate.[6, 7]

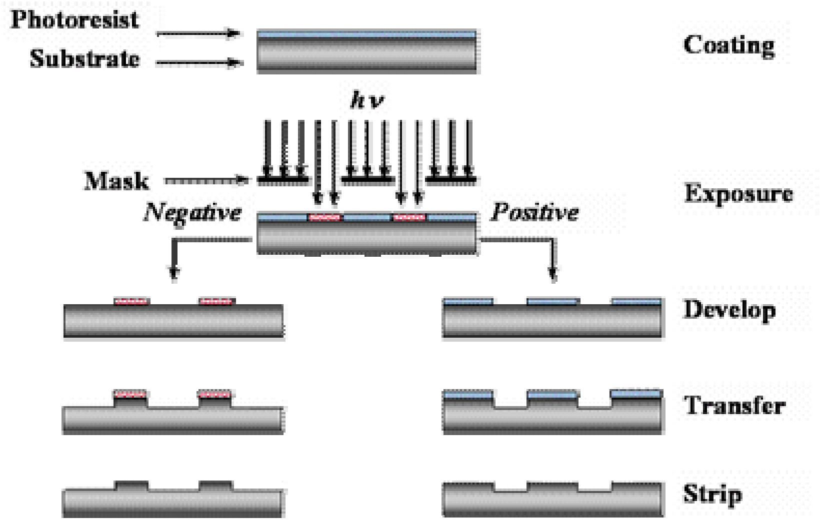

Figure 1.2: Negative and positive-tone photolithography

1.2.1 History of Optical Lithography

The earliest lithographic techniques relied on contact printing or proximity printing to expose the photoresist. In this system, the photomask was held in contact or close proximity to the wafer. For contact or proximity, the masks were designed with 1x magnification; no demagnification is possible since no lens elements can be used. Contact printing can provide higher resolution than proximity printing, but the mask suffers from repeated contact with the wafer. Despite extreme care, particles are continually ground into the surface of both the mask and photoresist-coated wafer. Frequent mask cleaning is necessary as photoresist fragments can adhere to the surface of the mask. Proximity printing precludes much of this damage to the mask but suffers from decreased resolution due to optical diffraction. With proximity printing techniques and optical or near-ultraviolet wavelengths, the minimum image size that can be practically achieved is approximately 2 – 3 μm.[8]

In the 1970s proximity printing was replaced with scanning projection lithography to increase resolution and avoid damaging the masks by contact with the wafer. In scanning lithography an image of the 1x masks used in proximity printing was projected through a series of lenses onto the resist. Due to the difficulty in designing a lens to project micron-scale images onto an entire 4- to 6-inch wafer, Perkin-Elmer Corporation developed a scanning technique to simultaneously scan the mask and wafer through a lens field shaped like a narrow arc until the entire wafer is exposed.[8]

To increase resolution, reduction steppers were introduced in the 1980s. With reduction steppers, a projection lens, with a fixed field size large enough to expose one or two semiconductor chips, is used to expose each field sequentially by repositioning the wafer after each exposure. Despite the increased time required to expose an entire wafer in this manner, stepper technology offers significant advantages over previous technologies. First, due to the different requirements for the lens, the stepper lens can be made with a greater NA than the full wafer lens. The stepper lens can also demagnify the mask pattern. The demagnification factor provides considerable relief in the minimum feature size tolerances on the mask.[8]

Step-and-scan systems were developed in the late 1980s to vary the size of the exposure field. Due to the differing size demands for different types of chips, the ability to vary exposure field size, not available in stepper systems, became necessary. Step-and-scan systems combine the technology of both scanners and steppers. The wafer is exposed by scanning across a rectangular slit aperture along a diameter of a conventional circular lens. The mechanical tolerances in this step-and-scan technology are very tight since the mask and wafer have to be moved simultaneously to within a few nanometers during each scan. Despite this complexity, scanning over the exposure field reduces localized aberrations and distortions in the lens by averaging the exposure along the scan direction. Step-and-scan lithographic equipment is the current state of the art in lithography tool design.[8]

1.2.2 Moore's Law

The semiconductor industry has continually improved the photolithographic process to reduce device size and thereby decrease cost on a per transistor basis and improve final product performance. In 1965 Gordon Moore, one of the founders of Intel, noticed that the number of discrete devices per integrated circuit had roughly doubled every year from 1959 to 1965. Moore predicted that semiconductor complexity would continue to increase at the same rate for at least 10 years.[9] Moore's prediction, now known as Moore's Law, has become something of a self-fulfilling prophecy as it has dictated the pace of resolution increase in the semiconductor industry for over 40 years. The economics of the semiconductor industry have become dependent on the exponential increase in resolution that causes products to become quickly obsolete and, thus, guarantees a continuous market for new products.[8] The Moore's Law rate of improvement is now built into the International Roadmap for Semiconductors (ITRS), an industry-wide technology roadmap published and updated yearly by the Semiconductor Industry Association (SIA).[10]

The increases in resolution required to perpetuate Moore's Law have been achieved primarily through decreases in the exposure wavelength with corresponding improvements in photoresist chemistry, optics, and resolution enhancement techniques.[11] The influence of these factors on the resolution that can be achieved with projection lithography is described by Rayleigh's equation:

$$R = \frac{k_1 \lambda}{NA} \tag{1.2}$$

where R is the half-pitch resolution of the image, k_1 is a resolution scaling factor that indicates the difficulty of the process (typical values from 0.3 to 0.8),[8, 11, 12] λ is the wavelength of exposure light, and NA is the numerical aperture of the lens. The increase in resolution with decreasing wavelength, and k_1 and NA used at each wavelength, is given in Figure 1.3.[11] With an exposure wavelength of 193 nm, features as small as 65 nm can be printed.[4]

Tool costs increase significantly with each decrease in the exposure wavelength. However, these costs are offset by increasing productivity, resulting from the increase in the number of transistors per chip, high throughput, and the ability to maintain long lifetimes for both the tool and mask.[13] Further decreasing the wavelength, from 193 nm to 157 nm, presents significant challenges primarily due to the difficulty in overcoming the high level of birefringence of CaF_2 for the lens material, developing transparent photoresists with the required etch characteristics and sensitivity, and designing a soft pellicle to protect the mask from defects. In addition to an increasing tool cost for 157 nm lithography, costs associated with complex photomasks, environmental control, and process materials would have required very high throughput to make 157 nm lithography cost-effective.[11, 13] As a result, 157 nm lithography was abandoned and alternatives to traditional wavelength reductions are needed to continue decreasing device size.

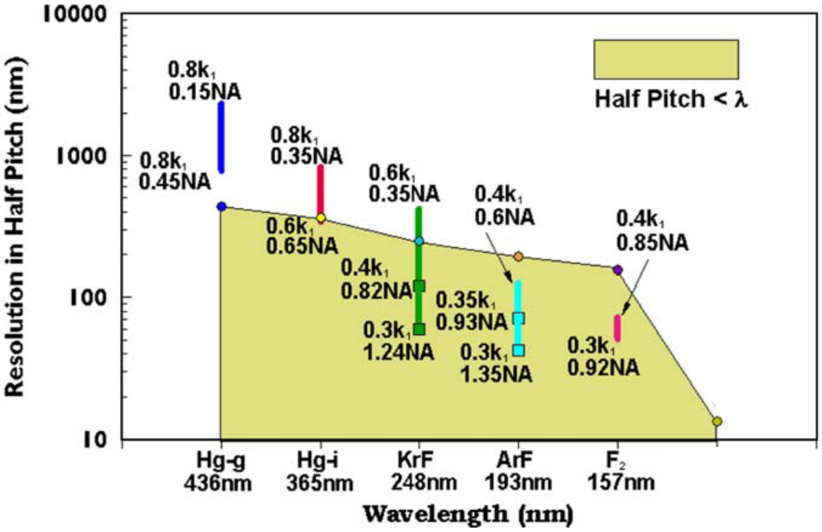

Figure 1.3: Increase in resolution with decreasing wavelength (436 nm to 157 nm)[11]

1.3 IMMERSION LITHOGRAPHY

The rising costs and other difficulties associated with the reduction in exposure wavelength to 157 nm raised interest in immersion lithography as a technique to increase resolution without decreasing the exposure wavelength. In immersion lithography, the traditional photolithographic process (Figure 1.2) is modified by inserting a fluid between the final lens element and photoresist. Since this fluid has a higher index of refraction than air, the use of a higher NA lens is possible. Increasing NA increases resolution, as demonstrated by Abbe and shown in Equation 1.2. Immersion lithography is an attractive patterning technique since, theoretically, the only variation required in the lithographic process is the introduction of a high index fluid between the lens and photoresist. The optical infrastructure and photoresists developed for exposure in a dry system should be generally compatible with an immersion system as well.[14, 15]

1.3.1 History of Immersion Lithography

While Abbe demonstrated high-NA optical immersion imaging over 100 years ago, immersion techniques to increase NA for lithography were first considered in the 1980s. In 1981, an oil immersion objective was used to increase resolution through a high NA exposure system, similar to a microscope, to image 200 nm isolated lines.[16] This resolution was approximately an order of magnitude better than the state of the art at that time. A method which used an index-matching fluid between the lens and photoresist to increase resolving capability by decreasing standing waves and other adverse affects was patented in 1982.[17] In 1992 an immersion oil with an index of 1.516 was used with an exposure wavelength of 404 nm and an NA of 1.25 to print patterns as small as 180 nm, a significant reduction from the 300 nm resolution that could be achieved at that time.[18] Immersion lithography with an exposure wavelength of either 193 nm or 157 nm was first proposed in 1992.[19] Images with a line-width of 40 nm were demonstrated in 1999 using an exposure source of 257 nm with cyclooctane ($n_{257} = 1.5$) as the immersion fluid.[20] While immersion lithography has been successfully demonstrated at a range of exposure wavelengths, implementation of these technologies was unnecessary due to the greater resolution increase that could be achieved with exposure wavelength reduction. Due to challenges associated with further wavelength reduction, and availability of high index fluids at 193 nm, immersion lithography at 193 nm had to be seriously considered as a potential path to further increases in resolution.

1.3.2 Benefits of Immersion Lithography

When light is incident on a boundary between two surfaces, a portion of the light is reflected and the remaining portion is transmitted (or refracted). Derived from continuity requirements, Snell's Law states that across the surfaces through which the light passes:

$$n_1 \sin\theta_1 = n_2 \sin\theta_2 = n_3 \sin\theta_3 = \ldots = n_k \sin\theta_k \tag{1.3}$$

where n_i is the index of refraction of the surface and θ_i is the angle the light makes with the normal, within the surface, so that the term $n \sin\theta$ is invariant for each of the layers in the film stack.[21] Snell's Law through a multilayer film stack is illustrated in Figure 1.4.

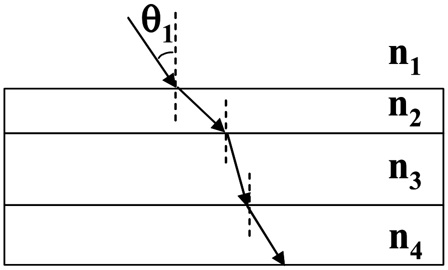

Figure 1.4: The propagation of light through a film stack obeys Snell's law; $n \sin\theta$ is invariant for each layer

Snell's Law also defines a critical angle (θ_c) which is the maximum angle that can be achieved in an incident layer (layer 1) to allow light to be transmitted into the subsequent layer (layer 2). When the second layer has a lower refractive index than the first layer (i.e. $n_2 < n_1$), a real value for θ_2 can only be obtained for values of θ_1 at which

$$\sin\theta_1 \le \frac{n_2}{n_1}. \tag{1.4}$$

Thus, the maximum value of θ_1, for which real values of θ_2 can be obtained, is θ_c. When $\theta_1 > \theta_c$, total internal reflection occurs such that the light is reflected back into the first layer rather than transmitted across the interface between the two layers.[21]

In photolithography, the film stack consists of the lens, the air or fluid layer between the lens and wafer, and the photoresist. The Lagrange invariant (or optical invariant) relates the angles entering and exiting the lens to the magnification factor (m) as

$$m = \frac{n_o \sin\theta_o}{n_i \sin\theta_i} \tag{1.5}$$

where n_o is the refractive index of the medium on the object side of the lens, θ_o is the angle of light entering the lens on the object side relative to the optical axis, n_i is the refractive index of the medium on the image side of the lens, and θ_i is the angle of light exiting the lens on the image side relative to the optical axis. The relationship between these variables for a lens system is given in Figure 1.5. For a lens with a de-magnification factor of 4x, m = ¼. Through the Lagrange invariant, the lens system behaves as a film which obeys Snell's law.[22]

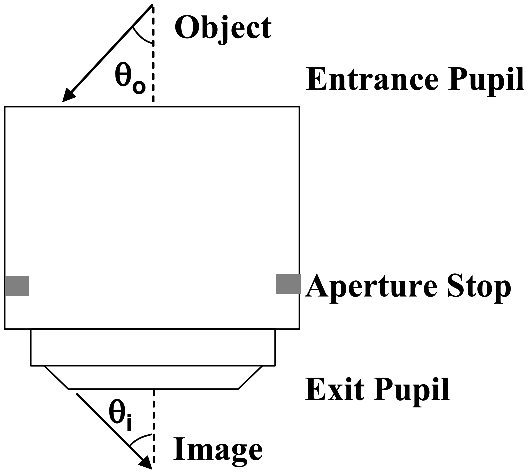

Figure 1.5: The angles of light that propagate through a lens can be described by the Lagrange invariant

In a photolithographic imaging system, light diffracts from a mask (or object of the imaging lens) at a particular angle. This diffracted light propagates through the lens and emerges on the imaging side of the lens at an angle given by the Lagrange invariant. The light then propagates through the medium between the lens and wafer and passes into the photoresist. Snell's Law dictates that $n\sin\theta$ is invariant through each of the layers in the film stack and determines the angle of the light in the photoresist.[22]

Replacing one of the layers in the film stack with a higher index layer, such as replacing the air layer with a fluid layer, enables $n\sin\theta$ to increase. The maximum value of $n\sin\theta$ is limited by the layer with the minimum index of refraction. When air (n = 1) is used as the layer between the lens and photoresist, the maximum angle that can be achieved in the lens is

$$\sin\theta_{lens,\max} = \frac{1}{n_{lens}}. \tag{1.6}$$

However, if a fluid layer ($n_{\text{fluid}} > 1$) is used in place of the air layer, the maximum angle that can be achieved in the lens increases, as

$$\sin\theta_{lens,\max} = \frac{n_{fluid}}{n_{lens}}. \tag{1.7}$$

Increasing the minimum index in the film stack by replacing the air layer with a fluid layer enables a higher maximum angle. If a lens is designed with a higher NA ($n\sin\theta$) that allows the larger angles to propagate into the resist, the resolution will increase, according to Rayleigh's equation (Equation 1.2). If the same high NA lens were designed for an air system, total internal reflection would occur in the air layer since the incident angle would exceed the critical angle (θ_c). The difference in the propagation of light for a high NA lens through an air layer or fluid layer is shown in Figure 1.6. The fluid simply enables the propagation of light at angles that would otherwise exceed the critical angle (θ_c).

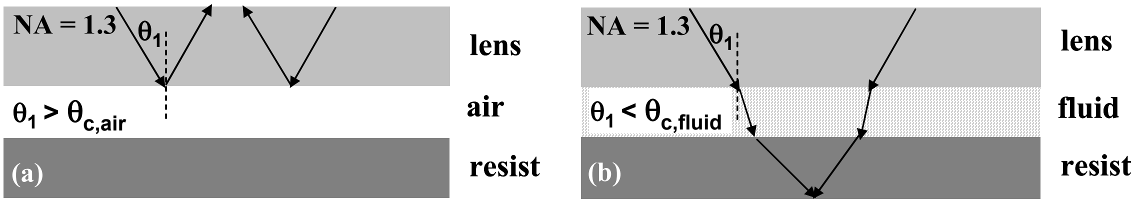

Figure 1.6: High NA lens with a dry system (a) in which total internal reflection occurs and with an immersion system (b) in which the light propagates to the resist

Alternatively, the resolution increase can be considered to result from an effective reduction in the exposure wavelength. The effective wavelength in the fluid is reduced from the wavelength in vacuum as

$$\lambda_{eff} = \frac{\lambda_o}{n} \tag{1.8}$$

where λ_{eff} is the effective exposure wavelength, λ_o is the vacuum wavelength, and n is the index of the air or fluid layer. For the air layer, the effective exposure wavelength is equal to the vacuum wavelength. However, for a fluid layer, the vacuum wavelength is reduced by the index of the fluid layer.[23, 24]

Immersion lithography introduces an additional benefit in a photolithographic system by increasing the depth of focus. Depth of focus (DOF) is a measure of the imaging tolerance to variations in path length difference from the lens to the imaging plane. A process with a greater depth of focus is more robust and can tolerate increased variation in topography on the wafer, resist thickness, wafer and mask flatness, tilts, focusing error, image plane nonuniformity, and scanning imperfections.[25]

An image is in focus when all of the diffraction orders that form the image are in phase at the same point. For the same NA, the angle of light for different diffraction orders is smaller within the fluid layer than within the air layer. Since these angles are smaller, smaller optical path differences exist between each diffracted orders. As a result, there is a smaller amount of image degradation when they are out of phase, or defocused, so that the DOF is greater for immersion lithography than dry lithography.[22, 26]

Lord Rayleigh derived a simple expression for estimating DOF, assuming a binary pattern of lines and spaces at the resolution limit in a low NA system. This expression is given by

$$DOF = k_2 \frac{\lambda}{NA^2} \tag{1.9}$$

where k_2 is the Rayleigh coefficient of DOF. To develop an expression for a high NA system without Lord Rayleigh's assumptions, an exact expression for the optical path difference (OPD) between the desired and defocused wavefronts should be included in the DOF equation. Accounting for OPD and using a Taylor series approximation, for a high numerical aperture system,

$$DOF = \frac{k_2}{2} \frac{\lambda}{(1-\cos\theta)} = \frac{k_2}{4} \frac{\lambda}{\sin^2\left(\frac{\theta}{2}\right)} \tag{1.10}$$

where k_2 is the Rayleigh coefficient of DOF and θ is the maximum angle at which a diffracted order will emerge from the lens.[22, 27] For imaging through a fluid layer, this equation becomes

$$DOF = \frac{k_2}{2} \frac{\lambda}{n_{fluid}(1-\cos\theta)} \ . \tag{1.11}$$

The angle, θ, can be related to the pitch of the diffracted orders from a line and space mask pattern by Bragg's condition,

$$n_{fluid} \sin\theta = \frac{m\lambda}{p} \tag{1.12}$$

where m is the diffracted order and p is the pitch, or total distance of one line and space feature. Combining Equations 1.11 and 1.12 to remove dependence on the angle and comparing to the DOF for a dry system (n_{fluid} is replaced by n_{air} and equals 1),

$$\frac{DOF_{immersion}}{DOF_{dry}} = \frac{1-\sqrt{1-\left(\lambda/p\right)^{2}}}{n_{fluid}-\sqrt{n_{fluid}^{2}-\left(\lambda/p\right)^{2}}}\,. \tag{1.13}$$

From this expression, DOF is improved by increasing the fluid index. $\mathrm{DOF}_{\mathrm{immersion}}$ increases over $\mathrm{DOF}_{\mathrm{dry}}$ still further with decreasing pitch.[22]

1.4 FIRST GENERATION IMMERSION LITHOGRAPHY

The use of immersion lithography at a wavelength longer than 193 nm would not provide a significant resolution benefit over 193 nm dry lithography. Thus, the successful implementation of immersion lithography required the identification of a fluid with a high index and low absorbance at 193 nm. The immersion fluid must have a high enough index of refraction at 193 nm to provide a sufficient increase in resolution over 193 nm dry lithography to justify the use of immersion lithography as an alternative patterning strategy. The fluid must also be transparent at 193 nm so that a substantial portion of the light will pass through the fluid layer and into the photoresist. In addition to the critical optical property requirements, the fluid must also have physical properties that facilitate high speed scanning as the wafer is exposed through the fluid. The fluid should preferably be non-toxic, and otherwise compatible with the clean room processing environment, and should not interact adversely with the photoresist by dissolving or swelling it. The fluid must be very pure and contain a very low concentration of particles. Particles and contaminants might remain on the resist and optics upon evaporation of the fluid and produce defects. Also, contaminants in the fluid can form absorbing photoproducts upon exposure. The index must not change significantly with temperature. Variations in the index due to temperature fluctuations could cause a focal shift of the imaging plane and spherical aberrations.[15, 24, 26]

Despite the lengthy list of requirements, water is an attractive candidate for immersion lithography. Water has a relatively high index of refraction, $n_{193} = 1.44$,[28] and low absorbance, $\alpha_{193} = 0.036\ \mathrm{cm}^{-1}$.[26] For $n_{\mathrm{fluid}} = 1.44$, the exposure wavelength is effectively decreased from 193 nm to 134 nm or NA is effectively increased to a maximum of 1.44 to provide a potential resolution improvement of 43%.[4] An absorption coefficient of $0.036\ \mathrm{cm}^{-1}$ would provide a working distance of 6 mm with 95% transmission. This working distance is less than the working distance in dry tools but is not a significant deviation.[29] Water also has a low viscosity and high surface tension. Since water is an existing component of wafer processing, compatibility with the semiconductor processing environment is not a significant concern.[15] Water has a relatively high thermo-optic coefficient, $dn/dT = -1.00 \times 10^{-4}$ /°C at 194.5 nm and 21.5 °C.[28] This thermal variation is approximately 20 times greater than the traditional N_2 ambient ($dn/dT = -0.9 \times 10^{-6}$ /°C), but engineering solutions could be designed to provide precise temperature control.[15, 28, 30]

Water has the necessary optical properties to enable a significant resolution increase using immersion lithography at 193 nm. Water also has the nominal physical property requirements for semiconductor manufacturing, but several key technical design challenges exist in the implementation of immersion lithography with water in full scale semiconductor manufacturing, such as the development of a fluid handling system or the understanding of bubble formation.

1.4.1 Fluid Handling System

A fluid handling system that can both easily contain the water and allow rapid exposure of the wafer is necessary for a high-throughput and economically viable process. Two concepts were proposed for the liquid containment in the scanner system. First, in the bath configuration, the wafer is fully immersed in a bath of fluid on the wafer stage, and the bottom of the lens is dipped into the bath. This configuration is shown in Figure 1.7a. This system provides a uniform fluid environment over the entire wafer area, easing concerns of exposure variation during scanning.[24, 31] With full immersion, metrology processes for wafer alignment and leveling would need to be re-designed to account for the fluid environment. Fluid dynamics simulations of the flow of a bath of fluid on the wafer show that each movement ("step") of the wafer stage causes significant perturbations to the bath. The long time required for the fluid to "relax," or stop flowing, would significantly decrease system throughput.[24] The second concept is the local fill (or shower) configuration, shown in Figure 1.7b. In the local fill design, the fluid is injected between the lens and wafer so that the fluid is present in the working optical area only. Since this design is more similar to dry systems, wafer alignment and leveling would not need to be re-designed.[24, 30] Due to the high surface tension and low viscosity of water, the fluid droplet could be contained between the lens and wafer, up to a maximum scanning speed. At speeds greater than the maximum, the droplet either leaves a tail of liquid on the wafer or dewets from the lens resulting in defects and decreased imaging quality. On surfaces with which water has a high contact angle (so that the droplet is less likely to wet the surface), scanning speeds greater than 600 mm/s have been demonstrated.[32, 33] A disadvantage of the local fill design is the difficulty of scanning near the wafer edge, which could result in fluid leakage or bubble formation when the shower overlaps the edge.[24] However, this difficulty was overcome by introducing a wide rim on the scanning stage that is level with the wafer surface.[31] The local fill design provides a fluid handling system that can best achieve high throughput with minimal deviation from the dry system.

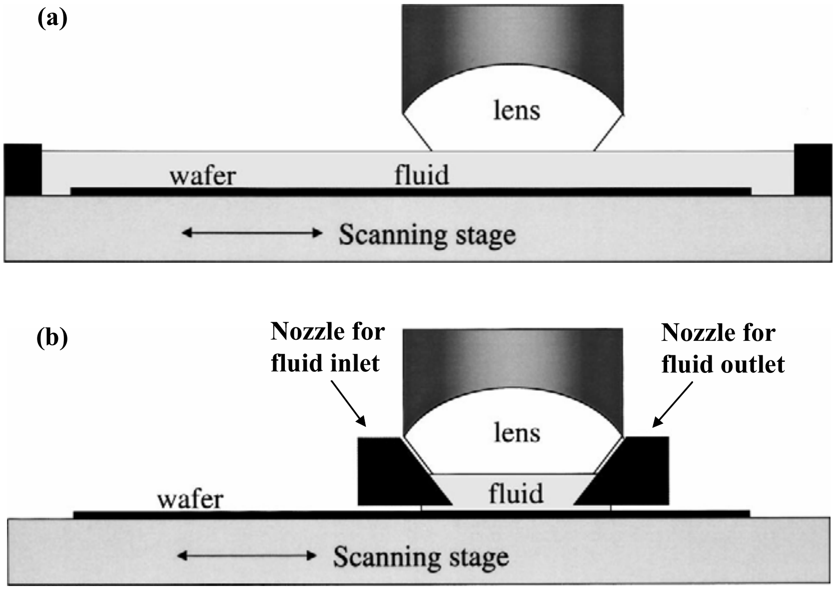

Figure 1.7: Bath (a) and local fill (b) configuration for an immersion fluid handling scanning system[24]

1.4.2 Fluid-Resist Interaction

Swelling or dissolution, chemical reaction between the liquid and resist, and/or leaching of resist components into the fluid or fluid into the resist could lead to imaging performance degradation.[31] Several researchers have studied these effects.[29, 34-36] For exposure times < 1 min, the thickness of photoresist soaked in water does not significantly change, so that swelling effects appear negligible.[29] With water as the immersion fluid, chemical reaction with the photoresist is also not a significant concern. Studies to determine the concentration of photoacid generator (PAG), base, and residual casting solvent extracted or leached from the resist film into water were performed using liquid scintillation counting (LSC), liquid chromatography mass spectrometry (LC/MS), and scanning electrochemical microscopy (SECM). PAG leaching from the resist into water was observed with each of the techniques. The LSC results were used to quantify this extraction. The amount of PAG leaching from a resist film is 30 – 50 ng/cm^2, depending on photoresist formulation, and base leaching is 2 ng/cm^2, independent of formulation.[35] The extractions occur within the first 30 s of fluid immersion and can be decreased with an initial water rinse. No significant leaching of residual casting solvent was observed with any of the techniques.[35] Despite leaching of these components, imaging is not significantly affected.[24, 34] Additionally, topcoats or barrier layers coated on the resist surface, can be used to block leaching if resist component extraction becomes a concern.[36]

1.4.3 Bubble Formation

Another potential problem with immersion lithography is bubble formation in the immersion fluid. The most significant effect of bubbles in the immersion fluid is scattering, which reduces image contrast by decreasing the intensity of light that reaches the wafer. This scattering effect is a function of bubble quantity and size and also depends on the distance from the resist surface.[23] Bubble formation could also lead to index inhomogeneities that could reflect or refract light differently than the bulk liquid and distort the local image projected into the resist.[15, 26] Bubbles might form by resist outgassing during exposure, by entrapping air during fluid filling or removal, and/or by pressure and temperature changes that induce dissolved gases to form bubbles. Bubbles have also been observed forming in air-saturated water as it spreads along a surface. Most typically, these surfaces are hydrophobic, and the bubbles form due to the energetic advantage created by having a gas layer isolating the water from the surface.[15, 23] Most bubble formation can be prevented by degassing the immersion fluid with commercially available degassing tools prior to use. Since the water is circulated continuously in a local fill configuration, air dissolution at the boundaries does not have time to saturate the fluid droplet. Since the fluid is not saturated, entrapped air quickly dissolves.[30] Resist outgassing is also not a significant concern. As with bubbles formed at the air-liquid interface, gas released into the liquid will quickly dissolve.[23] Finally, careful design of nozzles and filling procedures can prevent air entrapment.[30] With sophisticated fluid fill designs and a degassed fluid, bubble formation is not a substantial obstacle to the implementation of full scale immersion lithography. However, even if bubbles do form, experiments to determine scattering effects, using polystyrene microspheres of varying size to mimic the air bubble behavior, reveal that bubble formation is not a significant concern in immersion imaging for bubbles less than 0.5 μm in diameter.[37]

1.4.4 Thermal Aberrations

Defects caused by thermal aberrations are also a potential concern for immersion lithography. Water has a thermo-optical coefficient (dn/dT) approximately 20 times greater than that of air.[30] Thus, for an immersion system, heating during exposure could cause variations in the index of the fluid. Variations in index cause differences in the optical path length of the converging rays, resulting in focal shifts.[38] If the temperature change is homogeneous, focal shift and spherical aberrations can be easily corrected by repositioning the wafer stage. Local temperature fluctuations are more problematic since they cause local variations in focus and spherical aberrations.[24] Simulations of the heating process, using a "global" approach to account for heating between neighboring die, determined the focal change per die by considering the past stepping and scanning history of each die. Based on assumed or expected fluid flow conditions, the maximum temperature change was calculated to be 0.18 K. This temperature change results in a focal shift of approximately 7 – 9 nm.[38] The focal change during scanning should be readily controllable using automated focusing changes to reposition the wafer. Further control would be available by combining the automated focusing changes with an algorithm to predict heating effects and the subsequent focus shifts. Rapidly circulating the fluid droplet will also help to prevent temperature increases.[38]

1.4.5 Defectivity

Particle defects in semiconductor fabrication have long been a major concern, as evidenced by the major investment in “cleanroom” technologies. A switch to immersion lithography raises several concerns about particle defectivity. Particles can be generated in immersion systems from a variety of sources. First, particle contamination levels in water are much higher than in air. A state of the art water purification system can reduce particle levels to ~100 greater than 0.1 μm particles per liter. For air, the particle count can be reduced to < 1 greater than 0.1 μm particle per 28 liter.[39] However, since these particles are uniformly distributed through the fluid, some of them will be out of focus during imaging. Specific defectivity will only arise due to particles at, or very near, the fluid-resist interface. Another source of defectivity is evaporation of fluid droplets, depositing particles on the wafer. Finally, particles extracted from the fluid handling hardware are also an area of concern.[39] Improved filtration systems and careful design of fluid handling systems can be used to reduce particle counts in the fluid. The use of topcoats as a barrier layer on the photoresist and rinsing any droplets deposited on the wafer prior to their evaporation will also decrease defectivity on the wafer.

1.4.6 Polarization Effects

The polarization state of light becomes an important consideration as NA is increased with immersion lithography. For lower NA systems, polarization effects could largely be ignored.[40] However, when NA > 1 in the immersion systems, the angle of light through the optical path increases over dry systems, when NA < 1. With the high angles present for NA > 1, the interference of two beams of light, required to form an image, depends more strongly on the polarization state of the light. The orientation of the electric field relative to the plane of incidence describes the polarization state of light. In transverse electric (TE) polarization the electric field is perpendicular to the plane of incidence, and for transverse magnetic (TM) polarization the electric field is parallel to the plane of incidence. When light is oriented parallel to the plane of incidence (TM), the interference between two intersecting beams decreases as the angle between those beams increases, resulting in decreased image contrast at high NA. For the perpendicular orientation (TE), complete interference exists between two intersecting beams, independent of angle. Therefore, for high NA imaging, TE polarized light is essential to achieve adequate image contrast.[4, 41] To maintain a TE-polarized state when the light reaches the resist, the influence of polarization throughout the path of the lithographic exposure system needs to be understood and addressed. Through simulations to understand polarization effects, the design of an immersion exposure system using polarized light for adequate image contrast is feasible.[40]

1.5 NEXT GENERATION IMMERSION LITHOGRAPHY

In 2006 Nikon shipped the first water immersion scanner. This tool was designed with a lens NA of 1.3 and was able to image lines and spaces as small as 45 nm. Nikon used a local fill nozzle design, which continuously supplies and recovers water. Nikon achieved a bubble free droplet with no leakage on the wafer even at the maximum scanning speed of 500 mm/s. The reported defect levels were also lower than a conventional dry tool. Nikon developed simple optics to produce highly polarized light to achieve adequate image contrast with no loss of power.[42]

The successful demonstration that the critical issues associated with full-scale water immersion lithography manufacturing could be resolved raised interest in exploring the future capabilities of immersion lithography. To further increase the resolution possible with immersion lithography to sub-45 nm device features, fluids with an index of refraction greater than water are needed. In addition to a high index of refraction, the fluid must also have a low absorption coefficient at 193 nm and physical properties similar to those of water, to maintain compatibility with first generation immersion scanners. The desired optical and physical property requirements for the second and third generation immersion fluids are given in Table 1.1.[43] Attempts to identify next generation immersion fluid candidates have included many different types of fluids. First, aqueous solutions were studied by adding high index salts, surfactants, or nanoparticles to water in an attempt to obtain a high index solution with a low absorbance and physical properties similar to water. Saturated hydrocarbons are also promising high index fluid candidates.[43]

To enable further resolution increases with next generation immersion lithography, new high index lens materials and photoresists will be needed, in addition to a fluid with an index greater than water. For 193 nm lithography, quartz (n_{193} = 1.56) is used as the lens material. If the index of the immersion fluid is increased above 1.56, the lower index quartz lens material will limit the maximum achievable resolution increase, despite the high index fluid. Thus, alternative lens materials need to be identified. Lutetium aluminum garnet (LuAG) is the most promising candidate for the next generation lens material, with an index of 2.1 at 193 nm. However, the absorbance of LuAG needs to be decreased before this material can be used as a lens.[44] Additonally, the typical 193 nm acrylate photoresist has an index of approximately 1.7. For a third generation immersion fluid, with n_{193} = 1.8, the photoresist becomes the lowest index material in the film stack (assuming a new lens material is available). The design of new photoresist materials with a high index and low absorbance at 193 nm would be necessary for third generation immersion lithography.[45]

Table 1.1: Immersion Fluid Requirements for 38 nm and 32 nm features[43]

	Flat Last Lens		Concave Last Lens	
Half-pitch (nm)	≤ 38	≤ 32	< 38	< 32
Fluid Refractive Index	> 1.65	> 1.9	> 1.65	> 1.9
Fluid absorption (cm^{-1})	0.03		0.15	
Fluid dn/dT (/˚C)	2.5×10^{-6}		0.5×10^{-6}	
Differential Cost of Ownership	~ 1 – 2 $ / layer			
Rheology	Comparable to water			
Viscosity	< 3 cP			
Surface Tension	Similar to water			
Lifetime	Minimal photochemical effects			
Imaging	No degradation impact on imaging from interactions with resist/topcoat			

1.6 ALTERNATIVE NEXT GENERATION TECHNIQUES

High index immersion lithography is not the only option for sub-45 nm resolution. In addition to immersion lithography, several additional technologies have the potential to further decrease feature size.

The first of these techniques is step and flash imprint lithography (S-FIL). In S-FIL, a template is pressed into a monomer solution to form a pattern of the template in the solution. The monomer is then photocured so that when the mold is removed, the topography of the mold is transferred into the material.[46] The low cost and simplicity of this technique, and its success in transferring nanoscale patterns with high fidelity,[47] makes it attractive for photolithography. Since S-FIL is a mechanical process, the resolution is not limited by the diffraction of light or the photoresist chemistry and development, as in optical photolithography. Instead, the resolution of S-FIL depends on the minimum template feature size that can be fabricated. As the template fabrication process improves, imprint resolution should also improve.[46]

Secondly, double patterning or double exposure techniques are used to reduce feature size by combining two large images to form one small image. Double patterning is accomplished by first printing a large pattern with double the desired spacing. The position of the photomask is then shifted, and the large pattern is printed again, offset from the first pattern by half, to effectively reduce the pattern size by half. This technique is attractive since the large patterns can be easily imaged with existing technology, so that significant new process development is not required. However, double patterning increases cost and complexity since a doubling of the number of process steps and twice the number of tools is required.[48] Due to resist "memory" of each exposure, chemical development, and often pattern transfer (etch), of the first pattern is required prior to exposure with the second pattern so that the double printing does not appear as an exposure of the entire wafer. The complexity of double patterning would decrease if the resist could simply be exposed twice, through double exposure techniques. Double exposure techniques, however, require the development of new photoresist materials that are not yet available.[49]

Finally, extreme ultraviolet lithography (EUV) is a patterning strategy that can extend resolution to sub-45 nm features. In EUV a 13.5 nm source wavelength is used for projection patterning with reflective optics. Due to the complex light source necessary to produce high intensity 13.5 nm energy, required high vacuum, and optics, the expected cost of an EUV tool, \$54 – 89M, is prohibitive at current throughput levels.[50] Additionally, some of the critical issues for EUV have yet to be resolved, including the development of a resist with high sensitivity to print acceptably smooth lines (with low line edge roughness), a mask that can maintain low defect levels, and a greater intensity light source. While researchers are working to overcome these difficulties and reduce the cost of the tool by increasing throughput, EUV will likely not be ready for full scale production before 2013.[48, 51]

1.7 CONCLUSIONS

Maintaining Moore's law for the past 40 years, the semiconductor industry has continually increased resolution to decrease transistor cost and increase performance. Resolution increases have traditionally been achieved through reduction of the exposure wavelength. However, as further wavelength reductions became increasingly challenging, immersion lithography at 193 nm, using water as the immersion fluid, became the leading patterning strategy for printing 45 nm features. Optical immersion techniques have been used in microscopy to increase resolution by increasing NA since the 1880s, when Abbe designed the first high NA microscope. Immersion lithography is an attractive patterning technique since the optics, photoresists, and other exposure infrastructure developed for dry 193 nm lithography can be used with 193 nm immersion systems. Design challenges associated with the introduction of a water droplet between the final lens element and photoresist have been successfully overcome so that full scale water immersion lithography has been used since 2006.

Additional resolution increases can be achieved with immersion lithography by replacing water with a fluid of higher index. These next generation immersion techniques require not only the development of a high index and low absorbance fluid but also high index lens materials and photoresists. The identification of a high index and low absorbance fluid at 193 nm is critical for the success of next generation immersion lithography. The remaining chapters of this dissertation will focus on high index fluid development for next generation immersion lithography.

Alternative patterning strategies, such as S-FIL, double patterning, or EUV, are being developed for sub-45 nm device fabrication in conjunction with high index immersion lithography. While traditional wavelength reductions to increase resolution are no longer feasible, these new lithographic techniques have the potential to achieve resolution increases for future patterning nodes, in accordance with Moore's law.

1.8 REFERENCES

1. Bradbury, S., *The Evolution of the Microscope*. 1st. 1967, New York: Pergamon Press. pp. 357.
2. Hecht, E., *Optics*. 4th. 2002, San Francisco: Addison Welsey. pp. 698.
3. Kingslake, R., *Optical System Design*. 1983, New York: Academic Press. pp. 323.
4. Smith, B. W., Bourov, A., Kang, H., Cropanese, F., Fan, Y., Lafferty, N. and Zavyalova, L., *Water immersion optical lithography at 193 nm.* J. Microlith. Microfab. Microsys., 2004. **3**(1): p. 44-51.
5. Volkmann, H., *Ernst Abbe and His Work.* Appl. Opt., 1966. **5**(11): p. 1720-1731.
6. Thompson, L. F., Willson, C. G. and Bowden, M. J., *Introduction to Microlithography*. 2nd. 1994, Washington, D.C.: An American Chemical Society Publication. pp. 540.
7. Stewart, M. D., Patterson, K., Somervell, M. H. and Willson, C. G., *Organic imaging materials: a view of the future.* J. Phys. Org. Chem., 2000. **13**(12): p. 767-774.

8. Hibbs, M. S., *System Overview of Optical Steppers and Scanners*. 2nd. Microlithography: Science and Technology, Suzuki, K. and Smith, B. W. 2007, Boca Raton: CRC Press. pp. 96.

9. Moore, G. E., *Cramming more components onto integrated circuits.* Electronics Magazine, 1965. **38**(8).

10. *The International Technology Roadmap for Semiconductors.* http://public.itrs.net, 2008.

11. Lin, B. J., *The ending of optical lithography and the prospects of its successors.* Micro. Eng., 2006. **83**(4-9): p. 604-613.

12. Lin, B. J., *Optical lithography-present and future challenges.* C. R. Phys., 2006. **7**(8): p. 858-874.

13. Sreenivasan, S. V., Willson, C. G., Schumaker, N. E. and Resnick, D. J., *Low-cost nanostructure patterning using step and flash imprint lithography.* Proc. SPIE Int. Soc. Opt. Eng., 2002. **4608**(Nanostructure Science, Metrology, and Technology): p. 187-194.

14. Switkes, M. and Rothschild, M., *Immersion lithography at 157 nm.* J. Vac. Sci. Technol., B, 2001. **19**(6): p. 2353-2356.

15. Switkes, M., Kunz, R. R., Rothschild, M., Sinta, R. F., Yeung, M. and Baek, S. Y., *Extending optics to 50 nm and beyond with immersion lithography.* J. Vac. Sci. Technol., B, 2003. **21**(6): p. 2794-2799.

16. Feuer, M. D. and Prober, D. E., *Projection photolithography-liftoff techniques for production of 0.2-micron metal patterns.* IEEE Trans. Electron Devices, 1981. **ED-28**(11): p. 1375-8.

17. Tabarelli, W. and Loebach, E. W. 1982. *USA Patent No. 4346164*

18. Kawata, H., Matsumura, I., Yoshida, H. and Murata, K., *Fabrication of 0.2 micro m fine patterns using optical projection lithography with an oil immersion lens.* Jpn. J. Appl. Phys., Part 1, 1992. **31**(12B): p. 4174-7.

19. Owen, G., Pease, R. F. W., Markle, D. A., Grenville, A., Hsieh, R. L., Von Bunau, R. and Maluf, N. I., *1/8 micron optical lithography.* J. Vac. Sci. Technol., B, 1992. **10**(6): p. 3032-6.

20. Hoffnagle, J. A., Hinsberg, W. D., Sanchez, M. and Houle, F. A., *Liquid immersion deep-ultraviolet interferometric lithography.* J. Vac. Sci. Technol., B, 1999. **17**(6): p. 3306-3309.

21. Born, M. and Wolf, E., *Principles of Optics*. 2nd. 1964, New York: Pergamon Press. pp. 808.

22. Mack, C. A. and Byers, J. D., *Exploring the capabilities of immersion lithography through simulation.* Proc. SPIE Int. Soc. Opt. Eng., 2004. **5377**(Pt. 1, Optical Microlithography XVII): p. 428-441.

23. Lin, B. J., *Immersion lithography and its impact on semiconductor manufacturing.* J. Microlith. Microfab. Microsys., 2004. **3**(3): p. 377-395.

24. Mulkens, J., Flagello, D. G., Streefkerk, B. and Graeupner, P., *Benefits and limitations of immersion lithography.* J. Microlith. Microfab. Microsys., 2004. **3**(1): p. 104-114.

25. Lin, B. J., *Depth of focus in multilayered media - a long-neglected phenomenon aroused by immersion lithography.* J. Microlith. Microfab. Microsys., 2004. **3**(1): p. 21-27.

26. Rothschild, M., Bloomstein, T. M., Kunz, R. R., Liberman, V., Switkes, M., Palmacci, S. T., Sedlacek, J. H. C., Hardy, D. and Grenville, A., *Liquid immersion lithography: Why, how, and when?* J. Vac. Sci. Technol., B, 2004. **22**(6): p. 2877-2881.

27. Lin, B. J., *The k3 coefficient in nonparaxial l/NA scaling equations for resolution, depth of focus, and immersion lithography.* J. Microlith. Microfab. Microsys., 2002. **1**(1): p. 7-12.

28. Burnett, J. H. and Kaplan, S. G., *Measurement of the refractive index and thermo-optic coefficient of water near 193 nm.* J. Microlith. Microfab. Microsys., 2004. **3**(1): p. 68-72.

29. Switkes, M., Kunz, R. R., Sinta, R. F., Rothschild, M., Gallagher-Wetmore, P. M., Krukonis, V. J. and Williams, K., *Immersion liquids for lithography in the deep ultraviolet.* Proc. SPIE Int. Soc. Opt. Eng., 2003. **5040**(Pt. 2, Optical Microlithography XVI): p. 690-699.

30. Owa, S. and Nagasaka, H., *Advantage and feasibility of immersion lithography.* J. Microlith. Microfab. Microsys., 2004. **3**(1): p. 97-103.

31. Switkes, M., Rothschild, M., Kunz, R. R., Baek, S. Y., Cole, D. and Yeung, M., *Immersion lithography: beyond the 65 nm node with optics.* Microlithography World, 2003. **12**(2): p. 4-6, 18, 20.

32. Bassett, D. W. and Bonnecaze, R. T., *Immersion lithography for laser mask writing.* J. Vac. Sci. Technol., B, 2006. **24**(6): p. 2659-2667.

33. Harder, P. M. and Shedd, T. A., *Contact angles and liquid loss behavior of high index fluids.* Proc. SPIE Int. Soc. Opt. Eng., 2007. **6533**(European Mask and Lithography Conference, 2007): p. 653305/1-653305/12.

34. Hinsberg, W., Wallraff, G. M., Larson, C. E., Davis, B. W., Deline, V., Raoux, S., Miller, D., Houle, F. A., Hoffnagle, J., Sanchez, M. I., Rettner, C., Sundberg, L. K., Medeiros, D. R., Dammel, R. R. and Conley, W. E., *Liquid immersion lithography - Evaluation of resist issues.* Proc. SPIE Int. Soc. Opt. Eng., 2004. **5376**(Pt. 1, Advances in Resist Technology and Processing XXI): p. 21-33.

35. Taylor, J. C., LeSuer, R. J., Chambers, C. R., Fan, F.-R. F., Bard, A. J., Conley, W. E. and Willson, C. G., *Experimental Techniques for Detection of Components Extracted from Model 193 nm Immersion Lithography Photoresists.* Chem. Mater., 2005. **17**(16): p. 4194-4203.

36. Dammel, R. R., Houlihan, F. M., Sakamuri, R., Rentkiewicz, D. and Romano, A., *193 nm immersion lithography - Taking the plunge.* J. Photopolym. Sci. Technol., 2004. **17**(4): p. 587-602.

37. Smith, B. W., Bourov, A., Fan, Y., Zavyalova, L. V., Lafferty, N. V. and Cropanese, F. C., *Approaching the numerical aperture of water - Immersion lithography at 193 nm.* Proc. SPIE Int. Soc. Opt. Eng., 2004. **5377**(Pt. 1, Optical Microlithography XVII): p. 273-284.

38. Baek, S. Y., Wei, A., Cole, D., Nellis, G., Yeung, M., Abdo, A. and Engelstad, R., *Simulation of the coupled thermal/optical effects for liquid immersion micro-/nanolithography.* Proc. SPIE Int. Soc. Opt. Eng., 2004. **5377**(Pt. 1, Optical Microlithography XVII): p. 415-427.

39. Gil, D., Brunner, T. A., Fonseca, C., Seong, N., Streefkerk, B., Wagner, C. and Stavenga, M., *Immersion lithography: New opportunities for semiconductor manufacturing.* J. Vac. Sci. Technol., B, 2004. **22**(6): p. 3431-8.

40. Bailey, G. E. and Adam, K., *Polarization influences through the optical path.* Proc. SPIE Int. Soc. Opt. Eng., 2004. **5754**(Optical Microlithography XVIII): p. 1102-1112.

41. Estroff, A., Fan, Y., Bourov, A. and Smith, B., *Mask-induced polarization effects at high numerical aperture.* J. Microlith. Microfab. Microsyst., 2005. **4**(3): p. 031107/1-031107/8.

42. McCallum, M., Kameyama, M. and Owa, S., *Practical development and implementation of 193nm immersion lithography.* Micro. Eng., 2006. **83**(4-9): p. 640-642.

43. French, R. H., Sewell, H., Yang, M. K., Peng, S. P., McCafferty, D., Qiu, W., Wheland, R. C., Lemon, M. F., Markoya, L. and Crawford, M. K., *Imaging of 32-nm 1:1 lines and spaces using 193-nm immersion interference lithography with second-generation immersion fluids to achieve a numerical aperture of 1.5 and a k1 of 0.25.* J. Microlith. Microfab. Microsyst., 2005. **4**(3): p. 031103-1 - 031103-14.

44. Rice, B. J., *High-index materials research key to extending immersion lithography.* Solid State Technol., 2008. **51**(2): p. 28-30, 32-33.

45. Matsumoto, K., Costner, E. A., Nishimura, I., Ueda, M. and Willson, C. G., *High Index Resist for 193 nm Immersion Lithography.* Macromolecules, 2008. **41**(15): p. 5674-5680.

46. Stewart, M. D., Johnson, S. C., Sreenivasan, S. V., Resnick, D. J. and Willson, C. G., *Nanofabrication with step and flash imprint lithography.* J. Microlith. Microfab. Microsyst., 2005. **4**(1): p. 011002/1-011002/6.

47. Hua, F., Sun, Y., Gaur, A., Meitl, M. A., Bilhaut, L., Rotkina, L., Wang, J., Geil, P., Shim, M., Rogers, J. A. and Shim, A., *Polymer Imprint Lithography with Molecular-Scale Resolution.* Nano Lett., 2004. **4**(12): p. 2467-2471.

48. Gronheid, R., Hendrickx, E., Wiaux, V., Maenhoudt, M., Goethals, M., Vandenberghe, G. and Ronse, K., *Lithography options for the 32nm half pitch node and their implications on resist and material technology.* Proc. SPIE Int. Soc. Opt. Eng., 2008. **6827**(Quantum Optics, Optical Data Storage, and Advanced Microlithography): p. 68271V/1-68271V/10.

49. Lee, S., Byers, J., Jen, K., Zimmerman, P., Rice, B., Turro, N. J. and Willson, C. G., *An analysis of double exposure lithography options.* Proc. SPIE Int. Soc. Opt. Eng., 2008. **6924**(Pt. 1): p. 69242A-69242A-12.

50. Hazelton, A. J., Wuest, A., Hughes, G. and Lercel, M., *Predicting lithography costs - guidance for < 32 nm patterning solutions.* Proc. SPIE Int. Soc. Opt. Eng., 2008. **7028**: p. 70283N/1 - 70283N/10.

51. La Fontaine, B., Deng, Y., Kim, R.-h., Levinson, H. J., Okoroanyanwu, U., Sandberg, R., Wallow, T. and Wood, O., *Extreme ultraviolet lithography: From research to manufacturing.* J. Vac. Sci. Technol., B, 2007. **25**(6): p. 2089-2093.

Chapter 2: The Effect of Added Salts on the Optical Properties of Water

2.1 INTRODUCTION

The successful demonstration of water immersion lithography as a patterning technique for 45 nm features has generated interest in extending this technology to smaller patterns. To resolve features as small as 32 nm with 193 nm immersion lithography, fluids with a higher index of refraction than water are needed.

Initial approaches to high index fluid development involved doping water with high index additives. Since water was successfully implemented as the first generation fluid for immersion lithography,[1, 2] an aqueous fluid for next generation immersion lithography is the most straightforward option. With an aqueous fluid, fluid handling systems and other infrastructure, designed for water immersion lithography, would not need extensive re-designs.

Ideally, a high index additive would increase the index at 193 nm without significantly increasing the absorbance. To achieve 32 nm resolution, a next generation fluid with an index greater than 1.65 and absorption coefficient less than 0.15 cm^{-1} at 193 nm is needed.[3] To prevent the necessity of modifying the fluid handling systems, the surface tension and wetting properties should be similar to that of water, and the viscosity should not be more than three times that of water. Additionally, the cost of the fluid should be no more than one to two dollars per circuit layer printed, there should be minimal photochemical effects, and no negative impact from interactions with photoresists. Finally, the index of refraction should not change significantly with temperature, so that the change with temperature (dn/dT) is less than 2.5×10^{-6} /°C.[3]

A variety of additives have been investigated as immersion fluid candidates. Organic fluids, such as crown ethers, have been studied either as the immersion fluid or as additives to water to increase the solubility of ionic species.[4] Surfactants and nanoparticles have also been added to water in an attempt to increase the index.[5, 6] Various ionic additives have also been considered[7] and seem to result in the most significant increase in the index for an aqueous fluid.

To identify an ionic additive with the required index and absorbance characteristics for an immersion fluid, a systematic survey of the optical properties of a variety of salt species was completed. The salts studied include metal salts with halide and polyatomic anions, acids, sodium salts, and "microelectronics-friendly" quaternary ammonium salts. Both index of refraction and absorbance measurements were collected at 193 nm. The physical properties of these aqueous solutions were also evaluated to assess their compatibility with fluid handling systems designed for water.

Prior to developing a high index salt additive, the dependence of index and absorbance on the additive concentration and structure must be understood. Based on this systematic survey, increasing the additive concentration increases both the index of refraction and absorbance of the solution, with this increase being most dependent on the anion of the ionic species. Since the anion of the additive most strongly affects the optical properties, the choice of anion can be used to guide the development of semiconductor-friendly ionic additives. With some of the aqueous solutions studied, the index of water can be significantly increased using a high additive concentration. However, increasing the additive concentration also tends to increase the absorbance of the solution to prohibitively high levels and adversely affects both the viscosity and surface tension. As a result, while the index values of some of these aqueous fluids approach next generation targets, low transparencies limit the usefulness of these fluids for immersion lithography.

2.2 EXPERIMENTAL DETAILS

2.2.1 Materials

High performance liquid chromatography (HPLC) grade water obtained from EMD Chemicals, Inc. was used as the primary fluid for the high index additives experimentation. Alkali metal, ammonium and tetramethylammonium halide and acetate salts and acids were obtained from Fisher Scientific and Sigma-Aldrich Co. in the highest purity available and used as received. Solutions of 2 M concentrations were made in aliquots of 10 mL or 25 mL and diluted as needed. Quaternary ammonium salts were obtained from SACHEM, Inc. (Austin, TX) either already in solution or as hydroxide solutions that required neutralization with glacial acetic acid, also obtained from Fisher Scientific, prior to use. Methylsulfonate salt solutions were also prepared at SACHEM by neutralization of methanesulfonic acid with a metal hydroxide solution containing the desired cation. Salts from SACHEM were used as received.

2.2.2 Absorbance Measurements

Absorbance spectra were obtained in a nitrogen purged environment with an Acton Research Corporation CAMS-507 Spectrophotometer in increments of one nanometer from 180 – 250 nm. The absorbance edge (wavelength at which $\alpha = 1 \text{ cm}^{-1}$) was obtained by interpolating between the measured wavelength values. High purity cylindrical quartz cuvettes of 10 mm path length from Hellma-USA were used for the measurements. Prior to each experiment, each of the cuvettes was rinsed thoroughly three times with HPLC-grade water to remove any contaminates which might increase the absorbance of the sample.

To measure the absorbance, a reference was taken without a sample or quartz cuvette in the light path. With this method, the absorbance of the entire fluid sample could be measured, rather than the absorbance of simply the salt, if water had been used as the reference. When light passes through an interface, some of the light is reflected and some is transmitted. Therefore, when a reference sample is not used, light lost due to reflections at each of the quartz-nitrogen or quartz-fluid interfaces is not accounted for during the experiment. The Fresnel equation (see Equation 2.1), which provides a relationship between the transmitted and reflected light at an interface, was combined with Lambert's Law (see Equation 2.12) and used to calculate a reflection-corrected absorbance for the sample.[8]

Reflections occur at four interfaces in the light path: the nitrogen-quartz interface, the quartz-fluid interface, the fluid-quartz interface, and the quartz-nitrogen interface. A schematic of these reflections and a depiction of the intensity on either side of each interface are given in Figure 2.1. The Fresnel equation relates transmission and reflection at normal incidence as

$$T_i = 1 - R_i = 1 - \left(\frac{n_{t_i} - n_{o_i}}{n_{t_i} + n_{o_i}}\right)^2 \tag{2.1}$$

where T_i and R_i are the transmittance and reflectance values at a specific interface (*i*), n_{ti} is index of refraction of the material through which the light is transmitted, and n_{oi} is the index of refraction of the material at which the light is incident.

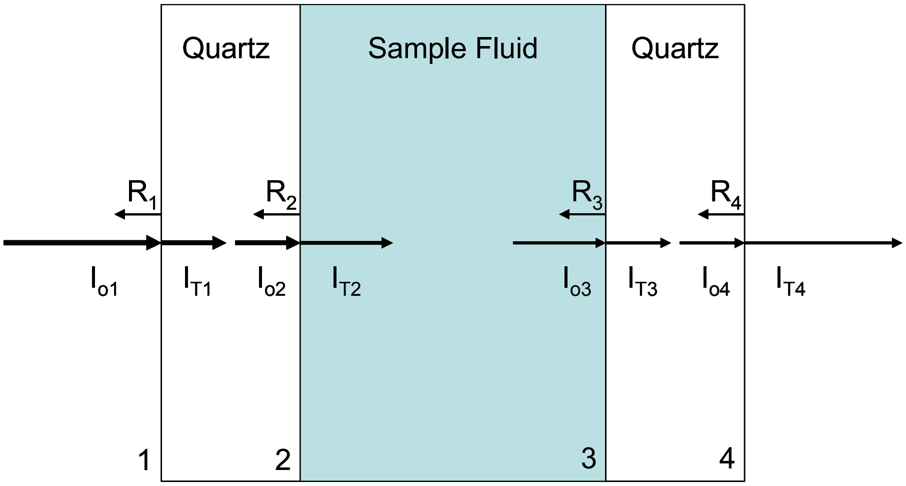

Figure 2.1: Reflection and transmission at each of the four interfaces through which the light travels in a cuvette

The transmission output given by the spectrometer is a ratio of the intensity of light at the final quartz-nitrogen interface (I_{T4}) to the initial nitrogen-quartz interface (I_{o1}). To isolate the amount of light absorbed by the sample, the transmission values at each of the interfaces can be combined to obtain a reflection-corrected absorbance spectrum for the sample. Transmission is the ratio of the intensity of transmitted to incident light. These rearrangements were accomplished as

$$\frac{I_{T_1}}{I_{o_1}} = T_1 \tag{2.2}$$

$$I_{o_2} = I_{T_1} = I_{o_1} T_1 \tag{2.3}$$

$$\frac{I_{T_2}}{I_{o_2}} = \frac{I_{T_2}}{I_{o_1} T_1} = T_2 \tag{2.4}$$

$$I_{o_3} = I_{T_2} T_{sample} = I_{o_1} T_1 T_2 T_{sample} \tag{2.5}$$

$$\frac{I_{T_3}}{I_{o_3}} = \frac{I_{T_3}}{I_{o_1} T_1 T_2 T_{sample}} = T_3 \tag{2.6}$$

$$I_{o_4} = I_{T_3} = I_{o_1} T_1 T_2 T_{sample} T_3 \tag{2.7}$$

$$\frac{I_{T_4}}{I_{o_4}} = \frac{I_{T_4}}{I_{o_1} T_1 T_2 T_{sample} \ T_3} = T_4 \tag{2.8}$$

$$\frac{I_{T_4}}{I_{o_1}} = T_1 T_2 T_{sample} \ T_3 T_4 \tag{2.9}$$

$$\frac{I_{T_4}}{I_{o_1} T_1 T_2 T_3 T_4} = T_{sample} \tag{2.10}$$

where the numbers in the indices correspond to a specific interface (see Figure 2.1). Using the expressions for the transmission of light through each interface, the value of the transmission of light through the sample can be isolated,

$$\frac{T_{measured}}{T_1 T_2 T_3 T_4} = T_{sample}, \tag{2.11}$$

where each T_i is calculated from the Fresnel equation (see Equation 2.1). Lambert's Law, to calculate the amount of light absorbed by the sample, is given by

$$T_{sample} = 10^{-\alpha z} \tag{2.12}$$

where T_{sample} is the amount of light transmitted through the sample, corrected for reflection losses, α is the absorption coefficient of the sample, and z is the path length. This equation can be rearranged to solve for the absorption coefficient (α) of the sample. All absorption coefficients that follow are reported in base 10.

A further correction is required since the quartz cuvette is slightly absorbing. By measuring the absorbance spectrum of the empty quartz cuvette and correcting that data for reflections, the fluid absorbance data can be normalized by the reflection-corrected empty cuvette absorbance data. This correction accounts for any quartz absorbance by assuming that the reflection-corrected empty cuvette transmission is the maximum transmission that can be obtained.

The index values at each interface are needed for the reflection-correction calculation. The index of nitrogen is 1 for the entire wavelength range. The index of quartz is well known with respect to wavelength and was obtained from literature values in the Woollam WVASE32 software. Measurement of the index of refraction of each of the aqueous solutions will be described in Section 2.2.3.

The transmittances of an empty quartz cuvette, both with and without the reflection-correction procedure, are given in Figure 2.2. Applying the reflection-correction procedure increases the transmittance to 100% for wavelengths at which the quartz cuvette does not absorb. Additionally, the reflection-corrected absorbance spectrum of water collected with the Acton is given in Figure 2.3. The absorption coefficient of HPLC-grade water measured on the Acton (from Figure 2.3) and reflection-corrected is 0.09 cm^{-1} at 193 nm. The absorbance of water is sensitive to impurities and can increase based on the type of container in which the water is stored and also the fluid handling method used. An absorption coefficient as low as 0.036 cm^{-1} at 193 nm has been reported for ultra-pure water.[2] An error analysis for the Acton from the empty cuvette transmission spectra is presented in Chapter 3, 3.2.4.

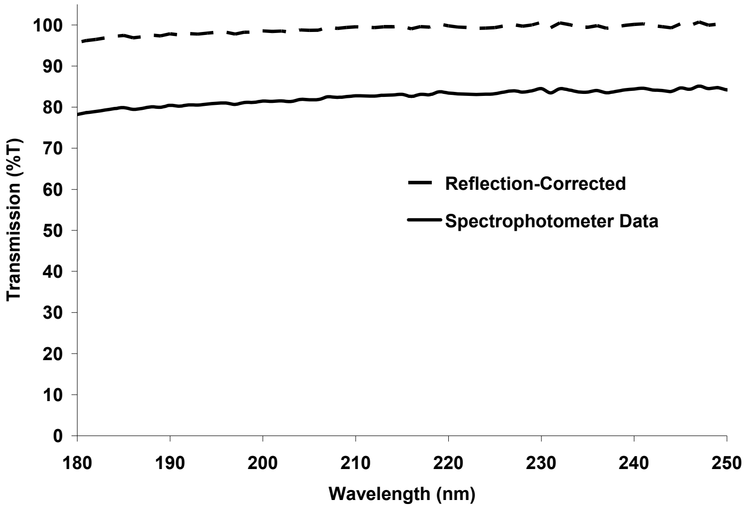

Figure 2.2: Empty cuvette transmission both with and without reflection-correction

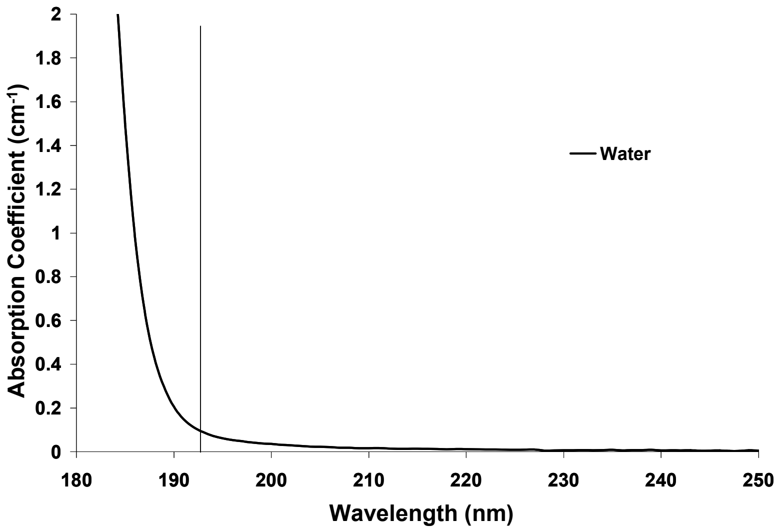

Figure 2.3: Reflection-corrected absorbance spectrum of HPLC-grade water

2.2.3 Index of Refraction Measurements

The index of refraction of the aqueous fluid samples was measured with spectroscopic ellipsometry. Ellipsometry is typically used to measure the optical properties, such as the index and absorbance, and thickness of thin films.[9] A modified ellipsometric technique was used to measure the index of the fluids.

2.2.3.1 Ellipsometry

Light can be described by an electromagnetic wave composed of a magnetic field vector ($\vec{B}$-field) and an electric field vector ($\vec{E}$-field) that are a function of position and time.[9] Since these vectors are mutually perpendicular, only one of them is needed to describe the properties of the light wave. The $\vec{E}$-field vector will be used here.

The orientation of the $\vec{E}$-field around the optical axis describes the polarization of the light beam. When the photons in the beam have electric fields oriented in all different directions, the light is unpolarized. Light is linearly polarized when the orientation of the $\vec{E}$-field is constant. The orthogonal x and y components of the $\vec{E}$-field of this linearly polarized wave have the same frequency and are in phase. When the x and y components are out of phase by 90° but have the same frequency and amplitude, the resultant wave is circularly polarized. If the phase shift of the x and y components is not 90° or if the amplitudes are unequal, the resultant light wave is elliptically polarized. Each of the polarization states is shown in Figure 2.4. Linear and circular polarization are specific cases of general elliptically polarized light.[9] The size of the ellipse describes the intensity or amplitude of the wave. The shape or curvature of the ellipse describes the polarization.

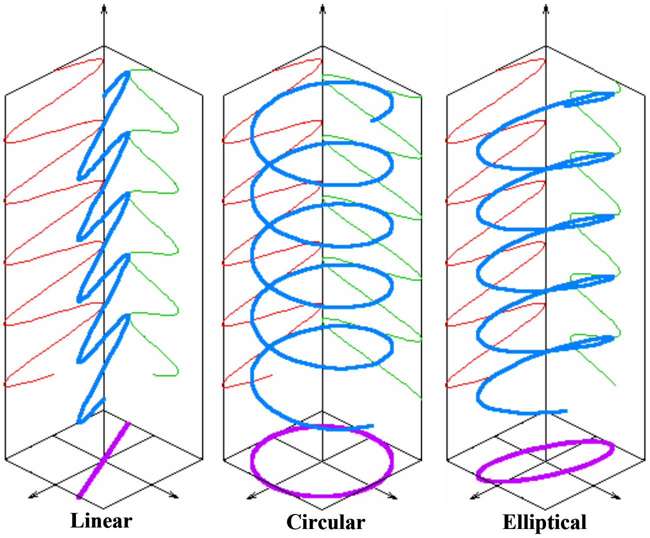

Figure 2.4: The x and y components, resulting wave, and view down the axis of propagation of linearly, circularly, and elliptically polarized light[10]

If light is incident on a sample, the incident beam and the surface normal define a plane of incidence perpendicular to the surface. This plane and the path of light incident on a sample are shown in Figure 2.5. The amplitude of the electric wave parallel to the plane of incidence is given by E_p, and the amplitude of the electric wave perpendicular to the plane of incidence is given by E_s. These waves are also referred to as p-polarized or transverse electric (TE) and s-polarized or transverse magnetic (TM), respectively.[9] The ratio of the amplitude of the reflected and incident light for these components is known as the reflectance (R_p or R_s). The equations for R_p and R_s are given by

$$R_p = \left[\frac{E_{p,r}}{E_{p,i}}\right]^2 \quad and \quad R_s = \left[\frac{E_{s,r}}{E_{s,i}}\right]^2 \tag{2.13}$$

where $E_{p,r}$ and $E_{p,i}$ are the amplitude of the p-polarized reflected and incident waves, respectively, and $E_{s,r}$ and $E_{s,i}$ are the amplitude of the s-polarized reflected and incident waves, respectively.[8]

When light is incident on a boundary between two media of different optical properties, the light is split into a transmitted wave which proceeds into the second medium and a reflected wave which propagates back into the first medium. These components are shown in Figure 2.5. The amount of energy transmitted or reflected depends on the optical properties of the two media. The smaller the difference in the index of refraction of the two media, the less energy reflected.[11]

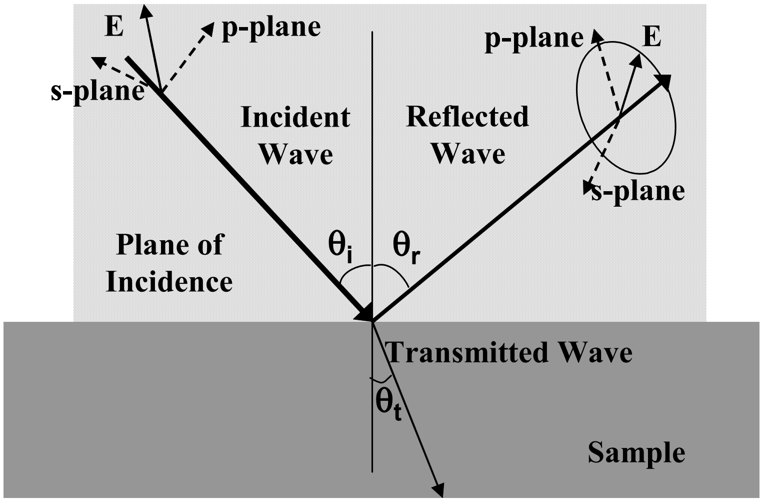

Figure 2.5: Plane of incidence and path of light incident on and reflected from a sample surface

Upon reflection from an interface, a phase shift between the incident and reflected beams can occur due to the different optical properties of each layer at the interface. If the phase difference between the p- and s-polarized waves before the reflection is defined by δ_1 and by δ_2 after the reflection, then the phase shift induced by the reflection is given by

$$\Delta = \delta_1 - \delta_2 . \tag{2.14}$$

The reflection will also induce an amplitude reduction for the p-polarized and s-polarized wave since a portion of the light is transmitted through the interface. This reduction will not necessarily be the same for both the p- and s-polarized components. The changes in amplitude for each component are described by the reflectance, R_p and R_s, defined in Equation 2.13. A variable, Ψ, can be defined by the magnitudes of the reflectances as

$$\tan\Psi = \frac{|R_p|}{|R_s|} . \tag{2.15}$$

The complex ratio of the reflectances is defined by ρ as

$$\rho = \frac{R_p}{R_s} . \tag{2.16}$$

Equations 2.14, 2.15, and 2.16 can be used to define the fundamental equations of ellipsometry:

$$\rho = \frac{R_p}{R_s} = \tan\Psi(e^{i\Delta}) \tag{2.17}$$

The ellipsometer measures the quantities Ψ and Δ. Since these quantities are properties of the light rather than the sample, the optical constants and thickness of the sample can be calculated using a model to fit the experimental Ψ and Δ to the model data. Since ellipsometry measures the ratio or difference between two quantities, no reference is required, and this technique is relatively insensitive to scatter and fluctuations.[9]

2.2.3.2 Ellipsometric Procedure

The index of refraction of the aqueous fluids was determined from ellipsometric measurements collected with a J.A. Woollam M2000 variable angle spectroscopic ellipsometer from 190 to 1000 nm. The fluids were measured by filling a 2 in. diameter Fluoroware cup with a curved bottom with approximately 5 mL of fluid. This method was adapted from a rough surface technique developed by J.A. Woollam Co.[12] Using the Woollam method, a fluid is deposited on a rough surface. The rough bottom surface scatters light transmitted through the fluid so that only reflections from the top surface of the fluid are collected for analysis. The curved and opaque bottom surface of the Fluoroware cup also scatters light transmitted through the fluid, as in the Woollam method. If the index and extinction coefficient (or absorption) are of the same order of magnitude, the reflected beam can be used to calculate both of the optical properties. However, in this case, the extinction coefficient ($\sim 10^{-7} - 10^{-6}$) is of much lower order than the index (~1), and the index dominates the reflected beam. In this case, the absorbance must be calculated from the change in the intensity of light that travels through the fluid and cannot be measured with the rough surface technique.

The index of refraction of water collected using the Fluoroware cup method compares favorably to previously reported index data collected with the prism minimum deviation technique.[12, 13] In this prism technique the fluid is inserted into a hollow prism. The index of refraction is determined by measuring the deviation angle of varying wavelengths of light passing through the prism.[13] The data collected with these methods are compared in Figure 2.6. At 193 nm, the index of refraction of water measured with the Fluoroware cup method is 1.438±0.008, where the error is the 90% confidence limits of the fit to the ellipsometric model equation parameters.

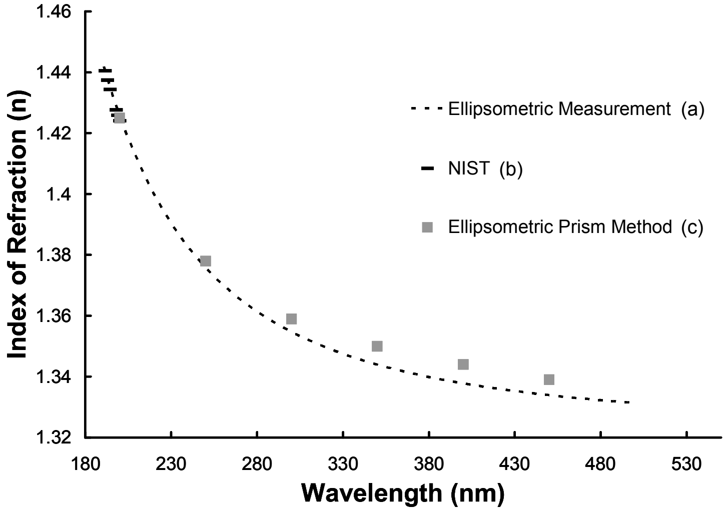

Figure 2.6: The index of refraction of water collected in the Fluoroware cup (a) and with the prism minimum technique at NIST[13] (b) and Woollam[12] (c)

The angle of incidence (θ_i, see Figure 2.5) used in ellipsometry is important for obtaining the maximum signal to noise ratio. The angle that provides the optimal ratio is Brewster's angle (θ_b). At Brewster's angle, the p-polarized component of the reflected light, R_p, approaches zero.[11] The maximum difference between R_p and R_s, and thus maximum measurement sensitivity, occurs in the region near Brewster's angle. This angle is defined by

$$\tan\theta_b = \frac{n_2}{n_1} \tag{2.18}$$

where n_2 is the index of refraction of the transmitted medium and n_1 is the index of refraction of the incident/reflected medium. Brewster's angle changes with the index of the sample. However, an incident angle of 70° is typically close to Brewster's angle for the fluid samples measured; 70° was used for all measurements.[9] Any small error in the incident angle simply reduces the sensitivity of the measurement slightly and should not affect the index values.

Ellipsometry uses a model fit procedure to relate the measured ellipsometric parameters (Ψ and Δ) to the optical properties of the sample. The reflectances, R_p and R_s, (or Ψ and Δ, Equation 2.17) depend on the optical properties of the sample and can be calculated when the optical properties of the incident layer, sample layer, and incident angle are known.[9] However, since the optical properties of the sample are unknown, a dispersion model for the optical constants of the sample is used to calculate the reflectances. These calculated reflectances, and thus Ψ and Δ, are then fit to the experimental Ψ and Δ by varying the parameters in the dispersion model to minimize the mean squared error (MSE) between the model and experimental data.

For the aqueous fluids measured, the Cauchy dispersion model was used to evaluate the index of refraction. The Cauchy model describes the index of refraction in normal dispersion when the absorbance is low and should be valid for an aqueous fluid for wavelengths to 190 nm. The validity of the Cauchy model will be further discussed in Chapter 3, 3.2.5. The parameters in the Cauchy model were adjusted with a linear regression technique to minimize the MSE function. The Cauchy equation is given by

$$n(\lambda) = A + \frac{B}{\lambda^2} + \frac{C}{\lambda^4}. \tag{2.19}$$

A, B, and C are the Cauchy model parameters that are adjusted to fit to the ellipsometric data.[9]

2.2.4 Physical Property Measurement

Surface tension, viscosity, and density were determined after ellipsometric and absorbance measurements. Surface tension measurements were made on a Ramé-Hart Inc. NRL C.A. goniometer using a pendant drop technique. A cone and plate rheometer was used to vary the shear stress on the fluid and measure the dynamic viscosity. The mass of known volumes of each fluid in 0.1 mL increments from 0.1 mL to 0.5 mL was measured using a Mettler Toledo AB204 balance to calculate the density.

2.3 OPTICAL PROPERTY DEPENDENCE ON CONCENTRATION

The refractive index was first measured for several solutions of sodium chloride (NaCl) of varying concentrations to study the effect of additive concentration on the index of a solution. Figure 2.7a shows that as the concentration of the ionic additive was increased, the index of refraction tended to increase. The index of refraction at 193 nm with increasing NaCl concentration is given in Figure 2.8. At low concentration, the index values were very similar to those of water and increase monotonically with increasing salt concentration. These results are consistent with mixing rules for the index of refraction, such as the Lorentz – Lorenz Equation,[14]

$$\frac{n_{12}^2-1}{n_{12}^2+2}=\phi_1\frac{n_1^2-1}{n_1^2+2}+\phi_2\frac{n_2^2-1}{n_2^2+2} \tag{2.20}$$

where n_{12}, n_1 and n_2 are the refractive indices of the solution, solvent, and solute, respectively and ϕ_i is the volume fraction of each component. This equation predicts only a small difference between the solution index and the index of water for low additive concentrations. At higher concentrations, the index increases linearly with concentration, as observed in Figure 2.8. This increase is limited only by the solubility of the salt in water.

The absorbance of NaCl solutions of different concentrations was also measured to evaluate the absorbance dependence on salt concentration. Figure 2.7b shows the absorption spectra of NaCl solutions with concentrations from 0.1 mM – 2 M. Like refractive index measurements, the absorption coefficient depends on concentration. Since absorption coefficient values only slightly greater than water at 193 nm can be tolerated for immersion lithography, even low concentrations of this solution are too strongly absorbing, and above 1 mM, these solutions were too opaque to obtain a measurement at 193 nm with a 10 mm path length. These results are expected since the index of refraction and absorbance are linked through a dispersion relationship that can be described by the Kramers-Kronig integral.[15-17] When the refractive index increases, the absorbance tends to increase as well. This phenomenon is evident in the increase in both the index and absorbance with increasing concentration of NaCl.

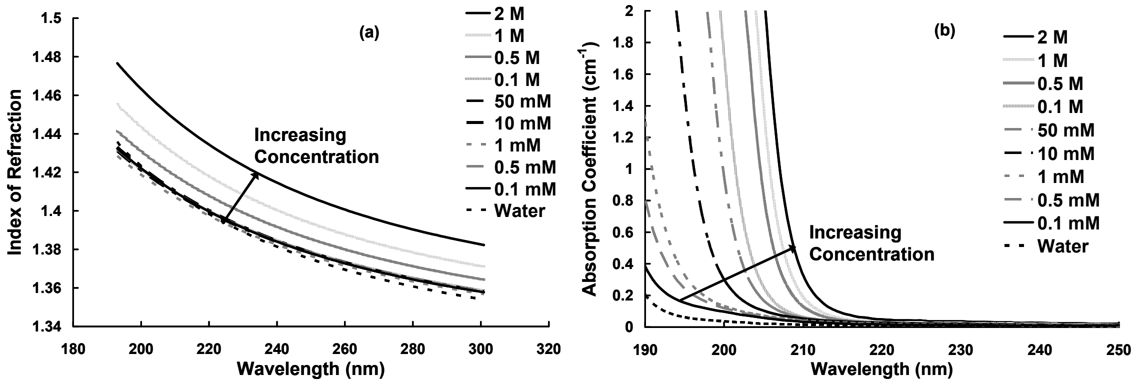

Figure 2.7: Index (a) and absorbance (b) of increasing concentration NaCl solutions

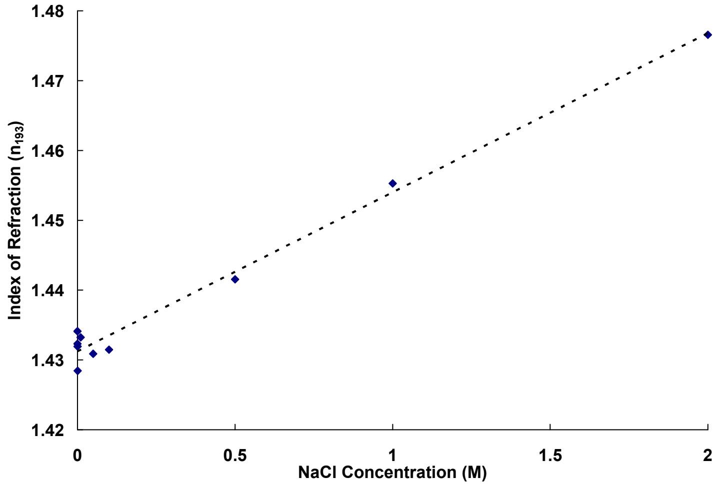

Figure 2.8: Index at 193 nm (n_{193}) of varying concentration NaCl solutions

2.4 EFFECT OF ADDITIVE ON REFRACTIVE INDEX

Since the ideal additive should have a high index and low absorbance at 193 nm, the index of refraction of the additive was studied to determine how different types of additives affect the index. The first series of ionic additives studied included chloride, bromide, and acetate salts. These salts were chosen since early screening of Group I metal-halogen salts showed that fluoride-containing salts had essentially no effect on the index values at 193 nm and that iodide salts had absorption peaks at wavelengths greater 193 nm.[18] Each of these anions was tested with lithium, sodium, potassium, rubidium, cesium, ammonium (NH_4^+) and tetramethylammonium (Me_4N^+) cations at 2 M concentration in water. The index value at 193 nm and Cauchy coefficients for each 2 M solution of the bromides, chlorides, and acetates are shown in Table 2.1, Table 2.2, and Table 2.3, respectively. The greatest increase in index at 193 nm is achieved with the bromide anion, with Me_4NBr having the highest index of the bromide salts, n = 1.552 at 193 nm. The anion appears to dictate the index of the solution since varying the cation causes only a small change in the index. Cations with a greater atomic radius, for both the monatomic and the ammonium cations, seem to have a slightly greater index; however, since the index of solutions with the same anion varies only slightly, the index variation with cation appears to be small.

Two additional series of solutions were tested to further evaluate the anion affect. The refractive indices of a series of sodium salts with complex anions and acids at a concentration of 2 M were compared. The index at 193 nm and Cauchy coefficients for these solutions are given in Table 2.4. Both the series of acids and series of sodium salts have a wide variation in index at 193 nm. The acids vary from n = 1.541 – 1.455, and the sodium salts from n = 1.553 – 1.454. Sodium thiocyanate (NaSCN), hydrogen bromide (HBr), sodium thiosulfate (NaS_2O_3) and sodium sulfite ($NaSO_3$) solutions have the highest index values, all above 1.5. The solutions of sulfuric acid (H_2SO_4), phosphoric acid (H_3PO_4), and sodium perchlorate ($NaClO_4$) have index values only slightly above that of water at 193 nm. The wider range of index values when the anion is varied further supports the observation that the anion has a stronger influence on the refractive index than the cation.

Table 2.1: Index of refraction at 193 nm and Cauchy coefficients of 2 M bromide solutions

	Index	Cauchy coefficients		
	n_{193}	A	B x10^3 (μm^4)	C x10^4 (μm^4)
LiBr	1.521	1.343	2.02	1.7
NaBr	1.535	1.348	1.57	2
KBr	1.528	1.348	1.72	1.9
RbBr	1.537	1.352	1.99	1.8
CsBr	1.533	1.353	2.34	1.6
NH_4Br	1.536	1.353	1.81	1.9
Me_4NBr	1.552	1.362	1.92	1.9

Table 2.2: Index of refraction at 193 nm and Cauchy coefficients of 2 M chloride solutions

	Index	Cauchy coefficients		
Salt	n_{193}	A	B x10^3 (μm^4)	C x10^4 (μm^4)
LiCl	1.469	1.336	2.46	0.928
NaCl	1.489	1.342	2.18	1.20
KCl	1.485	1.344	1.66	1.30
RbCl	1.480	1.343	2.55	0.941
CsCl	1.477	1.348	2.74	0.857
NH_4Cl	1.478	1.343	2.57	0.926
Me_4NCl	1.495	1.353	2.48	1.00

Table 2.3: Index of refraction at 193 nm and Cauchy coefficients of 2 M acetate solutions

	Index	Cauchy coefficients		
Salt	n_{193}	A	B x10^3 (μm^4)	C x10^4 (μm^4)
LiOAc	1.469	1.341	2.31	0.916
NaOAc	1.474	1.342	2.26	0.999
KOAc	1.479	1.347	1.47	1.3
RbOAc	1.508	1.367	2.43	1.1
CsOAc	1.516	1.375	2.26	1.1
NH_4OAc	1.479	1.346	2.4	0.948
Me_4NOAc	1.493	1.359	2.62	0.888

Table 2.4: Index of refraction at 193 nm and Cauchy coefficients of 2 M acid and sodium solutions

	Index	Cauchy coefficients		
Salt	n_{193}	A	B x10^3 (μm^4)	C x10^4 (μm^4)
NaSCN	1.553	1.357	1.98	2.00
HBr	1.541	1.351	2.15	1.84
$Na_2S_2O_3$	1.530	1.371	3.66	0.839
Na_2SO_3	1.524	1.367	2.81	1.10
$NaHSO_3$	1.493	1.350	2.37	1.10
HNO_3	1.491	1.337	2.74	1.10
$NaHSO_4$	1.465	1.346	2.54	0.707
HCl	1.463	1.338	2.77	0.701
H_2SO_4	1.456	1.336	3.44	0.379
H_3PO_4	1.455	1.345	2.89	0.436
$NaClO_4$	1.454	1.336	2.21	0.815
Water	1.438	1.322	1.96	0.875

2.5 EFFECT OF ADDITIVE ON ABSORBANCE

The absorbance of solutions of these ionic additives in water was also measured to evaluate the similarity in the absorbance and index trends. Since the absorbance increases with concentration, absorbance spectra were measured at a lower concentration than the index so that a value for the absorbance at 193 nm could be obtained and compared to water. The absorbance edge (λ_{edge}) was also evaluated. This edge is defined as the wavelength at which $\alpha = 1$ cm^{-1} and is the wavelength at which the absorbance starts to increase dramatically. Since these fluids must have a low absorbance at 193 nm, this absorbance edge should be at a wavelength less than 193 nm. To obtain a high index while maintaining a low absorbance at 193 nm, the absorbance edge should be very close, but slightly less, than 193 nm. Since index and absorbance tend to increase simultaneously, according to the Kramers-Kronig relations, a fluid with an absorbance edge just less than 193 nm should provide the best candidate for immersion lithography. The link between the index and absorbance will be explained in detail in Chapter 3.

The absorption coefficient at 193 nm and absorbance edge for solutions of 1 mM chloride, 0.1 mM bromide, and 1 mM acetate with varying monatomic and ammonium cations at 193 nm are given in Table 2.5. As observed in the index measurements, the absorption coefficient and absorbance edge of each series of anion solution were essentially constant, increasing only slightly with monatomic cations of increasing atomic radius. The absorption coefficient at 193 nm for each series of anion solution are given Figure 2.9. For this anion series, the absorption coefficient at 193 nm does not vary significantly with varying cation. The solutions with the complex cations NH_4^+ and Me_4N^+ have absorbances similar to those of the larger monatomic cations. Thus, the anion is the predominant factor in dictating the peak positions and intensities of the absorption spectra.

The effect of the anion was further investigated by measuring the absorption spectra of acid and sodium salt solutions. The absorption coefficient at 193 nm and absorbance edge for the 0.1 mM acids and sodium salts are given in Table 2.6. These solutions exhibited a wide range of absorption coefficients at 193 nm as well as absorbance edges. The absorption spectra of the nitric acid (HNO_3), sodium thiosulfate ($Na_2S_2O_3$), and sodium thiocyanate (NaSCN) solutions had an absorption edge greater than 193 nm, even at the low concentration measured. The absorption coefficients of these solutions were also much larger than those of the other solutions. The spectra of the sulfuric acid (H_2SO_4), phosphoric acid (H_3PO_4), sodium bisulfate ($NaHSO_4$), and sodium perchlorate ($NaClO_4$) solutions were very similar to each other and had almost identical absorption coefficient values at 193 nm, approximately $\alpha = 0.2$ cm^{-1}, a marginal increase over water. Addition of these salts shifts the absorption edge of water to only slightly higher wavelengths. From these data, the anion of the ionic additive influences the absorption spectra much more strongly than the cation. Varying the anion resulted in absorbance values corresponding to solution transmittances ranging from as high as 66% to as low as 5%, while varying the cation changed the solution transmittance by three percentage points or less (as measured in the bromide, chloride, and acetate series).

Table 2.5: Absorption coefficient at 193 nm and absorbance edge of bromide, chloride, and acetate solutions

Anion ▶	**Br$^-$**		**Cl$^-$**		**CH$_3$COO$^-$**	
Cation ↓	α_{193} (cm^{-1})	$\lambda_{edge,}$ $\alpha = 1$ cm^{-1}	α_{193} (cm^{-1})	$\lambda_{edge,}$ $\alpha = 1$ cm^{-1}	α_{193} (cm^{-1})	$\lambda_{edge,}$ $\alpha = 1$ cm^{-1}
Li$^+$	1.27	199.8	0.412	189.8	0.616	190.6
Na$^+$	1.27	199.8	0.427	190.2	0.646	190.6
K$^+$	1.32	200.4	0.478	190.4	0.702	191.1
Rb$^+$	1.28	199.8	0.486	190.5	0.695	191.0
Cs$^+$	1.42	201.4	0.481	190.4	0.706	191.1
NH$_4^+$	1.40	201.2	0.480	190.4	0.704	191.1
Me$_4$N$^+$	1.41	201.3	0.437	190.1	0.767	191.5

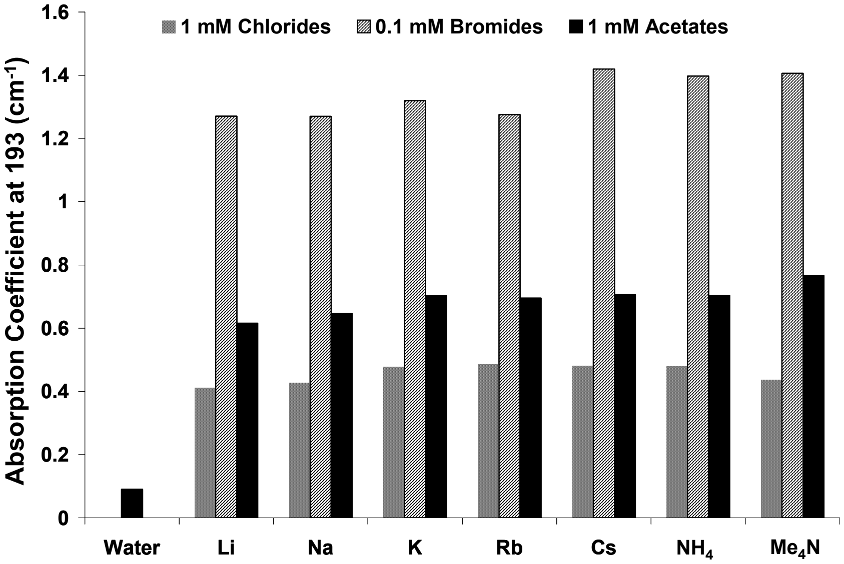

Figure 2.9: Absorption coefficient at 193 nm for the series of 1mM chloride solutions, 0.1 mM bromide solutions, and 1 mM acetate solutions

Table 2.6: Absorption coefficient at 193 nm and absorbance edge of the sodium and acid solutions

Salt	α_{193} (cm^{-1})	$\lambda_{edge,}$ $\alpha = 1\ cm^{-1}$
HBr	1.61	202.7
HNO_3	1.31	212.5
NaSCN	1.25	195.6
$Na_2S_2O_3$	0.811	190.0
$NaHSO_3$	0.400	187.1
Na_2SO_3	0.245	186.5
HCl	0.240	187.4
$NaClO_4$	0.199	186.2
H_3PO_4	0.184	186.3
$NaHSO_4$	0.184	186.3
H_2SO_4	0.183	186.3
Water	0.0902	185.9

The trends observed are consistent with previous studies of the absorbance of ionic additives in solution. In the visible and ultraviolet regions of the spectrum, absorbance typically occurs through intramolecular transitions, where an electron is excited from molecular ground to bound molecular excited states. The energy of the absorption maximum corresponds to the energy difference between the ground and excited states. However, for anions in solution, a special class of electronic transitions, known as charge transfer to solvent spectra (CTTS), occurs. CTTS spectra are intense transitions observed for anions. When light is absorbed, the electron is separated from the ion and forms a solvated electron, bound by a solvent cage, in an excited state around the parent anion. The difference in peak maxima between anions is due to the difference in ionization potential, or energy required to form the solvated electron. This energy varies both with the anion and type of solvent. The absorbance edge shifts to longer, lower energy wavelengths as the electron is more easily excited. For the simple halide ions, the absorption edge shifts as

$$F^- < Cl^- < Br^- < I^-$$

since an electron is most easily removed from iodide and least easily removed from fluoride. The cation is typically more stable in solution than the anion and varying the cation causes a shift in both the ionization energy and energy of formation, contradictory effects which tend to result in a very small or negligible shift in the excitation energy. Thus, the anion contributes more significantly to the optical properties than the cation and dominates the absorption peak energy and index of refraction.[18-22]

2.6 SEMICONDUCTOR FRIENDLY IONIC ADDITIVES

An aqueous solution with an ionic additive for use in second generation immersion lithography must not only meet the stated requirements for the optical properties, but must also be compatible with the semiconductor processing environment. The ionic compounds surveyed resulted in solutions with refractive indices significantly higher than that of water at high concentrations. Yet even at concentrations of 0.1 mM, nearly all of these solutions are too strongly absorbing to be used in immersion lithography. In addition to failing to meet the optical property requirements, the metal salts would be prohibited in a fabrication facility. However, since tetramethylammonium hydroxide is used as the standard photoresist developer in lithography processes, quaternary ammonium salts would be a viable alternative to metal salts. Therefore, additives with quaternary ammonium cations were investigated.

First, samples of different quaternary ammonium acetate salt solutions including tetrabutylammonium (Bu_4N), tetrapropylammonium (Pr_4N), tetraethylammonium (Et_4N), methyltriethylammonium ($MeEt_3N$), diethyldimethylammonium (Et_2Me_2N) and tetramethylammonium (Me_4N) acetate were obtained from SACHEM, Inc., and the optical properties were measured. The index of refraction of each solution was measured at 1.5 M, to account for the differing solubility of each salt in water, and the absorbance of each solution was measured at 1 mM. The index and absorbance for these solutions is given in Table 2.7. The alkyl ammonium cation affects the optical properties of the solution more significantly than the metal cations. The index and absorbance both increase with increasing length of the alkyl chains on the quaternary ammonium cation. The absorption edge also shifts to longer wavelengths as length of the alkyl chain increases.

Using these alkylammonium cations with the acetate anion would result in a prohibitively high absorbance at 193 nm if the high salt concentration needed to obtain a high index was used. Pairing these cations with a low absorbance anion would provide the best solution for developing a semiconductor-friendly high index and low absorbance fluid. The properties of the cation could then be selected to achieve the desired optical properties. The salts would also need to be more soluble in water than the acetate versions in order to achieve the target index.

Table 2.7: Optical properties of the quaternary ammonium acetate solutions

	Index	Cauchy Parameters			Absorbance	
Salt	n_{193}	A	B x10^3 (μm^4)	C x10^4 (μm^4)	α_{193} (cm^{-1})	$\lambda_{edge,}$ $\alpha = 1\ cm^{-1}$
Bu_4NOAc	1.533	1.387	2.36	1.15	1.095	193.5
Pr_4NOAc	1.518	1.384	2.17	1.05	0.860	192.2
Et_4NOAc	1.501	1.370	2.13	1.04		
$MeEt_3NOAc$	1.494	1.363	2.00	1.06	0.851	192.1
Et_2Me_2NOAc	1.495	1.357	2.48	0.990		
Me_4NOAc	1.472	1.340	3.37	0.574	0.767	191.5

2.7 METHYLSULFONATE SALT SOLUTIONS

Based on the index and absorption data collected and an additional screening of the absorption of acids, researchers from SACHEM, Inc. prepared solutions of additives with a methylsulfonate anion for characterization. At a 2 M concentration, methanesulfonic acid has an index value at 193 nm just above water, n = 1.46, but an absorption coefficient of $\alpha = 0.362\ cm^{-1}$ and absorption edge of 189.4 nm. To test the potential of the methylsulfonate anion, the first solutions were prepared with large, monatomic cations. These solutions included 2 M cesium, barium, and lanthanum methylsulfonate. The index of refraction and absorbance data are given in Figure 2.10 and Figure 2.11, respectively. A summary of the optical properties at 193 nm, Cauchy coefficients, and absorbance edge are given in Table 2.8. Increasing the oxidation state of the cation enabled larger concentrations of the anion to be achieved in proportion to the overall salt concentration. Since the anion most strongly dictates the optical properties of the fluid, this strategy should allow for the greatest increase in index even when the salt solution is saturated. For a saturated (approximately 2.82 M) solution of lanthanum methylsulfonate, an index of 1.58 was achieved at 193 nm. The absorbance coefficients were also measured, with the unexpected result that the absorption of the barium and lanthanum solutions was less than that of the cesium solution. Impurities resulting from the synthesis of the solutions are the suspected cause of the high absorption coefficient of the cesium solution, so additional purification steps were taken in the development of the barium and lanthanum solutions. The high purity of the saturated lanthanum methylsulfonate solution resulted in an absorption coefficient at 193 nm, $\alpha = 0.314\ \text{cm}^{-1}$, less than that measured for the acid and a lower absorption edge at 188.4 nm.

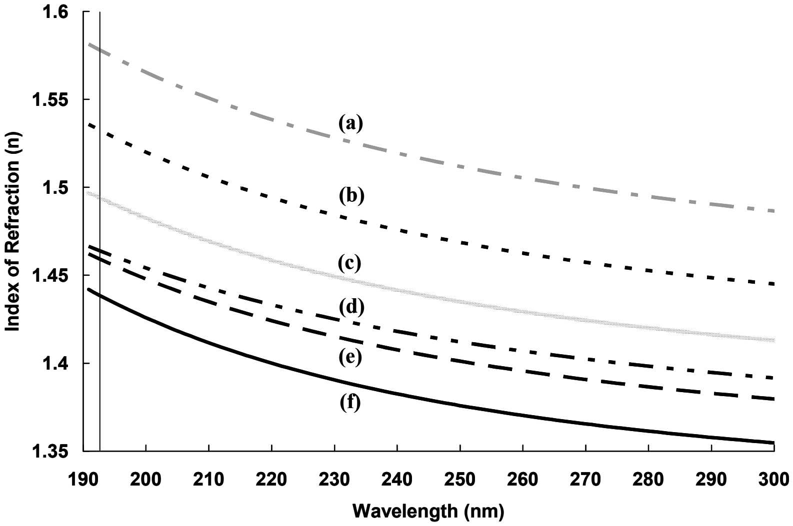

Figure 2.10: Index of refraction of (a) 2.82 M $La(O_3SCH_3)_3$ (sat'd), (b) 2 M $La(O_3SCH_3)_3$, (c) 2 M $Ba(O_3SCH_3)_2$, (d) 2 M $Cs(O_3SCH_3)$, (e) 2 M HO_3SCH_3, and (f) water

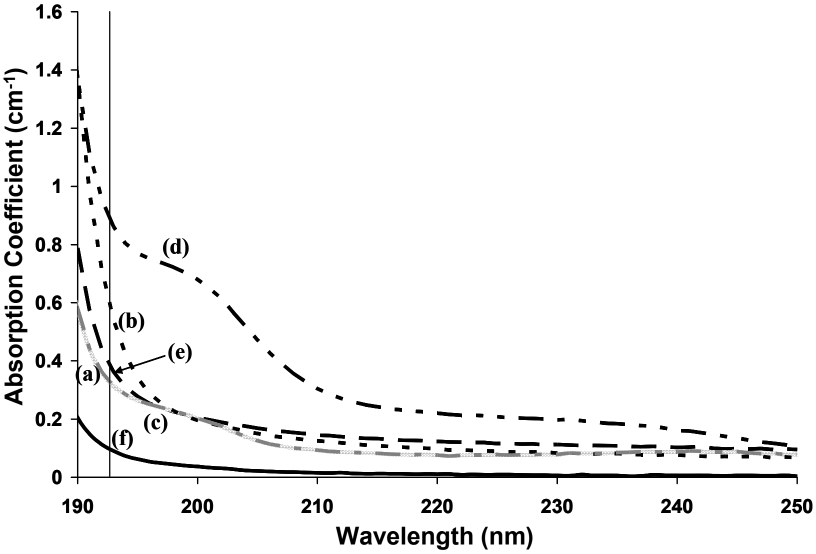

Figure 2.11: Absorbance spectra of (a) 2.82 M $La(O_3SCH_3)_3$ (sat'd), (b) 2 M $La(O_3SCH_3)_3$, (c) 2 M $Ba(O_3SCH_3)_2$, (d) 2 M $Cs(O_3SCH_3)$, (e) 2 M HO_3SCH_3, and (f) water

Table 2.8: Optical properties of the methylsulfonate solutions

	Index	Cauchy Coefficients			Absorbance	
Salt	n	A	B $\times 10^3$ (μm^4)	C $\times 10^4$ (μm^4)	α_{193} (cm^{-1})	λ_{edge}, $\alpha = 1\ cm^{-1}$
2.82 M $La(O_3SCH_3)_3$	1.577	1.439	3.70	0.544	0.314	188.4
2 M $La(O_3SCH_3)_3$	1.522	1.395	2.96	0.657	0.541	191.0
2 M $Ba(O_3SCH_3)_2$	1.493	1.373	2.96	0.568	0.314	188.4
2 M CsO_3SCH_3	1.463	1.351	3.28	0.339	0.861	191.7
2 M HO_3SCH_3	1.459	1.341	2.80	0.584	0.362	189.4

The low absorbance of the methylsulfonate anion can be compared to the low absorbance of sulfone structures (RSO_2R'). Sulfones are typically transparent down to 200 nm since the oxygen electrons require high energy for excitation, and sulfur has no non-bonding electrons.[23] As a result, high energies, corresponding to wavelengths lower than 200 nm, are required to excite the electrons in the sulfone and cause an absorbance.

The sulfone ionization potentials also suggest that these structures will have a low absorbance. When more energy is required for ionization, more energy is typically required for excitation (or absorbance) as well. Thus, with higher energy (low wavelength) ionization potentials, the absorbance also shifts to higher energies, or lower wavelengths. The ionization potentials of a series of structures with an increasing number of S=O groups, from n-butane to 1,3-dithietan-1,1,3,3-tetraoxide (a four-member ring with two sulfone structures), are given in Figure 2.12.[24, 25] Adding sulfur decreases the ionization energy (increases the wavelength). However, increasing the number of S=O groups decreases the wavelength (increases the energy) of the ionization potential so that structures with more S=O groups require higher energies (lower wavelengths) for excitation. Thus, due to the high energies required for electronic excitation, the methylsulfonate anion should have a low absorbance at 193 nm.

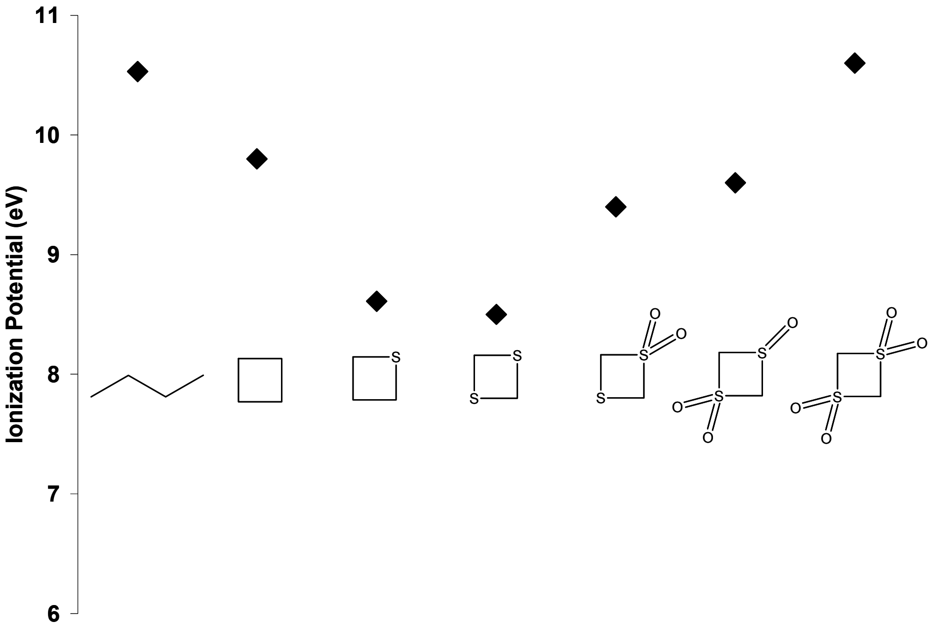

Figure 2.12: Ionization potential for structures with increasing S=O[24]

2.7.1 Methylsulfonate Solution Imaging

To evaluate the efficacy of the high index and low absorbance methylsulfonate solutions, an interferometric imaging system at the Rochester Institute of Technology was used to generate line and space patterns, Figure 2.13.[26] Each of the fluids was used to pattern 65 nm l/s images. Using the saturated lanthanum methylsulfonate solution, images of 45 nm half-pitch with NA = 1.05, 34.5 nm half-pitch with NA = 1.4, and 32 nm half-pitch with NA = 1.5 were achieved, Figure 2.14. These images are of good quality with few defects and no photoresist degradation.

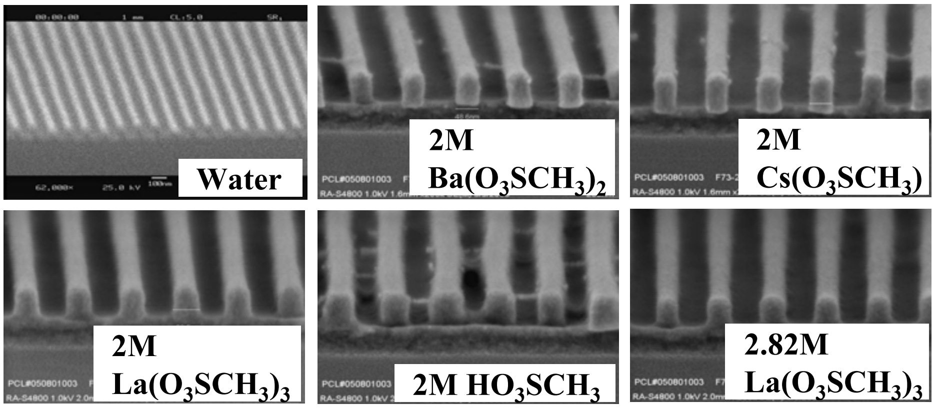

Figure 2.13: 65 nm line and space images using the methylsulfonate solutions as immersion fluids

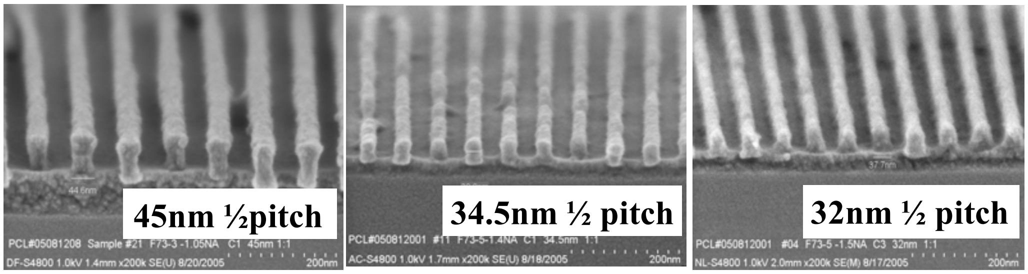

Figure 2.14: Line and space images: 2.82 M $La(O_3SCH_3)_3$ as the immersion fluid

2.7.2 Physical Properties of Methylsulfonate Solutions

The physical properties of the methylsulfonate salt solutions were also measured to evaluate their compatibility with immersion fluid handling systems. Since these systems were designed for water, the physical properties of the next generation immersion fluid should be similar to those of water.[27] The surface tension, density, and viscosity of each of the sulfonate salt solutions were measured and are given in Table 2.9. The surface tension of each of these fluids decreases from the surface tension of water due to the high salt concentration. The viscosity of the lanthanum solutions significantly increases over the viscosity of water. Both the high viscosity and low surface tension of the saturated lanthanum salt solution would make the implementation of this fluid in immersion lithography challenging. The importance of the physical properties will be discussed further in Chapter 3, 3.7.2. Additionally, due to the high concentration of salt in the saturated solution, evaporation of a droplet of fluid deposited on the wafer could leave salt crystals on the wafer and result in defects.

Table 2.9: Physical properties of methylsulfonate salt solutions

Fluid	Surface Tension (dyne/cm^2)	Density (g/cm^3)	Viscosity (cP)
Water	72.8	1.0	1.0
2 M CH_3SO_3H	20.6	1.0	1.1
2 M $Ba(O_3SCH_3)_2$	23.7	1.27	2.3
2 M $Cs(O_3SCH_3)$	24.2	1.27	1.1
2 M $La(O_3SCH_3)_3$	28.8	1.64	49.9
2.82 M $La(O_3SCH_3)_3$	28.2	1.67	92.8

2.8 CONCLUSIONS

A survey of ionic additives was completed to evaluate the effect of added salts on the optical properties of water. This survey revealed that the optical properties of these solutions were most significantly affected by the anion. The cation has a less significant effect, but as the atomic radius of the cation increased, slight increases in the index and absorption coefficient were observed. The trends observed in the index were also observed in the absorbance of these additives. The highest absorbance salts also yielded the highest index while the lowest absorbance salts yielded the lowest index. When the cation was varied, the bromides have the highest index followed by the acetates and then the chlorides. Similarly, the bromides have the highest absorbance, even at a lower concentration, followed by the acetates and then chlorides. The sodium salts and acids also follow the same index and absorbance trends. The highest index additives, NaSCN and HBr, also have high absorbances. The Kramers-Kronig relationship governs the optical properties of these solutions, and the absorbance edge should be the primary consideration in identifying a high index and low absorbance additive.

Solutions with the methylsulfonate anion have high refractive index values with an absorption edge less than 193 nm and moderate absorption coefficients, which could be reduced with additional purification. The saturated solution of lanthanum methylsulfonate has a refractive index of 1.58 at 193 nm, with an absorption coefficient of 0.314 cm^{-1}. Using the methylsulfonate anion, some of the highest reported refractive index values coupled with lowest absorption coefficients can be achieved for aqueous solutions.[28] With these potential immersion fluids, line and space patterns down to 32 nm half-pitch were successfully imaged with an interferometric imaging system. Further increases in the index of refraction of these fluids should allow patterning of sub-32 nm features.

While these studies provide valuable information about the optical properties of added salts in water at the 193 nm wavelength, none of these salts provided a fluid with all of the target properties. Further increases in refractive index are not likely with these solutions since the highest reported index solutions were saturated. Additionally, since metal contamination is an ongoing concern in a semiconductor processing environment, microelectronics-friendly cations, such as the alkylammonium ions, should be further studied with the methylsulfonate anion to develop a high index and low absorbance aqueous immersion fluid.

2.9 REFERENCES

1. Smith, B. W., Bourov, A., Kang, H., Cropanese, F., Fan, Y., Lafferty, N. and Zavyalova, L., *Water immersion optical lithography at 193 nm.* J. Microlith. Microfab. Microsys., 2004. B(1): p. 44-51.

2. Rothschild, M., Bloomstein, T. M., Kunz, R. R., Liberman, V., Switkes, M., Palmacci, S. T., Sedlacek, J. H. C., Hardy, D. and Grenville, A., *Liquid immersion lithography: Why, how, and when?* J. Vac. Sci. Technol., B, 2004. **22**(6): p. 2877-2881.

3. French, R. H., Sewell, H., Yang, M. K., Peng, S. P., McCafferty, D., Qiu, W., Wheland, R. C., Lemon, M. F., Markoya, L. and Crawford, M. K., *Imaging of 32-nm 1:1 lines and spaces using 193-nm immersion interference lithography with second-generation immersion fluids to achieve a numerical aperture of 1.5 and a k1 of 0.25.* J. Microlith. Microfab. Microsyst., 2005. **4**(3): p. 031103-1 - 031103-14.

4. Lopez-Gejo, J., Kunjappu, J. T., Turro, N. J. and Conley, W., *Amplification of the index of refraction of aqueous immersion fluids with crown ethers.* J. Micro/Nanolithogr. MEMS MOEMS, 2007. **6**(1): p. 013002/1-013002/5.

5. Chumanov, G., Evanoff, D. D., Jr., Luzinov, I., Klep, V., Zdryko, B., Conley, W. and Zimmerman, P., *Nanocomposite liquids for 193 nm immersion lithography: a progress report.* Proc. SPIE Int. Soc. Opt. Eng., 2005. **5753**(Pt. 2, Advances in Resist Technology and Processing XXII): p. 847-850.

6. Lee, K., Kunjappu, J., Jockusch, S., Turro, N. J., Widerschpan, T., Zhou, J., Smith, B. W., Zimmerman, P. and Conley, W., *Amplification of the index of refraction of aqueous immersion fluids by ionic surfactants.* Proc. SPIE Int. Soc. Opt. Eng., 2005. **5753**(Pt. 1, Advances in Resist Technology and Processing XXII): p. 537-553.

7. Zhou, J., Fan, Y., Bourov, A. and Smith, B. W., *Inorganic immersion fluids for ultrahigh numerical aperture 193 nm lithography.* Appl. Opt., 2006. **45**(13): p. 3077-3082.

8. Hecht, E., *Optics.* 4th. 2002, San Francisco: Addison Welsey. pp. 698.

9. Tompkins, H. G. and McGahan, W. A., *Spectroscopic Ellipsometry and Reflectometry: A User's Guide.* 1999, New York: John Wiley and Sons, Inc. pp. 228.

10. http://en.wikipedia.org/wiki/Polarization, 2009.

11. Born, M. and Wolf, E., *Principles of Optics.* 2nd. 1964, New York: Pergamon Press. pp. 808.

12. Synowicki, R. A., Pribil, G. K., Cooney, G., Herzinger, C. M., Green, S. E., French, R. H., Yang, M. K., Burnett, J. H. and Kaplan, S., *Fluid refractive index measurements using rough surface and prism minimum deviation techniques.* J. Vac. Sci. Technol., B, 2004. **22**(6): p. 3450-3453.

13. Burnett, J. H. and Kaplan, S. G., *Measurement of the refractive index and thermo-optic coefficient of water near 193 nm.* J. Microlith. Microfab. Microsys., 2004. **3**(1): p. 68-72.

14. Heller, W., *Remarks on refractive index mixture rules.* J. Phys. Chem., 1965. **69**(4): p. 1123-9.

15. Kramers, H. A., *The law of dispersion and Bohr's theory of spectra.* Nature, 1924. **113**: p. 673-4.

16. Kronig, R. d. L., *The theory of dispersion of x-rays.* J. Opt. Soc. Am., 1926. **12**: p. 547-57.

17. Smith, D. Y., *Dispersion Theory, Sum Rules, and Their Application to the Analysis of Optical Data.* Handbook of Optical Constants of Solids, Palick, E. D. 1985, New York: Academic Press, Inc. pp. 35-68.

18. Rabinowitch, E., *Electron-transfer spectra and their photochemical effects.* Rev. Mod. Phys., 1942. **14**: p. 112-31.

19. Blandamer, M. J. and Fox, M. F., *Theory and applications of charge-transfer-to-solvent spectra.* Chem. Rev., 1970. **70**(1): p. 59-93.

20. Fox, M. F. and Hunter, T. F., *Charge-transfer-to-solvent spectra.* Nature, 1969. **223**(5202): p. 177-8.

21. Smith, M. and Symons, M. C. R., *Solvation spectra. I. Effect of environmental changes upon the ultraviolet absorption of solvated iodide ions.* Trans. Faraday Soc., 1958. **54**: p. 338-45.

22. Smith, M. and Symons, M. C. R., *Solvation spectra. II. Nature of the electronically excited state of solvated iodide ions.* Trans. Faraday Soc., 1958. **54**: p. 346-52.

23. Rao, C. N. R., *Ultra-Violet and Visible Spectroscopy.* 3rd. 1975, England: Butterworth and Co. Ltd. pp. 242.

24. NIST Chemistry WebBook. http://webbook.nist.gov/, 2009.

25. Block, E., Corey, E. R., Penn, R. E., Renken, T. L., Sherwin, P. F., Bock, H., Hirabayashi, T., Mohmand, S. and Solouki, B., *Flash vacuum pyrolysis studies. 9. Photoelectron spectra and molecular properties. 101. Synthesis and thermal decomposition of 1,3-dithietane and its S-oxides.* J. Am. Chem. Soc., 1982. **104**(11): p. 3119-30.

26. Bourov, A., Fan, Y., Cropanese, F. C., Lafferty, N. V., Zavyalova, L., Kang, H. and Smith, B. W., *Immersion microlithography at 193 nm with a Talbot prism interferometer.* Proc. SPIE, 2004. **5377**(Pt. 3, Optical Microlithography XVII): p. 1573-1578.

27. Sewell, H., McCafferty, D., Markoya, L., Hendrickx, E., Hermans, J. and Ronse, K., *32nm node technology development using interference immersion lithography.* Proc. SPIE Int. Soc. Opt. Eng., 2005. **5753**(Pt. 1, Advances in Resist Technology and Processing XXII): p. 491-501.

28. Zhou, J., Fan, Y., Bourov, A., Lafferty, N., Cropanese, F., Zavyalova, L., Estroff, A. and Smith, B. W., *Immersion lithography fluids for high NA 193 nm lithography.* Proc. SPIE Int. Soc. Opt. Eng., 2005. **5754**(Pt. 2, Optical Microlithography XVIII): p. 630-637.

Chapter 3: Alkanes with High Transparency for Next Generation Immersion Lithography

3.1 INTRODUCTION

The most challenging aspect of fluid development for the next generation of immersion lithography is not identifying a fluid with a high index of refraction, but obtaining a high index accompanied by a low absorbance at 193 nm. The challenge arises since these optical properties are linked.

3.1.1 The Lorentz Model

As a light wave passes through a medium, the properties of the wave are affected by the interaction with the medium. The complex refractive index describes the change in the speed of light in the medium and is given by

$$\tilde{n} = \frac{c}{v}, \tag{3.1}$$

where ñ is the complex refractive index, c is the speed of light, and ν is the phase velocity of the light wave in the medium. The complex index is defined by

$$\tilde{n} = n + ik \tag{3.2}$$

where the real part of ñ, n, is the index of refraction and the imaginary part of ñ, k, is the absorbance. The index (n) determines the phase of the wave in the medium, and the absorbance determines the amplitude, or attenuation of the wave, in the medium.[1]

A simple description of the relationship between the index and absorbance was developed by H. A. Lorentz.[2] Lorentz defined a model of polarizable matter composed of independent, isotropic electrons, bound to their equilibrium position by elastic restoring forces that obey Hooke's law.[1-4] The motion (x) of these electrons can be expressed by the Newtonian law of dynamics as

$$m\frac{d^2x}{dt^2} + m\Gamma\frac{dx}{dt} + \beta x = -eE_o e^{-i\omega t} \quad . \tag{3.3}$$

where m is the mass of the electron, Γ is the damping constant, β is the spring constant (stiffness), e is the magnitude of the electron charge, and $E_o e^{-i\omega t}$ is the electric field or light wave "seen" by the medium and is a function of frequency (ω).[2, 4] The second term in Equation 3.3, the energy loss due to damping, is proportional to velocity and arises from the frictional force between the moving electron and the medium.[5, 6] The spring constant (β) can also be expressed in terms of the natural resonance frequency (ω_o) as $\beta = m\omega_o^2$. The solution to Equation 3.3, which describes the displacement of these electrons from equilibrium, is given by[2, 4]

$$x(t) = -\frac{eE_0}{m}\frac{e^{-i\omega t}}{(\omega_o^2 - \omega^2) - i\Gamma\omega} \quad . \tag{3.4}$$

According to Equation 3.4, the maximum displacement (or amplitude) occurs when $\omega = \omega_o$. When the frequency of the incident electric field approaches the resonance frequency (ω_o), the amplitude of the electron oscillations (x) becomes very large and out of phase with the incident field. The electron oscillations attenuate the amplitude, or energy, of the incident field in the medium, resulting in a strong absorbance at the resonance frequency. The phase shift between the incident field and electron oscillators results in an increase in the phase velocity of the incident field in the medium (and corresponding decrease in index, see Equation 3.1). Far from the resonance frequency, the electron oscillators have amplitudes that are similar to and almost in phase with the incident field.[3, 4]

The interference of the electron oscillators with the incident field to accelerate or retard the phase velocity (so that the index depends on the frequency of the incident field) is known as dispersion.[3, 6] In normal dispersion, when the frequency of the incident field is far from the resonance frequency, the properties of the wave in the medium are only slightly altered, and both the index and absorbance increase slightly with decreasing wavelength (increase with increasing frequency). At frequencies close to the resonance frequency (ω_o), a strong absorbance occurs, and the index decreases with decreasing wavelength. The decrease in index with decreasing wavelength is known as anomalous dispersion. Normal and anomalous dispersion for a one electron oscillator are shown in Figure 3.1.

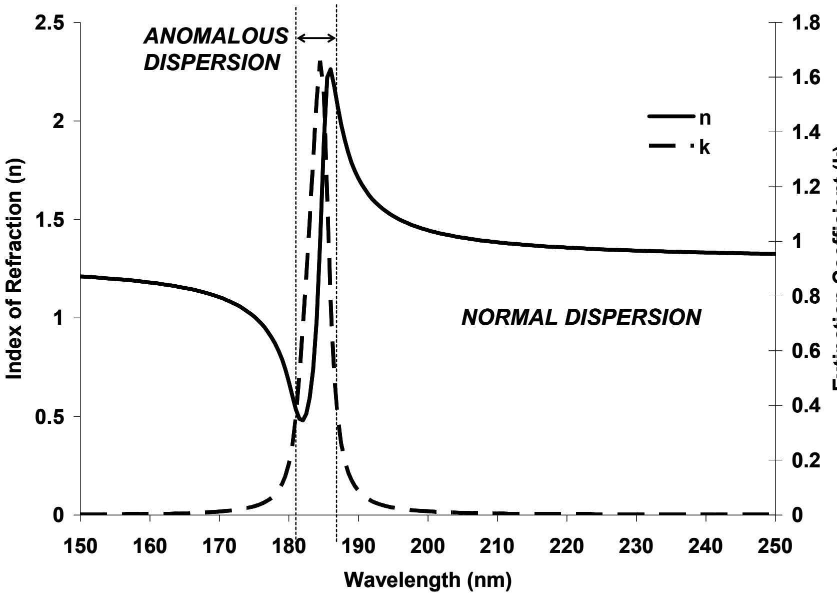

Figure 3.1: Normal and anomalous dispersion with one oscillator

The decrease in index observed in anomalous dispersion is due to the increase in the phase velocity of the incident field in the medium. At the resonance frequency, the electron oscillators shift out-of-phase with the incident wave, and the phase velocity of the incident field in the medium increases. Since the phase shift occurs at the resonance frequency (ω_o), the index is expected to be maximized at the resonance frequency. However, the index maximum occurs at a slightly longer wavelength than the resonance frequency. The offset in the frequency of the index maximum is due damping effects, which occur as energy is dissipated by the oscillating electrons.[5, 6]

3.1.2 Exploiting Anomalous Dispersion

The relationship between the index and absorbance dictates that the maximum index in the spectrum occurs with a strong absorbance. However, at the edge of the absorption peak, while the absorbance is still low, the index increases sharply, almost to its maximum value. If this absorbance edge is at 193 nm, the index should ideally be maximized while still maintaining a low absorbance. A fluid or class of fluids with an absorbance edge slightly less than 193 nm should therefore have the high index and low absorbance needed for a next generation immersion fluid.

Alkanes (saturated hydrocarbons) are composed only of sigma (σ) bonds. Since electronic transitions in these structures occur at high energies, or wavelengths less than 200 nm, alkanes should have a low absorbance at 193 nm.[7] The energy (or wavelength) of the electronic transitions depends on the energy difference, or gap, between the highest occupied molecular orbital (HOMO) and lowest unoccupied molecular orbital (LUMO), known as the HOMO-LUMO gap. These energies depend on the alkane structure and can be studied through Vacuum Ultra-Violet (VUV) absorbance spectra. Typically, alkanes have a very sharp absorbance edge.[8] If this sharp absorbance edge were to occur at a wavelength slightly less than 193 nm, the fluid would have a low absorbance and a high index and would be a good next generation immersion fluid candidate.

VUV absorbance data for a range of linear and cyclic alkanes have been reported in both the liquid and gas phase.[9-15] Trends in both the ionization potential and absorbance of a homologous series of linear alkanes ($C_1 - C_{10}$) have received extensive analysis.[14-22] The excited states of cycloalkanes have also been studied, but with less emphasis on the trends in a homologous series.[11, 15, 20-28] To identify structures which provide a high index and low absorbance at 193 nm for immersion lithography, a comprehensive survey of the variation in the absorbance edge of linear, cyclic, and complex cyclic alkanes, with a systematic range of structural variations, is needed.

The index of refraction and absorbance of a series of linear, cyclic, and complex cyclic alkanes were therefore studied. Index of refraction data are typically collected at 589 nm, and absorbance spectra are typically obtained to 200 nm. Index data at 193 nm and absorbance spectra below 200 nm, especially for neat fluids, are needed to study the optical properties of the alkane fluids. In addition to measurement of the optical properties, the physical properties of these fluids were evaluated to determine their compatibility with immersion fluid handling systems that have been designed for water.

3.2 EXPERIMENTAL DETAILS

3.2.1 Materials

n-Pentane [*Spectrophotometric Grade*, ≥99% (Acros Organics)], n-hexane [*ReagentPlus,* ≥99% (Aldrich)], n-heptane [*HPLC*, ≥96% (Fisher Chemical)], n-octane [≥99% (Acros Organics)], n-decane [≥99% (Acros Organics)], cyclopentane [*purum*, ≥98.5% (GC) (Fluka)], cyclohexane [≥99% (Acros Organics)], cycloheptane [>98% (GC) (TCI America)], cyclooctane [≥99% (Aldrich)], cyclodecane [96+% (ChemSampCo, Inc.)], methylcyclohexane [*ReagentPlus,* ≥99% (Sigma-Aldrich)], ethylcyclohexane [≥99% (Acros Organics)], propylcyclohexane [>98% (GC) (TCI America)], butylcyclohexane [≥99% (Aldrich)], decalin [*cis* + *trans* mix, anhydrous, ≥99% (Sigma-Aldrich)], *cis*-decalin [>98% (GC) (TCI America)], *trans*-decalin [>98% (GC) (TCI America)], bicyclohexyl [*puriss.*, ≥99% (GC) (Fluka)], perhydrofluorene [97% (Aldrich)], 1,3-dimethyladamantane [≥99% (Acros Organics)], and methylcubane [99%

(Boron Molecular)] were purchased at the highest purity available. The structure and carbon number of each of these fluids is given in Table 3.1. Methyltetracyclododecane was received from B.F. Goodrich and used without further purification.

Table 3.1: Structure and carbon number of the saturated hydrocarbons

Structure	Carbon Number	Structure	Carbon Number	Structure	Carbon Number
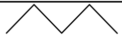 Pentane	5	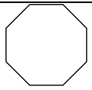 Cyclooctane	8	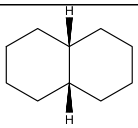 Cis-decalin	10
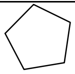 Cyclopentane	5	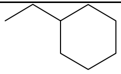 Ethylcyclohexane	8	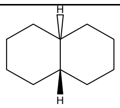 Trans-decalin	10
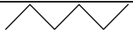 Hexane	6	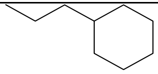 Propylcyclohexane	9	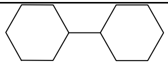 Bicyclohexyl	12
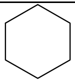 Cyclohexane	6	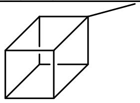 Methylcubane	9	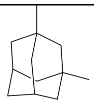 1,3-Dimethyladamantane	12
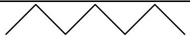 Heptane	7	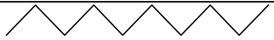 Decane	10	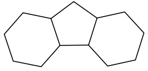 Perhydrofluorene	13
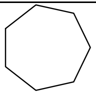 Cycloheptane	7	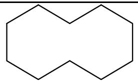 Cyclodecane	10	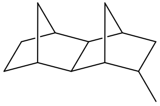 Methyldinorbornane	13
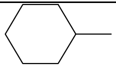 Methylcyclohexane	7	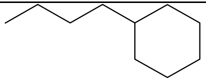 Butylcyclohexane	10		
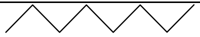 Octane	8	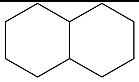 Decalin	10		

3.2.2 Purification Methods

Even at the highest-purity commercially available, alkane fluids exhibit a strong UV absorbance. Three purification methods, acid wash,[29, 30] column chromatography,[9, 29, 31] and distillation, were used to decrease the concentration of impurities. Each fluid was purified with at least one of these methods until the absorbance was minimized and constant with respect to further purification. Additionally, alkanes form a weak van der Waals complex with oxygen that is capable of undergoing a charge transfer between the subunits after photon absorption, resulting in a strong absorbance at 193 nm.[30, 32] Thus, all of the fluids were de-oxygenated by sparging with an inert gas such as N_2 or Ar prior to testing. The detailed purification sequence for each fluid, using at least one of the methods described below, is given in Appendix A. An example of the absorbance of cyclohexane with successive purifications is given in Figure 3.2. Achieving the ultimate purity level for each hydrocarbon is challenging, despite multiple purification steps.

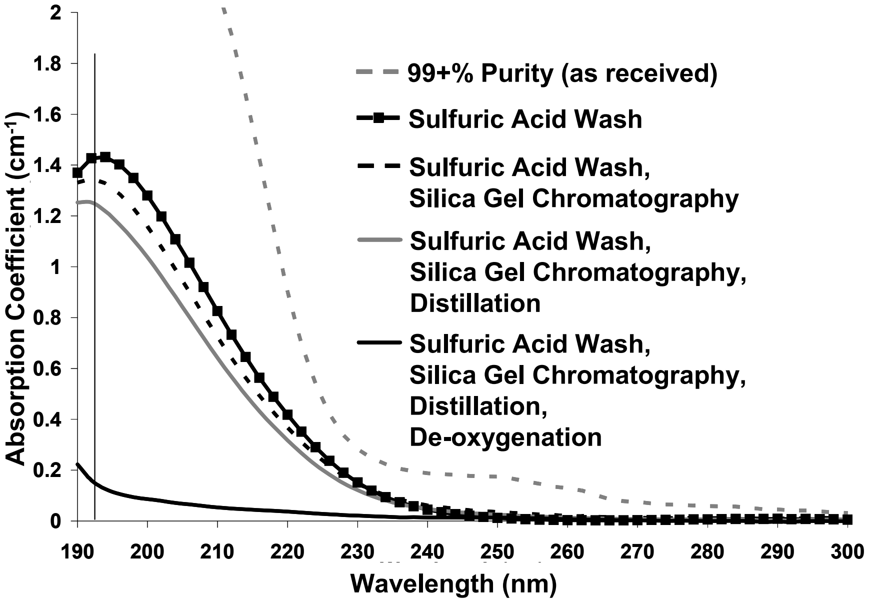

Figure 3.2: Purification example: Absorbance of spectral grade cyclohexane (99+% purity) following multiple purification steps

3.2.2.1 Purification by Sulfuric Acid Wash

For the sulfuric acid wash purification, the hydrocarbon was washed with concentrated sulfuric acid [Fisher Chemical, Certified ACS Plus] in an approximately 1:2 ratio by volume (hydrocarbon:acid) to remove olefinic (unsaturated) impurities. The non-miscible phases were stirred vigorously for at least 12 h. After stirring, the acid phase typically became yellow in color. The acid phase was then removed, and this process was repeated until the color of the acid layer remained unchanged after the wash. The hydrocarbon phase was separated from the acid phase for absorbance measurements.

3.2.2.2 Purification by Column Chromatography

The hydrocarbon was passed through a column of silica gel to remove polar impurities and/or silver nitrate on silica gel to remove olefinic impurities.[31] Prior to use, the silica gel was heated to approximately 200 ^{o}C for at least 24 hours and the silver nitrate on silica gel to 140 ^{o}C for approximately 2 hours. Due to the low volumes required, a small Pasteur pipette was typically used as the column. This process was repeated until impurity levels were minimized, as evidenced by a significant decrease in the absorbance and sharpening of the absorbance edge. Alternatively, following a sulfuric acid wash, the hydrocarbon fluid was mixed with a small amount of silica gel to remove any traces of the acid layer or other polar impurities.

3.2.2.3 Purification by Distillation

The hydrocarbon was distilled under a nitrogen atmosphere for fluids with boiling points up to 130 ^{o}C and under vacuum for fluids with boiling points greater than 130 ^{o}C. For the materials with boiling points greater than 130 ^{o}C, sufficient vacuum was applied to lower the boiling point to approximately 100 ^{o}C. The hydrocarbon was washed with sulfuric acid before distilling and then stirred with a small amount of silica gel after separation from the acid layer to remove all of the acid prior to distillation. Unintentional distillation over residual sulfuric acid resulted in an increase in the absorbance of the fluid. After the distillation, the hydrocarbon was typically treated with another acid wash and/or column separation to further reduce the impurity levels.

3.2.2.4 Purification by De-oxygenation

De-oxygenation of the hydrocarbon fluids was performed under an inert environment of N_2 or Ar in a glove bag. N_2 or Ar was bubbled through the fluid using a syringe needle for 5 – 15 minutes, depending on the sample volume. The fluid was then transferred to the cuvette and tightly sealed using Teflon tape and/or parafilm. The absorbance was measured immediately following de-oxygenation to prevent contamination. Alternatively, N_2 or Ar was bubbled for approximately 10 minutes through the sealed cuvette by inserting a syringe needle through a cap with a Teflon septum.

3.2.3 Synthesis and purification of methydinorbornane

Methyldinorbornane was synthesized by hydrogenation of methyltetracyclododecane (MTD) over a palladium on carbon catalyst (10 wt % loading). Approximately 50 mL of MTD was dissolved in approximately 50 mL of a 10% solution of methanol in ethyl acetate containing approximately 2 g of catalyst and then pressurized to 600 psi with hydrogen and stirred at room temperature in a high pressure Parr reactor. Once the hydrogen was consumed, the reactor was re-pressurized to 600 psi of hydrogen. This process was repeated until the consumption of hydrogen gas ceased. The solution was then filtered through a celite pad and reduced in vacuo. The resulting oil was washed twice with sulfuric acid overnight to remove any remaining olefinic impurities. The hydrocarbon was separated from the acid layer and filtered through basic alumina to remove any residual acid. The resultant fluid was distilled at 42 °C (0.38 torr). This fraction was washed with sulfuric acid once more to ensure removal of all remaining starting material.

3.2.4 VUV Absorbance Measurements

The absorbance spectra were collected in the liquid phase. Since electronically excited states interact readily with neighboring molecules, fine structure resulting from vibrational and rotational transitions are typically not observed in the condensed phases.[9] However, liquid phase spectra reveal the absorbance onset and can be used to identify trends based on structure and postulate the nature of the excited state.

Absorbance spectra were obtained with either an Acton Research Corporation CAMS-507 Spectrophotometer from 150 – 250 nm (in a nitrogen purged environment) or with the combination of a modified Varian Cary 400 Spectrophotometer from 185 – 200 nm (in a nitrogen-purged environment) and a Shimadzu UV-2401 UV/Vis Spectrophotometer from 200 – 250 nm. The absorbance edge (λ_{edge}) is defined here as the wavelength at which $\alpha = 2$ cm^{-1}. Decalin (mix, *cis*+*trans*), *cis*-decalin, *trans*-decalin, cyclooctane, cycloheptane, cyclodecane, and methyldinorbornane were measured with the Varian/Shimadzu combination. The remaining fluids were measured with the Acton Spectrophotometer. High purity quartz cuvettes of 1 mm path length from either Hellma-USA or Starna Cells, Inc. were used for the measurements. Using a 1 mm path length increases the sensitivity of the measurement so that the absorbance edge can accurately be identified. Methylcubane were measured in a 10 mm path quartz cuvette from Starna Cells, Inc. from 190 – 250 nm on the Shimadzu instrument.

To measure the absorbance, a reference spectrum was recorded with no sample cuvette in the light path. The absorbance of a cuvette filled with the sample was then measured. With this method, light lost due to reflections at each of the quartz-air or quartz-fluid interfaces was not accounted for during the experiment. The absorbance spectrum was corrected for reflections using the correction procedure described in Chapter 2, 2.2.2.

The index of refraction of methylcubane was not collected for the full spectrum and was extrapolated from longer wavelengths. As a result, the absorbance spectrum for this sample is not corrected for reflections. However, since the index values of the quartz cuvette are expected to be similar to the fluid, only a small amount of light is lost due to reflections and should result in less than 5% error.

Transmission of the 1 mm path length empty quartz cuvettes (without reflection-correction) was used to evaluate the error in the VUV absorbance measurements. For the Acton, the empty quartz cuvette transmission from 160 – 250 nm for 10 trials was averaged, and the 95% confidence limits were calculated. The maximum error in the spectrum occurs at 172 nm with a transmittance of 67.9±1.67%. The average transmission for the 10 trials and 95% confidence limits for the Acton are shown in Figure 3.3. For the Varian/Shimadzu, the empty quartz cuvette transmission collected from 185 – 250 nm for five trials was collected. The maximum error occurs at 185 nm for a transmittance of 79.8±1.13%. The average transmission and 95% confidence limits for the Varian/Shimadzu are given in Figure 3.3.

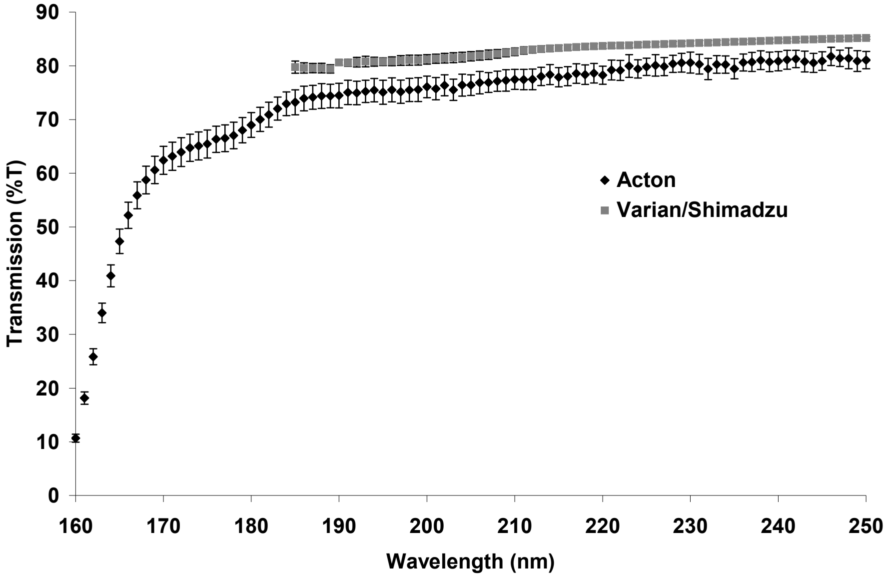

Figure 3.3: Average empty quartz cuvette transmission data and 95% confidence limits for 10 trials using the Acton and five trials using the Varian/Shimadzu

3.2.5 Index of Refraction Measurements

The index of refraction of the fluids was determined from ellipsometric measurements made on a J.A. Woollam M2000 variable angle spectroscopic ellipsometer from 190 to 1000 nm. The ellipsometric parameters Ψ and Δ were fit to a Cauchy dispersion model by the Woollam WVASE32 software. The fluids were measured by filling a 2 in. diameter Fluoroware cup with a curved bottom. Using this method, only reflections from the top surface of the fluid were collected for analysis.[33] This procedure is described in detail in Chapter 2, 2.2.3.

The Cauchy model provides a description of the index of refraction in normal dispersion, or wavelengths at which absorption is low. Since the hydrocarbon fluids were not de-oxygenated prior to this index measurement, these fluids should have a strong absorption at 193 nm (see Figure 3.2), and the Cauchy equation might not accurately model the index. To determine the validity of the Cauchy model, the index of de-oxygenated and oxygenated samples can be compared. Index of refraction values at 193 nm have been reported for de-oxygenated decane, cyclohexane, cyclooctane, and decalin (*cis* + *trans*, mix), measured using a prism minimum deviation technique, and are 1.549, 1.571, 1.615, and 1.641, respectively.[34-36] Without de-oxygenation, the index values at 193 nm for decane, cyclohexane, cyclooctane, and decalin (*cis* + *trans*, mix) are 1.544, 1.578, 1.611, and 1.654, respectively, according to the Cauchy model fit. Since the index values collected for the de-oxygenated and oxygenated fluids are similar, the Cauchy model seems to accurately predict the index, despite the known high absorbance due to dissolved oxygen. When the index is of much greater order than the extinction coefficient (or absorbance), the index dominates the beam reflected from the sample and collected by the detector. Thus, despite the presence of dissolved oxygen, the extinction coefficient must still be of much lower order than the index so that essentially only information about the index is contained in the reflected beam.

3.3 ALKANE ABSORBANCE

3.3.1 Linear Alkanes

The absorbance spectra of the normal alkane series from C_5 to C_{10} (excluding C_9) are given in Figure 3.4. The absorbance shifts to longer wavelengths (decreases to lower energies) as the number of carbons in the linear chain increases. This absorbance shift suggests that the energy between the HOMO and LUMO (HOMO-LUMO gap) decreases as the number of carbons in the linear chain increases.

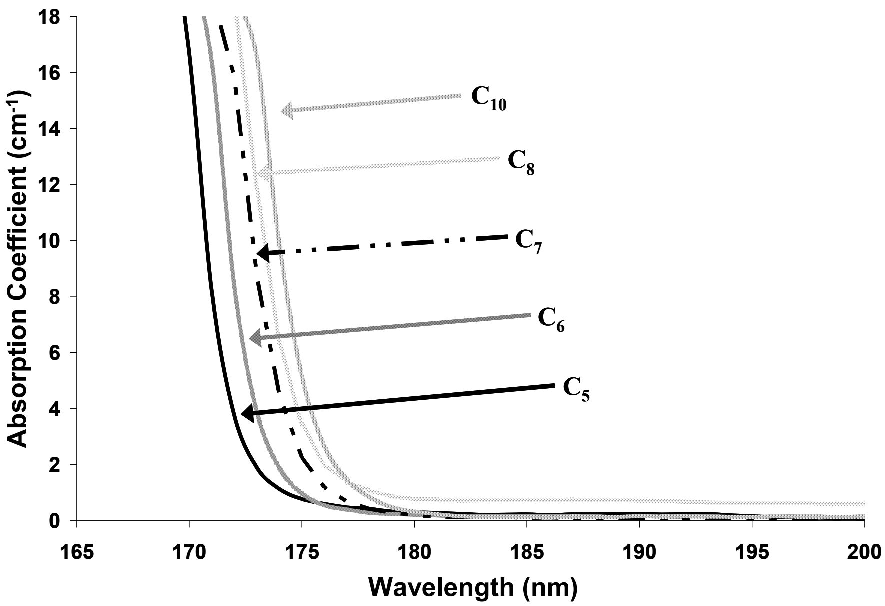

Figure 3.4: Absorbance spectra of the linear hydrocarbons, C_5 - C_{10} (excluding C_9). The baseline for C_8 (octane) is likely due to residual impurities.

To develop a hypothesis for the observed decrease in the HOMO-LUMO gap with the addition of carbon atoms, the change in the energy of the HOMO and LUMO as carbons are added should be evaluated. First, when carbons are added to the linear chain, the added electrons occupy orbitals of increasingly higher energy. With orbitals of higher energies occupied, the energy of the HOMO increases. The increase in the energy of the HOMO with the addition of carbon atoms is known as orbital “destabilization”. With the shift in the HOMO to higher energies, the energy of the LUMO must be either decreased or unaffected by increasing carbon number to achieve the observed decrease in the HOMO-LUMO gap.

Robert Mulliken identified that the lowest energy excited orbitals (LUMO) of these alkane systems are primarily Rydberg in character by studying methane and ethane.[37] A Rydberg orbital is a nonbonding orbital that is not in the valence shell. These orbitals have a much larger radius than that of the core orbitals.[22] Electronic excitations to Rydberg states occur in series and can be identified if their excitation energy (or frequency, ω) fits the Rydberg formula given by

$$\omega = IE - \frac{R_\infty}{(n-\delta)^2} \tag{3.5}$$

where IE is the ionization potential towards which the series converges, R_∞ is the Rydberg constant (109,737 cm^{-1}), n is the principal quantum number of the Rydberg orbital and can increase to infinity (for alkanes, n = 3, 4, 5, …), and δ is the quantum defect or Rydberg correction.[22] The difference between the ionization potential and Rydberg excitation energy is the term value (Δ). The term value is illustrated in Figure 3.5. The first three accessible Rydberg states for the alkanes are 3s, 3p, and 3d; these states are also shown in Figure 3.5. Based on term values calculated from gas-phase spectroscopic data for a range of linear alkanes (C_1 – C_{10}) and cycloalkanes, including cyclohexane, *trans*-decalin, and adamantane, the term value for each Rydberg state seems to be relatively independent of alkane geometry.[11, 17, 22, 25] For the 3p and 3d Rydberg transition, the term values are approximately 2.2 eV and 1.6 eV, respectively, regardless of alkane geometry.[25] The term value for the 3s transition is as large as 3.9 eV for methane, but converges to approximately 2.7 eV for the larger alkanes (> C_8).[22, 25] A mainly constant term value indicates that the position of the LUMO is essentially unaltered by the addition of carbon atoms, or other changes in alkane geometry. If the LUMO energy is essentially constant, and the HOMO energy is "destabilized" (increased) with the addition of carbon atoms, the HOMO-LUMO gap should decrease as the carbon number is increased.

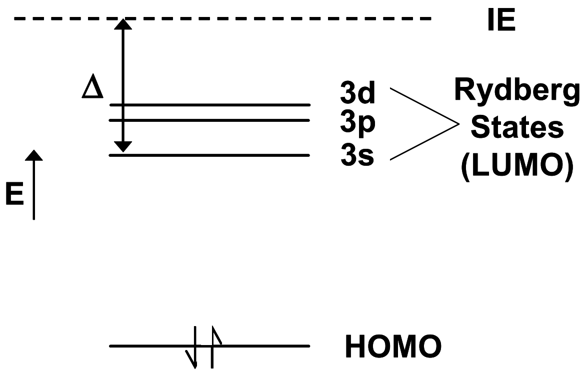

Figure 3.5: HOMO-LUMO gap in alkanes and Rydberg term value (Δ)

Assuming the LUMO of the alkanes in this study is a Rydberg state, the energy of the LUMO can be evaluated by comparing the term values of each alkane. The 1 mm path through which the absorbance spectra were measured did not allow measurement of the peak maximum, which would correspond to the lowest-energy Rydberg state and should be the energy used to calculate the term values. Since the energy, or wavelength, of the peak maximum was not detectable through the 1 mm path, the absorbance onset wavelength (λ_{edge}), defined as the wavelength at which $\alpha = 2\ cm^{-1}$, was used instead to calculate the term values. For each of these alkanes, the absorbance increases sharply, with only a small variation in wavelength up to $\alpha \sim 20\ cm^{-1}$, to form a sharp absorbance edge. Assuming that the absorbance continues to increase sharply up to the peak maximum, λ_{edge} should be a reasonable approximation for the peak maximum. If λ_{edge} reasonably approximates the peak maximum, the selection of $\alpha = 2\ cm^{-1}$ to define λ_{edge} should not significantly alter the calculated term values, and these term values should be consistent with the reported term values (~ 3 eV).[22, 25]

The λ_{edge}, ionization energies,[38] and term values (Δ) are given in Figure 3.6 for the linear alkane series. Both the ionization energy and energy of λ_{edge} decrease with increasing carbon number. From Figure 3.6, the ionization energy decreases from 10.28

eV (120.6 nm) for n-pentane to 9.65 eV (128.5 nm) for n-decane. The λ_{edge} energy decreases (or wavelength increases) from 7.2 eV (173 nm) for n-pentane to 7 eV (176 nm) for n-decane. The term values range from 3.1 eV for n-pentane to 2.7 eV n-decane. These term values are consistent with the previously reported term values (~ 3 eV).[22, 25] This consistency suggests that the choice of λ_{edge} to define the peak maximum is a reasonable approximation.

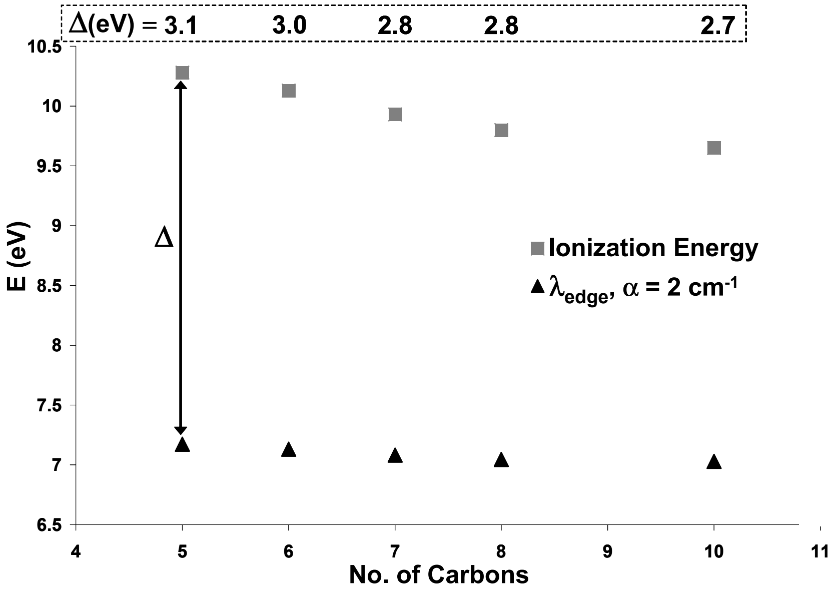

Figure 3.6: Ionization energies (squares), λ_{edge} (triangles), and term values (Δ) for the linear alkane series

Based on the agreement between the calculated and reported term values, the transitions observed in Figure 3.4 for the linear alkanes seem to be essentially Rydberg transitions. Due to the similarity in the term values calculated for each alkane in the linear series, the energy of the LUMO seems to be essentially unaltered by the addition of carbon atoms. Ryberg states are large, diffuse orbitals which are not significantly affected by the core electrons. Assuming the LUMO is a Rydberg state, it seems reasonable to postulate that the energy of these diffuse states would not be affected by increasing carbon number. Therefore, the hypothesis that the energy of the LUMO is essentially unaltered while the energy of the HOMO is "destabilized" with the addition of carbon atoms seems to explain the decrease in the HOMO-LUMO gap, or red-shift in λ_{edge}, observed with increasing carbon number. Finally, in the condensed phases, Rydberg states are broadened so that the exact nature of the vibronic transitions is not observed. Since the 3s Rydberg state has a much lower oscillator strength than the 3p or 3d states,[17] the observed absorptions are likely some mixture of electronic transitions to the 3s, 3p, and 3d states which are unresolved in the liquid phase. If the absorbance spectra of this linear series were measured through a shorter path, higher absorption coefficient values could be detected and might further reveal the nature of these Rydberg states.

3.3.2 Cycloalkanes

The absorbance spectra of the cycloalkane series (C_5 – C_{10}, excluding C_9) are given in Figure 3.7. As observed for the linear alkanes, the absorbance shifts to longer wavelengths (lower energies) with increasing carbon number, from C_5 to C_{10}. The term values (Δ) can be calculated for these cyclic structures as in the linear series, using the difference between λ_{edge} and the ionization energies.[38] The term values, ionization energies, and λ_{edge} are given in Figure 3.8.

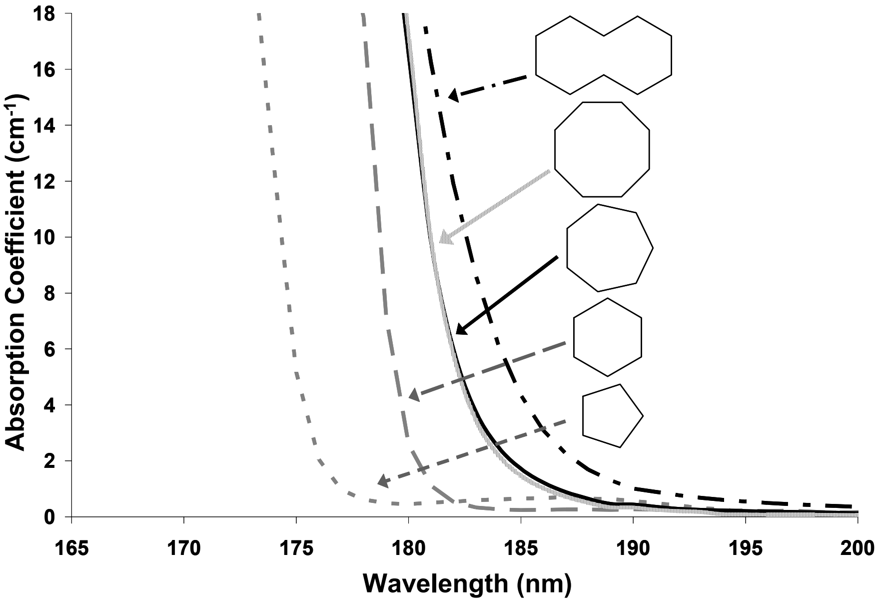

Figure 3.7: Absorbance spectra for the cycloalkane series, C_5 to C_{10} (excluding C_9)

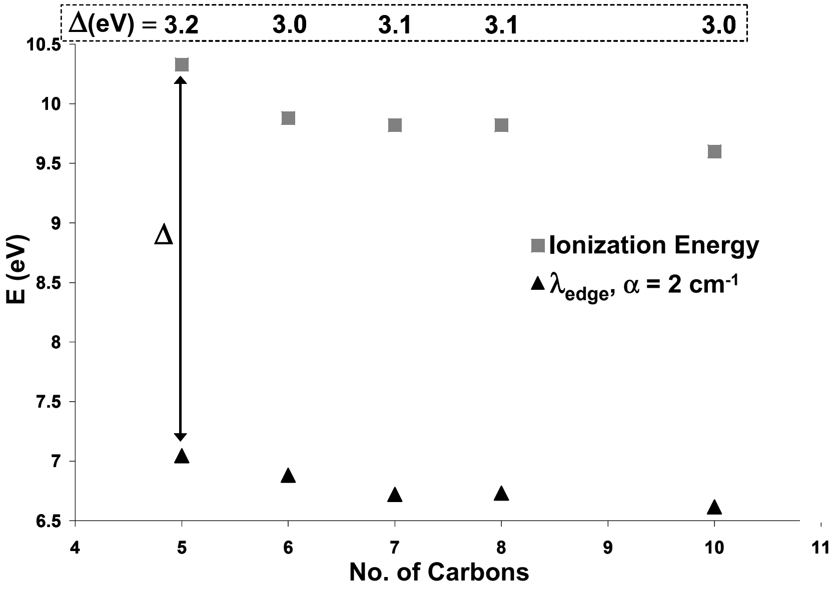

Figure 3.8: Ionization energies (squares), λ_{edge} (triangles), and term values (Δ) for the cycloalkane series

The ionization energy decreases from 10.33 eV (120 nm) for cyclopentane to 9.6 eV (129 nm) for cyclodecane. The λ_{edge} energy decreases (or wavelength increases) from 7.1 eV (176 nm) for cyclopentane to 6.6 eV (187 nm) for cyclodecane. The term values for the cycloalkane series range from 3.2 eV for cyclopentane to 3.0 eV for cyclodecane and are consistent with both the previously reported term values for the Rydberg state transitions and the term values calculated for the linear series (~3 eV).[22, 25] In addition, the term value reported for cyclohexane (3.0 eV) was also calculated in this work.[25] The similarity in the term values supports the theory that the energy of the LUMO (Ryberg orbital) is essentially unaffected by the geometry of the alkane. If the HOMO is "destabilized" with the addition of carbon atoms, the HOMO-LUMO gap will decrease as the carbon number increases and result in the red-shift in λ_{edge} with carbon number.

There is a greater shift in λ_{edge} over the series $C_5 - C_{10}$ for the cycloalkanes than for the linear alkanes. This shift over a homologus series will be represented by Δ_{shift}. Δ_{shift} for the cycloalkanes is 11 nm (0.4 eV) while for the linear series, Δ_{shift} is 3 nm (0.1 eV). This difference is illustrated in the plot of λ_{edge} for both the linear and cyclic alkanes and is given in Figure 3.9. Additionally, the λ_{edge} difference between structures of the same carbon number (i.e. n-hexane and cyclohexane) also seems to increase as carbon number increases.

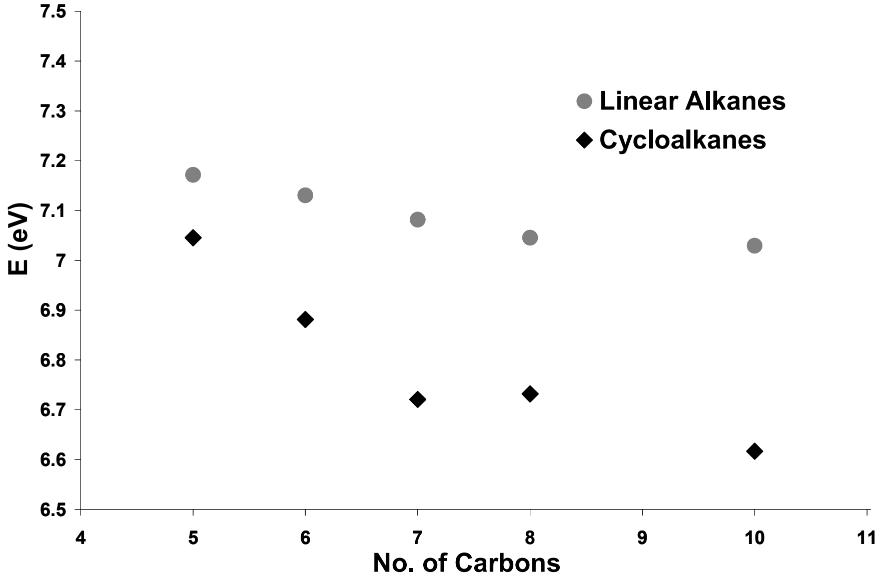

Figure 3.9: λ_{edge} for the linear and cyclic alkanes

Increasing strain energy shifts the HOMO to higher energies and could explain the difference in Δ_{shift} between the linear and cyclic homologs. However, the strain energies of the cycloalkanes do not increase monotonically with carbon number. Cyclopentane has bond angles of 108°, which differ only slightly from the normal tetrahedral state (109.5° bond angles) and result in a small amount of strain energy (27 kJ/mol). Cyclohexane has no ring strain because the "puckering" of the ring allows achievement of tetrahedral bond angles. Cycloalkanes larger than cyclohexane exhibit a small degree of ring strain, which increases with ring size up to C_9. The ring strain in cycloheptane is 27 kJ/mol, 42 kJ/mol in cyclooctane, and 50 kJ/mol in cyclodecane.[39] Therefore, an increase in the energy of the HOMO with increased strain energy does not seem to fully explain the difference in Δ_{shift} for the linear and cyclic alkanes, primarily due to the lack of strain in cyclohexane. The difference in λ_{edge} between linear and cyclic structures with the same carbon number is also not fully explained since n-hexane and cyclohexane would then have the same λ_{edge} since both structures have no strain energy.

Instead of evaluating strain energies, the difference in ionization energies for the linear and cyclic homologs might provide an explanation for the difference observed in Δ_{shift} and λ_{edge} for the linear and cyclic structures. However, the large difference in Δ_{shift} and energies of λ_{edge} is not observed in the ionization energies. The ionization energies of both the linear and cyclic alkanes are shown in Figure 3.10. The range in ionization energies is approximately the same for both the linear and cyclic homologs. While there is some variation in the difference in ionization energy between structures of the same carbon number, this variation does match the trend observed in λ_{edge}. Therefore, since the ionization energies are not appreciably different for the linear and cyclic structures, the ionization energies do not explain the difference in λ_{edge}.

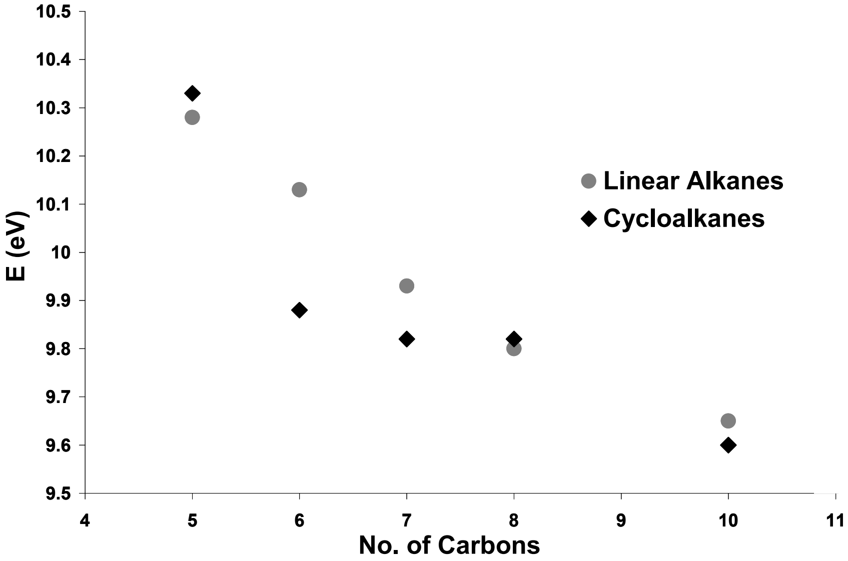

Figure 3.10: Ionization energies for the linear and cyclic alkanes

Finally, the difference in Δ_{shift} and λ_{edge} observed for the linear and cyclic homologs might be related to differences in dispersion for each of these structures. If the cycloalkanes have a slightly broader absorbance peak than their linear counterparts, λ_{edge} would red-shift slightly. This broadening in the dispersion of the transition for the cyclic structures would explain both the increase in Δ_{shift} and difference in λ_{edge}. This theory could be evaluated by measuring the absorbance spectra of these homologs in path lengths short enough to reveal the peak maximum.

3.3.3 Cyclohexane with Linear Substituents

A homologous series of cyclohexane fluids with linear subsitutents, from methyl to butyl, was also studied. The absorbance spectra for this series are given in Figure 3.11. The red-shift in the absorbance of cyclohexane with the addition of the methyl group is larger than the absorbance shift that occurs with further increases in the carbon number (ethyl to butyl).

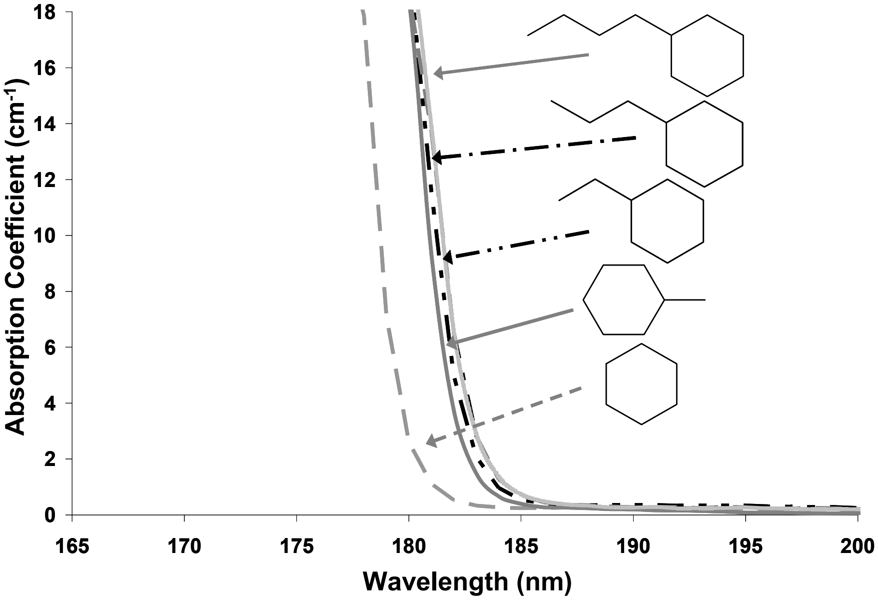

Figure 3.11: Absorbance spectra for cyclohexane with linear substituents

The term values (Δ) can be calculated for these structures, as in the linear and cyclic series, using the difference between λ_{edge} and the ionization energies.[38] The term values, λ_{edge}, and ionization energies are given in Figure 3.12. From Figure 3.12, the ionization energy decreases from 9.88 eV (126 nm) for cyclohexane to 9.64 eV (129 nm) for methylcyclohexane and to 9.41 eV (132 nm) for butylcyclohexane. The λ_{edge} energy decreases (or wavelength increases) from 6.9 eV (180 nm) for cyclohexane to 6.8 eV (183 nm) for methylcyclohexane. From methylcyclohexane to butylcyclohexane, the λ_{edge} energy decreases (or wavelength increases) only slightly, from 6.79 eV (183 nm) to 6.75 eV (184 nm). The term values for this series range from 3.0 eV for cyclohexane to 2.7 eV for butylcyclohexane.

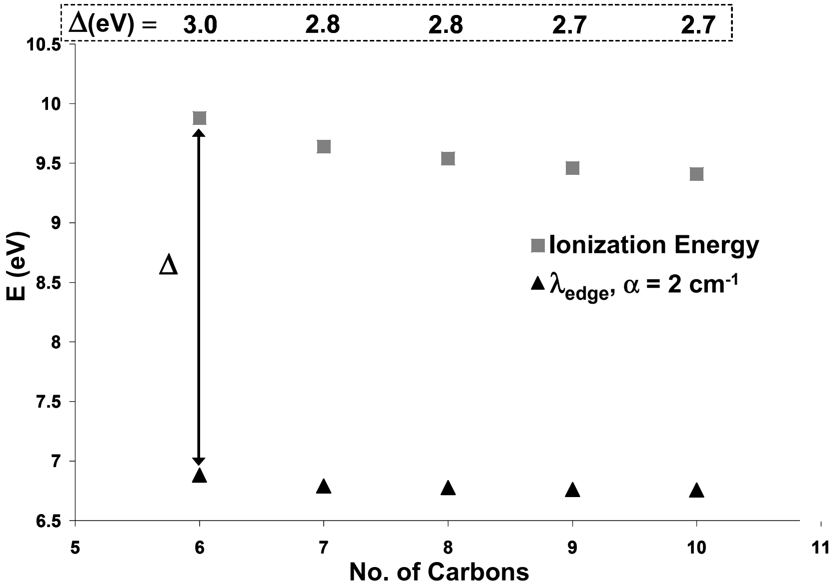

Figure 3.12: Ionization energies (squares), λ_{edge} (triangles), and term values (Δ) for cyclohexane (C_6), methylcyclohexane (C_7) to butylcyclohexane (C_{10})

As in the linear and cyclic series, the term values for cyclohexane with linear substituents are consistent with the reported term values for a Rydberg transition.[22, 25] The similarity in these term values also supports the theory that the energy of the LUMO (Rydberg orbital) is essentially unaffected by the addition of carbon atoms to the linear chain. With the addition of carbon atoms, the HOMO should be "destabilized" by the increased occupancy of the higher energy orbitals and shift to higher energies, decreasing the HOMO-LUMO gap with increasing carbon number (as in the linear and cyclic series). The difference in λ_{edge} between cyclohexane and methylcyclohexane suggests that addition of the methyl group "destabilizes" the HOMO, as expected based on the increased carbon number. From cyclohexane to methylcyclohexane, Δ_{shift} = 3 nm (0.1 eV). From methylcyclohexane to butylcyclohexane, however, Δ_{shift} = 1 nm (0.04 eV). Increasing the carbon number of the linear substituent on cyclohexane has essentially no effect on λ_{edge}, contrary to the trend previously observed.

Adding a linear substituent to cyclohexane disrupts the symmetry of the six carbon structure. This change in symmetry might alter which of the Rydberg states (3s, 3p, or 3d) is accessed. If the symmetry disruption is approximately equivalent for each of the structures studied (methyl – butylcyclohexane), then increasing the number of carbons in the n-alkane group should not significantly alter λ_{edge}. If this hypothesis is correct, the dominant factor in red-shifting λ_{edge} should be the linear substitution, rather than the increase in carbon number with the lengthening of the alkyl chain. To test this hypothesis, the absorbance edge of dimethylcyclohexane could be compared to ethylcyclohexane, for example. If the symmetry of cyclohexane is further disrupted, λ_{edge} for dimethylcyclohexane should be red-shifted from ethylcyclohexane.

3.3.4 Complex Cycloalkanes

The absorbance spectra for some large, complex cycloalkanes are given in Figure 3.13. For these alkanes, the monotonic red-shift in the absorbance with increasing carbon number, as in the linear and cyclic homologs, is not observed. While for these complex cyclic structures, a general red-shift in the absorbance with increasing carbon number is observed, exceptions to this trend exist. As a result, increasing carbon number does not seem to be the only factor that influences the HOMO-LUMO gap.

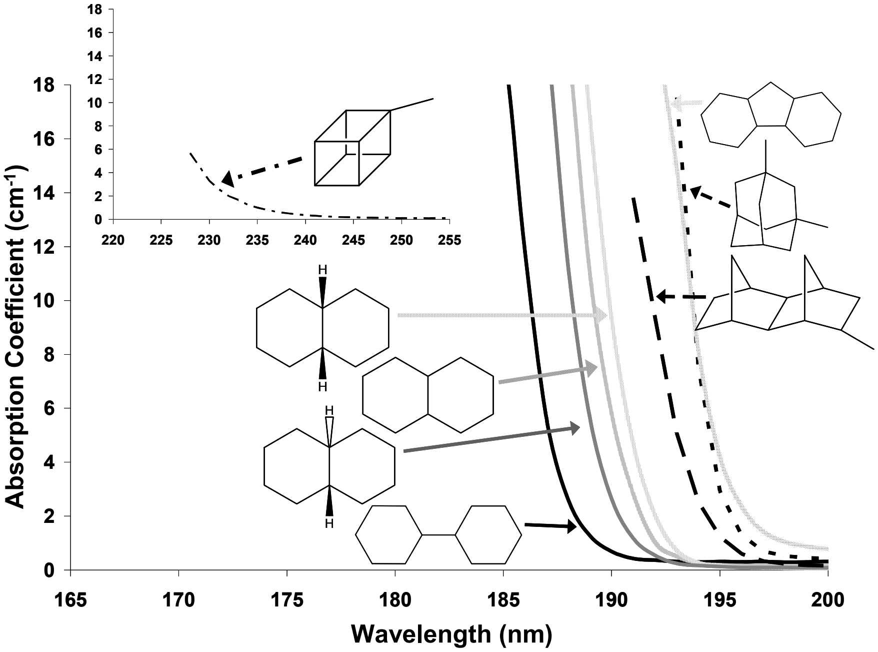

Figure 3.13: Absorbance spectra for the complex cycloalkanes; methylcubane shown in the inset, collected through a 10 mm path

The term values (Δ) can be calculated for these structures using the difference between λ_{edge} and the ionization energies,[38] as previously discussed. The term values, λ_{edge}, and ionization energies for the complex cycloalkanes are given in Figure 3.14. These term values are all approximately 3 eV and are consistent with the reported term values for excitation to Rydberg states.[22, 25] Specifically, the reported term value for *trans*-decalin is 2.7 eV[25] and is similar to the term value for trans-decalin reported in this work (2.8 eV). It seems that, as in the alkanes previously discussed, the energy of the LUMO is independent of the structure of the hydrocarbon. The difference in the HOMO-LUMO gap observed for these structures is more likely due to differing amounts of HOMO "destabilization".

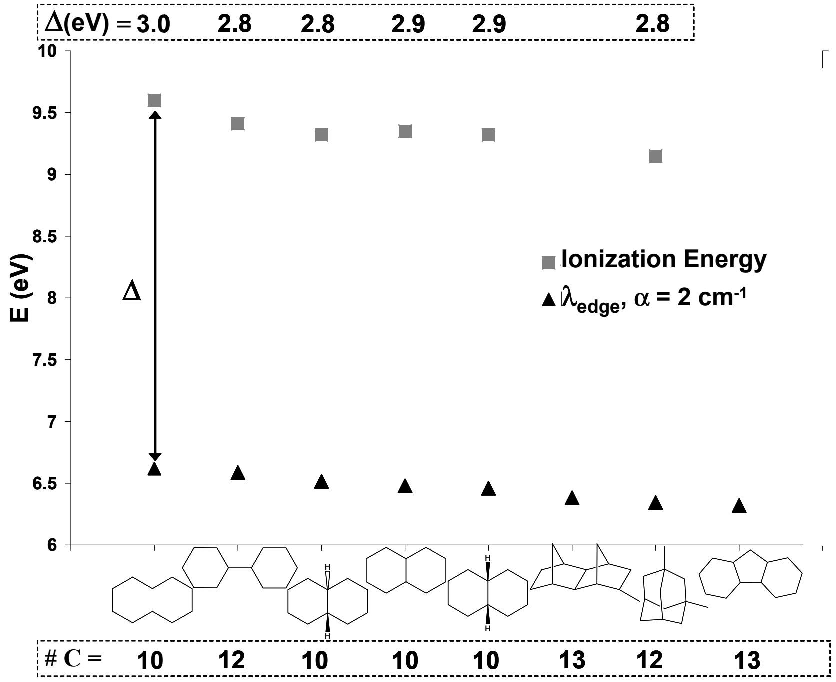

Figure 3.14: Ionization energies (squares), λ_{edge} (triangles), and term values (Δ) for the complex cycloalkanes; methylcubane, λ_{edge} = 5.3 eV (232 nm)

Methylcubane has the lowest energy λ_{edge} (longest wavelength) of the fluids studied (5.3 eV, 232 nm), despite consisting of nine carbons. While the ionization energy of methylcubane has not been reported, the ionization energy of cubane is 8.6 eV (144 nm.[38] Using the ionization energy of cubane as an approximation for methylcubane, the term value is 3.3 eV and is consistent with the alkane term values (~3 eV) such that the energy of the LUMO is likely approximately equivalent to the LUMO energy of the other alkanes. In methylcubane, six cyclobutane rings are fused into a highly strained cube with internal C-C angles of 90°. Due to the cubic structure, these rings cannot fold to relieve strain so that methylcubane should have significantly higher strain energy than the other alkanes. The strain energy of methylcubane is not reported, but the strain energy of cubane is 695 kJ/mol.[40] Increasing strain energies "destabilize" the HOMO so that the HOMO-LUMO gap of methylcubane should be decreased over unstrained structures.

3.4 INDEX OF REFRACTION OF ALKANES

The index of refraction was measured from 190 – 1000 nm. The Cauchy coefficients and index at 193 nm are given in Table 3.4. As λ_{edge} of these alkanes red-shifts (with increasing carbon number), the index at 193 nm also increases. Thus, within the linear and cyclic homologous series, a monotonic relationship exists between the optical properties. This relationship is shown in Figure 3.15 by a plot of the index at 193 nm (n_{193}) versus λ_{edge} (nm). The index and absorbance are linked, and both the index and absorbance increase as the wavelength of incident light approaches an absorption peak,[41] as illustrated in Figure 3.1.

Table 3.2: Density, index of refraction (n_{193}) and Cauchy coefficients

	Density[a]	**Index**	**Cauchy coefficients**[b,c]		
Hydrocarbon	**ρ (g/cm^3)**	**n_{193}**	**A**	**B (x10^3)**	**C (x10^4)**
Pentane	0.626	1.484	1.357	0.0022	9.22x10^{-5}
Hexane	0.655	1.501	1.363	0.0031	7.56x10^{-5}
Heptane	0.684	1.517	1.378	0.0020	1.18x10^{-4}
Octane	0.703	1.530	1.388	0.0022	1.15x10^{-4}
Decane	0.730	1.544	1.399	0.0024	1.14x10^{-4}
Cyclopentane	0.745	1.546	1.400	0.0028	9.86x10^{-5}
Cyclohexane	0.779	1.577	1.420	0.0021	1.40 x10^{-4}
Cycloheptane	0.811	1.587	1.438	0.0026	1.11 x10^{-4}
Cyclooctane	0.834	1.611	1.443	0.0029	1.25x10^{-4}
Cyclodecane	0.854	1.628	1.441	0.0054	5.82x10^{-5}
Methylcyclohexane	0.769	1.575	1.416	0.0026	1.22x10^{-4}
Ethylcyclohexane	0.788	1.579	1.419	0.0027	1.22x10^{-4}
Propylcyclohexane	0.793	1.579	1.423	0.0037	8.17x10^{-5}
Butylcyclohexane	0.818	1.588	1.433	0.0025	1.23x10^{-4}
Bicyclohexyl	0.864	1.645	1.466	0.0028	1.45x10^{-4}
trans-Decalin	0.870	1.638	1.468	0.0021	1.57x10^{-4}
Decalin (mix, *cis* + *trans*)	0.896	1.651	1.463	0.0015	2.04x10^{-4}
cis-Decalin	0.897	1.645	1.466	0.0030	1.38x10^{-4}
Perhydrofluorene	0.920	1.670	1.479	0.0043	1.04x10^{-4}
1,3-Dimethyladamantane	0.886	1.671	1.465	0.0030	1.74x10^{-4}
Methyldinorbornane[d]	0.980	1.687	1.497	0.0036	1.31 x10^{-4}
Methylcubane[d]	1.1	1.72			

[a] Density obtained from Sigma-Alrich unless otherwise noted [b]Cauchy units are: B (μm^2) and C (μm^4) [c]Cauchy equation is valid to 190 nm [d]Density evaluated experimentally

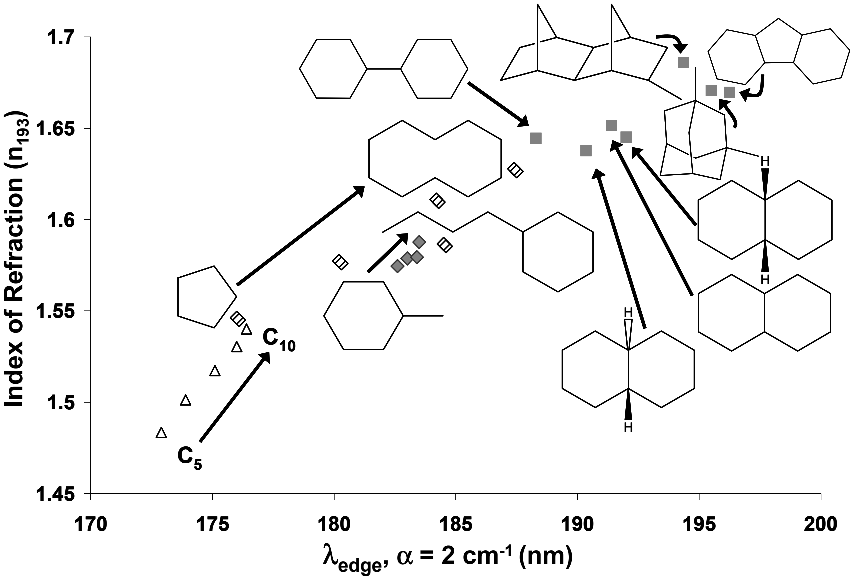

Figure 3.15: Monotonic relationship between the index at 193 nm and λ_{edge}

The index of refraction depends on both density and polarizability. One hypothesis for the index dependence on density is related to the "electron density" per unit volume. With greater density and better "packing efficiency" per unit volume, alkanes with higher density will also have higher "electron density". The interaction of light with an increased number of electrons per unit volume increases the index.[5, 42] The polarizability is a measure of the disruption of the charge distribution of a molecule by interaction with an external field. When a non-polar molecule is subjected to an external electric field, the electrons and nuclei are displaced with respect to each other, creating a dipole moment. The vector sum, or strength, of the dipole moments of all of the molecules in a unit volume is the polarization. If this external field is light, molecules that are more polarizable will have more ability to decrease the speed of light that passes through the molecule. These more polarizable molecules will have a higher index since the index of refraction describes the change in the speed of light in a medium (see Equation 3.1).[1, 5]

The Lorentz-Lorenz formula describes the relationship between the index (n), density (ρ), and polarizability (α) and is given by

$$\frac{n^2-1}{n^2+2}=\frac{4\pi}{3}\frac{N_m\rho\alpha}{M_w} \tag{3.6}$$

where N_m is Avogadro's number and M_w is the molecular weight.[5, 6] The index at 193 nm increases with increasing density. When the index at 193 nm is plotted against density (shown in Figure 3.16), an increase in the index with increasing density is observed, as expected based on Equation 3.6. For the linear alkanes, cycloalkanes, and alkyl-substituted cyclohexanes (methyl – butyl), the index at 193 nm increases monotonically with density. Based on Equation 3.6, either the polarizability increases with carbon number or has a negligible effect for these alkanes. For the complex cycloalkanes, the index at 193 nm generally increases with increasing density. Deviations from the trend seem to indicate differences in polarizability for these hydrocarbons.

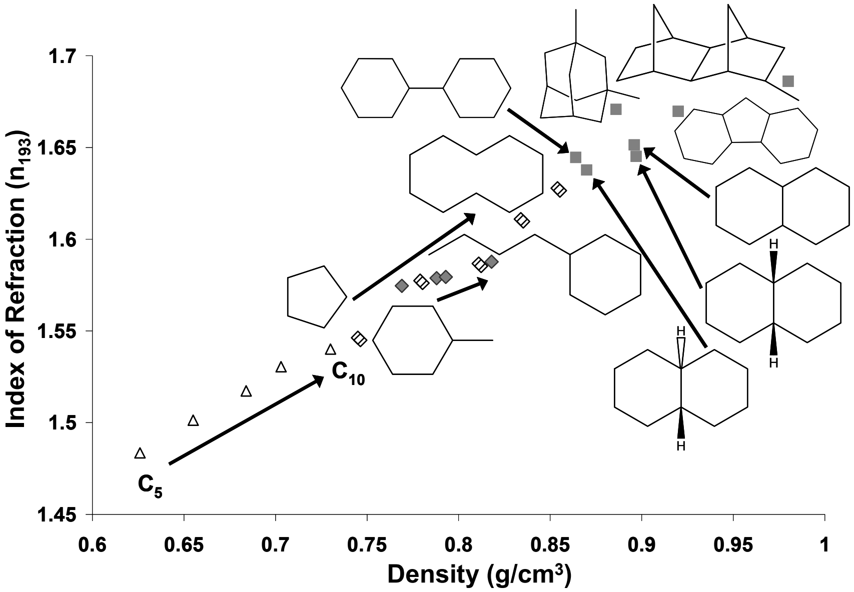

Figure 3.16: Index of refraction at 193 nm versus density

3.5 IMMERSION LITHOGRAPHY DEMONSTRATION

The fluid with the highest index, besides methylcubane, in this study is methyldinorbornane (n_{193} = 1.687). While the transmittance of methyldinorbornane at 193 nm is too low for use in immersion lithography manufacturing, imaging through a thin layer of this fluid was completed with interference immersion lithography[43] to demonstrate the patterning of 32 nm features with immersion lithography. 32 nm line and space images, printed with a numerical aperture of 1.5, are given in Figure 3.17. These images are of good quality with few defects and no observable photoresist degradation.

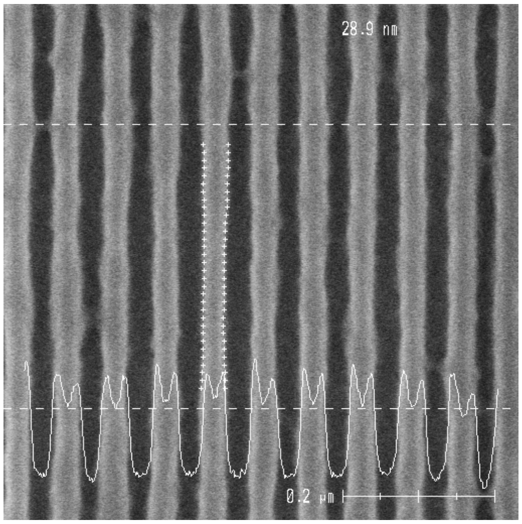

Figure 3.17: 32 nm line and space images printed with methyldinorbornane as the immersion fluid

3.6 MIXTURE ABSORBANCE

Decalin has an absorbance edge of 191 nm which provides high transparency at 193 nm. Decalin also meets the index target with an index of 1.654 at 193 nm. According to anomalous dispersion, the index could be further increased by red-shifting the absorbance edge of decalin towards 193 nm. One possible method to achieve this red-shift is to mix a low-transparency alkane ($\lambda_{edge} > 193$ nm), such as methyldinorbornane, and a high-transparency alkane ($\lambda_{edge} < 193$ nm), such as cyclohexane. Based on the ratio of the components in the mixture, the λ_{edge} of the component with high transparency at 193 nm could be red-shifted and λ_{edge} of the component with low transparency at 193 nm could be blue-shifted to obtain a mixture with a high index and low absorbance at 193 nm. By changing the ratio of components in the mixture, λ_{edge} could be tailored to a wavelength just less than 193 nm to achieve the maximum increase in index without decreasing transparency at 193 nm. Adjustment of

λ_{edge} was attempted based on this concept by mixing cyclohexane (high transparency at 193 nm) and methyldinorbornane (low transparency at 193 nm).

3.6.1 Experimental Details

Methyldinorbornane was added to cyclohexane in concentrations varying from 0.2 M to 0.84 M methyldinorbornane. These fluids were purified individually, prior to mixing. The purification procedure is given in Appendix A. The index of refraction from 190 – 1000 nm was measured using the procedure previously described, Section 3.2.5. Absorbance spectra of the deoxygenated fluids were collected from 190 – 820 nm using an HP 8452A Diode Array UV-Vis Spectrometer. Since the absorbance of the neat fluid was measured, the reflection correction procedure described in Chapter 2, 2.2.2 was applied to the data. Finally, the viscosity was measured using a capillary viscometer, and a pendant drop technique was used to calculate the surface tension.

3.6.2 Results

The absorbance spectra obtained from these mixtures are given in Figure 3.18. A summary of the absorption coefficient (cm^{-1}), index at 193 nm, surface tension, and viscosity is given in Table 3.3. The absorption coefficient of the mixture at 193 nm is much higher than the absorption coefficient of cyclohexane at 193 nm even at the lowest concentration of methyldinorbornane (0.2 M). The absorbance of the mixture rapidly approaches the absorbance of methyldinorbornane as the concentration of methyldinorbornane is increased to 0.84 M. Additionally, while the index at 193 nm increases with the addition of methyldinorbornane, a concentration greater than 0.84 M is needed to achieve an index of 1.65. Increasing the concentration of methyldinorbornane to obtain this index would further increase the absorbance. Therefore, this mixture is not a viable alternative to decalin. A mixture of decalin and methyldinorbornane might provide a better option to red-shift the λ_{edge} of decalin slightly. However, the index increase that could be achieved with this mixture would likely not be significant since a low concentration of methyldinorbornane would be necessary to maintain the required transparency at 193 nm.

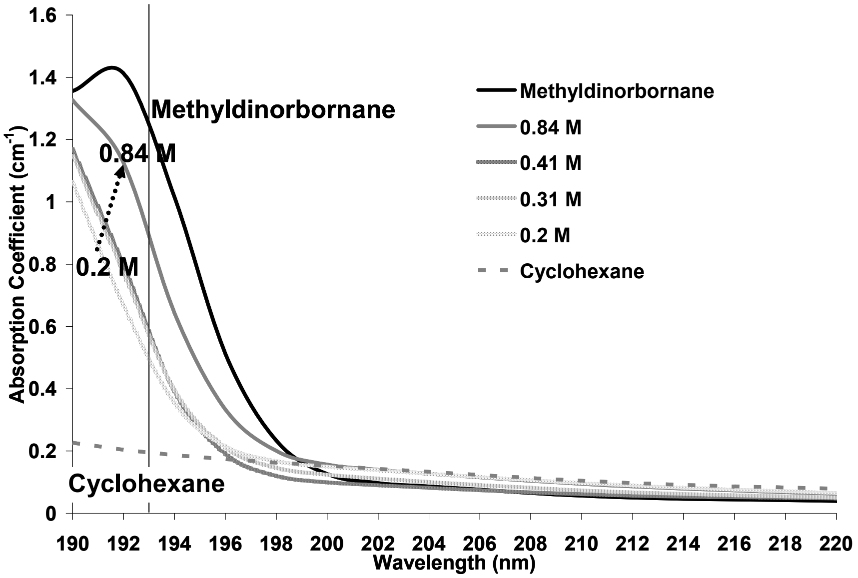

Figure 3.18: Absorbance spectra for methyldinorbornane in cyclohexane

Table 3.3: Index at 193 nm, absorption coefficient at 193 nm, viscosity and surface tension of mixtures of methyldinorbornane and cyclohexane

Concentration (M) Methyldinorbornane	**n_{193}**	**α_{193} (cm^{-1})**	**μ (cP)**	**γ (dyn/cm)**
0	1.571	0.2	0.9	24.9
0.2	1.578	0.45	0.86	26.1
0.31	1.581	0.58	0.99	27.4
0.41	1.587	0.59	1.04	29.1
0.84	1.593	0.88	1.33	31.4
Pure (100%)	1.687	1.1	9.2	34.5

3.7 PHYSICAL PROPERTIES OF ALKANES

The alkane fluid with optical properties that meets the second generation immersion fluid targets[35] is decalin. Decalin has an index of 1.654 at 193 nm and an absorbance edge at 191 nm, slightly less than 193 nm. Even though a high index and low absorbance can be achieved with an alkane fluid, the physical properties of these fluids make their implementation in manufacturing challenging. Since alkanes are not compatible with current fluid handling systems (designed for water), new designs are needed.

3.7.1 Fluid Lifetime

First, these fluids are difficult to purify and are sensitive to oxygen. As shown in Figure 3.2, even low levels of impurities (less than 1%) can significantly increase the absorbance at 193 nm. While potential immersion fluid candidates with high transparency (> 99%) at 193 nm have been developed to meet the absorbance targets,[44] photoproducts formed upon exposure can contaminate both the fluid sample (decreasing the transmittance)[45] and lens so that sophisticated recycle and lens cleaning processes are required.[46] The double-bonded and oxidation photoproducts can polymerize on the lens, creating a graphite-like (polymerized) hydrocarbon layer.[47, 48] Recycling processes have been developed to maintain a low fluid absorbance and so prevent formation of this layer.[47, 49] Additional cleaning processes have also been developed to remove any impurities that might deposit on the lens. In one method to remove the hydrocarbon deposits, the alkane is replaced with a layer of 0.1-1% peroxide in water. Irradiating this peroxide layer successfully removes the hydrocarbon deposits on the lens.[50] The recycle steps are expected to increase fluid lifetime from a few hours to as much as a week. With this increase in fluid lifetime, lens cleaning would only be necessary approximately once per day.[49, 51] While these recycle and lens cleaning methods represent significant progress, tool downtime for cleaning would still be required.

3.7.2 Fluid Handling System

For water immersion lithography, the photoresist can be exposed through the fluid by inserting a droplet between the lens and resist-coated wafer and dragging that droplet around the wafer to expose each spot, or die, on the wafer. To prevent imaging defects and the introduction of particles onto the wafer, the fluid must remain pinned between the wafer and lens. If the scanning speed is too fast, the fluid can de-wet from the advancing edge of the lens so that the droplet no longer fills the whole space between the lens and wafer. At the receding end, the droplet can form a long tail, leaving a trail of fluid on the wafer. The advancing and receding edge are defined with respect to the movement of the lens. These failure modes are shown, with decalin as the immersion fluid, in Figure 3.19.

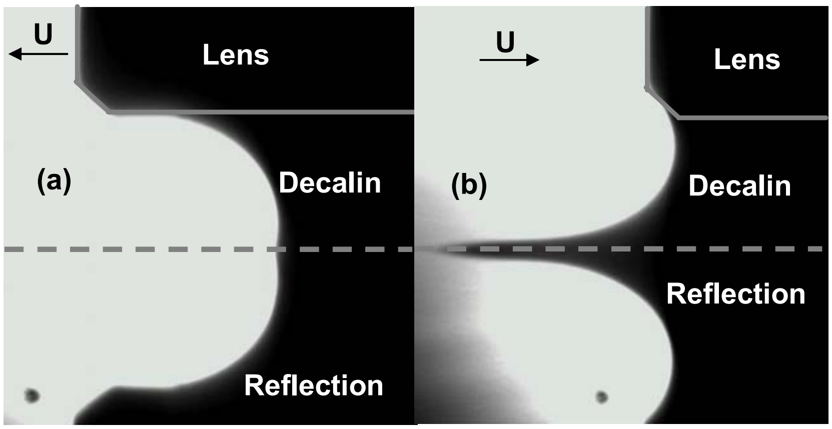

Figure 3.19: "Drag-a-drop" failure modes using decalin at U = 50 mm/s: (a) advancing edge dewetting and (b) receding edge tail

An expression for predicting the critical scanning velocity (v_{crit}) before liquid loss has been developed,[52]

$$v_{crit} \propto \frac{\gamma}{\mu}\theta_s^3 , \tag{3.7}$$

where γ and μ are the surface tension and viscosity of the fluid, respectively, and θ_s is the static contact angle of the fluid on the surface coating. The alkane surface tension is approximately half that of water and viscosity is approximately three times that of water. With the same contact angle, the critical velocity of the hydrocarbon fluid will be 1/6 that of water. Thus, to achieve high scanning speeds and acceptable throughput, low surface energy coatings that have a high contact angle with the hydrocarbon fluids are needed. Fluorinated coatings are one type of material with which a high contact angle with a hydrocarbon has been demonstrated.[53]

To mimic the effects of the fluorinated coatings, a fluorinated self-assembled monolayer (F-SAM) was generated on a silicon wafer by immersing a clean wafer in a 1.0 wt% solution of (tridecafluoro-1,1,2,2-tetrahydrooctyl)dimethylchlorosilane [Alfa Aesar, 90% (tech.)] in toluene for 1 hour. This monolayer has a static contact angle of 70-75^{o} with decalin. The maximum scanning velocity that can be obtained using this coating was studied with a "drag-a-drop" test stand designed and built by Derek Bassett (given in Figure 3.20) using a 1 mm gap between the lens and the wafer. A CCD camera was used to capture a video of the droplet scanning across the wafer at varying speeds. An image of the advancing and receding contact angle at each speed was then obtained from the video and processed with an edge-finding algorithm to determine the contact angle, also developed by Derek Bassett.[54] The results of this experiment for seven different trials are given in Figure 3.21. There is significant variation in the contact angle and maximum speed for each of the trials. This variation is most likely due to both the difficulty in obtaining a good focus to capture the image and to variability in the surface coating, resulting in variability in the static contact angle. The maximum speed obtained before failure is 100 mm/s for the advancing edge and 80 mm/s for the receding edge. For water, scanning speeds as high as 700 mm/s can be achieved before failure.[54]

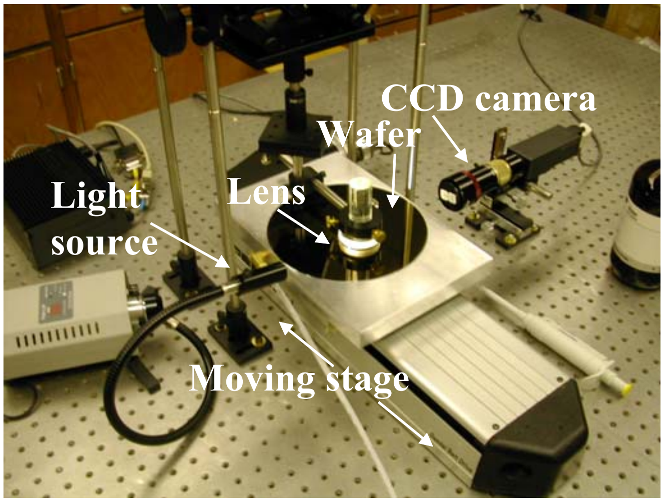

Figure 3.20: “Drag-a-drop” test stand

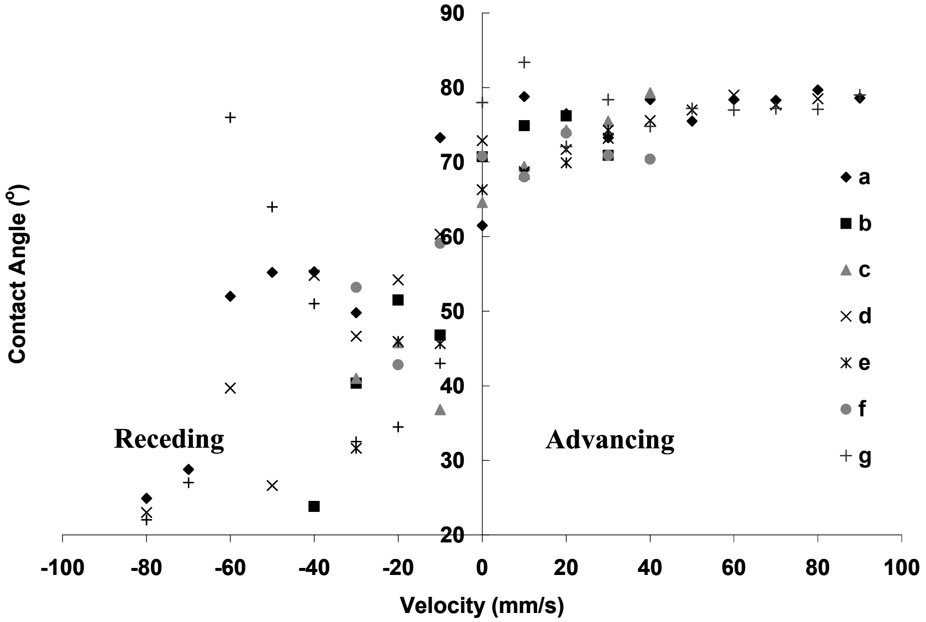

Figure 3.21: Receding (a) and advancing (b) edge contact angles for decalin on F-SAM at varying scan speeds for trials a - g

Development of new materials with contact angles > 120° is required to achieve scanning speeds greater than 500 mm/s with alkane fluids. Since a contact angle > 120° is not realistic, alternative techniques, such as full wafer immersion or simply accepting a fluid "tail," are necessary.[53] These alternative designs for use with low-contact-angle fluids can achieve higher scanning speeds but will require the design of a new fluid fill system to fully immerse and expose the wafer. This full wafer immersion design is a significant deviation from the local fill model used with water.[55] New photoresist materials might also be required since evaporation of the alkane fluids can leave rings of extracted material on the wafer unless a low surface energy coating is used.[53] Since the interaction time between the resist and immersion fluid increases in the new designs, dissolved particles in the fluid that could become defects on the wafer need to be carefully controlled.[51] Thus, significant development work is required in the design of scanning systems for immersion lithography with alkane fluids.

3.8 CONCLUSIONS

Based on the phenomenon of anomalous dispersion, when the absorbance edge is at a wavelength slightly lower than 193 nm, the absorbance at 193 nm will be low while the index approaches a maximum. A fluid with an absorbance edge at this wavelength should have the target optical properties at 193 nm for next generation immersion lithography. Alkanes are saturated systems which undergo electronic transitions at wavelengths < 200 nm and, therefore, should have a high index and low absorbance at 193 nm. The optical properties of a series of linear, cyclic, and complex cyclic alkanes were studied to evaluate this theory.

VUV absorbance spectra of linear and cyclic alkanes reveal that the absorbance edge red-shifts with increasing carbon number. This red-shift in the absorbance edge suggests that the HOMO-LUMO gap decreases with increasing carbon number. To develop a hypothesis for the appearance of this trend, the nature of the HOMO and LUMO must be established. First, the energy of the HOMO should increase with increasing carbon number as electrons are added to orbitals at higher energy states. Secondly, based on the agreement between term values reported for alkanes and calculated in this study (from the difference between the ionization energy[38] and absorbance edge), the excited state (LUMO) for these alkanes seems to be a Rydberg orbital. The term values are essentially constant (~3 eV) despite changes in alkane geometry, suggesting that the energy of the LUMO is relatively independent of carbon number. Thus, when the HOMO energy increases with the addition of carbon atoms, the HOMO-LUMO gap should decrease with increasing carbon number, as observed. Exceptions to this trend, observed in the complex cycloalkanes, seem to be primarily due to additional factors which shift the energy of the HOMO, such as an increase in strain energy.

The structural effects required to adjust the optical properties and develop a fluid for next generation immersion lithography have been characterized. Complex cycloalkanes provide the best known option for a high index and low absorbance at 193 nm. Decalin, with an absorbance edge of 191 nm, has the required high index (n_{193} = 1.654) and low absorbance needed for a next generation immersion fluid. However, the physical properties of these alkanes are significantly different from those of water and result in significant engineering challenges in the implementation of these fluids in large scale manufacturing.

Additionally, further increases in the index of these alkane fluids for use in future generations of immersion lithography do not seem possible without increasing the absorbance. While increases in the density and/or polarizability could be used to try to increase index, reaching the 3rd generation target index of 1.8 seems unlikely with this class of compounds. Currently, researchers are attempting to disperse high index nanoparticles, such as HfO_2, into decalin to increase the index of the fluid without increasing the absorbance.[56] While these fluids could have the required high index, this approach would not overcome the physical property limitations and design of new and ever more complex fluid handling systems would still be necessary.

3.9 REFERENCES

1. Korff, S. A. and Breit, G., *Optical Dispersion.* Rev. Mod. Phys., 1932. **4**(3): p. 471-504.
2. Bohren, C. F. and Huffman, D. R., *Absorption and Scattering of Light by Small Particles*. 1983, Weinheim: WILEY-VCH Verlag GmbH & Co. KGaA. pp. 530.
3. Kronig, R. d. L., *The theory of dispersion of x-rays.* J. Opt. Soc. Am., 1926. **12**: p. 547-57.
4. Peiponen, K.-E., Vartianinen, E. M. and Asakura, T., *Dispersion, Complex Analysis and Optical Spectroscopy*. 1999, New York: Springer. pp. 130.
5. Born, M. and Wolf, E., *Principles of Optics*. 2nd. 1964, New York: Pergamon Press. pp. 808.
6. Bottcher, C. J. F., *Theory of Electric Polarisation*. 1952, London: Elsevier Publishing Company. pp. 492.
7. Yadav, L. D. S., *Organic Spectroscopy*. 2005, Boston: Kluwer Academic Publishers. pp. 324.
8. Lagesson, V., Lagesson-Andrasko, L., Andrasko, J. and Baco, F., *Identification of compounds and specific functional groups in the wavelength region 168-330 nm using gas chromatography with UV detection.* J. Chromatogr., A, 2000. **867**(1 + 2): p. 187-206.
9. Kaye, W. I., *Far ultraviolet spectroscopy. II. Analytical applications.* Appl. Spectrosc., 1961. **15**: p. 130-44.

10. Pickett, L. W., Muntz, M. and McPherson, E. M., *Vacuum ultraviolet absorption spectra of cyclic compounds. I. Cyclohexane, cyclohexene, cyclopentane, cyclopentene, and benzene.* J. Am. Chem. Soc., 1951. **73**: p. 4862-5.

11. Raymonda, J. W., *Rydberg states in cyclic alkanes.* J. Chem. Phys., 1972. **56**(8): p. 3912-20.

12. Schoen, R. I., *Absorption, ionization, and ion-fragmentation cross sections of hydrocarbon vapors under vacuum-ultraviolet radiation.* J. Chem. Phys., 1962. **37**: p. 2032-40.

13. Sowers, B. L., Arakawa, E. T. and Birkhoff, R. D., *Optical properties of six-member carbon ring organic liquids in the vacuum ultraviolet.* J. Chem. Phys., 1971. **54**(6): p. 2319-24.

14. Lombos, B. A., Sauvageau, P. and Sandorfy, C., *Electronic spectra of n-alkanes.* J. Mol. Spectrosc., 1967. **24**(3): p. 253-69.

15. Raymonda, J. W. and Simpson, W. T., *Experimental and theoretical study of sigma-bond electronic transitions in alkanes.* J. Chem. Phys., 1967. **47**(2): p. 430-48.

16. Holmes, J. L. and Lossing, F. P., *Ionization energies of homologous organic compounds and correlation with molecular size.* Org. Mass Spectr., 1991. **26**(6): p. 537-41.

17. Au, J. W., Cooper, G., Burton, G. R., Olney, T. N. and Brion, C. E., *The valence shell photoabsorption of the linear alkanes, CnH2n+2 (n = 1-8): absolute oscillator strengths (7-220 eV).* Chem. Phys., 1993. **173**(2): p. 209-39.

18. Kameta, K., Kouchi, N., Ukai, M. and Hatano, Y., *Photoabsorption, photoionization, and neutral-dissociation cross sections of simple hydrocarbons in the vacuum ultraviolet range.* J. Electron Spectrosc., 2002. **123**(2-3): p. 225-238.

19. Honig, R. E., *Ionization potentials of some hydrocarbon series.* J. Chem. Phys., 1948. **16**: p. 105-12.

20. Potts, A. W. and Streets, D. G., *Photoelectron spectra of linear valence shells. 1. Saturated hydrocarbons.* J. Chem. Soc., Faraday Trans. 2, 1974. **70**(5): p. 875-84.

21. Dewar, M. J. S. and Worley, S. D., *Photoelectron spectra of molecules. I. Ionization potentials of some organic molecules and their interpretation.* J. Chem. Phys., 1969. **50**(2): p. 654-67.

22. Robin, M. B., *Higher Excited States of Polyatomic Molecules*. 1. 1974, New York: Academic Press. pp. 374.

23. Bodor, N., Dewar, M. J. S. and Worley, S. D., *Photoelectron spectra of molecules. III. Ionization potentials of some cyclic hydrocarbons and their derivatives, and heats of formation and ionization potentials calculated by the MINDO[minimum neglect of differential overlap]SCF MO method.* J. Am. Chem. Soc., 1970. **92**(1): p. 19-24.

24. Heilbronner, E., Honegger, E., Zambach, W., Schmitt, P. and Guenther, H., *The equivalent bond orbital model revisited. II. The persistence of ribbon orbitals in polycyclic alkanes.* Helv. Chim. Acta, 1984. **67**(7): p. 1681-90.

25. Heath, B. A., Kuebler, N. A. and Robin, M. B., *Multiphoton ionization spectra of polycyclic alkanes.* J. Chem. Phys., 1979. **70**(7): p. 3362-8.

26. Nesselrodt, D. R., Potts, A. R. and Baer, T., *Stereochemical Analysis of Methyl-Substituted Cyclohexanes Using 2 + 1 Resonance-Enhanced Multiphoton Ionization Spectroscopy.* Anal. Chem., 1995. **67**(23): p. 4322-9.

27. Shang, Q. Y. and Bernstein, E. R., *(s3s) Rydberg states of cyclohexane, bicyclo[2.2.2]octane, and adamantane.* J. Chem. Phys., 1994. **100**(12): p. 8625-32.

28. Basch, H., Robin, M. B., Kuebler, N. A., Baker, C. and Turner, D. W., *Optical and photoelectron spectra of small rings. III. The saturated three-membered rings.* J. Chem. Phys., 1969. **51**(1): p. 52-66.

29. Klevens, H. B. and Platt, J. R., *Ultraviolet-transmission limits of some liquids and solids.* J. Am. Chem. Soc., 1947. **69**: p. 3055-62.

30. Lopez-Gejo, J., Kunjappu, J. T., Conley, W., Zimmerman, P. and Turro, N. J., *Methods for the synthesis and purification of polycycloalkane candidates for photolithography immersion fluids at 193 nm: requirements for removal of oxygen.* J. Micro/Nanolithogr. MEMS MOEMS, 2007. **6**(3): p. 033003/1-033003/7.

31. Murray, E. C. and Keller, R. N., *Purification of hydrocarbon solvents with a silver nitrate column.* J. Org. Chem., 1969. **34**(7): p. 2234-5.

32. Parsons, B. F. and Chandler, D. W., *On the Dissociation of van der Waals Clusters of X2-Cyclohexane (X = O, Cl) Following Charge-Transfer Excitation in the Ultraviolet.* J. Phys. Chem. A, 2003. **107**(49): p. 10544-10553.

33. Synowicki, R. A., Pribil, G. K., Cooney, G., Herzinger, C. M., Green, S. E., French, R. H., Yang, M. K., Burnett, J. H. and Kaplan, S., *Fluid refractive index*

measurements using rough surface and prism minimum deviation techniques. J. Vac. Sci. Technol., B, 2004. **22**(6): p. 3450-3453.

34. French, R. H., Peng, S. and Wheland, R. C. 2005. *USA Patent No. 2005119371*

35. French, R. H., Sewell, H., Yang, M. K., Peng, S. P., McCafferty, D., Qiu, W., Wheland, R. C., Lemon, M. F., Markoya, L. and Crawford, M. K., *Imaging of 32-nm 1:1 lines and spaces using 193-nm immersion interference lithography with second-generation immersion fluids to achieve a numerical aperture of 1.5 and a k1 of 0.25.* J. Microlith. Microfab. Microsyst., 2005. **4**(3): p. 031103-1 - 031103-14.

36. French, R. H., Yang, M. K., Lemon, M. F., Synowicki, R. A., Pribil, G. K., Cooney, G. T., Herzinger, C. M., Green, S. E., Burnett, J. H. and Kaplan, S. G., *Immersion fluid refractive indices using prism minimum deviation techniques.* Proc. SPIE, 2004. **5377**(Pt. 3, Optical Microlithography XVII): p. 1689-1694.

37. Mulliken, R. S., *Electronic structures of polyatomic molecules. IX. Methane, ethane, ethylene, acetylene.* J. Chem. Phys., 1935. **3**: p. 517-28.

38. *NIST Chemistry WebBook.* http://webbook.nist.gov/, 2009. p.

39. Solomons, T. W. G. and Fryhle, C. B., *Organic Chemistry*. 7th. 2000, New York: John Wiley and Sons, Inc. pp. 1258.

40. Schleyer, P. v. R., Williams, J. E., Jr. and Blanchard, K. R., *Evaluation of strain in hydrocarbons. The strain in adamantane and its origin.* J. Am. Chem. Soc., 1970. **92**(8): p. 2377-86.

41. Wooten, F., *Optical Properties of Solids*. 1972, New York: Academic Press. pp. 260.

42. Lopez-Gejo, J., Kunjappu, J. T., Zhou, J., Smith, B. W., Zimmerman, P., Conley, W. and Turro, N. J., *Polycycloalkanes as Potential Third-Generation Immersion Fluids for Photolithography at 193 nm.* Chem. Mater., 2007. **19**(15): p. 3641-3647.

43. Smith, B. W., Bourov, A., Fan, Y., Cropanese, F. and Hammond, P., *Amphibian XIS: an immersion lithography microstepper platform.* Proc. SPIE Int. Soc. Opt. Eng., 2005. **5754**(Pt. 2, Optical Microlithography XVIII): p. 751-759.

44. Furukawa, T., Kishida, T., Miyamatsu, T., Kawaguchi, K., Yamada, K., Tominaga, T., Slezak, M. and Hieda, K., *High-refractive index material design for ArF immersion lithography.* Proc. SPIE Int. Soc. Opt. Eng., 2007. **6519**(Pt. 1, Advances in Resist Materials and Processing Technology XXIV): p. 65190B/1-65190B/10.

45. Zimmerman, P. A., van Peski, C., Rice, B., Byers, J., Turro, N. J., Lei, X., Gejo, J. L., Liberman, V., Palmacci, S., Rothschild, M., Whittaker, A., Blakey, I., Chen, L., Dargaville, B. and Liu, H., *Status of high-index materials for generation-three 193nm immersion lithography.* J. Photopolym. Sci. Technol., 2007. **20**(5): p. 643-650.

46. Sewell, H., Mulkens, J., Graeupner, P., McCafferty, D., Markoya, L., Donders, S., Cortie, R., Meijers, R., Evangelista, F. and Samarakone, N., *High-n immersion lithography.* Proc. SPIE Int. Soc. Opt. Eng., 2008. **6924**(Pt. 1, Optical Microlithography XXI): p. 692415/1-692415/12.

47. Furukawa, T., Kishida, T., Yasuda, K., Shimokawa, T., Liu, Z., Slezak, M. and Hieda, K., *High refractive index materials design for the next generation ArF immersion lithography.* Proc. SPIE Int. Soc. Opt. Eng., 2008. **6924**(Pt. 1, Optical Microlithography XXI): p. 692412/1-692412/8.

48. O'Connor, N. A., Liberman, V., Lei, X., Lopez-Gejo, J., Turro, N. J. and Zimmerman, P. A., *Degradation of hydrocarbon fluids in the immersion lithography at 193 nm.* J. Photopolym. Sci. Technol., 2008. **21**(5): p. 607-611.

49. French, R. H., Tran, H. V., Adelman, D. J., Rogado, N. S., Kaku, M., Mocella, M., Chen, C. Y., Hendrickx, E., Van Roey, F., Bernfeld, A. S. and Derryberry, R. A., *High-index immersion fluids enabling cost-effective single-exposure lithography for 32 nm half pitches.* Proc. SPIE Int. Soc. Opt. Eng., 2008. **6924**(Pt. 1, Optical Microlithography XXI): p. 692417/1-692417/8.

50. Liberman, V., Rothschild, M., Palmacci, S. T., Bristol, R., Byers, J., Turro, N. J., Lei, X., O'Connor, N. and Zimmerman, P. A., *High-index immersion lithography: preventing lens photocontamination and identifying optical behavior of LuAG.* Proc. SPIE Int. Soc. Opt. Eng., 2008. **6924**(Pt. 1, Optical Microlithography XXI): p. 692416/1-692416/11.

51. Sakai, K., Iwasaki, Y., Mori, S., Yamada, A., Ogusu, M., Yamashita, K., Nishikawara, T., Hara, S.-i. and Watanabe, Y., *Feasibility study on immersion system using high-index materials.* Jpn. J. Appl. Phys., 2008. **47**(6, Pt. 2): p. 4853-4861.

52. Harder, P. M. and Shedd, T. A., *Contact angles and liquid loss behavior of high index fluids.* Proc. SPIE Int. Soc. Opt. Eng., 2007. **6533**(European Mask and Lithography Conference, 2007): p. 653305/1-653305/12.

53. Sanders, D. P., Sundberg, L. K., Brock, P. J., Ito, H., Truong, H. D., Allen, R. D., McIntyre, G. R. and Goldfarb, D. L., *Self-segregating materials for immersion lithography.* Proc. SPIE Int. Soc. Opt. Eng., 2008. **6923**(Pt. 1, Advances in Resist Materials and Processing Technology XXV): p. 692309/1-692309/12.

54. Bassett, D. W. and Bonnecaze, R. T., *Immersion lithography for laser mask writing.* J. Vac. Sci. Technol., B, 2006. **24**(6): p. 2659-2667.

55. Ohmura, Y., Nakashima, T., Nagasaka, H., Sukegawa, A., Ishiyama, S., Kamijo, K., Shinkai, M. and Owa, S., *Current status of high-index immersion lithography development.* Proc. SPIE Int. Soc. Opt. Eng., 2007. **6520**(Pt. 1, Optical Microlithography XX): p. 652006/1-652006/9.

56. Zimmerman, P. A., Byers, J., Rice, B., Ober, C. K., Giannelis, E. P., Rodriguez, R., Wang, D., O'Connor, N., Lei, X., Turro, N. J., Liberman, V., Palmacci, S., Rothschild, M., Lafferty, N. and Smith, B. W., *Development and evaluation of a 193nm immersion generation-three fluid candidates.* Proc. SPIE Int. Soc. Opt. Eng., 2008. **6923**(Pt. 1, Advances in Resist Materials and Processing Technology XXV): p. 69230A/1-69230A/10.

Chapter 4: Novel Salts with Absorbance Edge Dependence on Structure for Next Generation Immersion Lithography

4.1 INTRODUCTION

The index of refraction and absorbance are linked through an association that can be described by the Kramers-Kronig relations.[1] The linkage between these properties dictates that the maximum index of refraction in the spectrum occurs as the absorbance is increasing to a maximum level, or forming an absorbance peak. The index and absorbance spectra in the region of an absorbance peak are shown in Figure 3.1. This type of dispersion is observed for all types of chemical structures. Since most compounds absorb at UV wavelengths, identification of a fluid with a low absorbance and high index at 193 nm is challenging. However, due to the phenomenon of anomalous dispersion, described in detail in Chapter 3, the maximum index of refraction occurs at a slightly longer wavelength (lower energy) in the spectrum than the maximum absorbance.[2] Thus, to obtain the maximum increase in the index of refraction, the absorbance should increase sharply to the peak maximum at wavelengths slightly lower than 193 nm, resulting in a sharp absorbance edge.

As discussed in Chapter 3, saturated hydrocarbon fluids have electronic transitions with an absorption edge < 200 nm.[3] Based on their absorbance band edge dependence on structure, these fluids have the potential to provide the required index and absorbance at 193 nm for next generation immersion lithography. Saturated hydrocarbons fluids with the index of refraction and absorbance targets for second generation immersion lithography have been identified (see Chapter 3). However, these fluids are difficult to purify, sensitive to oxygen, degrade upon exposure to UV light to form absorbing photoproducts, and have a low surface tension so that high scanning speeds are difficult to achieve.

Fluids with index and absorbance characteristics similar to those of the saturated hydrocarbons but with the stability and physical properties of water would be ideal immersion fluid candidates. A straightforward method of introducing a saturated hydrocarbon into an aqueous fluid is to incorporate saturated hydrocarbon subgroups into a salt and add that salt to water. As discussed in Chapter 2, the anion most significantly influences the optical properties of an aqueous salt solution, and the methylsulfonate anion has the highest index and lowest absorbance of the anions studied.[4] Therefore, large (> five carbon) cycloalkane subgroups were attached to a sulfonate anion and paired with metal cations, such as sodium and potassium. Based on the study of quaternary ammonium acetates, discussed in Chapter 2, as the number of carbons attached to the quaternary ammonium increases, the absorbance edge seems to shift to longer wavelengths. This observation was studied further with the incorporation of large (> five carbon) linear and cyclic saturated hydrocarbon subgroups into a quaternary ammonium cation. The quaternary ammonium cation was paired with a methylsulfonate anion. Additionally, quaternary ammoniums are considered to be "semiconductor-friendly" additives due to their use in aqueous base developer solutions and should provide an acceptable alternative to metal cations. The index of refraction and absorbance of aqueous solutions of these high-index salts were tested to evaluate the efficacy of both types of solutions as next generation immersion fluids.

The optical property targets for these salt solutions are an index of 1.65 and an absorption coefficient (α) less than 0.15 cm^{-1} at 193 nm.[5] With these index and absorbance values, printing features as small as 32 nm should be possible. The fluid should also have surface tension and wetting properties similar to those of water, and the viscosity should not be more than three times that of water to maintain compatibility with fluid handling systems designed for water.[5]

Unfortunately, the sulfonate salts with a large hydrocarbon attached to the sulfonate anion are surfactants and are not acceptable immersion fluids due to the potential for bubble formation. Bubble formation degrades imaging by scattering, which reduces image contrast by decreasing the intensity of light that reaches the wafer.[6] The absorbance of these salt solutions is also much greater than the target value, even at low salt concentrations, and does not appear to depend on the structure of the hydrocarbon in the anion. In contrast, the absorbance of the quaternary ammonium salt solutions does depend on the structure of the hydrocarbon, as observed with the hydrocarbon fluids and the quaternary ammonium acetate salts. The absorbance edge of the quaternary ammonium salt solution increases to longer wavelengths with increasing carbon number of the hydrocarbon. However, even when water is saturated with these salts, an index of 1.65 cannot be obtained. Additionally, the high salt concentrations necessary also significantly increase the absorbance and viscosity. While a saturated hydrocarbon can be incorporated into a quaternary ammonium cation and added to water to produce an aqueous solution with an absorbance edge that depends on structure, due to the high viscosity and absorbance of these fluids, they are not viable immersion fluid candidates.

4.2 EXPERIMENTAL DETAILS

4.2.1 Optical Property Measurement

The index of refraction of each of the aqueous fluids was measured with a J.A. Woollam M2000 variable angle spectroscopic ellipsometer from 190 to 1000 nm. The ellipsometric procedure was described in detail in Chapter 2, 2.2.3. Briefly, the fluids were measured in a 2 in. diameter Fluoroware cup with a curved bottom so that only reflections from the top surface of the fluid were collected for analysis. The ellipsometric parameters Ψ and Δ were collected by the ellipsometer and fit to a Cauchy model by the Woollam WVASE32 software to determine the index of refraction.

The absorbance spectrum of each of these fluids was collected using a HP 8452A Diode Array Spectrophotometer through a 10 mm path quartz cuvette (Hellma Cells, Inc.) from 190 – 820 nm in increments of two nanometers. The absorbance edge (wavelength at which $\alpha = 1$ cm^{-1}) was obtained by interpolating between the measured wavelength values. The reflection-correction procedure, described in detail in Chapter 2, 2.2.2, was also used to correct the absorbance data collected for these aqueous solutions.

4.2.2 Physical Property Measurement

Surface tension, viscosity, and density were determined after ellipsometric and absorbance measurements. Surface tension measurements were made on a Ramé-Hart Inc. NRL C.A. goniometer using a pendant drop technique. The kinematic viscosity was measured according to ASTM Standard D 446 using a Cannon-Fenske viscometer, size 150. The mass of known volumes of each fluid in 0.5 mL increments from 0.5 mL to 2 mL was measured using a Mettler Toledo AB204 balance to calculate the density.

4.2.3 Salt Synthesis and Structure

The structures of the salts studied, that have a hydrocarbon group incorporated into a sulfonate anion, are given in Table 4.1. Sodium cyclohexylsulfonate (NaCy) was purchased from Fluka and used as received. The remaining salts were synthesized by Kazuya Matsumoto, a visiting graduate student from the Tokyo Institute of Technology. Prior to use, each salt was dried overnight under vacuum to remove any residual water or solvent. The salt was then dissolved in HPLC-grade water to the desired concentration for optical property measurement. The details of the synthesis and purification of these salts are given in Appendix B.

Table 4.1: Salt structures with the hydrocarbon in the anion

Name	**Structure**	**Name**	**Structure**
Sodium cyclohexane-sulfonate (NaCy)	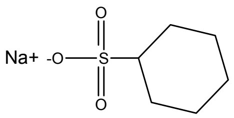	Sodium cyclohexyl-methanesulfonate (NaCyMs)	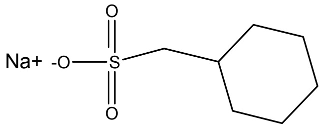
Sodium decahydro-napthalene-2-sulfonate (NaDc)	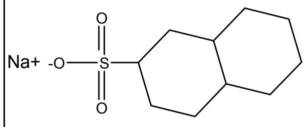	Potassium 1-adamantane-methanesulfonate (KAdMs)	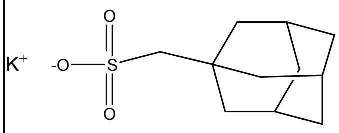
Potassium 1-adamantane-sulfonate (KAd)	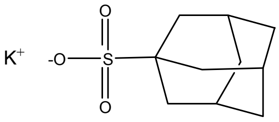		

Quaternary ammonium methylsulfonate salts, with a large hydrocarbon group incorporated on the ammonium cation, were also studied. The structures of these salts are given in Table 4.2. The synthesis and purification of each of these salts is described in Appendix B. Following synthesis and purification, these salts were washed with hexanes and dried under vacuum for at least 12 h to remove any residual solvent. The salts were dissolved in HPLC-grade water to the desired concentration prior to optical property measurement.

Table 4.2: Structures of salts with the hydrocarbon in the quaternary ammonium cation

Name	Structure	Name	Structure	Name	Structure
DMS	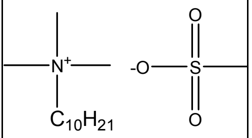	HDMS	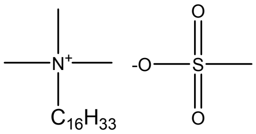	CyMS	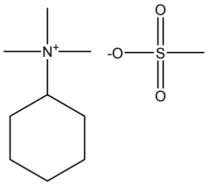
ChpMS	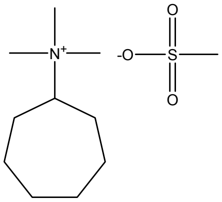	AdMS	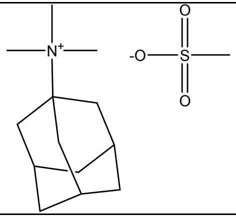	AdHMS	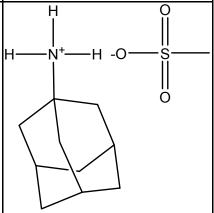
dCyMS	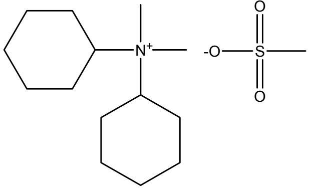				
PdMS	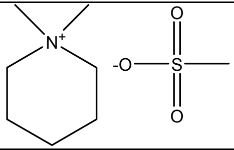	DHQMS	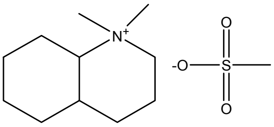	QuinMS	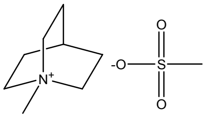
PzMS	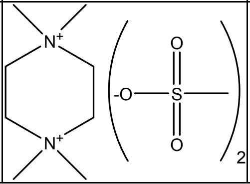	DabMS	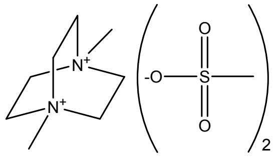		

4.3 SULFONATE SALTS

The structures of the sulfonate salts with a large hydrocarbon attached to the anion are given in Table 4.1. The absorbance spectra for these salts are given in Figure 4.1. Each of the salts was tested at 0.01 M, except for sodium decahydronapthalene-1-sulfonate (NaDc), which was tested at 0.003 M so that an absorbance peak could be observed. Despite the low concentrations, all of these salts have an absorbance that significantly exceeds the target value of 0.15 cm^{-1} at 193 nm, except for sodium cyclohexylsulfonate (NaCy). Additionally, at these low concentrations, the index of refraction of these salts increases only slightly over the index of water ($n_{193,water} = 1.435$). These index values are given in Table 4.3. The highest index of these low concentration solutions is achieved with 0.01 M sodium cyclohexylmethanesulfonate (NaCyMs), $n_{193} = 1.456$.

Since NaCy has the lowest absorbance of these salts, NaCy was added to water in higher concentration (> 0.01 M) to attempt to increase the index at 193 nm without significantly increasing the absorbance. Increasing the concentration of NaCy to 1 M increases the index of the solution to 1.465 at 193 nm. However, the absorption coefficient also increases above 2 cm^{-1} at 193 nm. Thus, while higher salt concentrations would further increase the index, the absorbance also increases to prohibitively high levels.

While the high absorbance of these salt solutions might be due to impurities, these salts tend to act as surfactants and form micelles due to the hydrophobicity of the large hydrocarbon groups at high salt concentrations (> 0.01 M). This surfactant behavior increases the likelihood of bubble formation in the fluid, leading to scattering as the light travels through the fluid which can reduce image contrast.[6] Bubbles also introduce differences in the index within the fluid layer, or index inhomogeneities, that could reflect or refract light differently than the bulk liquid and distort the local image projected into the resist.[7, 8] Thus, despite the likelihood of an increased index at higher salt concentrations, the high absorbance and micelle formation prevent the use of this class of salts in immersion lithography.

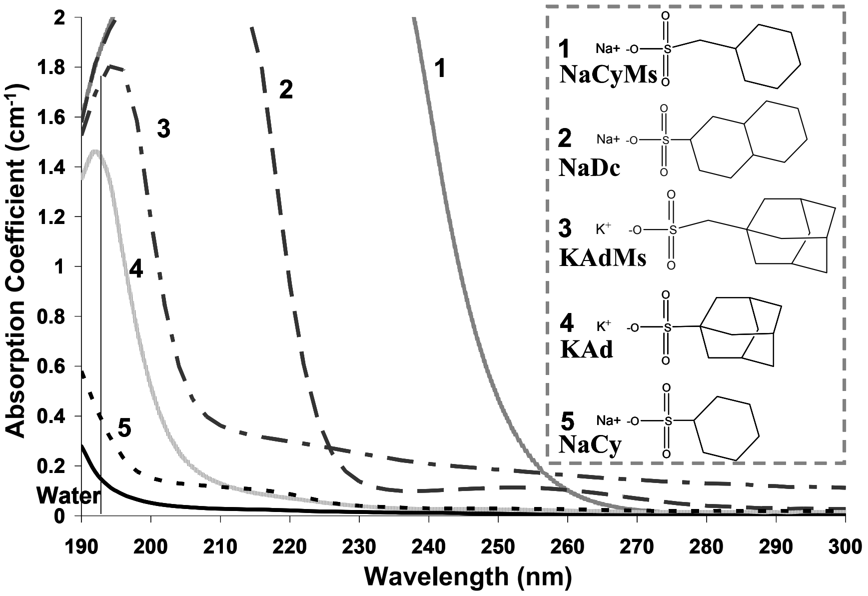

Figure 4.1: Absorbance spectra of the aqueous solutions of the sulfonate salts. Salts 1, 3, 4, 5 were tested at 0.01 M, and salt 2 was tested at 0.003 M.

Table 4.3: Index of refraction at 193 nm and Cauchy coefficients for sulfonate salts

Salt	n_{193}	**Cauchy coefficients**		
		A	**B x10^3 (μm^4)**	**C x10^4 (μm^4)**
NaCy (1 M)	1.465	1.347	2.83	0.581
NaCyMs (0.01 M)	1.456	1.340	3.68	0.242
KAd (0.01 M)	1.454	1.337	4.03	0.123
KAdMs (0.01 M)	1.443	1.319	2.60	0.750
NaDc (0.003 M)	1.433	1.322	2.27	0.703
NaCy (0.01 M)	1.431	1.319	2.76	0.525

4.4 QUATERNARY AMMONIUM SALTS

Based on the use of quaternary ammonium developer solutions in a semiconductor processing environment and the known effects of these cations on the wafer, quaternary ammonium cations are considered to be "semiconductor-friendly." These quaternary ammonium cations provide a convenient method of including a saturated hydrocarbon in a salt to try to develop a solution with the absorbance edge dependence on structure of a saturated hydrocarbon while maintaining the physical properties of water. The cations studied were paired with low absorbance, high index methylsulfonate anions. The structures of these salts are given in Table 4.2.

4.4.1 Ammonium vs Quaternary Ammonium

Two different methods of hydrocarbon incorporation in the cation were considered, using either an ammonium or a quaternary ammonium cation. Both trimethyladamantylammonium methylsulfonate (AdMS) and adamantylammonium methylsulfonate (AdHMS) were studied to compare these cations and consider differences in optical properties and solubility. The absorbance spectra for 1 M AdMS and 1 M AdHMS are given in Figure 4.2. 1 M AdMS has a lower absorbance at 193 nm than 1 M AdHMS. The index of refraction of both of these 1 M salt solutions is 1.506 at 193 nm.

While the slightly higher absorbance at 193 nm of 1 M AdHMS might be due to residual impurities, the solubility of AdMS in water is much higher than the solubility of AdHMS. AdMS is soluble to approximately 70 g/100 g at room temperature while AdHMS is soluble only to approximately 20 g/100 g at room temperature. Typically, ammonium salts are more soluble in water than tetramethylammonium salts. However, tetramethylammonium chloride is more soluble in water than ammonium chloride, based on the difference in their heats of solution. The heat of solution ($\Delta_{sol}H^{\circ}$) of ammonium chloride is 14.78 kJ/mol and 4.08 kJ/mol for tetramethylammonium chloride.[9] Since this surprising solubility result has been observed for chloride solutions, the greater solubility of the quaternary ammonium methylsulfonate salt seems plausible. Since higher salt concentrations lead to a higher index of refraction, salts with a greater solubility in water are preferred. Thus, since 1 M AdMS and AdHMS have the same index of refraction at 193 nm, quaternary ammonium salts, rather than ammonium salts, were studied.

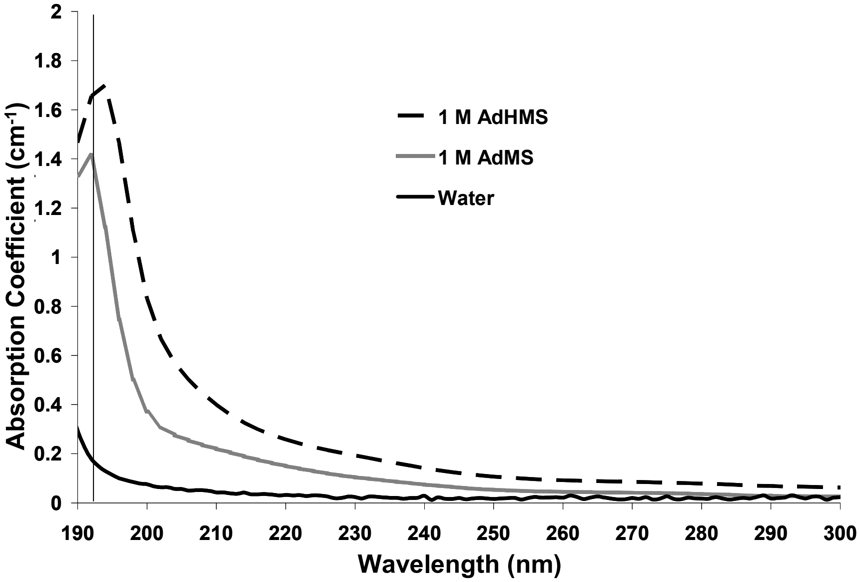

Figure 4.2: Absorbance spectra of 1 M AdHMS and 1 M AdMS

4.4.2 Index of Refraction

The quaternary ammonium salt solutions are divided into two classes. First, Class I describes salts of cations that have an attached alkane group. Class II describes salts of cations in which nitrogen is within the hydrocarbon ring. The index of refraction of the Class I and Class II salt solutions is given in Figure 4.3 and Figure 4.4, respectively. The index values at 193 nm and Cauchy coefficients are also summarized in Table 4.4. The index of each of the solutions was measured at 1 M, except for HDMS, which was measured at 0.8 M due to solubility limits.

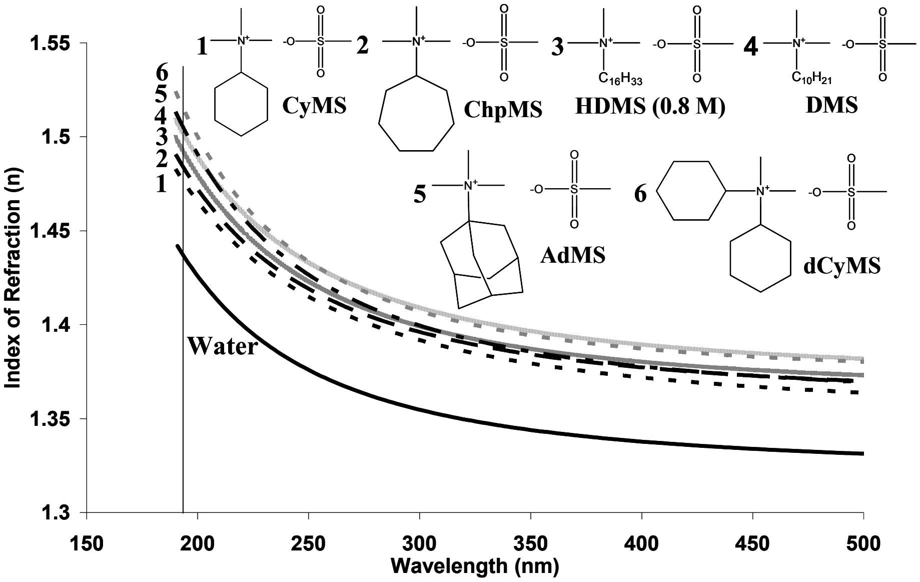

Figure 4.3: Index of refraction of 1 M Class I quaternary ammonium solutions

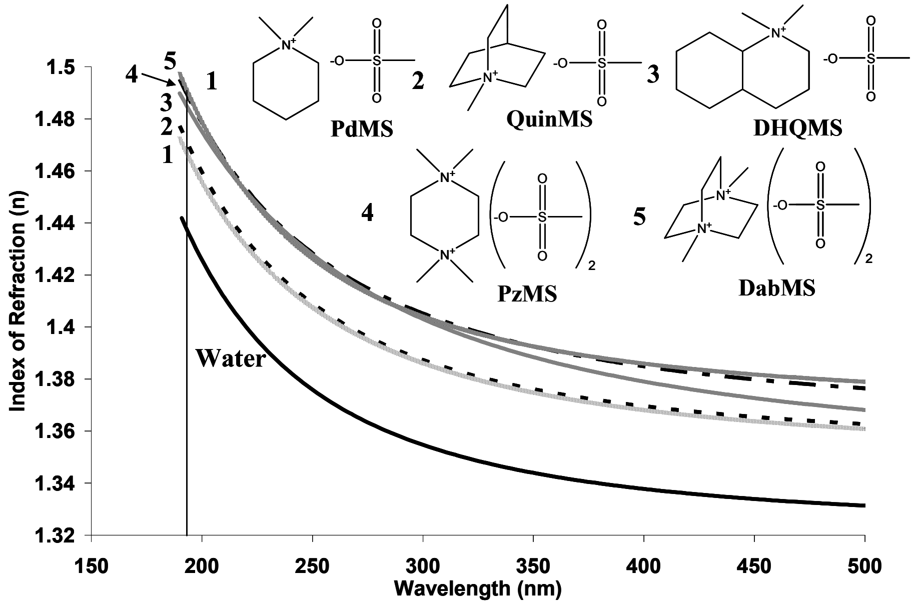

Figure 4.4: Index of refraction of 1 M Class II quaternary ammonium solutions

Table 4.4: Index of refraction and Cauchy coefficients for 1 M quaternary ammonium solutions

	Salt (1 M)	$\mathbf{n_{193}}$	**Cauchy coefficients**		
			A	**B x10^3 (μm^4)**	**C x10^4 (μm^4)**
Class I	dCyMS	1.516	1.371	1.69	1.38
	AdMS	1.506	1.358	2.52	1.12
	AdHMS	1.506	1.349	2.64	1.20
	DMS	1.503	1.371	2.41	0.932
	HDMS (0.8 M)	1.493	1.362	2.14	1.01
	ChpMS	1.485	1.359	2.38	0.856
	CyMS	1.477	1.351	2.95	0.654
Class II	DabMS	1.491	1.369	2.18	0.887
	PzMS	1.490	1.363	3.16	0.583
	DHQMS	1.489	1.363	2.20	0.936
	QuinMS	1.472	1.353	2.22	0.826
	PdMS	1.467	1.350	2.51	0.694

Within both the Class I and Class II salts, the index increases with increasing size of the alkane group. For Class I, the index at 193 nm increases from 1.477 for the salt solution with the cyclohexyl group (CyMS), a carbon number of six, to 1.516 for the salt solution with two cyclohexyl groups (dCyMS), a carbon number of 12. The salt solution with the hexadecyl group (HDMS), which has the largest carbon number (16), was tested at 0.8 M and has an index of 1.493. Increasing the concentration of HDMS would increase the index and likely maintain the trend of increasing index with increasing carbon number. The salt solutions with a carbon number of 10, the salt with the decyl group (DMS) and with the adamantyl group (AdMS), have an index of 1.503 and 1.506 at 193 nm, respectively. For saturated hydrocarbon fluids with the same number of carbons, cyclic structures have a higher index than linear structures. Finally, for the Class II salts, the index at 193 nm increases from 1.467 for the salt solution with the cyclohexane group (PdMS), a carbon number of five, to 1.489 for the salt solution with the decalin group (DHQMS), a carbon number of nine.

Additionally, monovalent and divalent cations were compared by testing quaternary ammonium salts containing a cyclohexane ring and a bicyclo[2.2.2]octane ring with both one and two nitrogens. Increasing the number of moles of anion in the solution should increase the index, as observed with the lanthanum methylsulfonate solutions discussed in Chapter 2.[4] Increasing the valency of the salt provides a convenient means of increasing the moles of anion in solution. Thus, a salt with a divalent cation should have a higher index than a salt with a monovalent cation. PzMS and DabMS are the divalent cations of PdMS, with a cyclohexyl ring, and QuinMS, with a bicyclo[2.2.2]octane ring, respectively. As expected, increasing the valency increases the index at 193 nm from 1.467 to 1.490 for the cyclohexane ring salt solution and from 1.472 to 1.491 for the bicyclo[2.2.2]octane ring salt solution. However, an index of 1.489 at 193 nm, approaching these values, can be achieved by increasing the carbon number up to nine (DHQMS).

The Class I and II cyclohexane salts, CyMS and PdMS, respectively, can be compared to determine which class of salt results in the greatest index. Attaching the alkane results in a higher index, since the index of CyMS is 1.477 at 193 nm and the index of PdMS is 1.467 at 193 nm.

4.4.3 Absorbance

The absorbance spectra for the quaternary ammonium salt solutions were also measured and are given in Figure 4.5 for Class I and Figure 4.6 for Class II. The absorbance at 193 nm and absorbance edge, defined as the wavelength at which $\alpha = 1$ cm^{-1}, are given in Table 4.5. All of these solutions were tested at a concentration of 1 M, except for HMDS which was tested at 0.8 M due to solubility limits.

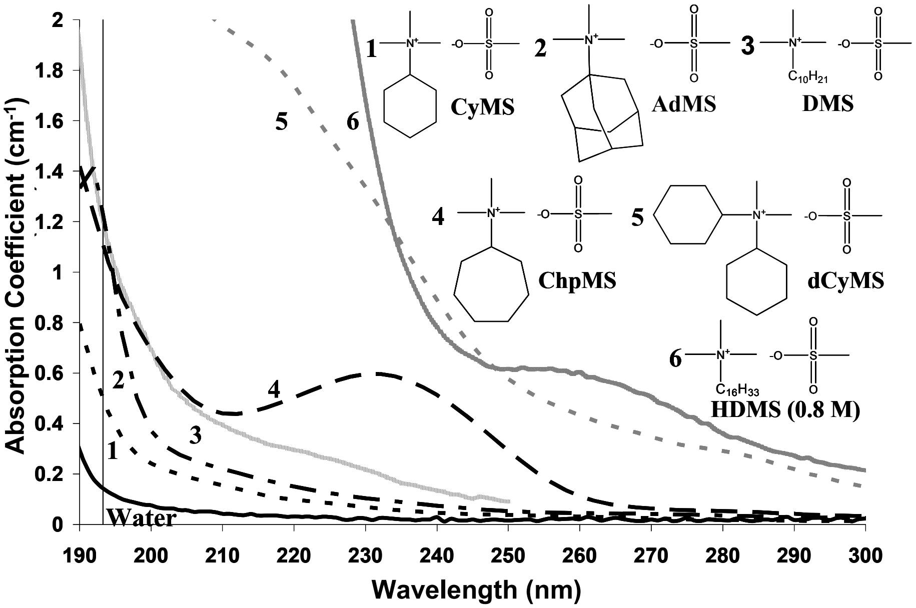

Figure 4.5: Absorbance spectra of 1 M Class I quaternary ammonium solutions

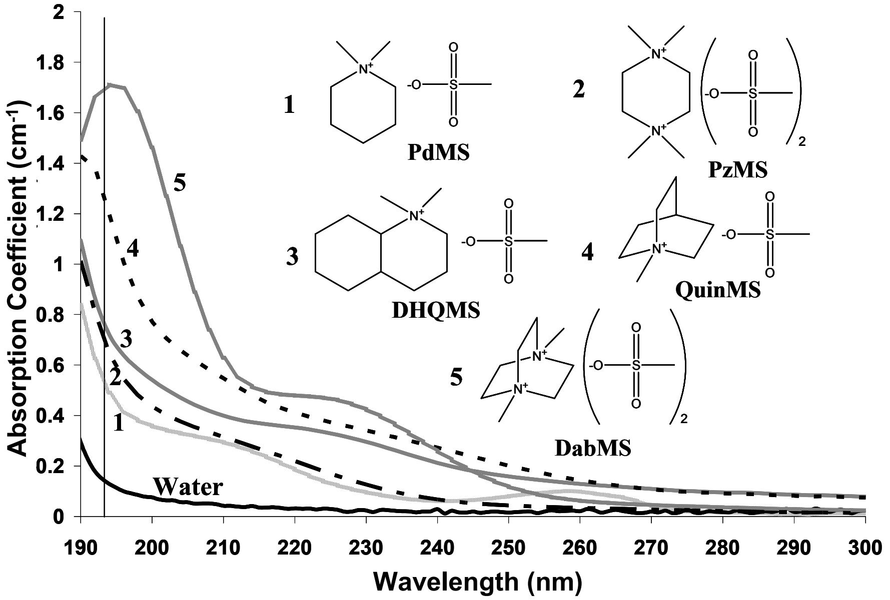

Figure 4.6: Absorbance spectra of 1 M Class II quaternary ammonium solutions

Table 4.5: Absorption coefficient at 193 nm and absorbance edge for 1 M quaternary ammonium solutions

	Salt (1 M)	**α_{193} (cm^{-1})**	**λ_{edge} ($\alpha = 1\ cm^{-1}$)**
Class I	dCyMS	>2	238
	HDMS (0.8 M)	>2	236
	AdHMS	>2	199
	DMS	1.23	195
	AdMS	1.25	195
	ChpMS	1.15	195
	CyMS	0.51	<190
Class II	DabMS	1.70	205
	QuinMS	1.29	196
	DHQMS	0.80	191
	PzMS	0.78	190
	PdMS	0.68	<190

As observed with the index of refraction data, the absorbance also depends on the carbon number of the alkane group. The absorbance edge generally decreases with decreasing size of the alkane group. For the Class I salts, the absorbance edge of dCyMS, with a carbon number of 12, is 238 nm while the absorbance edge of CyMS, with a carbon number of six, is < 190 nm. HDMS is generally excluded from this comparison due to the lower salt concentration. However, HDMS has the largest alkane group (16 carbons) with an absorbance edge of 236 nm. The absorbance edge is expected to red-shift with higher salt concentration and should be consistent with the trend. The 10-carbon salts, DMS and AdMS, both have absorbance edges of 195 nm, consistent with the similarity in their index values at 193 nm. For the Class II salts, a similar shift in absorbance edge with structure is observed. For the divalent salts, PzMS (four carbons) and DabMS (six carbons), the absorbance edge increases from 190 nm for PzMS to 205 nm for DabMS. These divalent cations also have a longer wavelength absorbance edge than their corresponding monovalent cations, PdMS (< 190 nm) and QuinMS (196 nm), respectively. Upon increasing the moles of anion in solution with a divalent cation, the absorbance edge should red-shift slightly since the methylsulfonate anion has a low absorbance at 193 nm (see Chapter 2). DHQMS, with a nine carbon alkane group, has a shorter wavelength absorbance edge, 191 nm, than QuinMS (196 nm) which contains a seven carbon alkane group. This discrepancy in the trend of increasing absorbance edge with increasing alkane group size is likely due to residual impurities in the QuinMS solution.

The difference in absorbance edge between the Class I and Class II salts can be compared through CyMS (Class I) and PdMS (Class II), which both contain a cyclohexane alkane group. Both of these solutions have an absorbance edge < 190 nm. Since wavelengths < 190 nm could not be measured with the UV-Vis absorbance tool, these solutions can be compared based on their absorbance at 193 nm. CyMS has a lower absorption coefficient at 193 nm than PdMS, 0.51 cm^{-1} and 0.68 cm^{-1}, respectively. The slightly higher absorbance of the Class II salt solution (PdMS) is surprising since the index of the Class II solution is lower than the Class I solution (CyMS). Based on the relationship between index and absorbance, as the absorbance at 193 nm increases, the index at 193 nm should also increase. However, the wavelength of the absorbance edge is also an important indicator of the index. Since the wavelength of the absorbance edge could not be measured, this discrepancy cannot be fully evaluated. The greater absorbance of PdMS could simply be due to residual impurities in the PdMS solution at 193 nm.

4.4.4 Cation Dependence

For the salts of metal cations discussed in Chapter 2, the optical properties depend most significantly on the anion. A slight increase in absorbance edge and index at 193 nm has also been observed for quaternary ammonium acetates with hydrocarbon groups of increasing size (see Chapter 2). Charge transfer to solvent (CTTS) transitions cause the observed absorbance of salts in water. The increased size of the quaternary ammonium cations relative to the metal cations seems to alter the charge transfer to solvent (CTTS) transitions so that the optical properties depend on cation size. These intense CTTS transitions are typically observed for anions. When light is absorbed, the electron is separated from the ion and forms a solvated electron, bound by a solvent cage, in an excited state around the parent anion.[10-12] For large cations, the increased distance between the charge centers of the cation and anion decreases the electronic stabilization of the ion pair and reduces the amount of energy required for excitation.[13] Thus, significantly increasing the size of the cation by incorporating increasingly larger alkane groups into the quaternary ammonium should red shift the absorbance edge and increase the index at 193 nm, as observed for both the Class I and Class II salts.

4.4.5 High Index Salts

The most promising salts, based on the index and absorbance values measured at a concentration of 1 M, were added to water in higher concentration to increase the index of the solution. However, since the salt with the highest index necessarily has a high absorbance, a tradeoff exists between the index that can be achieved and the absorbance that can be tolerated. Considering this tradeoff, solutions with high concentrations (> 1 M) of CyMS, AdMS, DHQMS, and PzMS were prepared. The index of refraction at 193 nm, Cauchy coefficients, absorption coefficient at 193 nm and absorbance edge of these high concentration solutions are given in Table 4.6. The 2 M (saturated) solution of PzMS is too strongly absorbing ($\alpha_{193} > 2$ cm^{-1}). While AdMS is soluble in water up to approximately 70 g/100 g at room temperature, solutions above 2 M would be too strongly absorbing. DHQMS is soluble in water up to approximately 65 g/100 g at room temperature and could likely be added to water to approximately 2.5 M. However, due to the limited available sample size of DHQMS, the maximum concentration tested was 2 M. However, the index at 193 of 2.5 M DHQMS was calculated using the Lorentz-Lorenz equation:[14]

$$\frac{n_{12}^{2}-1}{n_{12}^{2}+2}=\phi_1\frac{n_1^{2}-1}{n_1^{2}+2}+\phi_2\frac{n_2^{2}-1}{n_2^{2}+2} \qquad (4.1)$$

where n_{12}, n_1 and n_2 are the refractive indices of the solution, salt, and water, respectively, and ϕ_i is the volume fraction of the salt and water. An average value for the index of the salt (n_1) was calculated from the index (n_{12}) of both the 1 M and 2 M solutions, assuming a salt density of 1 g/mL. Thus, for $n_{1,193\ \mathrm{nm}} = 1.644$ and $n_{2,193\ \mathrm{nm}} = 1.435$, the index of a 2.5 M solution of DHQMS at 193 nm is approximately 1.569. Thus, the 3.4 M (saturated) CyMS solution provides the greatest increase in index with the lowest in absorbance at 193 nm, with $n_{193} = 1.58$ and $\alpha_{193} = 1.43\ \mathrm{cm}^{-1}$. The index and absorbance of this solution are plotted in Figure 4.7.

Table 4.6: Optical properties of high concentration solutions

Salt	**n_{193}**	**Cauchy coefficients**			**α_{193} (cm^{-1})**	**λ_{edge} (α= 1 cm^{-1})**
		A	**B x10^3 (μm^4)**	**C x10^4 (μm^4)**		
3.4 M CyMS	1.580	1.436	2.73	0.978	1.43	198.8
2 M AdMS	1.556	1.411	2.66	1.01	1.80	198.5
2 M DHQMS	1.538	1.402	2.24	1.04	1.28	197.5
2 M PzMS	1.537	1.409	2.62	0.793	> 2	215.0

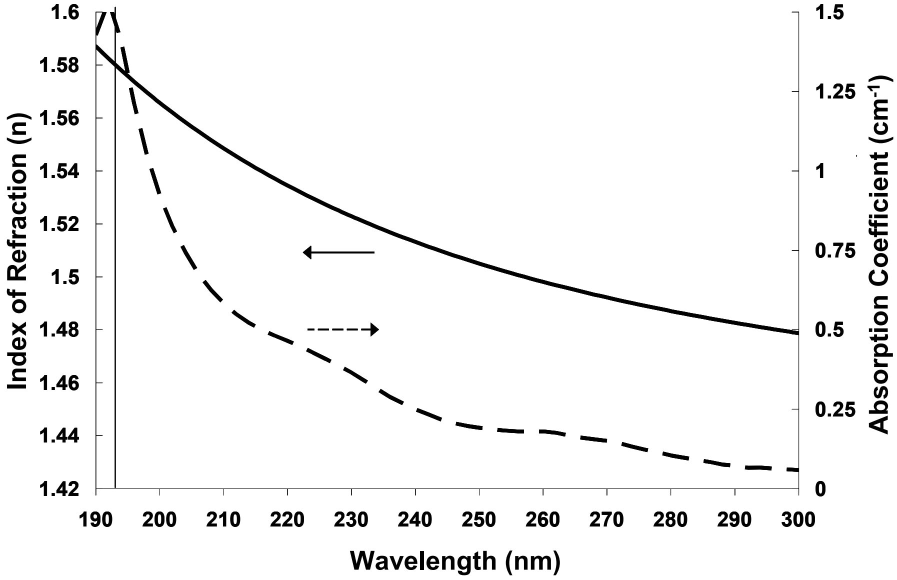

Figure 4.7: Index of refraction and absorbance of 3.4 M CyMS

4.4.6 Physical Properties and Imaging

Since these aqueous solutions were designed to provide an alternative to the saturated hydrocarbons immersion fluids, the physical properties of 3.4 M CyMS were measured and compared to both water and decalin, as an example of a typical cycloalkane. These data are given in Table 4.7. To achieve the highest scanning speeds, the fluid should have physical properties similar to those of water, or a high surface tension and low viscosity. First, the surface tension of this aqueous fluid, while lower than that of water, is significantly higher than that of decalin. However, the viscosity of the aqueous solution is higher than the viscosity of decalin due to the very high salt concentration. An equation for the critical scanning speed (v_{crit}) that can be obtained before liquid loss has been developed,[15]

$$v_{crit} \propto \frac{\gamma}{\mu}\theta_s^3, \tag{4.2}$$

where γ and μ are the surface tension and viscosity of the fluid, respectively, and θ_s is the static contact angle of the fluid on the surface coating. To obtain sufficiently high scanning speeds, a high surface tension and low viscosity are needed. The high viscosity of 3.4 M CyMS effectively negates the potential gain in scan speed due to the increase in surface tension over decalin.

The photodegradation of this fluid was also tested using the laser irradiation setup at MIT Lincoln Labs.[16] These data are given in Figure 4.8. At very high doses, as much as 0.1 kJ/cm^2, the transmission of the saturated CyMS solution decreases. After irradiation at these high doses, the transmission at 193 nm decreases from about 10 % to about 3 %. While this transmission loss is significant, irradiation at this level also causes transmission loss in saturated hydrocarbons.[17] At lower dose levels, the irradiation effects are expected to decrease.

Imaging with 3.4 M CyMS was completed using interference imaging at SEMATECH in Albany for NA = 0.75, 1.05, and 1.5. These images are given in Figure 4.9. Using this solution as the immersion fluid, 32 nm l/s images were patterned with 1.5 NA (Figure 4.9c), confirming the feasibility of imaging with these salt solutions to generate high resolution features. These images are of good quality with few defects and no photoresist degradation.

Table 4.7: Physical properties of water, 3.4 M CyMS, and decalin

	Surface Tension (dyn/cm)	**Viscosity (cP)**	**Density (g/cm^3)**
Water	72.9	1	1
3.4 M CyMS	52.2	21.4	1.1
Decalin	32.18	3.381	0.896

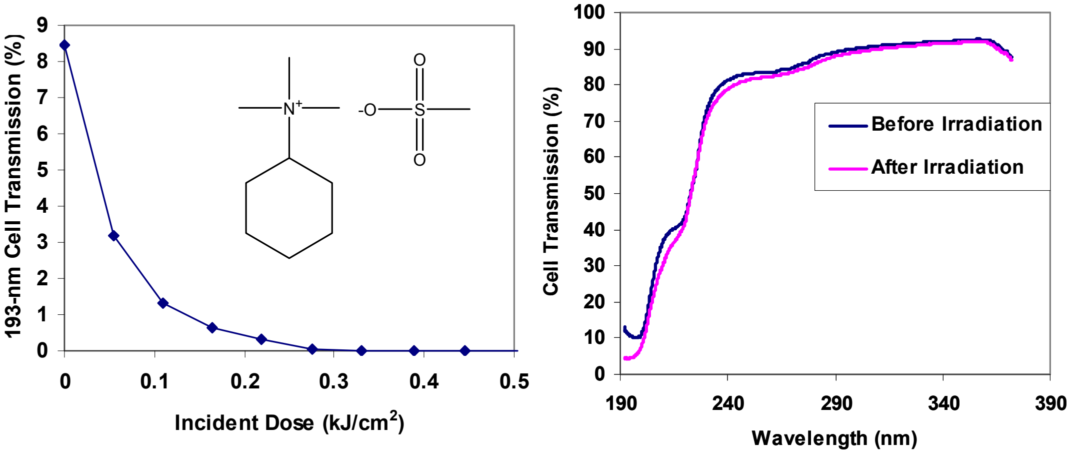

Figure 4.8: Laser irradiation results for the fluid at increasing dose levels (a) and for the transmission of the fluid both before and after irradiation (b)

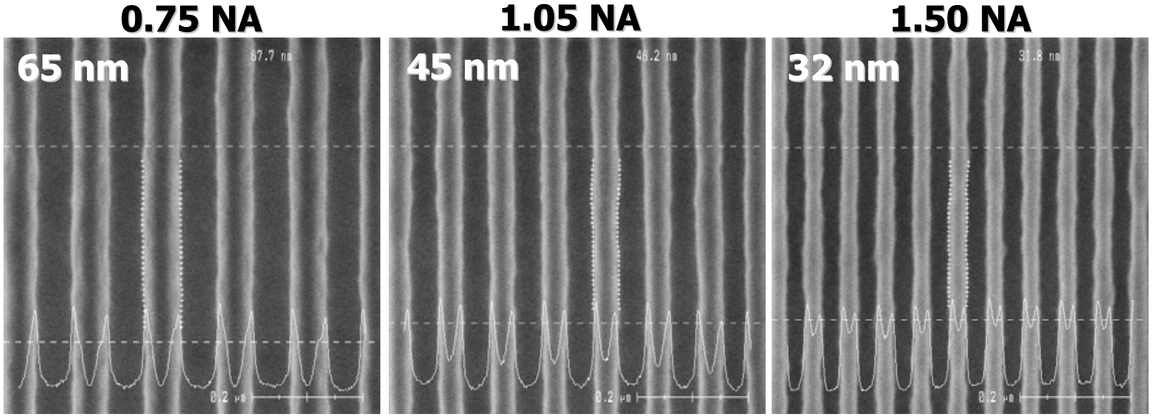

Figure 4.9: Interference imaging with 3.4 M CyMS \to generate 65 nm l/s images (a), 45 nm l/s images (b), and 32 nm l/s images (c)

4.5 CONCLUSIONS

To exploit the properties dictated by anomalous dispersion and the Kramers-Kronig relation and develop a fluid with a high index at 193 nm without a high absorbance, the fluid should have an absorbance edge at a wavelength just less than 193 nm. Thus, the identification of a class of fluids with a structure-dependent absorbance edge is necessary to design a fluid with an absorbance edge just less than 193 nm. Saturated hydrocarbons possess an absorbance edge that is “adjustable” based on structure but are difficult to incorporate into immersion fluid handling systems due to their physical properties, photodegradation, sensitivity to oxygen, and flammability. Aqueous fluids should be more compatible with fluid handling systems designed for water but do not have an index at 193 nm as high as the hydrocarbon fluids. Also, high salt concentrations tend to result in prohibitively high absorbances and viscosities. Therefore, hydrocarbons were incorporated into a salt so that the salt could be added to water in an attempt to develop an aqueous solution with an “adjustable” absorbance edge.

The methylsulfonate anion was also identified as an attractive high index and low absorbance candidate at 193 nm.[4] Thus, hydrocarbons were incorporated into sulfonate anions. These anions were paired with metal ions and added to water in high concentrations. However, the optical properties of these solutions do not depend on structure and are strongly absorbing at 193 nm. These solutions also act like surfactants and exhibit micelle formation at high concentration. Large hydrocarbons were also incorporated into “semiconductor-friendly” quaternary ammonium cations. These cations were paired with methylsulfonate anions. For these quaternary ammonium methylsulfonate salt solutions, the optical properties vary based on the size of the hydrocarbon incorporated into the ammonium cation, creating a salt solution with a structure-dependent absorbance edge. The absorbance edge can be shifted to longer wavelengths by increasing the size of the alkane in the ammonium cation.

An aqueous quaternary ammonium fluid with an index of 1.58 and absorption coefficient of 1.43 cm^{-1} at 193 nm has been identified. This solution is saturated and contains a salt with a cyclohexyl group incorporated into a trimethylammonium cation paired with a methylsulfonate anion. 32 nm l/s images at 1.5 NA confirm the feasibility of generating high resolution patterns with these fluids. However, since this aqueous fluid has a higher absorbance, lower index, and greater viscosity than the saturated hydrocarbon fluids, such as decalin, these quaternary ammonium salt solutions are not viable alternatives to the alkane fluids.

4.6 REFERENCES

1. Wooten, F., *Optical Properties of Solids.* 1972, New York: Academic Press. pp. 260.
2. Born, M. and Wolf, E., *Principles of Optics.* 2nd. 1964, New York: Pergamon Press. pp. 808.
3. Yadav, L. D. S., *Organic Spectroscopy.* 2005, Boston: Kluwer Academic Publishers. pp. 324.
4. Taylor, J. C., Costner, E. A., Goh, S., Wojtczak, W., Dewulf, D. and Willson, C. G., *The effect of added salts on the optical properties of water for high index immersion lithography fluids.* J. Vac. Sci. Technol., B, 2008. **26**(2): p. 506-513.
5. French, R. H., Sewell, H., Yang, M. K., Peng, S. P., McCafferty, D., Qiu, W., Wheland, R. C., Lemon, M. F., Markoya, L. and Crawford, M. K., *Imaging of 32-nm 1:1 lines and spaces using 193-nm immersion interference lithography with second-generation immersion fluids to achieve a numerical aperture of 1.5 and a k1 of 0.25.* J. Microlith. Microfab. Microsyst., 2005. **4**(3): p. 031103-1 - 031103-14.
6. Lin, B. J., *Immersion lithography and its impact on semiconductor manufacturing.* J. Microlith. Microfab. Microsys., 2004. **3**(3): p. 377-395.
7. Rothschild, M., Bloomstein, T. M., Kunz, R. R., Liberman, V., Switkes, M., Palmacci, S. T., Sedlacek, J. H. C., Hardy, D. and Grenville, A., *Liquid immersion lithography: Why, how, and when?* J. Vac. Sci. Technol., B, 2004. **22**(6): p. 2877-2881.
8. Switkes, M. and Rothschild, M., *Immersion lithography at 157 nm.* J. Vac. Sci. Technol., B, 2001. **19**(6): p. 2353-2356.

9. *Enthalpy of Solution of Electrolytes.* CRC Handbook of Chemistry and Physics, 89th Edition (Internet Version 2009), Lide, D. R., ed., Boca Raton, FL: CRC Press/Taylor and Francis.

10. Fox, M. F. and Hunter, T. F., *Charge-transfer-to-solvent spectra.* Nature, 1969. **223**(5202): p. 177-8.

11. Stein, G. and Treinin, A., *Absorption spectra of anions in solution. III. Ionic effects.* Trans. Faraday Soc., 1960. **56**(1): p. 1393-403.

12. Rao, C. N. R., *Ultra-Violet and Visible Spectroscopy.* 3rd. 1975, England: Butterworth and Co. Ltd. pp. 242.

13. Griffiths, T. R. and Wijayanayake, R. H., *Effects of cations upon absorption spectra. 5. Charge-transfer-to-solvent spectrum of iodide and ion-pair formation.* Trans. Faraday Soc., 1970. **66**(7): p. 1563-73.

14. Heller, W., *Remarks on refractive index mixture rules.* J. Phys. Chem., 1965. **69**(4): p. 1123-9.

15. Harder, P. M. and Shedd, T. A., *Contact angles and liquid loss behavior of high index fluids.* Proc. SPIE Int. Soc. Opt. Eng., 2007. **6533**(European Mask and Lithography Conference, 2007): p. 653305/1-653305/12.

16. Liberman, V., Rothschild, M., Palmacci, S. T., Zimmerman, P. A. and Grenville, A., *Laser durability studies of high index immersion fluids: fluid degradation and optics contamination effects.* Proc. SPIE Int. Soc. Opt. Eng., 2007. **6520**(Pt. 3, Optical Microlithography XX): p. 652035/1-652035/10.

17. Liberman, V., Rothschild, M., Palmacci, S. T., Bristol, R., Byers, J., Turro, N. J., Lei, X., O'Connor, N. and Zimmerman, P. A., *High-index immersion lithography: preventing lens photocontamination and identifying optical behavior of LuAG.* Proc. SPIE Int. Soc. Opt. Eng., 2008. **6924**(Pt. 1, Optical Microlithography XXI): p. 692416/1-692416/11.

Chapter 5: Development of an Immersion Fluid Model

In addition to an experimental evaluation of both aqueous solutions and saturated hydrocarbons (see Chapters 2 – 4), a computer modeling approach could also be used to guide rapid screening of spectral characteristics and generate "designer" spectra corresponding to fluids with the target optical properties for next generation immersion lithography at 193 nm. The modeled spectra could be used to guide the selection of high index immersion fluid candidates. Thus, a model for the optical properties was developed to calculate index and absorbance spectra with the target high index and low absorbance at 193 nm.

5.1 IMMERSION FLUID MODELING APPROACH

In this immersion fluid model, absorbance spectra are first generated using an oscillator model. The index variation with wavelength is then calculated from the absorbance spectra. Since the index and absorbance are linked through the Kramers-Kronig relations, only one of these properties needs to be specified. An iterative approach can then be used to vary the absorbance spectra and obtain the target index and absorbance values.

Both a model for the absorbance spectra and a solution to the Kramers-Kronig integral (to calculate the index) are needed in this immersion fluid modeling approach. A variety of oscillator models exist which define the absorbance spectra for different types of materials. Each oscillator model differs in the calculation of the absorbance peaks, through differences in broadening functions, for example. The identification of the oscillator model that provides the most accurate representation of the absorbance of a fluid with a high index and low absorbance at 193 nm will be described. For some oscillator models, an analytical solution to the Kramers-Kronig intergrals exists; while for other oscillator models, the Kramers-Kronig integrals must be solved. Various Kramers-Kronig solution methods to calculate the index from the absorbance spectrum will also be discussed.

5.2 KRAMERS-KRONIG RELATIONS

The Kramers-Kronig dispersion relations define the relationship between the index of refraction and absorbance. These relations connect the real and imaginary parts of a complex function which is analytic in the upper half plane (positive values on the y-axis).[1] Since the Kramers-Kronig relations describe the link between the index and absorbance, an index spectrum can be determined from an absorbance spectrum (or vice versa) using these relations.

5.2.1 Causality and Dispersion Relations

Causality defines a relationship in which the response of a system is at a later instant than the cause of the response, or an effect cannot precede a cause, and dictates the relationship between the index and absorbance.[1, 2] An absorption at one wavelength must be accompanied by a compensating phase shift at all other wavelengths to avoid a violation of causality.[1] The index of refraction and absorbance are functions of wavelength and cannot be specified independently. Both the index and absorbance are needed to fully describe the nature of light in a medium.

The complex index of refraction ($\widetilde{n}$) describes the propagation of a monochromatic plane wave in a homogenous medium and is given by

$$\widetilde{n} = n + ik \tag{5.1}$$

where n is the index of refraction and k is the extinction coefficient (absorbance).[1, 3] The complex dielectric constant ($\tilde{\varepsilon}$) is related to $\tilde{n}$ by Maxwell's relation

$$\tilde{\varepsilon} = \tilde{n}^2, \tag{5.2}$$

when the magnetic permeability $\mu = 1$.[1] The real and imaginary components of the complex dielectric constant are related to the index and extinction coefficient through

$$\mathrm{Re}\{\tilde{\varepsilon}\} = \varepsilon_1 = n^2 - k^2 \tag{5.3}$$

$$\mathrm{Im}\{\tilde{\varepsilon}\} = \varepsilon_2 = 2nk \tag{5.4}$$

Kramers[4] and Kronig[5] independently developed dispersion relations to couple the wavelength-dependent absorption and index. These general relations are known as the Kramers-Kronig dispersion relations and link the index and absorbance as

$$\mathrm{Re}\{\tilde{\varepsilon}(E)\} = \frac{2}{\pi} P \int_0^\infty \frac{E' \,\mathrm{Im}\{\tilde{\varepsilon}(E')\}}{E'^2 - E^2} dE' \tag{5.5}$$

$$\mathrm{Im}\{\tilde{\varepsilon}(E)\} = \frac{2}{\pi} P \int_0^\infty \frac{E \,\mathrm{Re}\{\tilde{\varepsilon}(E')\}}{E'^2 - E^2} dE' \tag{5.6}$$

$$\varepsilon_1(E) = \varepsilon_{offset} + \frac{2}{\pi} P \int_0^\infty \frac{E' \varepsilon_2(E')}{E'^2 - E^2} dE' \tag{5.7}$$

$$\varepsilon_2(E) = \frac{2}{\pi} P \int_0^\infty \frac{E \varepsilon_1(E')}{E'^2 - E^2} dE' \tag{5.8}$$

where P designates the Cauchy principal value integral and $\varepsilon_{\text{offset}}$ is a fitting parameter. If the spectral range includes data over the entire integrated range (from zero to infinity), then $\varepsilon_{\text{offset}} = \varepsilon_\infty = 1$.[1, 6] However, the generated or experimental spectral range typically does not include data over the entire integrated range. As a result, $\varepsilon_{\text{offset}}$ can be used as an additional fitting parameter to account for the contribution of data that is outside the generated or experimental range ($\varepsilon_{\text{offset}} > 1$).[6]

The index and absorbance are also subject to the following symmetry conditions:

$$\varepsilon_1(-E) = \varepsilon_1(E);\ n(-\lambda) = n(\lambda) \tag{5.9}$$

$$\varepsilon_2(-E) = -\varepsilon_2(E);\ k(-\lambda) = -k(\lambda). \tag{5.10}$$

The real part of the complex index of refraction is an even function, and the imaginary part is an odd function. These symmetry conditions must be satisfied for the function to satisfy the Kramers-Kronig integral relationship (Kramers-Kronig consistency).[2, 7]

5.3 OSCILLATOR MODELS

Energy can be absorbed by a molecule from a light wave to excite an electron from a ground state to an excited state. This absorption occurs when the light wave is in resonance with the electron oscillators. The electronic states are quantized so that only one electron is excited in each absorption event. From this understanding of absorbance, it seems that absorbance spectra should consist of a series of discrete lines, each of which represents an electronic transition at the energy or wavelength of the absorbed light.[8] These discrete lines are observed in the spectra of atoms since the electronic states in atoms can be described by specifying the orbits of their valence electrons. For a molecule, however, broad peaks, rather than discrete lines, are typically observed. In molecules, the motion of the nuclei relative to each other (through vibrations or rotations) also need to be considered to define the electronic state.[8] A molecular electronic transition does not consist of a single quantized transition but rather a series of transitions which each correspond to different nuclear geometries in the initial and final (or ground and excited) states. Each electronic transition is accompanied by vibrational and rotational transitions superimposed upon the electronic transition.[8, 9] Absorption by a molecule in the vapor phase consists of a series of closely spaced lines which may be only partially resolved or are completely unresolved. In the liquid or solid phase, interactions between molecules further broaden the absorbance lines.[8]

To create a model for the absorbance spectra of an immersion fluid, an accurate model for the broadening or dispersion of the electronic transition is needed. Oscillator models are dispersion formulae that provide a description of the response of an oscillator, or electron, to an external field, such as light by defining the broadening, amplitude, and energy of absorption for different types of chemical structures. For immersion fluid modeling, an important consideration in the selection of an oscillator model is the fit to the absorbance edge. A sharp absorbance edge at 193 nm is necessary to obtain the highest index with a low absorbance, according to anomalous dispersion (see Figure 3.1).

5.3.1 Lorentz Oscillator Model

The Lorentz oscillator model (LOM) is derived from a consideration of the classical theory of an electron as a small mass bound to a large mass (nucleus) by a spring.[10] This model includes a damping term (Br_n) that accounts for energy dissipation by the electron oscillators. The LOM is given by

$$\tilde{\varepsilon} = \varepsilon_{offset} + \sum_n \frac{A_n E_n}{{E_n}^2 - E^2 - iBr_n E} \tag{5.11}$$

Dividing this function into the real and imaginary parts to calculate the index and absorbance,

$$\mathrm{Re}\{\tilde{\varepsilon}\} = \varepsilon_1(E) = \varepsilon_{offset} + \sum_n \frac{A_n E_n (E_n^2 - E^2)}{({E_n}^2 - E^2)^2 + Br_n^2 E^2} \tag{5.12}$$

$$\mathrm{Im}\{\tilde{\varepsilon}\} = \varepsilon_2(E) = \sum_n \frac{A_n Br_n E_n E}{({E_n}^2 - E^2)^2 + Br_n^2 E^2} \tag{5.13}$$

where n is the number of oscillators, or electronic transitions, E_n is the energy, or wavelength, of peak maximum (resonance energy), Br_n is the width of the peak, and A_n is the amplitude of the peak, and E has energy units of eV or cm^{-1}.[10] This oscillator model has an analytical solution to the Kramers-Kronig integral for both the real and imaginary parts of the function (Equations 5.12 and 5.13, respectively).

5.3.2 Frequency-Damped Lorentz Oscillator Model

A modified Lorentz oscillator model has also been developed by Djurisic et al. to provide "frequency-dependent damping" in the broadening parameter of the LOM.[11] The real and imaginary parts of the frequency-damped Lorentz oscillator model (FDLOM) are given by Equations 5.10 and 5.11, respectively. However, the parameter Br_n is replaced with the modified parameter Γ_n as

$$\Gamma_n(E) = Br_n \exp\left[-\alpha_n\left(\frac{E-E_n}{Br_n}\right)^2\right]. \tag{5.14}$$

This damping parameter produces a lineshape, or absorbance edge, that is more similar to a Gaussian shape than a Lorentizian and provides a sharper absorbance edge than the LOM.[11] The use of the FDLOM has been demonstrated in modeling the optical constants of organic thin films to provide a better fit to the experimental data than the LOM.[11]

5.3.3 Tauc-Lorentz Oscillator Model

The Tauc-Lorentz oscillator model (TLOM) was developed to model the optical properties of thin film amorphous materials.[12, 13] This model combines the Tauc equation for the imaginary part of the dielectric function (ε_2) at energies greater than the absorbance band edge (E_g), and the LOM for the imaginary part of the dielectric function (described in 5.3.1). These functions are multiplied to give

$$\begin{aligned} \varepsilon_2(E) &= \left[\frac{AE_oC(E-E_g)^2}{(E^2-E_o^2)^2+C^2E^2}\cdot\frac{1}{E}\right], E > E_g \\ &= 0 \qquad\qquad\qquad\qquad\qquad E \le E_g \end{aligned} \tag{5.15}$$

where A is a fitting parameter for the amplitude, E_o is the peak transition energy (resonance energy), C is the broadening term, and E_g is the optical band gap. Each of these parameters has units of eV. This oscillator model provides a sharp absorbance edge since absorbance values at energies less than E$_g$ are set to zero. The real part of this function can be calculated by integrating Equation 5.15 with the Kramers-Kronig relation in Equation 5.7. This integral has an analytical solution given by

$$\begin{aligned} \varepsilon_1(E) = \varepsilon_{offset} &+ \frac{AC}{\pi\zeta^4}\cdot\frac{a_{\ln}}{2\alpha E_o}\ln\left(\frac{E_o^2+E_g^2+\alpha E_g}{E_o^2+E_g^2-\alpha E_g}\right) - \frac{A}{\pi\zeta^4}\frac{a_{a\tan}}{E_o}\left[\begin{array}{l}\pi - a\tan\left(\dfrac{2E_g+\alpha}{C}\right)\\ + a\tan\left(\dfrac{-2E_g+\alpha}{C}\right)\end{array}\right] \\ &+ 2\cdot\frac{AE_o}{\pi\zeta^4\alpha}\cdot E_g\cdot(E^2-\gamma^2)\cdot\left[\pi + 2\cdot a\tan\left(2\frac{\gamma^2-E_g^2}{\alpha C}\right)\right] \qquad (5.16) \\ &- \frac{AE_oC(E^2+E_g^2)}{\pi\zeta^4 E}\cdot\ln\left(\frac{\left|E-E_g\right|}{E+E_g}\right) + \frac{2AE_oCE_g}{\pi\zeta^4}\cdot\ln\left[\frac{\left|E-E_g\right|\cdot(E+E_g)}{\sqrt{((E_o^2-E_g^2)^2+E_g^2C^2)}}\right] \end{aligned}$$

where

$$a_{\ln} = (E_g^2-E_o^2)E^2 + E_g^2C^2 - E_o^2(E_o^2+3E_g^2), \qquad (5.17a)$$

$$a_{a\tan} = (E^2-E_o^2)(E_o^2+E_g^2) + E_g^2C^2, \qquad (5.17b)$$

$$\zeta^4 = (E^2-\gamma^2)^2 + \frac{\alpha^2C^2}{4}, \qquad (5.17c)$$

$$\alpha = \sqrt{4E_o^2 - C^2}, \qquad (5.17d)$$

$$\gamma = \sqrt{E_o^2 - \frac{C^2}{2}}. \qquad (5.17e)$$

Each of the parameters (A, C, E$_o$, E$_g$) is defined as in Equation 5.15.[12, 13] As in the LOM and FDLOM, multiple absorbance peaks, or oscillators, can be calculated with this model by summing each of the transitions for ε_1 and ε_2.

5.3.4 Gaussian Oscillator Model

A Gaussian function can also be used to broaden an electronic transition into an absorbance peak. The Gaussian function decays quickly to provide a sharp absorbance edge. The Gaussian oscillator model (GOM) for the imaginary part of the complex dielectric function is given by

$$\varepsilon_2(E) = \sum_n (A_n e^{-\left(\frac{E-E_n}{Br_n}\right)^2} - A_n e^{-\left(\frac{E+E_n}{Br_n}\right)^2}) \qquad (5.18)$$

where n is the number of electron oscillators or peaks, A_n is the amplitude of the peak, E_n is the energy at the peak maximum (or resonance energy), and Br_n is the peak broadening.[2] This form of the Gaussian function differs from the traditional Gaussian function so that the symmetry conditions shown in Equation 5.10, to make this function Kramers-Kronig consistent, can be satisfied.

Also, there is not an analytical solution to the Kramers-Kronig equation for the GOM. Thus, to obtain ε_1 for this oscillator model, a technique to solve the Kramers-Kronig integral (given in Equation 5.7), such as a numerical integration method, is needed. Kramers-Kronig solution methods will be discussed in Section 5.5.

5.4 IMMERSION FLUID MODEL

Each oscillator model was evaluated to determine which model provides a sharp absorbance edge and a functional form most similar to the absorbance peaks of a typical immersion fluid. Since decalin has a high index (n_{193} = 1.645) and low absorption coefficient at 193 nm, experimental absorbance data for decalin were used to evaluate these oscillator models. The oscillator model that provides the best fit to the experimental absorbance data for decalin should be the best oscillator model to use in next generation immersion fluid modeling.

The best fit was determined by comparing a spectrum calculated from each of the oscillator models described in Section 5.3 (LOM, FDLOM, TLOM, and GOM) to experimental data for the absorbance of decalin from 188 to 250 nm. The error was calculated according to:

$$Error = \sum_{n=188}^{250} \frac{\left|\varepsilon_{2,osc}(n) - \varepsilon_{2,\exp}(n)\right|}{\varepsilon_{2,\exp}(n)} \tag{5.19}$$

where $\varepsilon_{2,osc}$ is the imaginary part of the complex dielectric constant calculated from the oscillator model and $\varepsilon_{2,exp}$ is the imaginary part of the complex dielectric constant for the experimental decalin absorbance data. Each spectrum was calculated using three oscillators, or absorbance peaks. The parameters for each of the absorbance peaks were adjusted manually to minimize the error (Equation 5.19) between the model and the experimental data. The oscillator model spectra and experimental data are given in Figure 5.1.

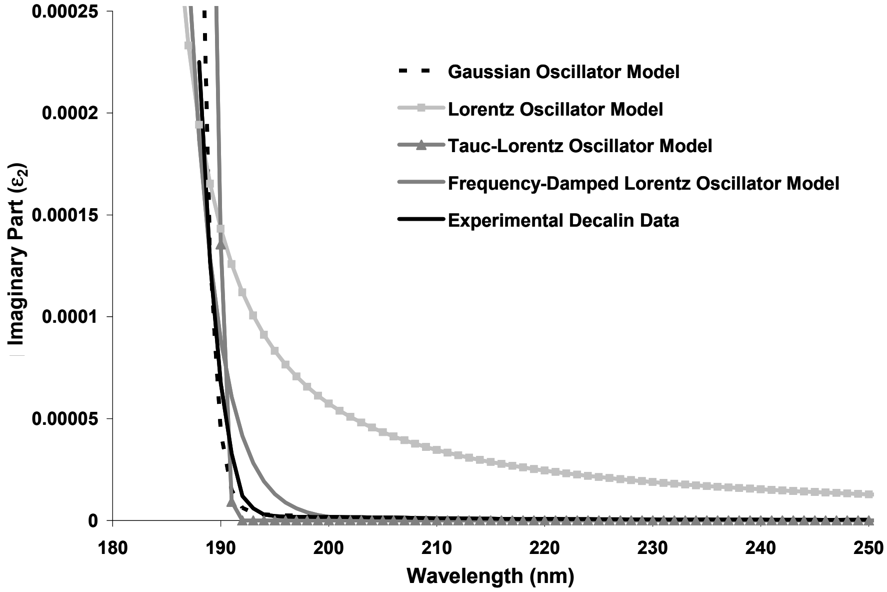

Figure 5.1: Oscillator model comparison to experimental absorbance for decalin

As observed in the spectra shown in Figure 5.1, the broad absorbance edge of the LOM does not accurately model the sharp absorbance edge of decalin to obtain a low absorbance value at 193 nm. The absorbance edge modeled by the TLOM is slightly too sharp, since this model is set to zero at energies less than the band gap energy (see Equation 5.15). The GOM and FDLOM provide the best fit to the experimental data. The error between the GOM and experimental data is 45.7 while with the FDLOM, the error is 68.8.

In addition to modeling the functional form of the absorbance edge accurately, the oscillator model should also provide an accurate fit to the index. To test the index fit with the GOM, multiple Gaussian oscillators, or absorbance peaks, were used to fit the GOM to experimental data for the index and absorbance of decalin from 188 to 250 nm. This fit was achieved using the WVASE32 software to insert Gaussian peaks into the spectrum from 100 to 1000 nm. The WVASE32 software package then solved the Kramers-Kronig equation to calculate ε_1. The index (n) and extinction coefficient (k) were calculated from ε_1 and ε_2 by[10]

$$n = \left\{ \frac{1}{2} \left[\left(\varepsilon_1^2 + \varepsilon_2^2 \right)^{1/2} + \varepsilon_1 \right] \right\}^{1/2} \tag{5.20}$$

$$k = \left\{ \frac{1}{2} \left[\left(\varepsilon_1^2 + \varepsilon_2^2 \right)^{1/2} - \varepsilon_1 \right] \right\}^{1/2} . \tag{5.21}$$

Since the Kramers-Kronig integral is not evaluated over the entire range (from zero to infinity), the $\varepsilon_{\text{offset}}$ term (see Equation 5.7) was used as a fitting parameter to account for the contribution of data outside the measured range. Therefore, in addition to adjusting the Gaussian peak parameters, the $\varepsilon_{\text{offset}}$ term was adjusted to fit the calculated index to the experimental index for decalin at 193 nm and 589 nm. Since 193 nm is close to an absorbance (and index) peak and 589 nm is far from an absorption peak, use of both of these wavelengths prevents unrealistically high values at 193 nm and specifies both the magnitude and tilt of the index peak. 589 nm was chosen since a significant amount of literature data exists at this wavelength. The index at 193 nm and 589 nm with varying $\varepsilon_{\text{offset}}$ values is given in Table 5.1. Also, the spectra for ε_2 and ε_1, with varied $\varepsilon_{\text{offset}}$

values, are given in Figure 5.2. The $\varepsilon_{\text{offset}}$ value that provides the best-fit to the target values at 193 nm and 589 nm is 1.479. The index and absorbance spectrum calculated using $\varepsilon_{\text{offset}}$ = 1.479 provides a good fit to the experimental data for decalin. These spectra are given in Figure 5.3. The parameters for each of the Gaussian peaks, as defined in Equation 5.18, used to generate this spectrum are given in Table 5.2.

Table 5.1: Index at 193 nm and 589 nm with varying $\varepsilon_{\text{offset}}$

$\varepsilon_{\text{offset}}$	1	1.479 (fit)	2
n_{193}	1.47	1.63	1.78
n_{589}	1.31	1.49	1.65
$n_{193,\ \text{target}} = 1.65$		$n_{589,\ \text{target}} = 1.47$	

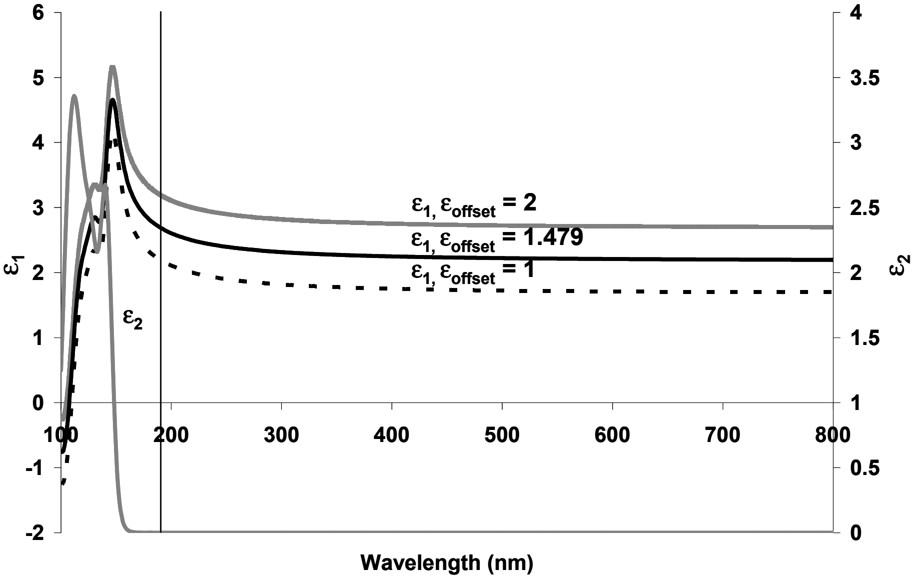

Figure 5.2: ε_1 and ε_2 calculated using WVASE32 with varying $\varepsilon_{\text{offset}}$ values

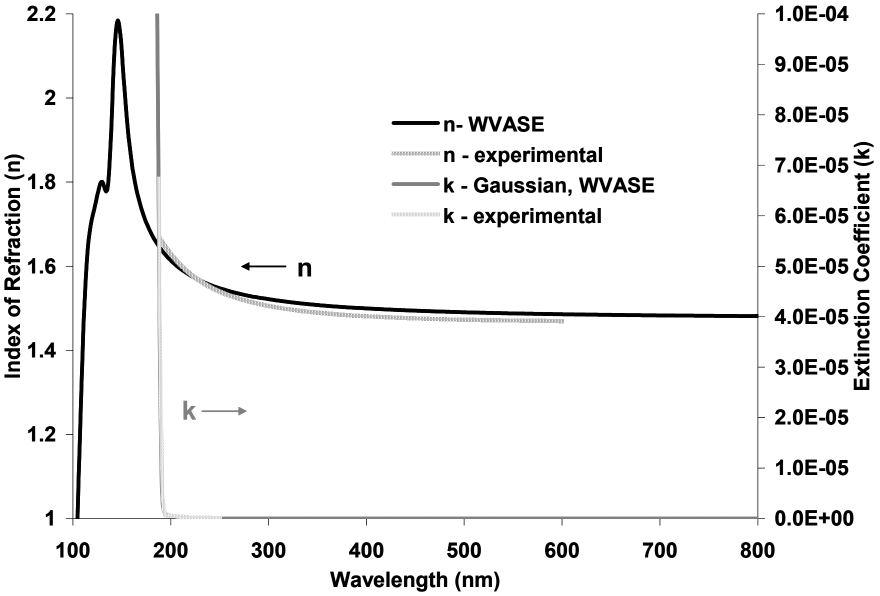

Figure 5.3: Comparison between experimental and calculated index and absorbance for decalin ($\varepsilon_{\mathrm{offset}} = 1.479$)

Table 5.2: Gaussian peak parameters for the spectra of decalin

n	**1**	**2**	**3**	**4**	**5**	**6**	**7**
A_n	1.50×10^{-6}	1.21×10^{-4}	6.29×10^{-4}	1.861	1.917	1.048	2.489
E_n (eV)	6.200	6.637	6.837	8.762	9.626	10.797	11.41
Br_n (eV)	0.270	0.0844	0.164	0.414	0.872	0.872	1.17

5.5 KRAMERS-KRONIG SOLUTION METHODS

Since there is not an analytical solution to the Kramers-Kronig integral for the real part of the complex dielectric constant (ε_1) from the GOM, a method to solve the Kramers-Kronig relations with the GOM is needed. The Kramers-Kronig integral can be solved using a variety of methods. In this case, numerical integration,[14] generalized sum rules,[15] or Hilbert transform methods[7, 16] were studied. The GOM spectrum developed from the experimental absorbance data for decalin, described in Section 5.4, was used to evaluate each of these solution methods.

Both Maclaurin's forumla and a trapezium formula were used to compute the Kramers-Kronig integral numerically.[14] A detailed description of the solution methods and the code for the MATLAB program written for each of these methods is given in Appendix C.

An additional MATLAB program which solves the Kramers-Kronig integral was provided with the text by Lucarini et al.[15] This method also uses a numerical integration technique to solve the Kramers-Kronig integral.

Finally, a Hilbert transform can be used to solve the Kramers-Kronig relations. The Kramers-Kronig integrals are the Hilbert transforms of even and odd functions on the positive real axis.[7] The Hilbert transform of a function f is defined by

$$(Hf)(x) = \frac{1}{\pi} P \int_{-\infty}^{\infty} \frac{f(s)ds}{x-s} \tag{5.22}$$

where P is the Cauchy principal value integral. For the interval (0, ∞), the Hilbert transform becomes,

$$(Hf)(x) = \frac{1}{\pi} P \int_{0}^{\infty} \left\{ \frac{f(y)}{x-y} + \frac{f(-y)}{x+y} \right\} dy . \tag{5.23}$$

If f(x) is an odd function [f(-x) = -f(x)], Equation 5.23 simplifies to

$$(Hf)(x) = \frac{2}{\pi} P \int_{0}^{\infty} \frac{yf(y)}{x^2 - y^2} dy , \tag{5.24}$$

and if f(x) is an even function [f(-x) = f(x)], Equation 5.23 simplifies to

$$(Hf)(x) = \frac{2x}{\pi} P \int_{0}^{\infty} \frac{f(y)}{x^2 - y^2} dy . \tag{5.25}$$

Equations 5.24 and 5.25 are analogous to the Kramers-Kronig integrals given in Equations 5.5 and 5.6, respectively.[7] The Signal Processing Toolbox (Version 6.5) in MATLAB R2006a contains a function which solves the Hilbert transform. This

MATLAB function was used to solve the Hilbert transform of the GOM for decalin to calculate the index.

Each method was used to solve the Kramers-Kronig integral for the Gaussian spectrum developed for decalin in Section 5.4. The real part of the complex dielectric constant (ε_1) calculated with each solution method is given in Figure 5.4. After calculating the index with Equation 5.20, the ε_{offset} fitting parameter was determined by minimizing the sum of the squared error between the experimental and calculated values for the index of decalin at both 193 nm and 589 nm. These ε_{offset} terms, resulting index values at 193 nm and 589 nm, and error are given in Table 5.3.

The Hilbert transform method provides the best fit to the target index at 193 nm and 589 nm since this method provides the lowest error (see Table 5.3). Therefore, the Hilbert transform function solution method was used with the GOM to generate index and absorbance spectra of next generation immersion fluids.

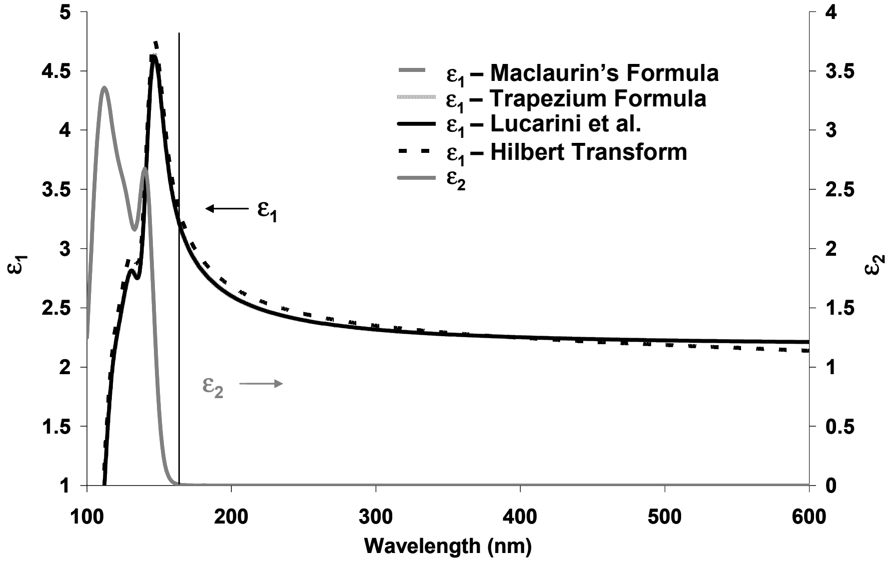

Figure 5.4: ε_1 (ε_2, GOM for decalin) calculated with various Kramers-Kronig solution methods

Table 5.3: Index at 193 nm and 589 nm for the Kramers-Kronig solution methods

Method	**ε_{offset}**	**n_{193}**	**n_{589}**	**Error**
Experimental	------	1.645	1.474	------
Maclaurin Sum[14]	1.532	1.630	1.488	4.10×10^{-4}
Trapezium Sum[14]	1.532	1.630	1.488	4.09×10^{-4}
Lucarini et al.[15]	1.532	1.630	1.488	4.09×10^{-4}
Hilbert Transform	2.150	1.656	1.464	2.23×10^{-4}

5.6 CONCLUSIONS

A model for the index and absorbance, which could be used to generate spectra for immersion fluids with a high index and low absorbance at 193 nm, was developed. For this model, a method to calculate the absorbance spectrum for a typical immersion fluid is needed. Oscillator models provide a description of the dispersion of an electronic transition. A variety of oscillator models were studied to determine which model best fits the absorbance behavior of decalin, a fluid with a high index and low absorbance at 193 nm. The fit to the absorbance edge is most important in the model since the absorbance should increase sharply at wavelengths just less than 193 nm to provide the highest possible index, according to anomalous dispersion. Gaussian peaks provide the best-fit to the sharp absorbance edge of decalin, a fluid with a high index and low absorbance at 193 nm. The index can be calculated from the absorbance using the Kramers-Kronig integral relations. While a number of analytical and numerical solutions exist to solve the Kramers-Kronig integrals, the Hilbert transform solution method provides the best-fit to the index of decalin. Since the Kramers-Kronig integral is integrated over the entire energy range (0, ∞) and data from zero to infinity cannot be obtained, an additional fitting parameter is needed to account for the contribution of data outside the measured or calculated range (ε_{offset}). Thus, in addition to fitting the Gaussian peak parameters, an ε_{offset} fitting parameter is also used.

Using the Gaussian oscillator model and Hilbert transform solution method, index and absorbance spectra can be generated to model the optical characteristics of a typical immersion fluid. An additional program is needed to iteratively vary the parameters of the Gaussian peaks and identify spectra that are both physically realistic and provide the target index and absorbance at 193 nm. These spectra can then be used in the development of immersion fluid candidates.

5.7 REFERENCES

1. Nussenzveig, H. M., *Causality and dispersion relations.* 1972, New York: Academic Press. pp. 435.

2. Peiponen, K.-E., Vartianinen, E. M. and Asakura, T., Dispersion, *Complex Analysis and Optical Spectroscopy.* 1999, New York: Springer. pp. 130.

3. Korff, S. A. and Breit, G., *Optical Dispersion.* Rev. Mod. Phys., 1932. **4**(3): p. 471-504.

4. Kramers, H. A., *La diffusion de la luniere par les atoms.* Atti Cong. Intern. Fisica, 1927. **2**: p. 545-557.

5. Kronig, R. d. L., *The theory of dispersion of x-rays.* J. Opt. Soc. Am., 1926. **12**: p. 547-57.

6. Nitsche, R. and Fritz, T., *Determination of model-free Kramers-Kronig consistent optical constants of thin absorbing films from just one spectral measurement: application to organic semiconductors.* Phys. Rev. B: Condens. Matter, 2004. **70**(19): p. 195432/1-195432/14.

7. King, F. W., *Efficient numerical approach to the evaluation of Kramers-Kronig transforms.* J. Opt. Soc. Am. B: Opt. Phys., 2002. **19**(10): p. 2427-2436.

8. Turro, N. J., *Modern Molecular Photochemistry.* 1978, Menlo Park: The Benjamin/Cummings Publishing Company, Inc. pp. 628.

9. Yadav, L. D. S., *Organic Spectroscopy.* 2005, Boston: Kluwer Academic Publishers. pp. 324.

10. Wooten, F., *Optical Properties of Solids.* 1972, New York: Academic Press. pp. 260.

11. Djurisic, A. B. and Li, E. H., *Modeling the index of refraction of insulating solids with a modified Lorentz oscillator model.* Appl. Opt., 1998. **37**(22): p. 5291-5297.

12. Jellison, G. E., Jr. and Modine, F. A., *Parameterization of the optical functions of amorphous materials in the interband region.* Appl. Phys. Lett., 1996. **69**(3): p. 371-373.

13. Jellison, G. E., Jr. and Modine, F. A., *Parameterization of the optical functions of amorphous materials in the interband region. [Erratum to document cited in CA125:207104].* Appl. Phys. Lett., 1996. **69**(14): p. 2137.

14. Ohta, K. and Ishida, H., *Comparison among several numerical integration methods for Kramers-Kronig transformation.* Appl. Spectrosc., 1988. **42**(6): p. 952-7.

15. Lucarini, V., Saarinen,J.J., Peiponen,K.-E. and Vartiainen,E.M., *Kramers-Kronig Relations in Optical Materials Research.* 2005, Germany: Springer. pp. 160.

16. Weideman, J. A. C., *Computing the Hilbert Transform on the Real Line. Mathematics of Computation,* 1995. **64**(210): p. 745-762.

Chapter 6: Immersion Fluid Modeling Program and Simulation Results

In Chapter 5, the development of a model for the optical properties of an immersion fluid was described. Using Gaussian peaks to model the absorbance and the Hilbert transform to solve the Kramers-Kronig integrals and calculate the index, the optical properties of an immersion fluid can be modeled. To use this model to identify index and absorbance spectra with a high index and low absorbance at 193 nm, a program was written to iteratively vary the Gaussian peak parameters and then calculate the index from the Gaussian spectrum using the Hilbert transform. A simulated annealing optimization technique was used to identify spectra with the best fit to a target spectrum or target index and absorbance values. The simulated annealing program and initial results obtained with the program will be discussed.

6.1 MODELING PROGRAM

To determine the location and size of the absorbance peaks that would provide a high index and low absorbance at 193 nm, a MATLAB program was written to develop absorption spectra using the Gaussian oscillator model (GOM). The index was calculated from these Gaussian peaks with the Hilbert transform function, provided with the Signal Processing Toolbox (Version 6.5) in MATLAB R2006a. The GOM peak parameters were then iteratively varied to minimize the error between the model and target index and absorbance.

6.1.1 Simulated Annealing

Optimizing the GOM peaks to identify the spectrum with the lowest error, or global minimum configuration, is challenging. Each Gaussian peak is defined by three parameters. For a spectrum with multiple Gaussian peaks, the number of parameters can become quite large. Simulated annealing is an optimization technique used to identify the global minimum of a function with many dependent variables[1] and was developed from an analogy with the mechanism of metal cooling and annealing. If a molten metal is cooled slowly, the atoms are able to line up in an ordered state to form a pure crystal at the lowest energy state for the system. By contrast, if the metal is cooled quickly, it is more likely to reach an amorphous or polycrystalline state at a higher energy.[1] The Boltzmann probability distribution describes the distribution of energy states (E) that exist for a system at a given temperature (T) by

$$P(E) \propto \exp(\frac{-E}{k_b T}) \tag{6.1}$$

where k_b is Boltzmann's constant. Even at a low temperature, there is some probability of a system "getting stuck" in a high energy state and obtaining a local energy minimum rather than the global minimum energy state.[1, 2]

Metropolis developed an algorithm using the principles of annealing.[3] At each step of the algorithm, the system is changed slightly, and the resulting energy change (ΔE) is calculated. If $\Delta E \leq 0$, the change is accepted, and the new system configuration is used as the starting point for the next step of the algorithm. For $\Delta E > 0$, a probability of acceptance ($P(\Delta E)$) is calculated using Boltzmann's equation (Equation 6.1). A random number in the interval (0, 1) is generated and compared to $P(\Delta E)$. If the random number is less than $P(\Delta E)$, the new configuration is accepted; if not, the original configuration is used to start the next step.[1-3] With this Metropolis algorithm, the system avoids getting "stuck" in a local energy minimum since moves to higher energy states can be accepted based on the probability distribution.[3] To obtain the optimal annealing rate, or rate of acceptance, and avoid local energy minima, the temperature can also be increased or decreased. The rate of acceptance is checked at specified intervals. If the rate of acceptance is lower than a specified target, the temperature is increased to increase P(ΔE), and if the rate of acceptance is higher than the target, the temperature is decreased to decrease P(ΔE).

6.1.2 Immersion Fluid Model Optimization

For the immersion fluid modeling program, the "energy" to be minimized is an equation for the error between the target and calculated index (n) and absorbance (k) at 193 nm and 589 nm. The error is calculated as

$$\begin{aligned} Error = & \left(\frac{n_{193,calc} - n_{193,target}}{n_{193,target}} \right)^2 + \left(\frac{n_{589,calc} - n_{589,target}}{n_{589,target}} \right)^2 + \left(\frac{n_{589,calc} - n_{589,target}}{n_{589,target}} \right)^2 \\ & + \left| k_{589,calc} - k_{589,target} \right| . \end{aligned} \quad (6.2)$$

The k_{589} term differs from the rest of the terms since $k_{589,target} = 0$. This error value is minimized by varying the Gaussian peak parameters according to the Metropolis annealing schedule. ΔE, described in the Metropolis annealing schedule, is the difference between the error of the trial configuration and current configuration. Configurations that provide negative values of ΔE are always accepted; positive values of ΔE are accepted based on the probability of acceptance, described in Section 6.1.1.

To define new configurations, the Gaussian peak parameters were varied using random numbers in the interval (0, 1). First, each parameter was assigned an interval between 0 and 1. If a random number (R1) is within this interval, then that parameter would be varied. For example, for four parameters (A, B, C, and D), A is varied for $0 < R1 < 0.25$, B varied for $0.25 < R1 < 0.5$, C varied for $0.5 < R1 < 0.75$, and D varied for $0.75 < R1 < 1$. The amount of variation in each parameter is determined by a second random number (R2) within the interval (0, 1). The value of the new parameter (P_{trial}) is limited to values between a previously specified maximum (P_{max}) and minimum (P_{min}) value, calculated by

$$P_{trial} = R2 \cdot (P_{\max} - P_{\min}) + P_{\min} \, . \tag{6.3}$$

This trial parameter replaces the original parameter to create a new configuration (A, B, C, D becomes A, B, C_{trial}, D, for example). The error (Equation 6.2) is then calculated using the index and absorbance from the trial spectrum, and the trial is accepted or rejected based on the Metropolis annealing schedule. The simulated annealing code was written in MATLAB R2006a by Saul Lee. This code is given in Appendix C, C.2.

6.2 PROGRAM DEMONSTRATION

The simulated annealing program was used to vary absorbance spectra composed of three Gaussian peaks and obtain spectra corresponding to three different target index and absorbance values (given in Table 6.1). Each of the Gaussian peak parameters was varied between a minimum and maximum value, given in Table 6.2, to solve the Gaussian equation (Equation 5.18). This range of peak parameters was chosen so that a spectrum with peaks of increasing energies and sizes could be obtained, if necessary. The lowest energy (E_n) value was also limited to help exclude peaks that would result in a strong absorbance at 193 nm. These ranges allow three different target index values (1.65 – 2.00) to be obtained. The spectra with the minimum error (according to Equation 6.2), obtained after 100,000 iterations, for each of the target values are given in Figure 6.1. The peak parameters used in these spectra are given in Table 6.2.

Table 6.1: Target index and absorption coefficient values at 193 nm and 589 nm

	n_{193}	n_{589}	α_{193} (cm^{-1})	k_{193}	α_{589} (cm^{-1})	k_{589}
Spectrum A	1.65	1.48	0.01	$3.54\text{x}10^{-8}$	0	0
Spectrum B	1.80	1.50	0.01	$3.54\text{x}10^{-8}$	0	0
Spectrum C	2.00	1.58	0.01	$3.54\text{x}10^{-8}$	0	0

Table 6.2: Gaussian peak parameters used to generate spectra

Parameter	**Minimum**	**Maximum**	**Spectrum A**	**Spectrum B**	**Spectrum C**
E_{offset}	1.8	2.5	2.194	2.254	2.495
An_1	2	5	3.481	3.733	4.975
En_1	6.5	8	7.863	6.976	7.275
Brn_1	0.1	0.22	0.166	0.128	0.204
An_2	1.6	5	3.524	4.425	4.980
En_2	8	10	9.498	8.313	8.000
Brn_2	0.15	2	0.363	0.150	0.243
An_3	3	7	3.000	6.038	6.902
En_3	10	12	11.915	11.877	10.013
Brn_3	0.1	3	1.330	1.289	0.760

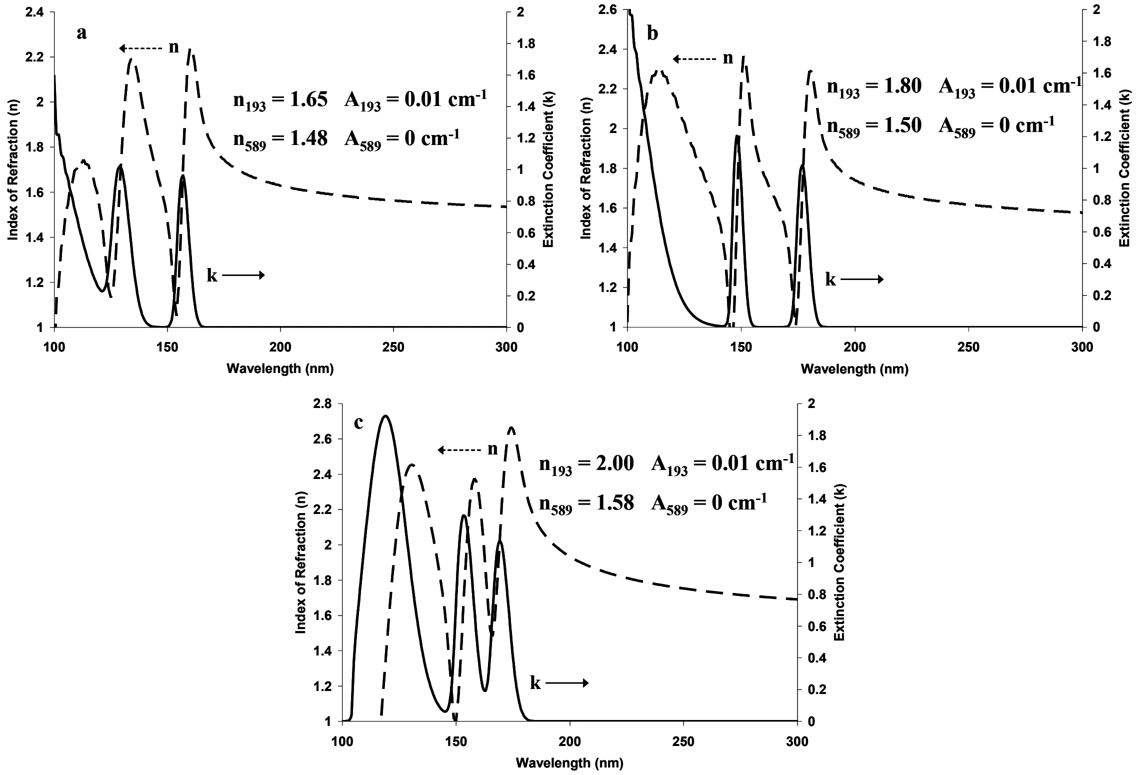

Figure 6.1: Examples of index and absorbance spectra generated with the immersion fluid modeling program

Using this immersion fluid modeling program, a variety of spectra corresponding to a range of index values can be generated with only three Gaussian peaks. Within this range of peak parameters, these absorbance spectra are not the only solution to provide the target index and absorbance values. Initially, these peak parameters were chosen somewhat arbitrarily simply to obtain the target index and absorbance. However, since many peak configurations exist to obtain the target values, constraints are needed to limit the program to physically realistic solutions.

6.3 WATER

To try to develop constraints for the immersion fluid modeling program, literature data for the index and absorbance of water were used as a guide for the selection of peak parameter ranges. These data are available from 10 nm to 1349 nm in the Handbook of Optical Constants of Solids II,[4] and are shown in Figure 6.2.

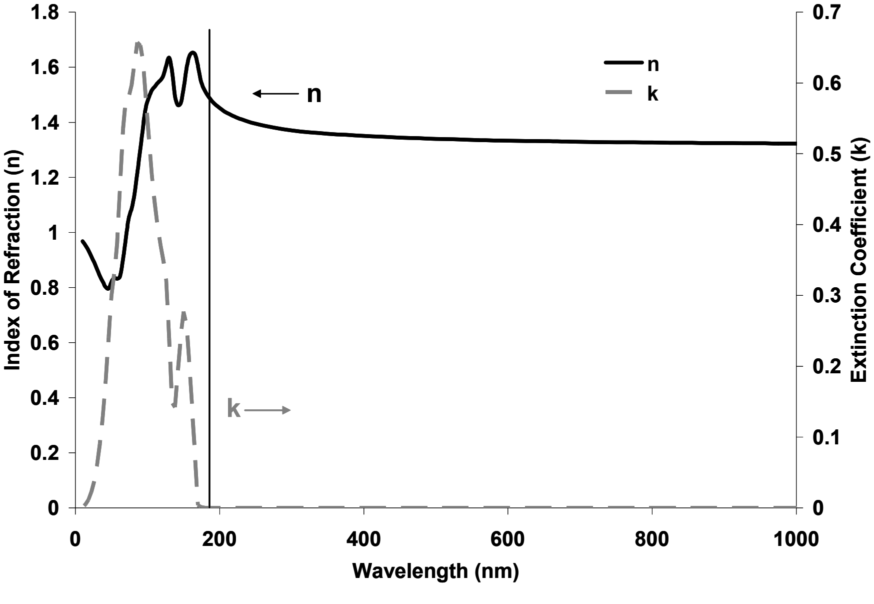

Figure 6.2: Handbook of Optical Constants index and absorbance of water[4]

In the example spectra given in Figure 6.1, high energy peaks (< 100 nm) were not calculated. Without the contribution of these peaks to the spectrum, the three calculated absorbance peaks could be overestimated, with greater amplitudes or broadening, to compensate for the lack of high energy peaks. While the $\varepsilon_{\text{offset}}$ fitting parameter should help to account for the contribution of peaks outside the calculated range, constraints on the size of the peaks are still needed if the spectra are to be used to identify fluids with the target properties. The wide range of data available for water should help to develop constraints for the peak parameters and avoid this overestimation.

First, ten Gaussian peaks were fit manually to the absorbance data for water. These peaks and their summation to fit the water spectrum are given in Figure 6.3. The five absorbance peaks in Figure 6.3 with $E_n > 12.4$ eV (100 nm) were inserted into the model spectrum as fixed peaks and were not adjusted during the simulation. These fixed peaks were included to provide a constant contribution to the spectrum from the higher energy transitions. The parameters of these fixed peaks are given in Table 6.3. While the spectrum shown in Figure 6.3 has five peaks with $E_n < 12.4$ eV, three adjustable absorbance peaks were used in the immersion fluid modeling program to try to simplify the solution set.

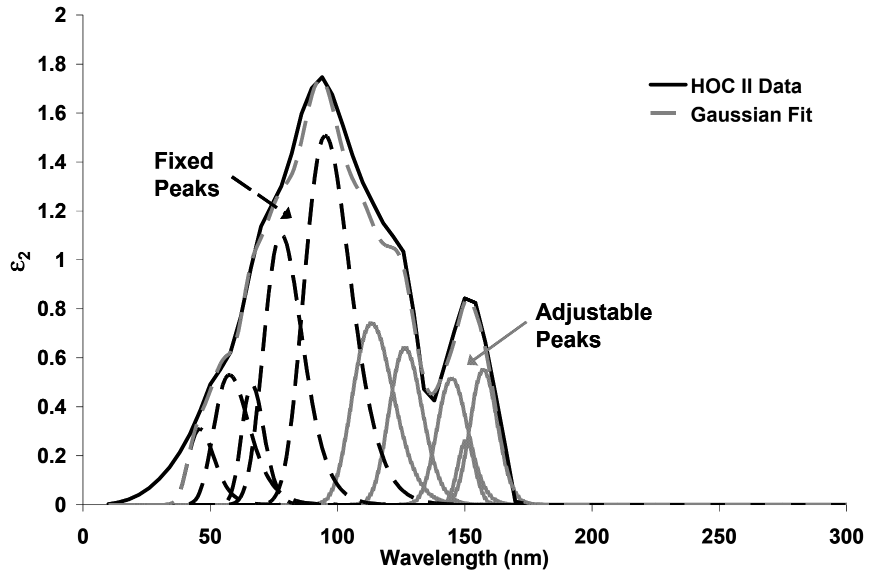

Figure 6.3: Gaussian peaks fit to the Handbook of Optical Constants absorbance (ε_2) data for water

Table 6.3: Fixed Gaussian parameters for Handbook of Optical Constants water data

n	**1**	**2**	**3**	**4**	**5**
A_n	1.508	1.105	0.491	0.531	0.310
E_n (eV)	13.015	15.906	18.649	21.527	27.010
Br_n (eV)	1.742	2.170	1.715	3.592	4.174

In addition to holding the high energy peaks constant, additional constraints were added to the immersion fluid modeling program to obtain the best fit to the Handbook of Optical Constants data for water. Since the high energy (fixed) peaks should provide the maximum absorbance in the spectrum, each of the trial spectra were evaluated prior to acceptance to ensure that the maximum absorbance (or ε_2) value occurred due to the high energy peaks (i.e. $\lambda_{max} < 100$ nm). Trial spectra that did not meet this criterion were rejected. The MATLAB sub-routine written to identify the wavelength of maximum absorbance (λ_{max}) and provide an acceptance or rejection decision is given in Appendix

C, C.3. Additionally, to further limit the number of possible solutions, the differences in the location and size of each of the peaks were also evaluated prior to acceptance. With this constraint, only peaks of increasing size with decreasing wavelength were accepted for simulated annealing evaluation. A minimum separation between each E_n value was also specified to prevent the acceptance of trial solutions in which the peaks could converge into one large peak. The MATLAB sub-routine written to restrict the peak shapes and positions is given in Appendix C, C.3. This peak shape and position constraint could likely be achieved by limiting the peak ranges as well.

Multiple trials of 100,000 iterations each were completed to identify the spectra with the lowest error between the target and calculated index and absorbance at 193 nm. Of these trials, the spectrum with the best fit to the Handbook of Optical Constants data for water is given in Figure 6.4. The peak parameter ranges and final, lowest-error peak parameters that provide the spectrum in Figure 6.4 (including the fixed peak parameters given in Table 6.3) are given in Table 6.4. Using the literature data for the absorbance of water as a guide, constraints for the immersion fluid model have been developed. With these constraints, target absorbance spectra of water can be developed.

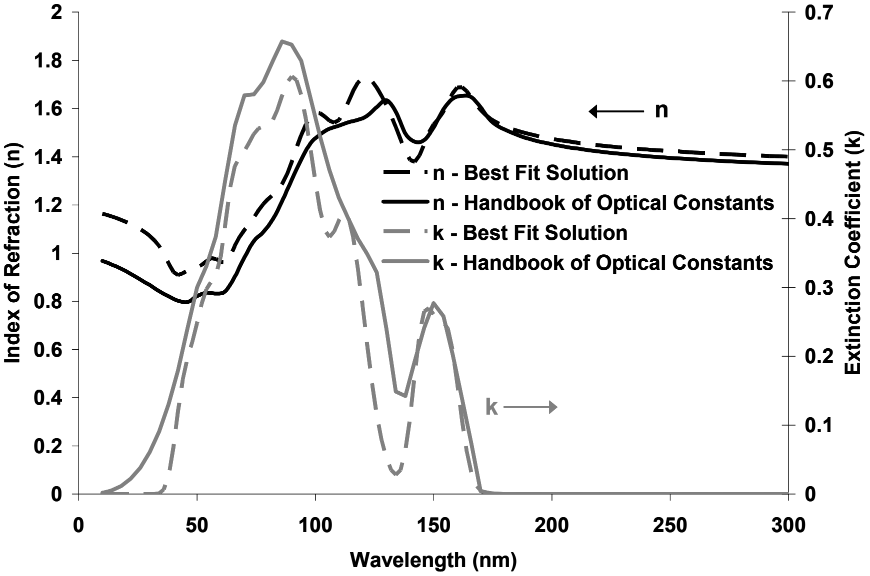

Figure 6.4: Best fit spectra for the Handbook of Optical Constants data for water

Table 6.4: Gaussian peak parameter ranges and best-fit values for water

Parameter	**Minimum**	**Maximum**	**Water**
E_{offset}	1	1.8	1.791
An_1	0.2	0.7	0.563
En_1	7.5	8	7.881
Brn_1	0.3	0.7	0.306
An_2	0.35	0.8	0.777
En_2	8	9.5	8.425
Brn_2	0.401	1	0.440
An_3	0.51	1	0.993
En_3	9.5	11	10.738
Brn_3	0.71	1	0.853

6.4 SATURATED HYDROCARBONS

The immersion fluid modeling program was further evaluated using theoretical absorbance spectra for the saturated hydrocarbons since saturated hydrocarbons have a high index and low absorbance at 193 nm. These spectra were used to guide the solutions obtained with the immersion fluid modeling program and further evaluate the constraints needed in the program.

6.4.1 Spartan Absorbance Spectra

The theoretical absorbance data for the saturated hydrocarbons were obtained using Spartan ’06 by Wavefunction, Inc. These calculations were performed with density functional theory (DFT) calculations using the three-parameter Becke style (B3LYP) hybrid functional, commonly used with organic molecules.[5] This method has been used previously to calculate the VUV absorbance spectra of organic molecules for 157 nm lithography photoresist development.[6, 7] Geometry optimization was first performed for each structure using DFT with the 6-311G* basis set. Following the geometry optimization, the electronic transitions and oscillator strengths were calculated with DFT-B3LYP using the 6-311+G** basis set.

The absorbance spectrum output provided by Spartan ‘06 is a series of discrete electronic transitions and oscillator strengths. The calculated electronic transitions and oscillator strengths for n-hexane, cyclohexane, and *trans*-decalin are shown in Figure 6.5. For n-hexane, 188 electronic transitions were calculated from 103 – 164 nm; for cyclohexane, 210 electronic transitions from 100 – 173 nm, and for *trans*-decalin, 69 electronic transitions from 139 – 184 nm. The number of electronic transitions was specified prior to starting the calculation. If too many electronic transitions were requested, the program ran out of memory and terminated prior to completion. These electronic transitions are the maximum number that could be calculated and likely do not represent the full absorbance spectrum for each of these fluids. However, these simulated spectra can still provide target spectra to guide the development of the immersion fluid modeling program.

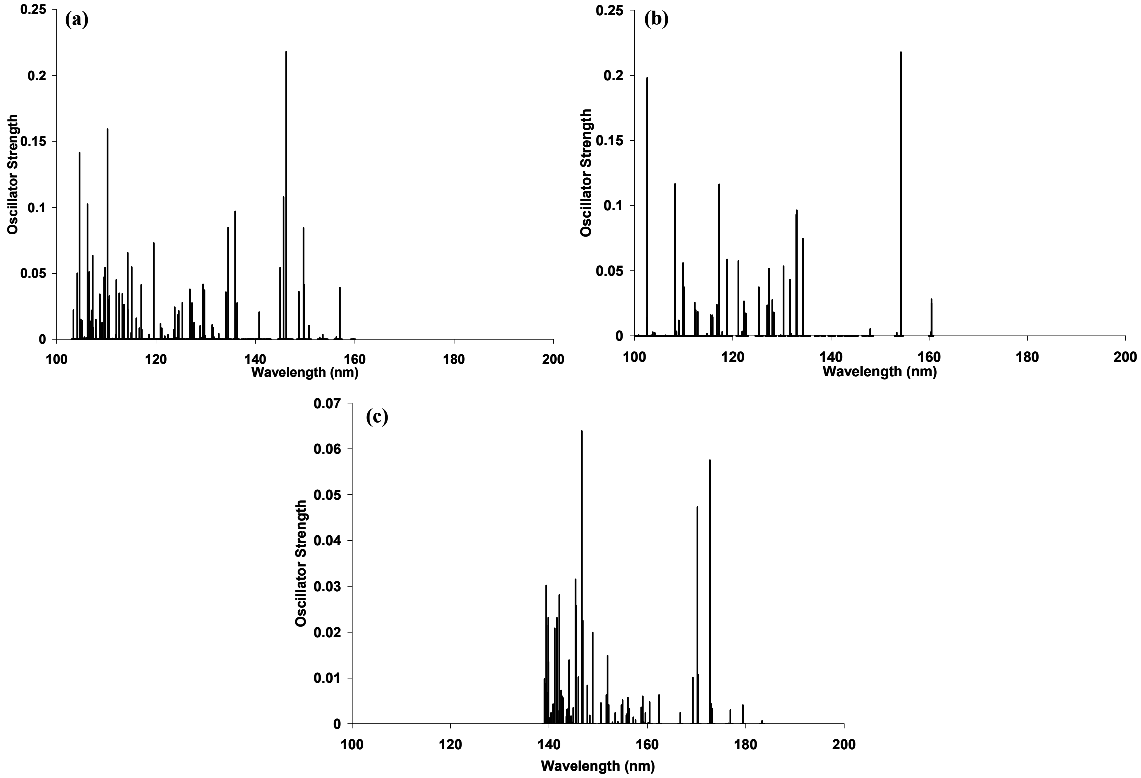

Figure 6.5: Oscillator strength data for n-hexane (a), cyclohexane (b), and *trans*-decalin (c) calculated with DFT using Spartan '06

The discrete, delta function transitions, shown in Figure 6.5, need to be broadened to provide an absorbance spectrum. Therefore, each oscillator strength value was multiplied by the Gaussian function to provide Gaussian broadening. For each Gaussian peak, the parameter E_n is given by the energy of the electronic transition, and the broadening (Br_n) and amplitude (A_n) parameters were determined by comparison to the experimental absorbance data obtained for that hydrocarbon. The same Br_n and A_n were applied to each oscillator to generate the absorbance spectrum. This approximation greatly reduces the number of spectra that can be generated with the Spartan data. To further improve the fit, an ε_{offset} value was calculated by fitting to the experimental data for the index at 193 nm and 589 nm.

The broadening, amplitude, and $\varepsilon_{\text{offset}}$ which provide the spectrum with the lowest error when fit to the experimental data for each hydrocarbon are given in Table 6.5. The broadened Spartan spectra fit to the experimental absorbance data for n-hexane, cyclohexane, and *trans*-decalin are shown in Figure 6.6.

Table 6.5: Gaussian peak parameters used to broaden the Spartan oscillator spectra

	A_n	Br_n	$\varepsilon_{\text{offset}}$	**Error***
n-Hexane	5	0.25	1.862	$4.03\text{x}10^{-5}$
Cyclohexane	7	0.27	1.972	$7.02\text{x}10^{-6}$
***trans*-Decalin**	35	0.08	2.123	$9.53\text{x}10^{-7}$

*Sum of the squared error between the experimental and calculated index at 193 nm and 589 nm

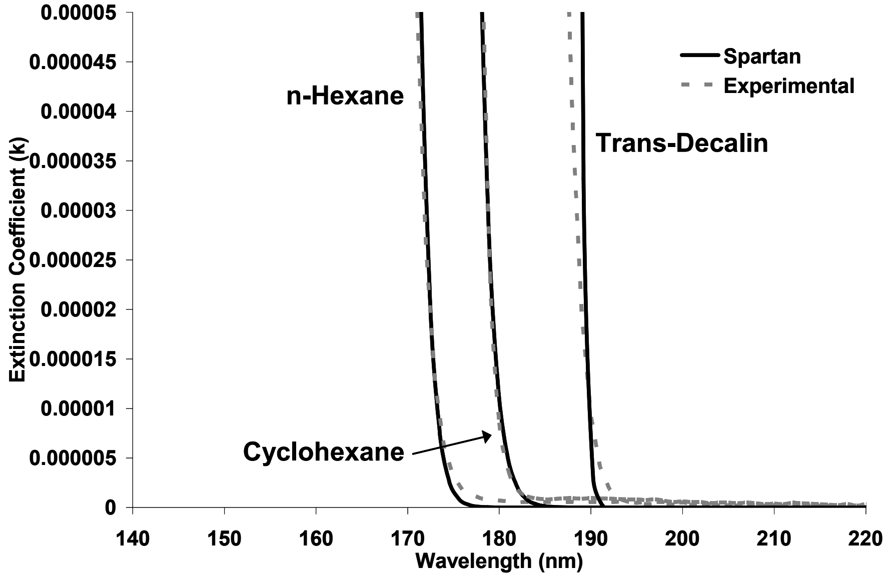

Figure 6.6: Broadened Spartan ’06 absorbance fit to experimental absorbance

6.4.2 Modeling Results with Spartan Absorbance Data

The immersion fluid modeling program was used to generate the broadened Spartan oscillator spectra for n-hexane, cyclohexane, and *trans*-decalin. Instead of applying the program constraints developed with the Handbook of Optical Constants data for water, the peak parameter ranges were specified to guide the selection of the desired spectra. Since the program constraints restrict the solutions to certain peak parameters, further limiting the peak parameters should provide equivalent limits to the solution set. As described previously, the peak parameters were varied to generate target index and absorbance values at 193 nm and 589 nm.

For n-hexane, four Gaussian peaks were used to obtain the spectrum. The best-fit solution to the n-hexane spectrum, following multiple trials of 100,000 iterations, is shown in Figure 6.7. The Gaussian peak parameter ranges for n-hexane and final best-fit parameters are given in Table 6.6. For cyclohexane, five Gaussian peaks were used, and the best-fit parameters are given in Figure 6.8. The Gaussian peak ranges and final best-fit parameters are given in Table 6.7. For *trans*-decalin, four Gaussian peaks were used. The best-fit spectrum for *trans*-decalin is shown in Figure 6.9 with the peak ranges and best-fit parameters given in Table 6.8.

The immersion fluid modeling program can be used to generate spectra based on the Spartan '06 data for n-hexane, cyclohexane, and *trans*-decalin by fitting to target index and absorbance values at 193 nm and 589 nm. The model obtains spectra which closely match the Spartan '06 data after multiple 100,000 iteration trials with parameter ranges targeted to obtain the desired spectra. The fit could be improved by applying constraints to the program to further restrict the absorbance edge position, for example, or by adding target index and absorbance values at additional wavelengths to better fit the higher energy peaks ($\lambda < 193$ nm). The addition of target index and absorbance values at lower wavelengths would likely be the best method to help obtain the desired solution since all of the absorbance peaks occur at wavelengths less than 193 nm.

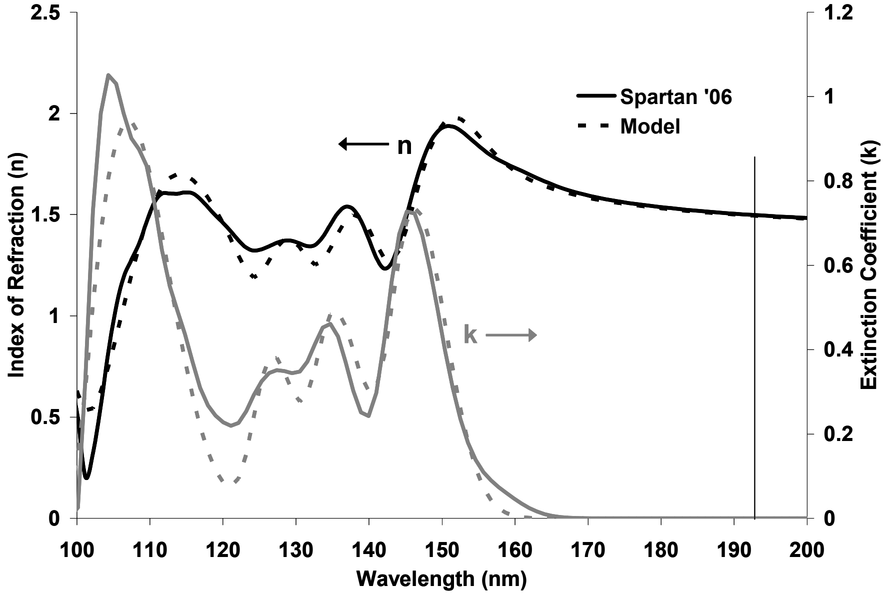

Figure 6.7: Model fit to Spartan '06 index and absorbance for n-hexane

Table 6.6: Gaussian peak ranges and best-fit parameters for n-hexane

Parameter	**Minimum**	**Maximum**	**n-Hexane**
E_{offset}	1.5	2	1.873
An_1	2.2	2.45	2.444
En_1	8.4	8.9	8.407
Brn_1	0.23	0.3	0.297
An_2	1	1.4	1.364
En_2	9.1	9.4	9.120
Brn_2	0.23	3	0.293
An_3	0.75	1	0.999
En_3	9.7	10	9.750
Brn_3	0.23	3	0.295
An_4	2.1	2.5	2.493
En_4	11.3	11.6	11.336
Brn_4	0.5	0.65	0.648

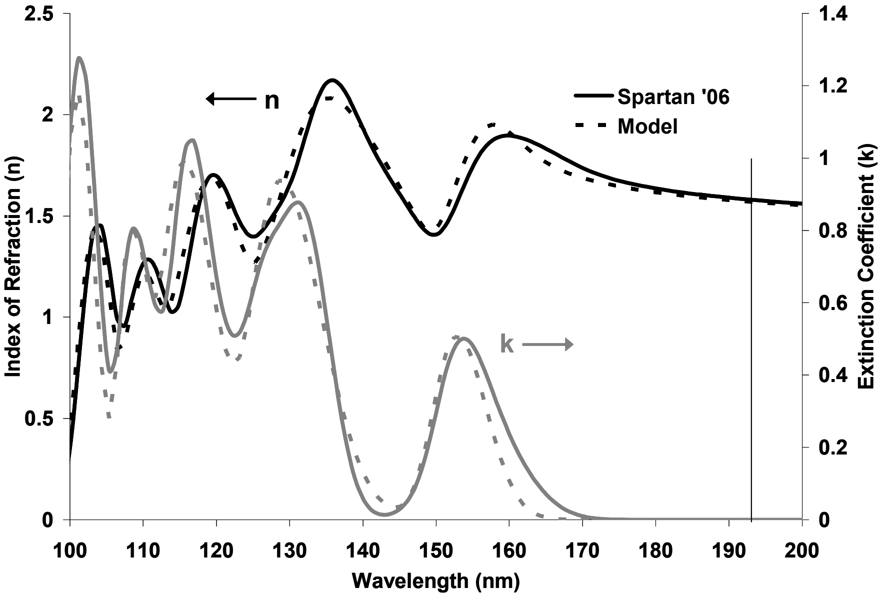

Figure 6.8: Model fit to Spartan '06 index and absorbance for cyclohexane

Table 6.7: Gaussian peak ranges and best-fit parameters for cyclohexane

Parameter	**Minimum**	**Maximum**	**Cyclohexane**
E_{offset}	1.5	2	1.982
An_1	1.6	2	1.749
En_1	7.7	8.1	8.068
Brn_1	0.25	0.35	0.263
An_2	3	3.3	3.252
En_2	9.2	9.6	9.499
Brn_2	0.45	0.6	0.470
An_3	2.8	3.2	2.871
En_3	10.3	10.7	10.610
Brn_3	0.4	0.5	0.406
An_4	1.6	1.9	1.726
En_4	11.25	11.4	11.368
Brn_4	0.25	0.3	0.286
An_5	2.5	3	2.644
En_5	11.9	12.2	12.134
Brn_5	0.25	3	0.262

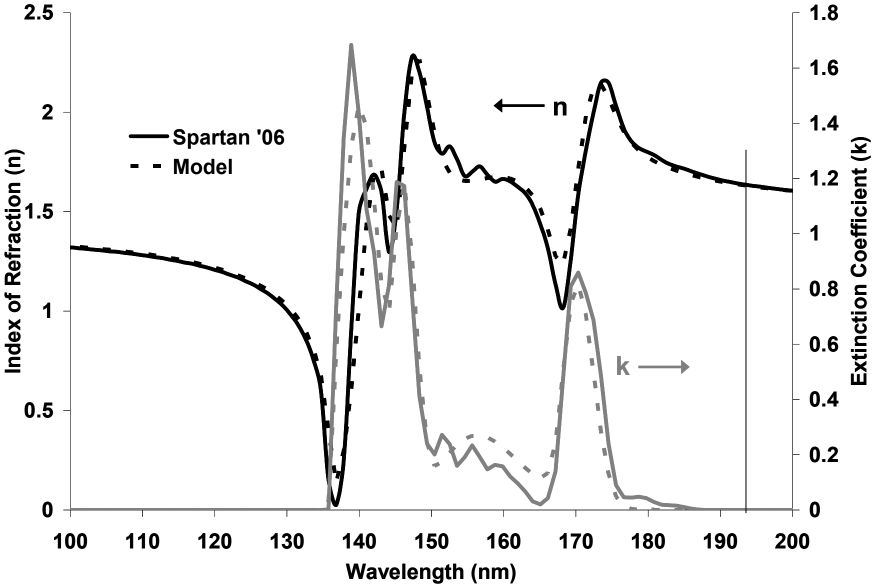

Figure 6.9: Model fit to Spartan '06 index and absorbance for *trans*-decalin

Table 6.8: Gaussian peak ranges and best-fit parameters for *trans*-decalin

Parameter	**Minimum**	**Maximum**	***trans*-Decalin**
E_{offset}	1.5	2.5	2.136
An_1	2.5	3	2.833
En_1	7	7.4	7.257
Brn_1	0.11	0.16	0.117
An_2	0.7	1	0.899
En_2	7.7	8.1	7.925
Brn_2	0.4	0.7	0.411
An_3	3.9	4.3	4.221
En_3	8.3	8.6	8.454
Brn_3	0.11	0.16	0.110
An_4	4	4.4	4.048
En_4	8.7	9	8.771
Brn_4	0.15	0.2	0.162

6.5 CONCLUSIONS

This simulated annealing program can be used with the immersion fluid model to vary the parameters of a Gaussian peak and develop absorbance spectra that provide target index and absorbance values. Using only three Gaussian peaks, a spectrum with an index as high as 2.00 at 193 nm has been developed with this program (see Figure 6.1). These spectra show that the highest index is provided with a sharp absorbance edge at 193 nm, as dictated by anomalous dispersion.

In addition to providing spectra with target index and absorbance values, the program can also generate absorbance spectra for both water and saturated hydrocarbons, providing the appropriate program constraints and peak parameter ranges are used. Since many different absorbance spectra solutions exist to provide the target optical properties, the application of program constraints and peak parameter ranges, defined from experimental or simulated absorbance data, are necessary to exclude solutions which are not physically realistic.

While the initial results obtained with the immersion fluid modeling program show that both target values and absorbance spectra can be obtained, additional work is necessary to further limit the number of possible solutions and develop a more rigorous program. This program could be improved by including additional high energy ionization peaks and setting a reasonable limit on the maximum absorbance value. Additional target index and absorbance values, at wavelengths both above and below 193 nm, could also be applied to further direct the solution.

Finally, a method to identify the chemical structures from the generated absorbance spectra is also needed. A solution to this “inverse problem” could be used to directly calculate the structures from the generated absorbance spectra, or oscillator strengths and electronic transitions. Alternatively, the generated absorbance spectra could be compared to a database of simulated or experimental absorbance data to identify structures with the target absorbance characteristics. Either of these methods could be used to rapidly identify high index and low absorbance immersion fluid candidates from absorbance spectra generated with the immersion fluid modeling program.

6.6 REFERENCES

1. Press, W. H., Teukolsky, S. A., Vetterling, W. T. and Flannery, B. P., *Numerical recipes: The art of scientific computing.* 3rd. 2007: Cambridge University Press. pp. 1235.

2. Kirkpatrick, S., Gelatt, C. D. and Vecchi, M. P., *Optimization by Simulated Annealing.* Science, 1983. **220**(4598): p. 671-680.

3. Metropolis, N., Rosenbluth, A. W., Rosenbluth, M. N., Teller, A. H. and Teller, E., *Equation-of-state calculations by fast computing machines.* J. Chem. Phys., 1953. **21**: p. 1087-92.

4. Querry, M. R., Wieliczka, D. M. and Segelstein, D. J., *Water (H2O).* Handbook of Optical Constants of Solids II, Palick, E. D. 1991, New York: Academic Press, Inc. pp. 1059 - 1077.

5. Young, D., *Computational Chemistry: A Practical Guide for Applying Techniques to Real World Problems.* 2001, New York: Wiley-Interscience. pp. 381.

6. Ando, S., Fujigaya, T. and Ueda, M., *DFT calculations of photoabsorption spectra in the VUV region for design of photoresist materials for 157 nm lithography.* J. Photopolym. Sci. Technol., 2002. **15**(4): p. 559-568.

7. Ando, S. and Ueda, M., *DFT calculations of photoabsorption spectra for alicyclic and heterocyclic compounds in the VUV region.* J. Photopolym. Sci. Technol., 2003. **16**(4): p. 537-544.

Chapter 7: Conclusions and Recommendations

Immersion lithography, with water as the immersion fluid, has been successfully implemented as the leading patterning technique to obtain 45 nm features using an exposure wavelength of 193 nm.[1] To increase the resolution that can be printed with this technology, fluids with an index of refraction higher than water are needed. In addition to a high index of refraction at 193 nm, these high index fluids should have a low absorbance at 193 nm and a low viscosity and high surface tension (approximately equal to water) to facilitate high scanning speeds.

7.1 METAL SALT ADDITIVES

Since immersion systems were designed for water, an aqueous high index fluid presents the most straightforward path to resolution enhancement. A systematic survey of ionic additives was completed to identify an aqueous solution with a high index of refraction and low absorbance at 193 nm. The salts studied included metal salts with halide anions, acids, sodium salts, and "micro-electronics friendly" quaternary ammonium salts. For all of these salts, the index of refraction increases with increasing salt concentration. However, this index increase is accompanied by an increase in absorbance. While many of these salts could provide a significant increase in the index of water at high concentration, high absorbance levels prohibit the use of these fluids in immersion lithography. In addition, it was observed that the optical properties of the solution depend more strongly on the anion than the cation since varying the metal cation produces only a small change in the index and absorbance.

The methylsulfonate anion has the highest index accompanied by the lowest absorbance of all the anions studied. This anion was paired with a trivalent lanthanum cation and added to water until the solution was saturated. Using cations of increased valency increases the amount of anion that can be added to the solution per mole of salt. The 2.82 M lanthanum methylsulfonate solution has an index of 1.58 and absorption coefficient of 0.314 cm^{-1} at 193 nm. This solution was used to generate 32 nm line and space images using interference lithography. Despite the demonstrated use of this fluid in immersion lithography, the high concentration of salt in this solution leads to a prohibitively high viscosity. The high viscosity would limit the scanning speed to < 100 mm/s (water scanning speed = 600 mm/s) and decrease throughput. Additionally, metal cations are not desirable in a clean room environment.

While higher salt concentrations might lead to the target index of 1.65 at 193 nm, the increase in viscosity and presence of heavy metal cation contaminants limit the usefulness of these fluids. Thus, even with increased purification, which might further decrease the absorbance of these fluids, these aqueous solutions are not viable options for next generation immersion lithography fluids.

7.2 SATURATED HYDROCARBONS

Since electronic transitions occur at high energies (< 200 nm) in saturated systems, saturated hydrocarbons were studied as potential immersion fluids. Due to the link between the index of refraction and absorbance, defined by the Kramers-Kronig relations, a high index of refraction is generally accompanied by a high absorbance. However, due to the phenomenon of anomalous dispersion, the index begins to increase at slightly higher wavelengths than the absorbance. Therefore, if a fluid with an absorbance edge at 193 nm can be identified, this fluid should have a high index without also having a high absorbance.

The VUV absorbance and index of a series of linear, cyclic, and complex polycyclic alkanes were measured. The absorbance edge of a saturated hydrocarbon fluid depends on the structure of the hydrocarbon. As the number of carbons in a linear or cyclic alkane increases, the absorbance edge shifts to longer wavelengths. Based on the comparison of the Rydberg term values in these hydrocarbons, the LUMO of these observed transitions is expected to be a Rydberg orbital. The energy of the LUMO is essentially constant with increasing carbon number while the energy of the HOMO is "destabilized" as electrons are added to fill higher energy orbitals. Thus, the HOMO-LUMO gap decreases as carbon number increases and red-shifts the absorbance edge. Additionally, the absorbance edge of highly strained hydrocarbon structures is red-shifted relative to structures with lower strain energy due to further "destabilization" of the HOMO with strain. Large polycycloalkanes ($> C_{10}$) provide a greater shift in the absorbance edge than the linear or monocyclic structures. As the absorbance edge shifts closer to 193 nm, the index also increases. Thus, these polycycloalkanes also have a greater index at 193 nm. The hydrocarbon with the highest index and lowest absorbance at 193 nm is decalin. Decalin has an index of 1.645 at 193 nm and absorbance edge of 191 nm.

Unfortunately, while a saturated hydrocarbon fluid (decalin) meets the optical property requirements for next generation immersion lithography, the physical properties of saturated hydrocarbons make the integration of these fluids in a high volume manufacturing process challenging. The absorbance of these hydrocarbons is very sensitive to impurities and the presence of dissolved oxygen. Stringent purification and de-oxygenation procedures are required to obtain high transparencies. These fluids also degrade upon exposure to UV light so that constant fluid recycle and purification is required. Additionally, these impurities can contaminate the lens; as a result, tool downtime for frequent lens cleanings is also necessary. The low surface tension of these fluids makes high scanning speeds, necessary for high throughput, difficult to obtain. Finally, the flammability of these fluids leads to safety concerns. If these technical challenges can be overcome, decalin can be used for second generation immersion lithography.

A saturated hydrocarbon with a higher index than decalin, and equivalent transparency at 193 nm, might exist. For example, additional purification of some of the hydrocarbon fluids that were rejected based on a strong absorbance at 193 nm, such as methyldinorbornane, decahydroguaiazulene, or tetradecahydromethylcyclopentadiene dimer, might lead to a higher index fluid candidate. Structural modifications to the fluids included in this study, to slightly red-shift the absorbance edge, might also provide a higher index. Addition of methyl groups to either decalin or bicyclohexyl should red-shift the absorbance edge towards 193 nm to increase the index without significantly increasing the absorbance. However, the 193 nm index target for a third generation immersion fluid is 1.8, and a hydrocarbon fluid is not likely to provide this index with a low absorbance.

Further study of the optical property trends observed in the alkane series could be completed by measuring the absorbance spectra of these alkane fluids through a shorter path length (< 1 mm). With a shorter path length, larger absorbance values can be measured, and the peak maximum and other features of the spectrum beyond the absorbance edge could potentially be identified. These data could be used to help establish the presence of Rydberg transitions and verify the theories presented for the origin of the trends in the absorbance edge with alkane size. High purity quartz cuvettes with a path length as low as 0.1 mm are available from Hellma Cells, Inc.

7.3 SATURATED HYDROCARBON SALT ADDITIVES

Salts with saturated hydrocarbon subgroups were synthesized in an attempt to develop a solution with the physical properties of water and the structure-dependent absorbance edge of the saturated hydrocarbons. Large hydrocarbons were incorporated in the anion using salts of metal cations, such as sodium or potassium, paired with sulfonate anions with large hydrocarbons, such as cyclohexane or adamantane, attached. Quaternary ammonium cations were paired with methylsulfonate anions and used to incorporate large hydrocarbons in the cation.

Unfortunately, the salts with the hydrocarbon incorporated in the anion behave as surfactants and form micelles at high concentration in water. Additionally, the salts have a strong absorbance, even at low concentration (< 0.1 M). While additional purification could decrease the absorbance of these solutions, bubble formation, since these salts are surfactants, would cause imaging defects. Quaternary ammonium methylsulfonate salts, however, provide the absorbance edge dependence on structure expected based on the saturated hydrocarbon fluids previously studied. As the number of carbons in the alkane on the quaternary ammonium cation increases, the absorbance edge red-shifts. The salt with the best high index and low absorbance combination at 193 nm is trimethylcyclohexylammonium methylsulfonate. When this salt is added to water until the solution is saturated (3.4 M), the index of the solution is 1.58 and absorption coefficient is 1.43 cm^{-1} at 193 nm. The feasibility of imaging with this solution was demonstrated using interference immersion lithography and a NA of 1.5 to generate 32 nm line and space images. However, due to the high salt concentration, the viscosity of this solution increases significantly over both the viscosity of water and decalin. The index of this solution also does not meet the target value of 1.65 at 193 nm.

Additional methylsulfonate salts, with decalin attached to the cation for example, could perhaps be added to water in lower concentration to reduce the viscosity without significantly decreasing the index or increasing the absorbance. Additional purification could also be used to potentially reduce the absorbance of these solutions. However, increasing the index to reach the target value (1.65), without increasing the viscosity, does not seem possible with these salt solutions. Thus, while these aqueous solutions are not flammable or sensitive to oxygen, the optical property targets cannot be achieved, and the viscosity and surface tension are not improved over the saturated hydrocarbons. These salt solutions would likely not be viable immersion fluid candidates.

7.4 IMMERSION FLUID MODELING

A model for the index and absorbance was designed using Gaussian peaks to develop an absorbance spectrum. A Gaussian oscillator provides the most accurate representation of the sharp absorbance edge of the hydrocarbon fluids when compared to alternative oscillator models, such as the Lorentzian. Since there is not an analytical solution to the Kramers-Kronig integrals for the Gaussian oscillator model, Kramers-Kronig solution methods were also studied. A Hilbert transform solution method coupled with an additional offset fitting parameter (ε_{offset}) to fit to the optical properties at 193 nm and 589 nm provides the best-fit to the experimental hydrocarbon data. This model for the index and absorbance can be used to generate absorbance spectra that provide the target optical properties at 193 nm.

A MATLAB program was written to iteratively vary the Gaussian peak parameters to generate absorbance spectra and solve the Kramers-Kronig integrals to calculate the index using the Hilbert transform method. Through a simulated annealing technique with Metropolis acceptance criteria, the absorbance spectrum with the best fit to a set of target optical properties can be identified. Simulation of absorbance spectra that correspond to water, n-hexane, cyclohexane, and *trans*-decalin was demonstrated. To correctly generate these spectra, constraints, such as the limitation of the peak ranges and addition of high energy transitions, must be applied to the program.

To further improve the performance of this program and limit the number of possible solutions, additional constraints are needed. First, experimental absorbance data for wavelengths < 190 nm, collected using short path lengths (< 1 mm), would help to provide realistic physical limits on the values of the peak parameters. Alternatively, simulated absorbance spectra, including high energy transitions, could also be used to guide the peak parameter limits. These constraints should be included so that only physically realistic absorbance spectra are generated as potential solutions.

Finally, this immersion fluid modeling program was developed to provide a rapid screening method for identification of fluids with the target optical properties. Therefore, a method to use the spectra generated with this program to solve the "inverse problem" and identify fluid candidates which provide these spectra should also be developed. The "inverse problem" could be solved in two ways. First, the generated spectra could be compared to a database of absorbance spectra (experimental or simulated) to identify structures with spectra similar to the generated spectra. The "inverse problem" could be more rigorously solved by calculating a chemical structure from the generated spectra. A rigorous solution method to calculate a chemical structure from a given absorbance spectrum does not exist and would be needed to implement this solution method.

7.5 FUTURE OF NEXT GENERATION IMMERSION LITHOGRAPHY

Some of the technical challenges related to the use of a saturated hydrocarbon fluid in next generation immersion lithography have been overcome. For example, lens contamination due to the formation of absorbing photoproducts in the hydrocarbon fluid has been decreased by addition of a small amount of water into the hydrocarbon. With this water-addition and active recycle, the necessity for lens cleaning decreases from three times per day to once a week.[2] High scanning speeds can also be obtained by developing fluid containment procedures which allow residual liquid to remain on the wafer during scanning.[2]

The development of high index lens materials, however, is an ongoing concern. Since the index of refraction of the quartz lens is 1.56 at 193 nm, increasing the fluid index to 1.65 necessitates the design of high index lens materials to enable the maximum increase in resolution. Lutetium-aluminum garnet (LuAG) has an index of 2.14 at 193 nm.[3, 4] While lab-scale samples of this material have been developed, target absorbance levels have not been reached. A large scale sample is also not yet available and is not likely to be available in time for the introduction of 32 nm technologies.[3]

The technology shift to immersion lithography with a saturated hydrocarbon fluid, such as decalin, from water immersion lithography provides only a 12% improvement in resolution.[5] While many of the technical challenges associated with second generation immersion lithography have been resolved, the lack of available lens material raises concerns about the introduction of this technology on pace with the industry roadmap to maintain Moore's Law. Additionally, overcoming the remaining challenges to provide a resolution increase of only 12% does not seem necessary if other technologies, such as double patterning, EUV, or imprint lithography, are available. Thus, in 2008, major tool suppliers Nikon and Canon decided not to continue to pursue the development of next generation immersion lithography tools.[2, 5] As a result, next generation immersion lithography will likely not be used.

7.6 REFERENCES

1. McCallum, M., Kameyama, M. and Owa, S., *Practical development and implementation of 193nm immersion lithography.* Micro. Eng., 2006. **83**(4-9): p. 640-642.

2. Sakai, K., Mori, S., Sakamoto, E., Iwasaki, Y., Yamashita, K., Hara, S.-i., Watanabe, Y. and Suzuki, A., *Progress of high-index immersion exposure system.* 5th International Symposium on Immersion Lithography Extensions, 2008. (Conference Presentation).

3. Rice, B. J., *High-index materials research key to extending immersion lithography.* Solid State Technol., 2008. **51**(2): p. 28-30, 32-33.

4. Zimmerman, P. A., van Peski, C., Rice, B., Byers, J., Turro, N. J., Lei, X., Gejo, J. L., Liberman, V., Palmacci, S., Rothschild, M., Whittaker, A., Blakey, I., Chen, L., Dargaville, B. and Liu, H., *Status of high-index materials for generation-three 193nm immersion lithography.* J. Photopolym. Sci. Technol., 2007. **20**(5): p. 643-650.

5. Owa, S. and Umatate, T., *High index lithography (HIL) progress and plans.* 2008 SEMATECH Litho Forum, 2008. (Conference Presentation).

Appendix A: Purification of Saturated Hydrocarbons

A.1 INTRODUCTION

Each hydrocarbon fluid received from commercial sources contains at least a small concentration of impurities. Even at low concentrations, these impurities contribute significantly to the absorbance at 193 nm. Because the impurity and quantity of impurity varies for each fluid, the purification method varies for each fluid. The procedure used to purify each fluid will be described. An overview of these methods is given in Chapter 3, 3.2.2. The details of each procedure will be given here. The structures of these fluids are given in Chapter 3, Table 3.1.

The correct procedure for each fluid was identified through testing various purification methods and measuring the resulting absorbance spectra on an HP 8452A Diode Array Spectrophotometer (UV-Vis) through a 10 mm path length. With this spectrometer, absorbance spectra were collected from 190 – 820 nm. After purification with the method that provided the lowest absorbance, the absorbance spectrum was collected in the VUV. VUV spectra, through both a 10 mm and 1 mm path, were collected with either an Acton VUV Spectrophotometer (150 – 250 nm) (Acton) or a combination of a modified Varian Cary 400 Spectrophotometer (180 – 200 nm) and a Shimadzu UV-2401 UV/Vis Spectrophotometer (200 – 250 nm) (Varian/Shimadzu).

A.2 LINEAR SATURATED HYDROCARBONS PURIFICATION

A.2.1 n-Pentane

n-Pentane [*Spectrophotometric Grade*, ≥99% (Acros Organics)] was purified with a sulfuric acid wash, using a 1:1 mixture of acid:hydrocarbon, stirred overnight. The mixture was separated, and the hydrocarbon was then de-oxygenated and tested. n-Pentane was also purified further in an inert environment by mixing the hydrocarbon with silica gel in an approximately 5:1 ratio (fluid:silica gel) and filtered. Additionally, the silica gel treatment was performed without an acid wash in an inert environment. The absorbance spectra following each of these purifications are given in Figure A.1. Since the sulfuric acid wash and de-oxygenation result in the lowest absorbance, the spectrum of this sample was measured in the VUV with the Acton and is given in Figure A.2.

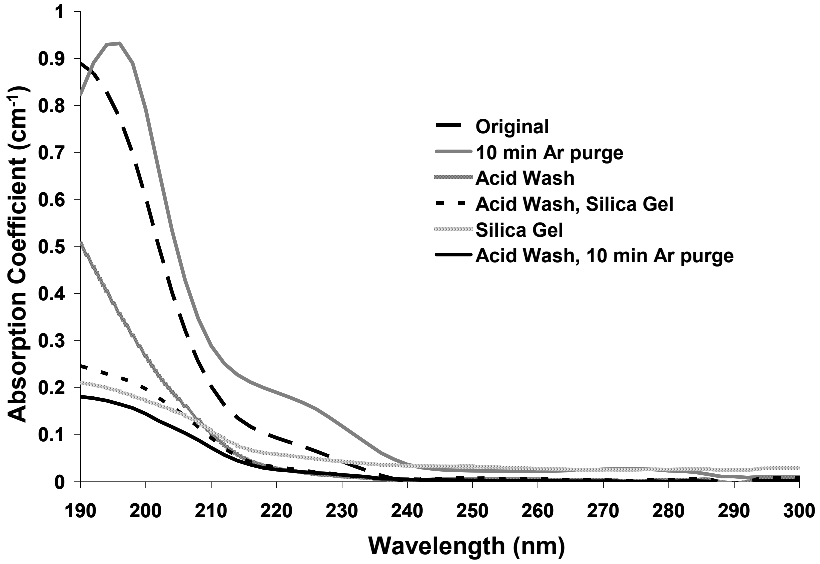

Figure A.1: UV-Vis absorbance spectra for n-pentane using various purifications

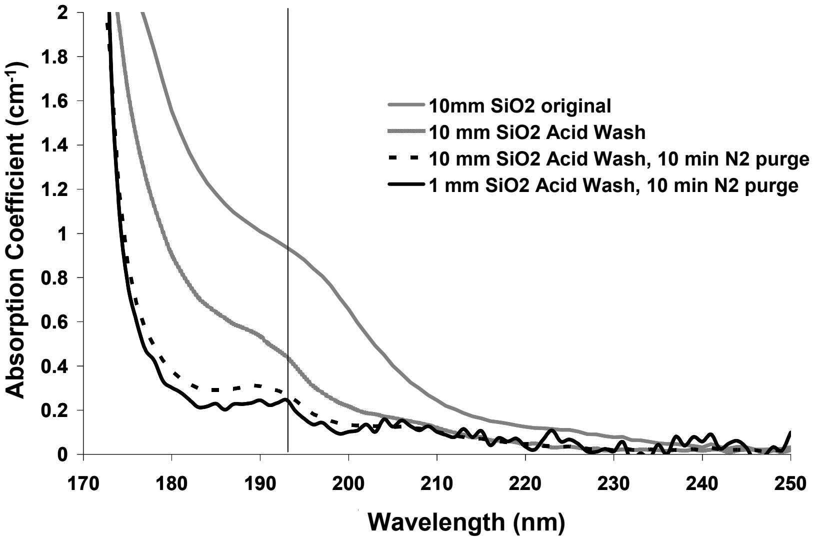

Figure A.2: VUV absorbance spectra of n-pentane after purification

A.2.2 n-Hexane

n-Hexane [*ReagentPlus,* ≥99% (Aldrich)] was purified using a sulfuric acid wash with a 1:1 mixture of acid:hydrocarbon. The mixture was separated, and the hydrocarbon layer was de-oxygenated. The spectrum of this sample was collected in the VUV using the Acton and is given in Figure A.3.

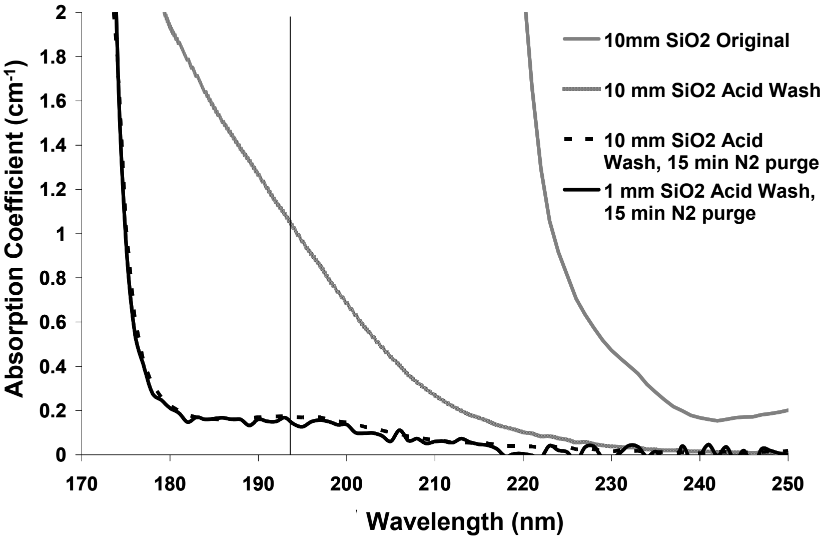

Figure A.3: VUV absorbance spectra for the acid wash and de-oxygenation of n-hexane

A.2.3 n-Heptane

n-Heptane [*HPLC*, ≥96% (Fisher Chemical)] was purified following the same procedure as n-pentane (given in A.2.1), except the purification with silica gel (without an acid wash) was not performed. The UV-Vis spectra are given in Figure A.4. The lowest absorbance was obtained with the acid wash and de-oxygenation procedure. The VUV absorbance spectra collected using the Acton are given in Figure A.5.

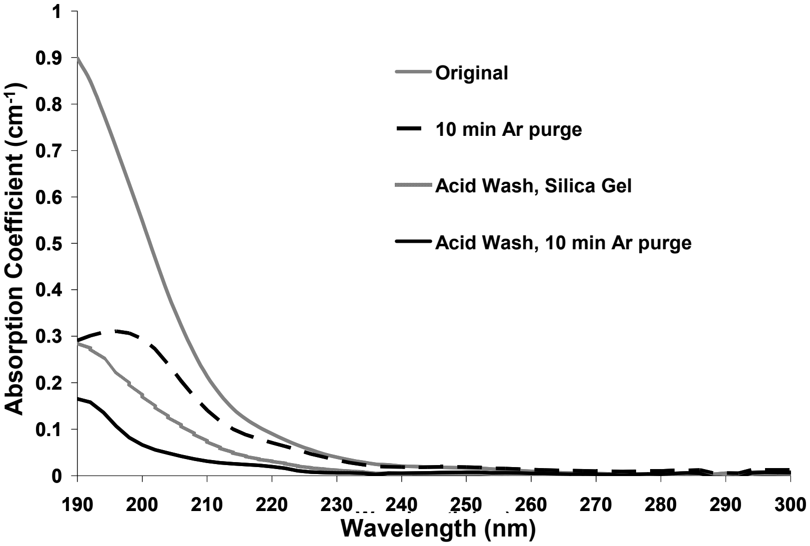

Figure A.4: UV-Vis absorbance spectra following the purification of n-heptane

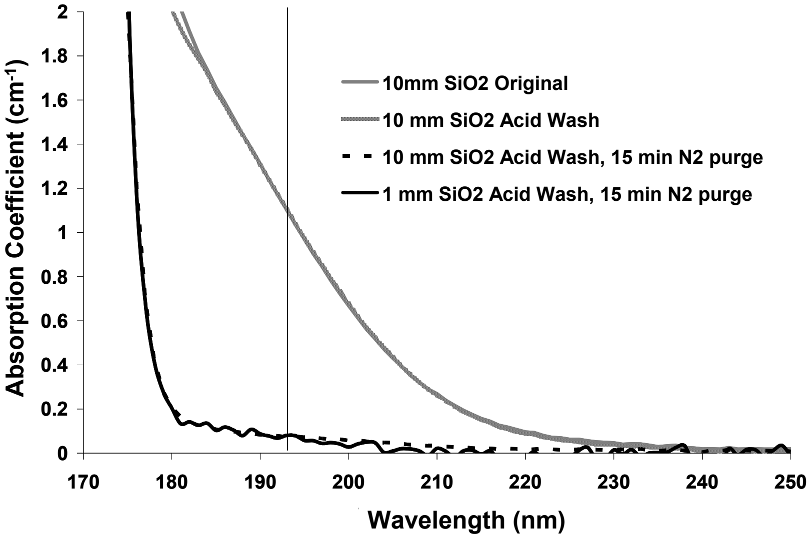

Figure A.5: VUV absorbance spectra after the acid wash and de-oxygenation of n-heptane

A.2.4 n-Octane

n-Octane [≥99% (Acros Organics)] was purified using the procedures described for n-pentane (A.2.1). The UV-Vis spectra for these purifications are given in Figure A.6. While the acid wash and de-oxygenation does not remove the residual absorbance at 193 nm, this purification results in the lowest absorbance of the purification methods studied. The VUV spectra for the sample purified using an acid wash and de-oxygenation was collected with the Acton and is given in Figure A.7.

An additional sample of n-octane [>98.5% (GC) (TCI America)] was purified in an attempt to remove the residual absorbance at 193 nm. This fluid was purified first with two sulfuric acid wash repetitions (2:1, acid:hydrocarbon), until the acid layer remained colorless after the procedure. The hydrocarbon layer was mixed with approximately 0.5 g of silica gel to remove any remaining acid in the hydrocarbon layer. These treatments were followed by a distillation under nitrogen. While the distillation increased the absorbance of the sample, an additional acid wash and de-oxygenation minimized the absorption at 193 nm. However, the decrease in absorption following the distillation could be due to a lower concentration of dissolved oxygen in the sample. The UV-Vis spectra following these purification steps are given in Figure A.8. The VUV spectrum of this sample was not obtained. Since the absorbance edge is defined as the wavelength at which $\alpha = 2\ \text{cm}^{-1}$, a low level residual absorbance should not result in an absorbance edge shift.

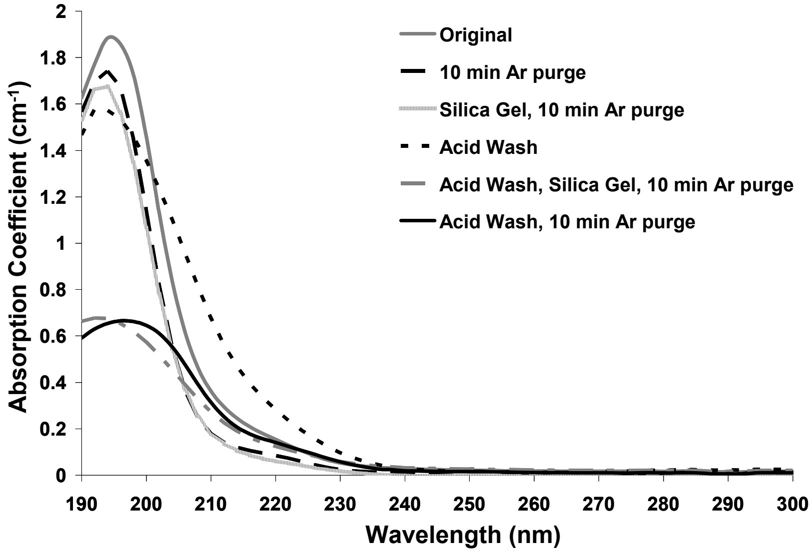

Figure A.6: UV-Vis absorbanc spectra following the purification of n-octane (Acros Organics)

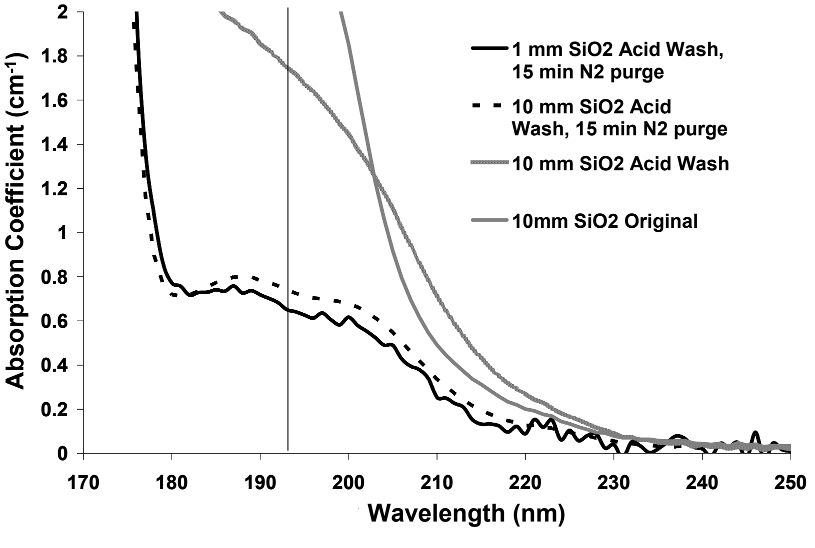

Figure A.7: VUV absorbance spectra following the acid wash and de-oxygenation of n-octane (Acros Organics)

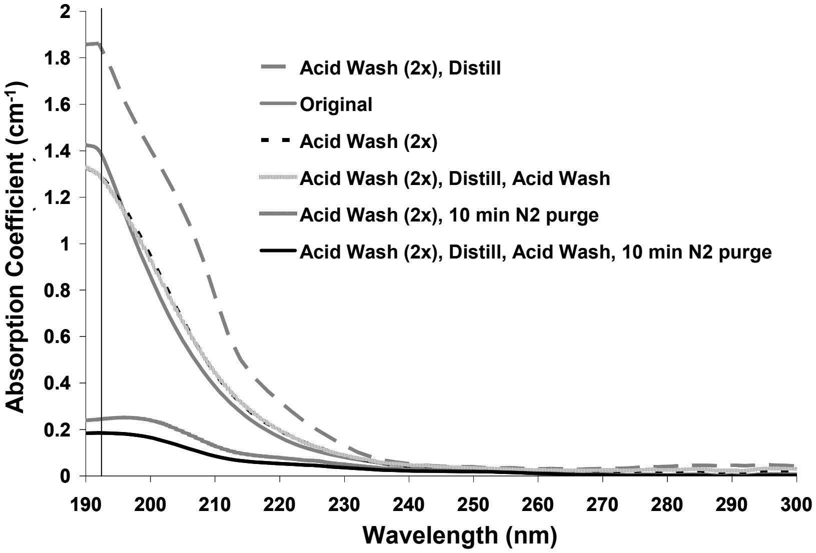

Figure A.8: UV-Vis absorbance spectra for purification of n-octane (TCI America)

A.2.5 n-Decane

n-Decane [≥99% (Acros Organics)] was purified with a sulfuric acid wash overnight using a 1:1 mixture of hydrocarbon:acid. The layers were separated, and the hydrocarbon was de-oxygenated. This purification procedure resulted in a low absorbance for n-decane; the UV-Vis spectra are given in Figure A.9. The VUV spectra, collected using the Acton, are given in Figure A.10.

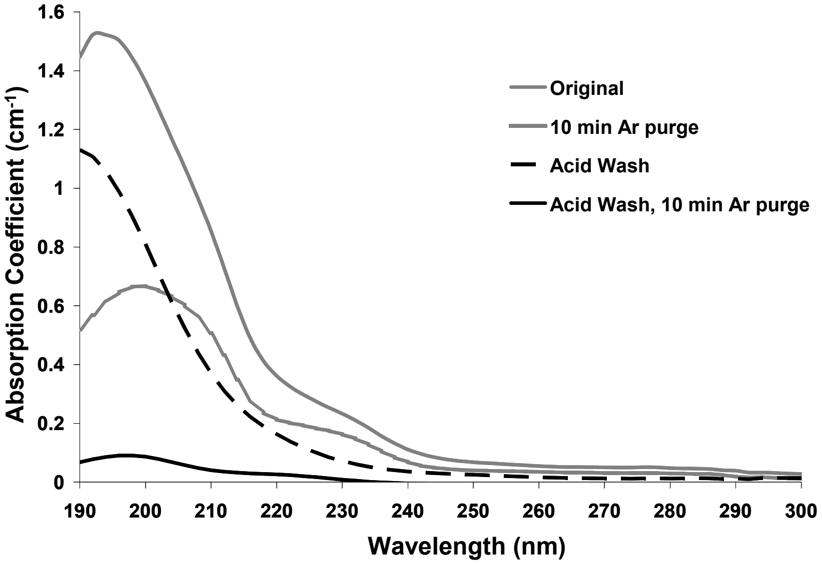

Figure A.9: UV-Vis spectra following the purification of n-decane

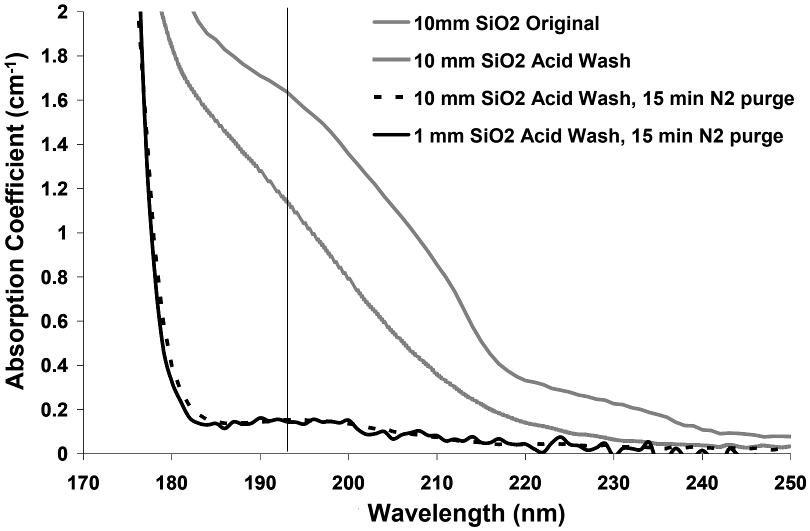

Figure A.10: VUV absorbance spectra after acid wash, de-oxygenation of n-decane

A.3 CYCLIC SATURATED HYDROCARBONS PURIFICATION

A.3.1 Cyclopentane

The purification of cyclopentane [*purum*, ≥98.5% (GC) (Fluka)] was attempted according to the same methods as n-heptane (A.2.3). The spectra resulting from these purifications are given in Figure A.11. The lowest absorbance is obtained following the acid wash and de-oxygenation. The VUV absorbance of this sample was measured on the Acton. These data are given in Figure A.12. The residual absorbance (<190 nm) was not detectable with the UV-Vis.

To remove the residual absorbance, an additional sample of cyclopentane [≥99% (Aldrich)] was purified. The purification procedure which resulted in the minimum absorbance included two repetitions of the acid wash and distillation procedure. The UV-Vis absorbance spectra following these purifications are given in Figure A.13. The hydrocarbon was mixed with sulfuric acid in a 1:2 (hydrocarbon:acid) ratio overnight. The acid layer was removed, and the hydrocarbon stirred with a small amount (< 1 g) of silica gel to remove any remaining acid. The hydrocarbon was then distilled. Repeating this procedure twice decreased the absorbance; however, the absorbance spectrum of cyclopentane < 190 nm purified with this method was not obtained so that a residual peak < 190 nm could still exist. However, this residual absorbance likely does not affect the absorbance edge since the absorbance decreases following the peak maximum at 187 nm and then increases sharply.

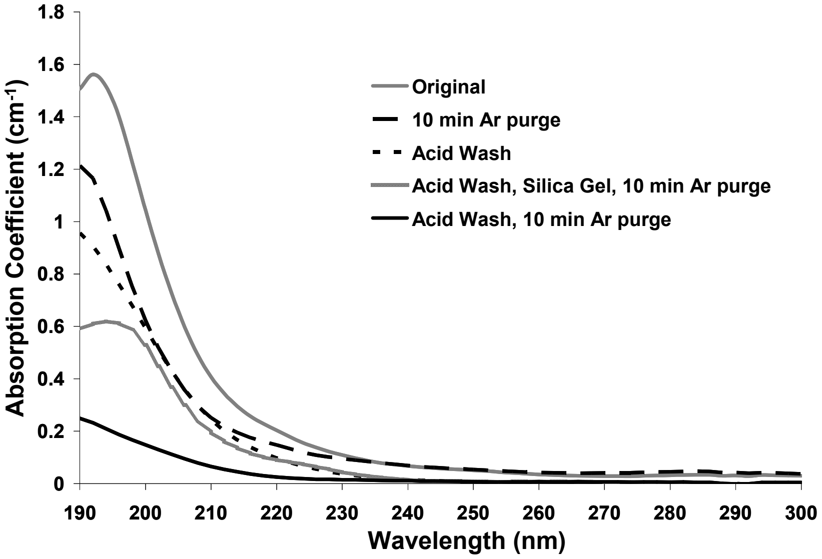

Figure A.11: UV-Vis absorbance spectra following the purification of cyclopentane (Fluka)

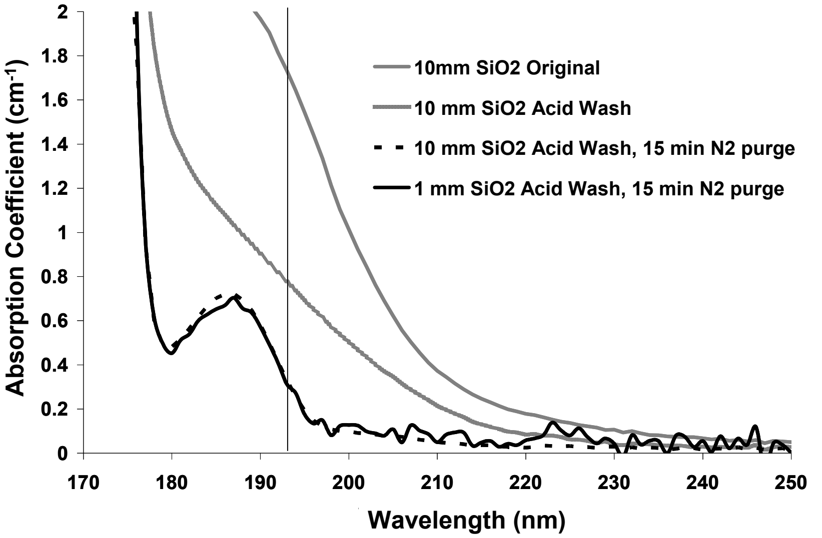

Figure A.12: VUV absorbance spectra after an acid wash and de-oxygenation of cyclopentane (Fluka)

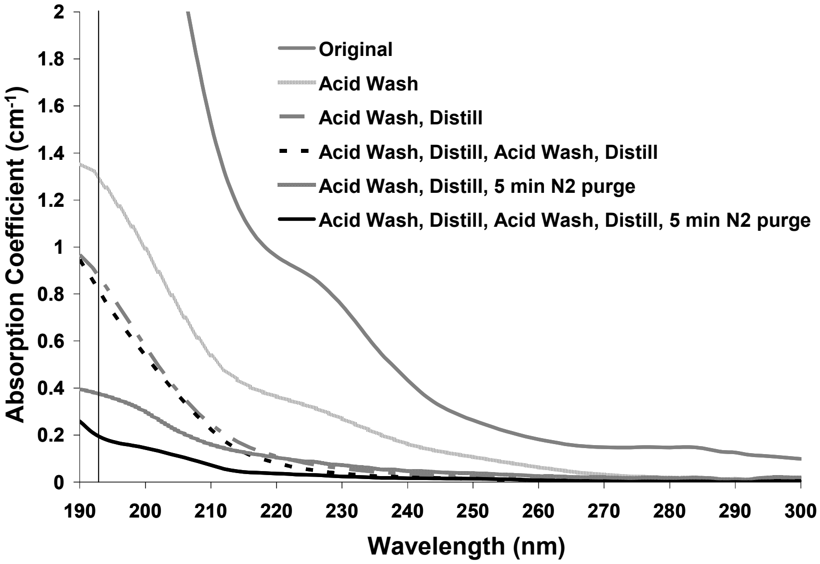

Figure A.13: UV-Vis spectra following the purification of cyclopentane (Aldrich) to remove the residual absorbance < 190 nm

A.3.2 Cyclohexane

Cyclohexane [≥99% (Acros Organics)] was purified with a sulfuric acid wash overnight using a 1:1 ratio of hydrocarbon:acid and de-oxygenated. The VUV absorbance spectra following these purifications are given in Figure A.14. The absorbance of this fluid can be further reduced by distilling the fluid after the acid wash and silica gel treatment steps. The UV-Vis spectra resulting from the additional purification are given in Figure A.15. Even though distilling the fluid reduces the absorbance at 193 nm, the absorbance edge is not likely affected by removing the residual absorbance.

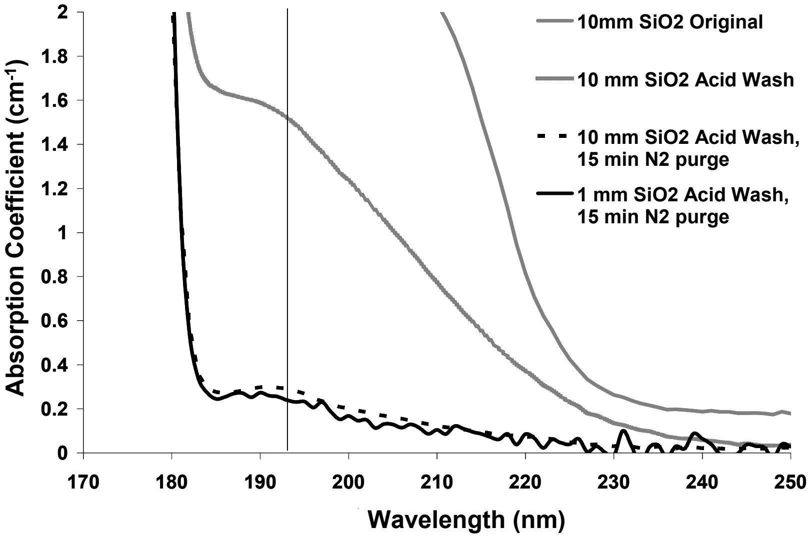

Figure A.14: VUV absorbance spectra following the acid wash and de-oxygenation of cyclohexane

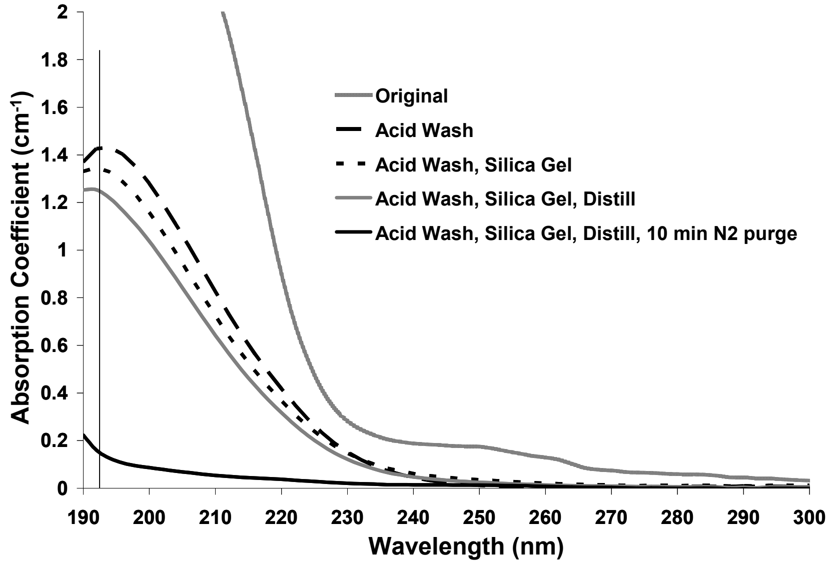

Figure A.15: UV-Vis absorbance spectra of cyclohexane including distillation

A.3.3 Cycloheptane

Cycloheptane [98% (Aldrich)] was purified using a combination of sulfuric acid washes, treatment with silica gel, and distillation. The fluid was first washed with sulfuric acid (2:1, acid:fluid) overnight. After the layers were separated, the hydrocarbon layer was mixed with a small amount (< 1 g) of silica gel to remove any residual acid prior to the distillation. The sample was then distilled under nitrogen. The fluid was washed with acid once more and treated with silica gel. This de-oxygenated sample yielded the lowest absorbance at 193 nm. The UV-Vis absorbance spectra for these purifications are given in Figure A.16.

Cycloheptane [>98% (GC) (TCI America)] was also purified using a Pasteur pipette column of activated silica gel and silver nitrate on silica gel. The fluid was passed through the column several times, until the absorbance was minimized, de-oxygenated, and tested. The VUV absorbance spectrum obtained using a 1 mm path length on the Varian/Shimadzu combination is given in Figure A.17.

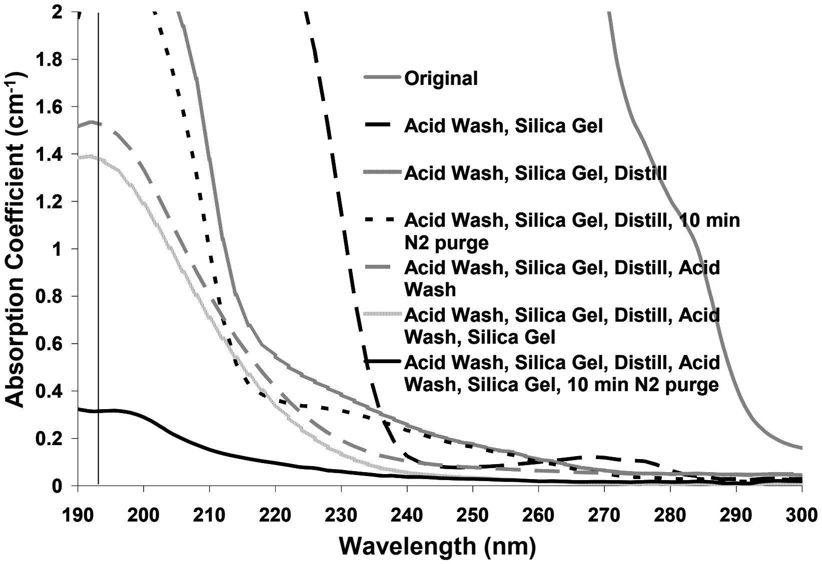

Figure A.16: UV-Vis spectra following the purification of cycloheptane (Aldrich)

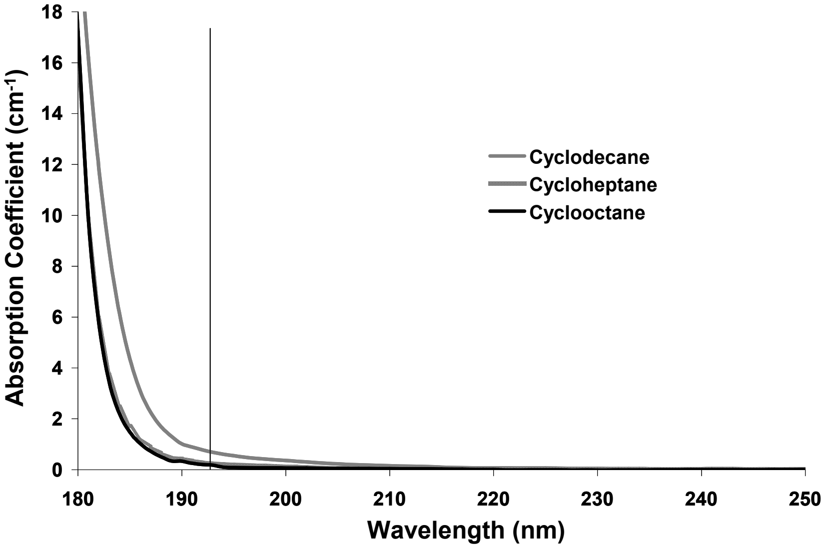

Figure A.17: VUV absorbance spectra collected in a 1 mm path for cycloheptane, cyclooctane, and cyclodecane

A.3.4 Cyclooctane

Cyclooctane [≥99% (Aldrich)] was purified using a method similar to that described for cycloheptane (Aldrich) (A.3.3). Cyclooctane was first washed with sulfuric acid (2:1, acid:hydrocarbon) overnight. The layers were separated, and the hydrocarbon layer was mixed with a small amount (< 1 g) of silica gel. The resulting fluid was then distilled at 95 ˚C (160 torr). This fraction was purified further with an additional sulfuric acid wash. After the layers were separated, the hydrocarbon layer was mixed with a small amount of silica gel. De-oxygenating this fluid resulted in the lowest absorbance measured. The UV-Vis absorbance spectra for these purification steps are given in Figure A.18.

Cyclooctane was also purified as cycloheptane (TCI America) (A.3.3). The VUV absorbance spectrum was obtained using a 1 mm path length on the Varian/Shimadzu. This spectrum is given in Figure A.17.

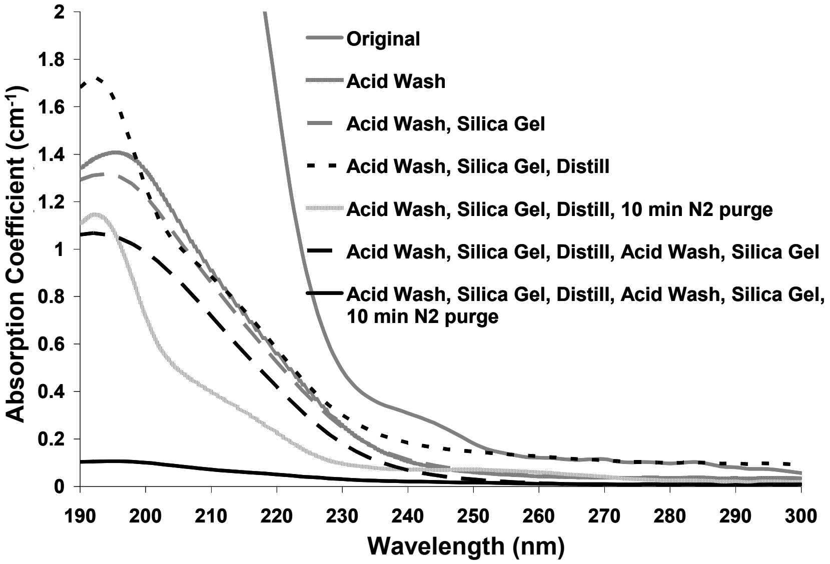

Figure A.18: UV-Vis absorbance spectra following the purification of cyclooctane

A.3.5 Cyclodecane

Cyclodecane [96+% (ChemSampCo, Inc.)] was purified according to the same procedure as cycloheptane (TCI America) (A.3.3). The VUV spectrum is given in Figure A.17. This spectrum was obtained using a 1 mm path length on the Varian/Shimadzu.

A.4 CYCLOHEXANE WITH LINEAR SUBSTITUENTS PURIFICATION

A.4.1 Methylcyclohexane

Methylcyclohexane [*ReagentPlus,* ≥99% (Sigma-Aldrich)] was purified with a distillation, sulfuric acid wash (1:1 acid:hydrocarbon, overnight), and de-oxygenation. The VUV spectra obtained using the Acton are given in Figure A.19.

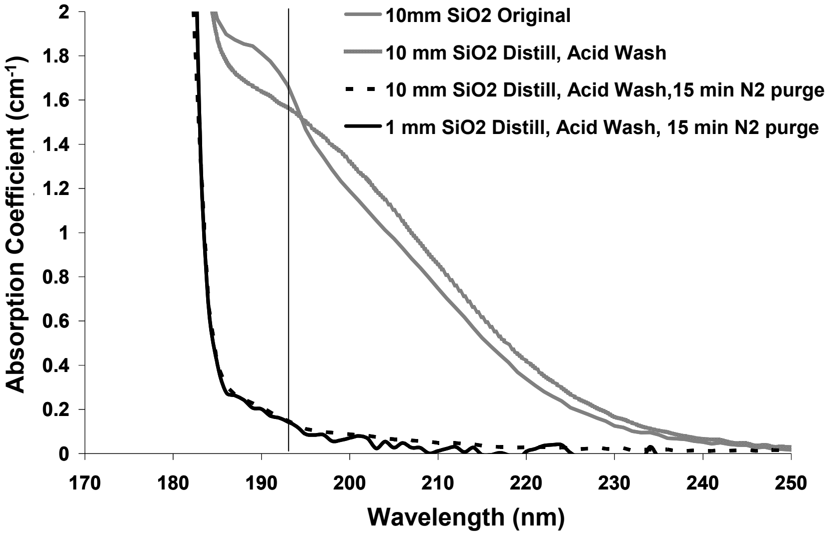

Figure A.19: VUV absorbance spectra following the purification of methylcyclohexane with a distillation, acid wash and de-oxygenation

A.4.2 Ethylcyclohexane

Ethylcyclohexane [≥99% (Acros Organics)] was purified with a sulfuric acid wash overnight (2:1, acid: hydrocarbon). This sample was then de-oxygenated, and the VUV absorbance spectrum was obtained with the Acton. This data is given in Figure A.20.

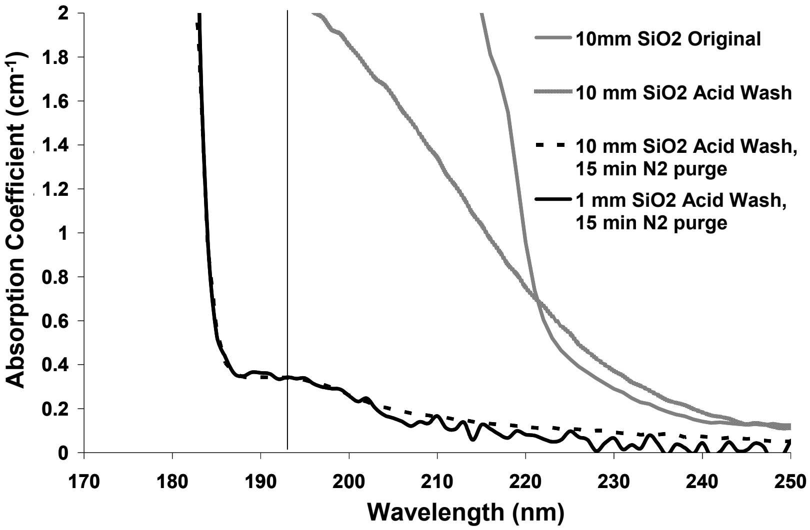

Figure A.20: VUV absorbance spectra following the purification of ethylcyclohexane with an acid wash and de-oxygenation

A.4.3 Propylcyclohexane

A combination of methods were attempted to minimize the absorbance of propylcyclohexane [>98% (GC) (TCI America)]. The lowest absorbance was obtained with a sulfuric acid wash (2:1, acid:fluid). After the mixture was separated, the hydrocarbon was mixed with silica gel (1:3, silica gel:fluid) in an inert environment, filtered, and de-oxygenated. The UV-Vis spectra of these purification steps are given in Figure A.21. The VUV spectra of propylcyclohexane collected with the Acton following these purifications steps are given in Figure A.22.

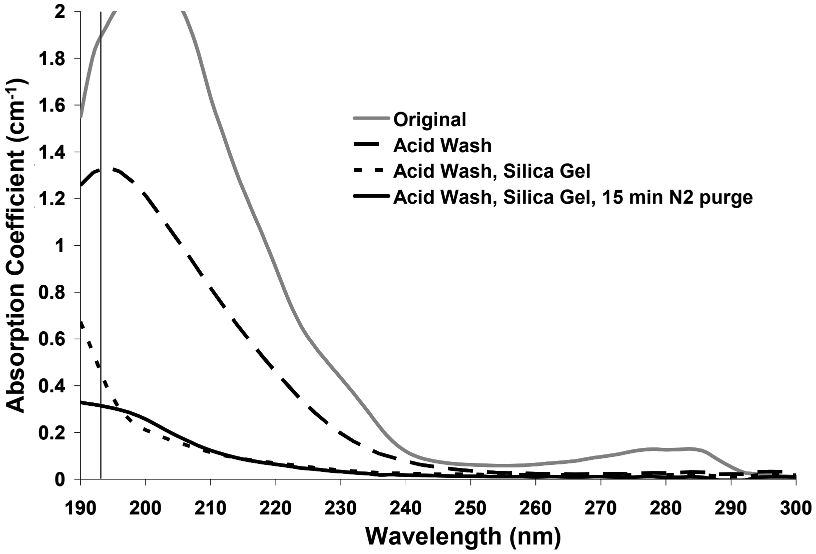

Figure A.21: UV-Vis absorbance spectra for the purification of propylcyclohexane

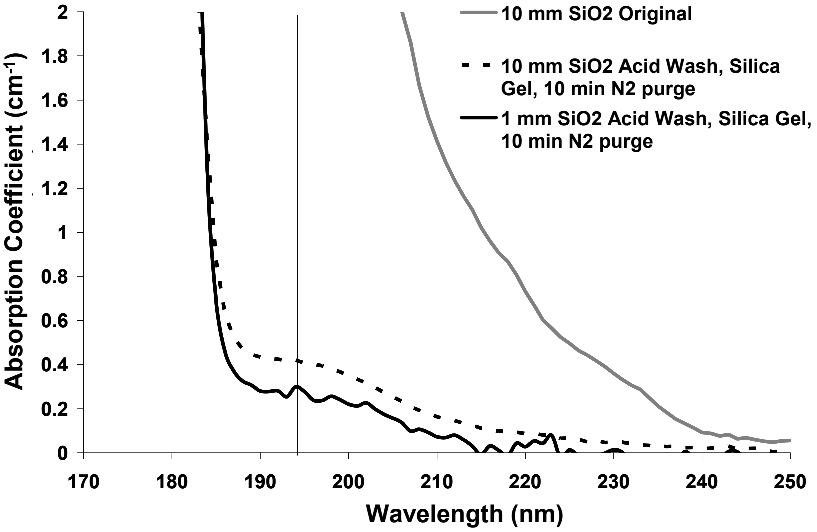

Figure A.22: VUV absorbance spectra for propylcyclohexane

A.4.4 Butylcyclohexane

The minimum absorbance for butylcyclohexane [≥99% (Aldrich)] was obtained using a sulfuric acid wash (2:1, acid:fluid) overnight and de-oxygenation. The UV-Vis spectra of these purifications are given in Figure A.23. The VUV absorbance spectra collected with the Acton are given in Figure A.24.

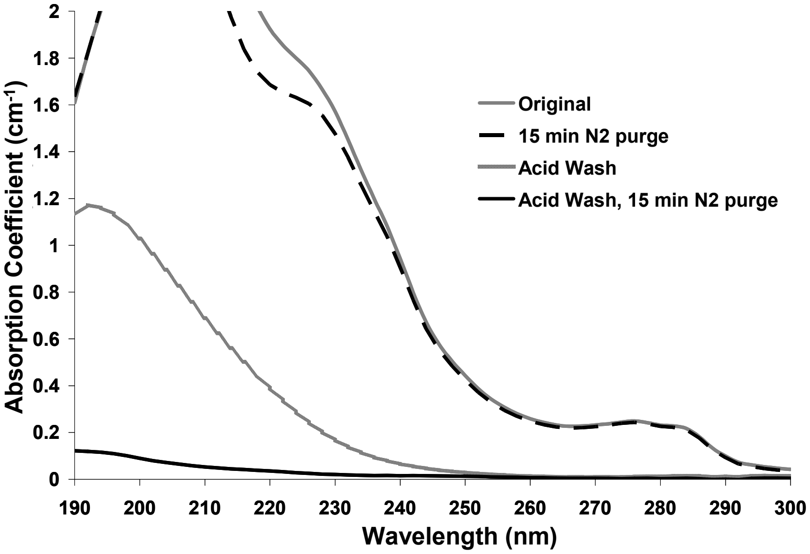

Figure A.23: UV-Vis absorbance spectra for the purification of butylcyclohexane with a sulfuric acid wash and de-oxygenation

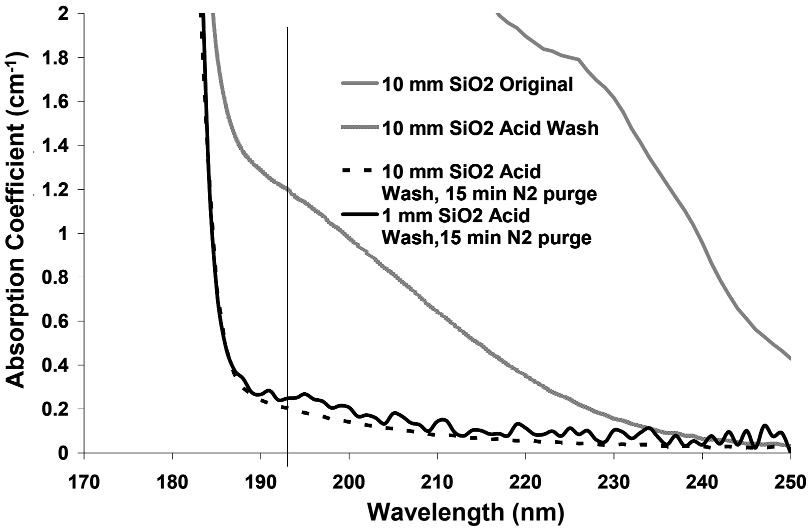

Figure A.24: VUV absorbance spectra following purification of butylcyclohexane

A.5 COMPLEX POLYCYCLIC ALKANES PURIFICATION

A.5.1 Decalin

Decalin [*cis* + *trans* mix, anhydrous, ≥99% (Sigma-Aldrich)] was purified using a silica gel treatment in an inert environment. Decalin was mixed with silica gel (5:1, hydrocarbon:silica gel) and filtered to remove the silica particles. The fluid was then de-oxygenated, and the absorbance was measured on the Acton. These data are given in Figure A.25. A sulfuric acid wash was also attempted to purify decalin, but this procedure increased the absorbance ($\alpha > 3$ cm^{-1}, 190 – 300 nm).

Decalin was also purified through a Pasteur pipette column of silica gel and silver nitrate on silica gel, repeating the procedure to obtain an absorbance minimum. The fluid was then de-oxygenated and tested on the Varian/Shimadzu in a 1 mm path length cell. The absorbance spectrum is given in Figure A.26.

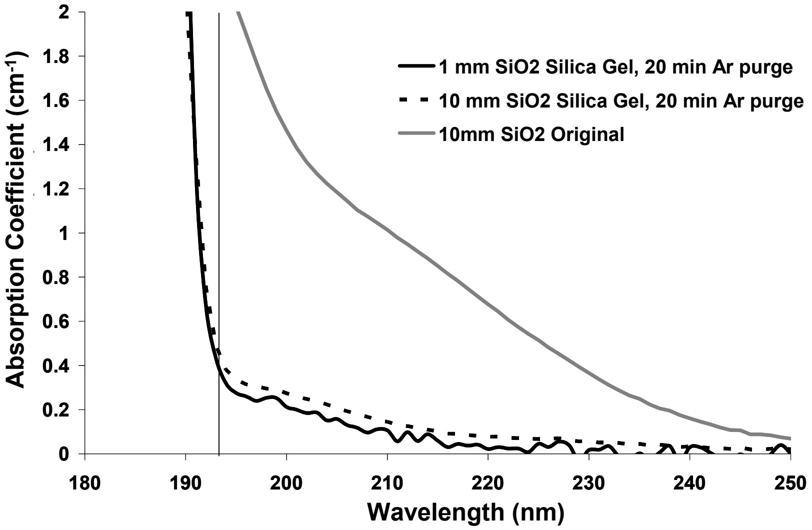

Figure A.25: VUV absorbance of decalin collected on the Acton

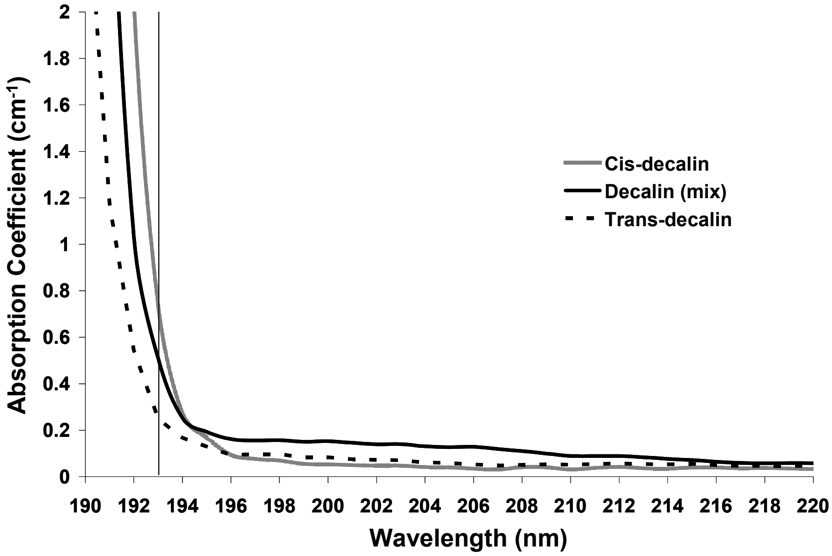

Figure A.26: VUV absorbance of decalin (mixture of *cis* and *trans*), *cis*-decalin, and *trans*-decalin collected on the Varian/Shimadzu

A.5.2 *cis*-Decalin

cis-Decalin [>98% (GC) (TCI America)] was purified by passing the fluid though a Pasteur pipette column of activated silica gel and silver nitrate on silica gel. This procedure was repeated until further purifications did not reduce the absorbance. Figure A.26 shows the absorbance spectrum obtained using a 1 mm path length on the Varian/Shimadzu combination.

A.5.3 *trans*-Decalin

trans-Decalin [>98% (GC) (TCI America)] was purified through the same procedure as *cis*-decalin (A.2.5). The absorbance spectrum was collected using a 1 mm path length on the Varian/Shimadzu combination and is given in Figure A.26.

A.5.4 Bicyclohexyl

Bicyclohexyl [*puriss.*, ≥99% (GC) (Fluka)] was initially purified using a sulfuric acid wash and de-oxygenation. The acid-washed fluid was also treated with silica gel (5:1, fluid:silica gel) in an inert environment and de-oxygenated. The UV-Vis absorbance spectra resulting from these purification methods are given in Figure A.27. Bicyclohexyl was also distilled under vacuum and de-oxygenated. The distillation step significantly reduced the absorbance of this fluid at 193 nm. The VUV absorbance spectrum of this fluid was obtained using the Acton and is given in Figure A.28.

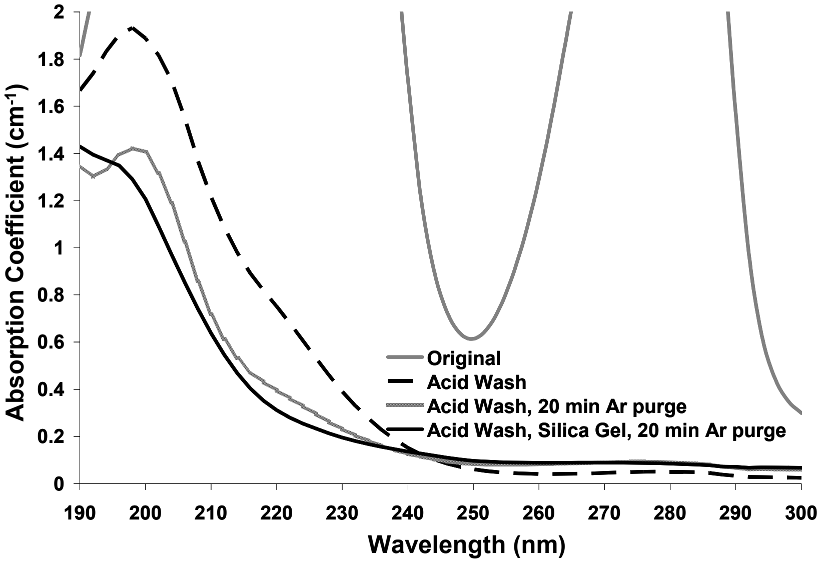

Figure A.27: UV-Vis absorbance spectra for the purification of bicyclohexyl

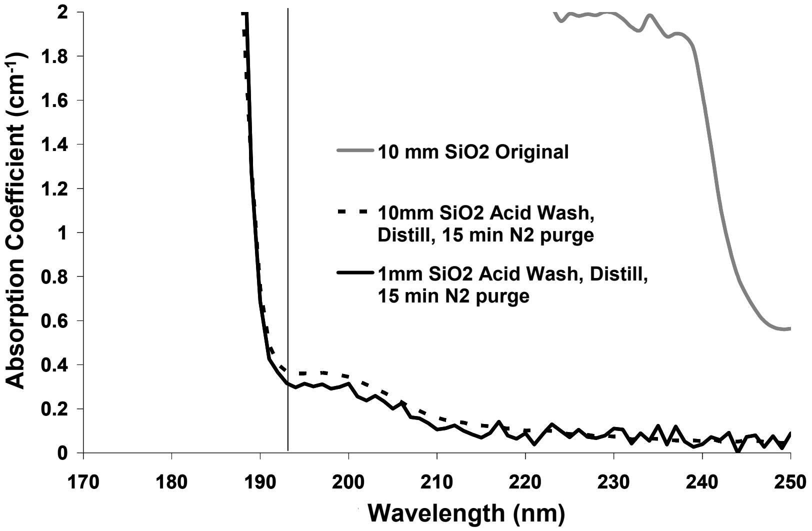

Figure A.28: VUV absorbance spectra of bicyclohexyl following an acid wash and distillation

A.5.5 1,3-Dimethlyadamantane

1,3-Dimethyladamantane [≥99% (Acros Organics)] was purified with a sulfuric acid wash (2:1, acid:fluid) and de-oxygenation. The UV-Vis spectra resulting from these purifications are shown in Figure A.29. These spectra were also collected with the Acton and are given in Figure A.30.

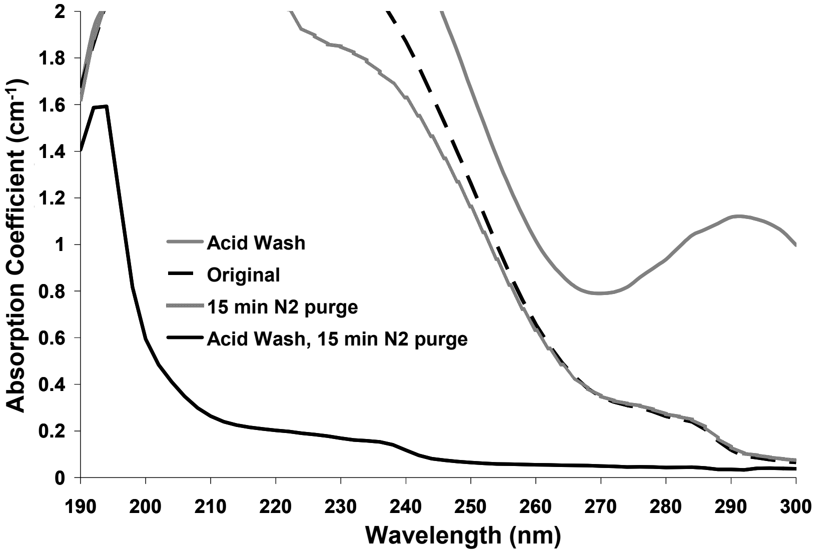

Figure A.29: UV-Vis spectra for the purification of 1,3-dimethyladamantane

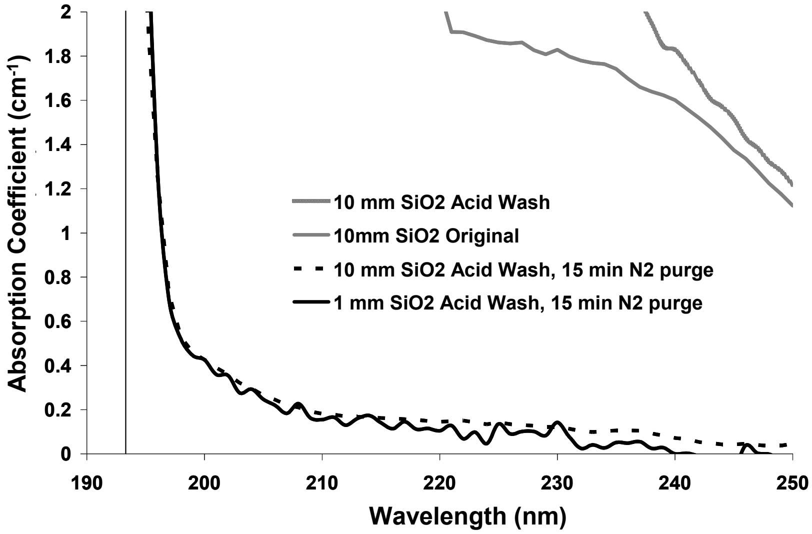

Figure A.30: VUV absorbance spectra obtained using the Acton for 1,3-dimethyladamantane

A.5.6 Perhydrofluorene

The purification procedure for perhydrofluorene [97% (Aldrich)] that results in the lowest absorbance is repetitions of the silica gel treatment. Silica gel was mixed with the fluid (3:1, fluid:silica gel) in an inert environment. The fluid was then filtered and de-oxygenated. The silica gel treatment was repeated four times. The UV-Vis absorbance data following these purifications is given in Figure A.31. The VUV absorbance spectrum following these purifications was also obtained on the Acton and is shown in Figure A.32.

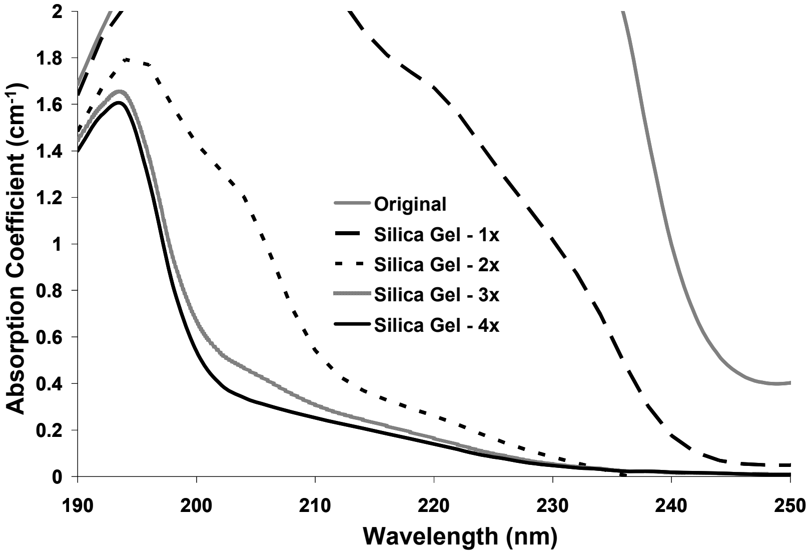

Figure A.31: UV-Vis spectra for the purifications of perhydrofluorene with four treatments with silica gel

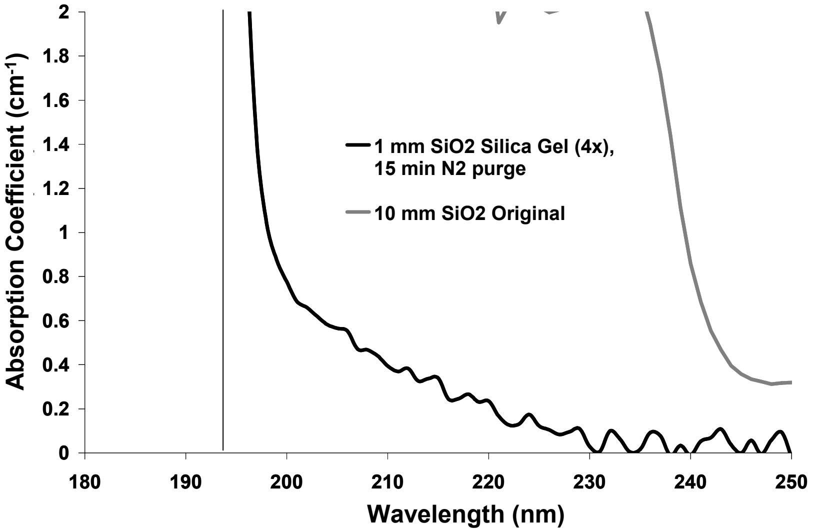

Figure A.32: VUV absorbance spectrum for perhydrofluorene purified with four repetitions of the silica gel treatment

A.5.7 Methyldinorbornane

The synthesis and purification of methyldinorbornane were described previously (Chapter 3, 3.2.3). The UV-Vis absorbance spectra for those purifications are given in Figure A.33. Interestingly, even though the acid wash following the distillation increases the absorbance, after the sample is de-oxygenated, the absorbance decreases to a minimum level. The sample that was tested immediately following the distillation step (and before the final acid wash) might not have been fully de-oxygenated. The VUV absorbance spectrum for methyldinorbornane was also collected using the Varian/Shimadzu through a 1 mm path. These data are shown in Figure A.34.

There is some discrepancy in the absorbance at 193 nm between the UV-Vis spectrum collected through the 10 mm path length and the spectrum collected through the 1 mm path with the Varian/Shimadzu. Since the sensitivity of the UV-Vis decreases at wavelengths less than 200 nm for strongly absorbing compounds, the VUV data is likely more reliable. Thus, the VUV tool must be used to obtain an accurate measurement of the absorbance at 193 nm for methyldinorbornane.

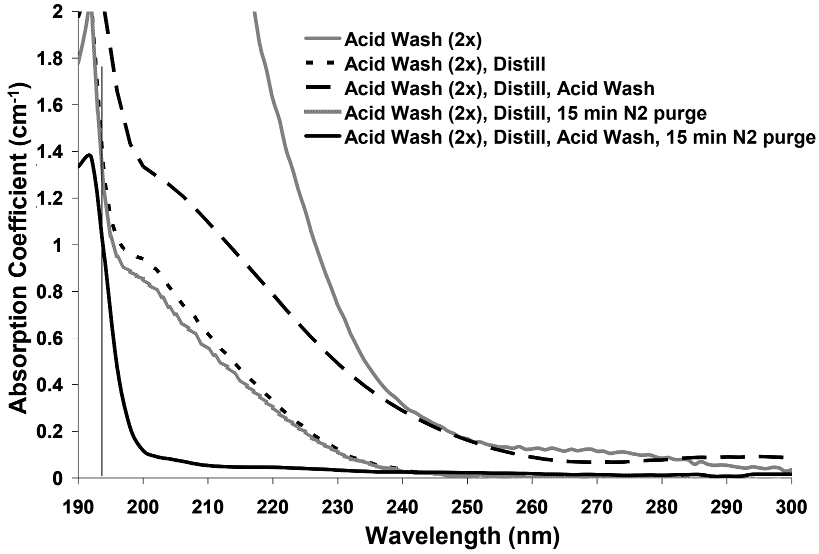

Figure A.33: UV-Vis absorbance spectra following the purification of methyldinorbornane

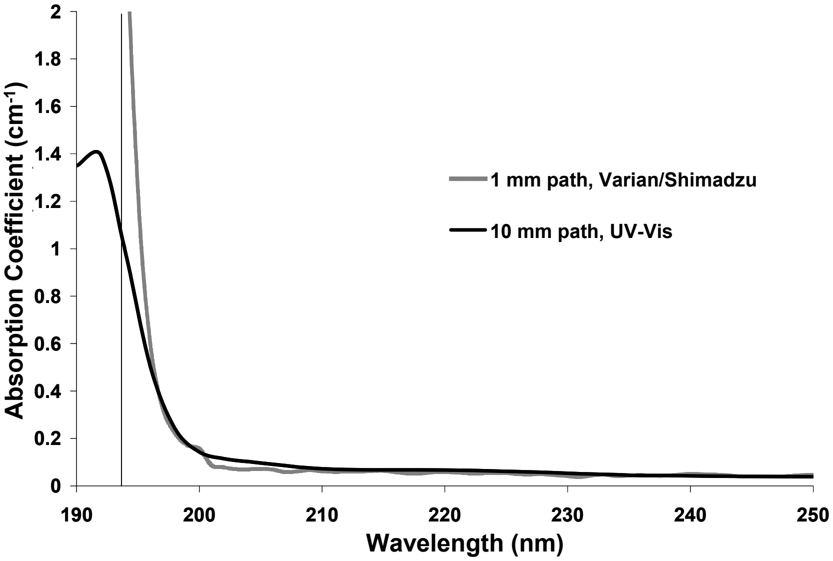

Figure A.34: 1 mm path length VUV absorbance spectrum and 10 mm path length UV-Vis absorbance spectrum for methyldinorbornane

A.5.8 Decahydroazulene

Azulene [99%, (Alfa Aesar)] was hydrogenated over a palladium catalyst to synthesize decahydroazulene. Approximately 5 g of azulene (initially blue) was dissolved in a 10% solution of methanol in ethyl acetate containing approximately 2 g of catalyst (palladium, 10% on carbon). This solution was pressurized to 800 psi with hydrogen and stirred at room temperature in a high pressure Parr reactor. Once the hydrogen was consumed, the reactor was re-pressurized to 800 psi of hydrogen. This process was repeated until the consumption of hydrogen gas ceased. The solution was then filtered through a celite pad and reduced in vacuo. Since the resulting oil retained a slightly blue color, the hydrogenation was repeated as above. When the consumption of hydrogen gas ceased, the solution was filtered through a celite pad and reduced in vacuo. The resultant fluid was distilled at 89 – 91 °C (45 torr). The fluid was then passed through a Pasteur pipette column containing a plug of silver nitrate on silica gel and activated silica gel. The fluid was passed through the column three times and de-oxygenated. The UV-Vis absorbance spectra following these purifications are given in Figure A.35. The lowest absorbance at 193 nm is obtained by minimizing the oxygen concentration in the fluid with an increase in the nitrogen purge time.

The index of refraction of this fluid at 193 nm is 1.633. Although the absorbance of this fluid could likely be decreased by additional purification steps, the index of decahydroazulene is lower than the index of decalin so that decahydroazulene is not a better immersion fluid candidate than decalin.

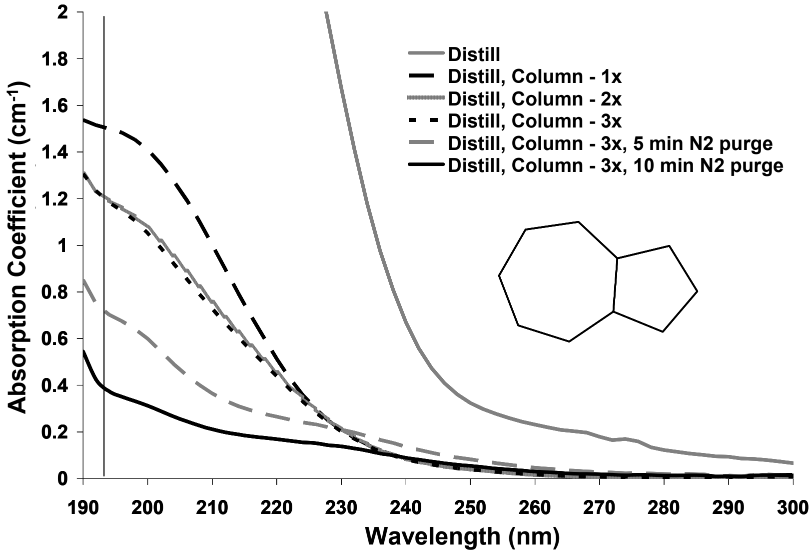

Figure A.35: UV-Vis absorbance spectra for the purification of decahydroazulene

A.5.9 Decahydroguaiazulene

Decahydroguaiazulene was synthesized by hydrogenating guaiazulene [99% (Aldrich)] over a palladium catalyst according to the procedure described for the synthesis of decahydroazulene (A.5.8) using 10 g of decahydroguaiazulene. Following the hydrogenations and removal of the catalyst and solvent, the fluid was distilled at 124 °C (20 torr). This fraction was washed twice with sulfuric acid (2:1, acid: fluid). The fluid was then passed through silica gel four times in a Pasteur pipette column in an inert environment and de-oxygenated. The absorbance spectra resulting from these purifications are given in Figure A.36.

The index of decahydroguaiazulene at 193 nm is 1.635. Since this index is lower than the index of decalin, decahydroguaiazulene is not a better immersion fluid candidate. Thus, even though this fluid seems to contain residual impurities, additional purification steps were not attempted.

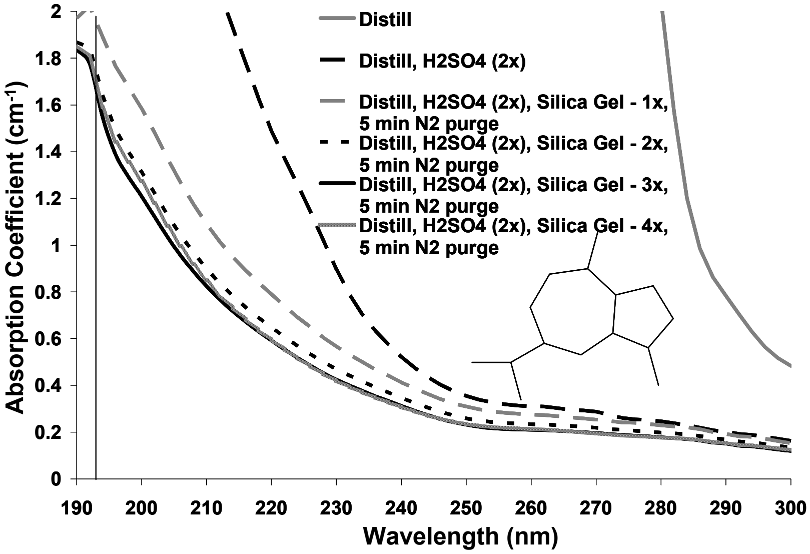

Figure A.36: UV-Vis absorbance spectra following the purification of decahydroguaiazulene

A.5.10 Tetradecahydromethylcyclopentadiene dimer

Methylcyclopentadiene dimer [93% (Aldrich)] was hydrogenated over a palladium catalyst to synthesize tetradecahydromethylcyclopentadiene dimer (HMCP), following the procedure described for the hydrogenation of azulene (A.5.8) with approximately 50 mL of the dimer. Following both hydrogenation steps and removal of the catalyst and solvent, the fluid was distilled at 50 – 52 °C (5 torr). The fluid was passed through a Pasteur pipette column with both silica gel only and silver nitrate on silica gel/silica gel. The absorbance spectra as a result of these purifications are given in Figure A.37. The sulfuric acid wash purification was also attempted, but this procedure significantly increased the absorbance ($\alpha > 3$ cm^{-1} from 190 – 300 nm).

For this fluid, de-oxygenation did not substantially decrease the absorbance. Since HMCD should form an absorbing charge transfer complex with oxygen, this fluid must contain some residual impurities that are not sensitive to oxygen. Since the purity of methylcyclopentadiene dimer is low (93%), the dimer was distilled at 62 – 64 °C (7 torr) prior to hydrogenation. The fraction was then hydrogenated according to the procedure described previously. HMCD was purified by passing it through a Pasteur pipette column of both silica gel and silver nitrate on silica gel. The absorbance spectra are given in Figure A.38. The absorbance does not decrease with the distillation of the dimer.

The index of refraction of HMCD is 1.6831. Even though this index is higher than the index of decalin, HCMD has a higher absorbance than decalin. The higher absorbance leads to a higher index. Although additional purification should reduce the absorbance of HMCD, the index will also decrease. Thus, HMCD is probably not a better immersion fluid candidate than decalin.

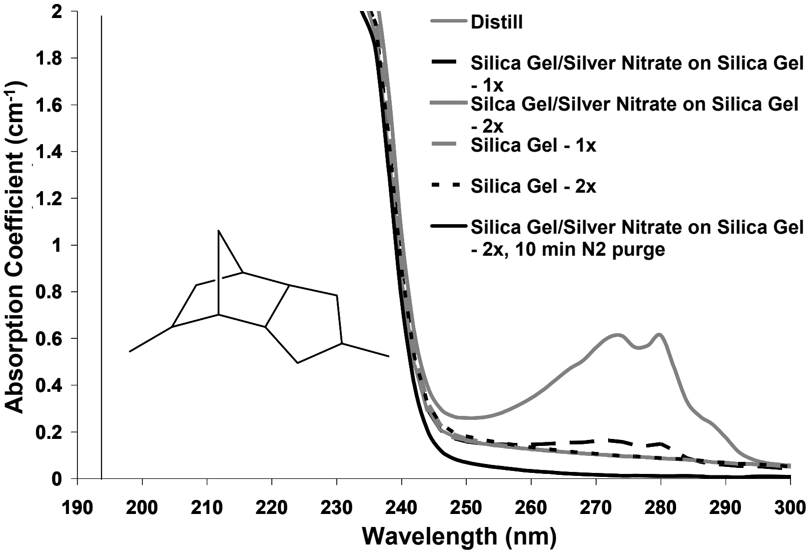

Figure A.37: UV-Vis absorbance spectra for the purification of HMCD

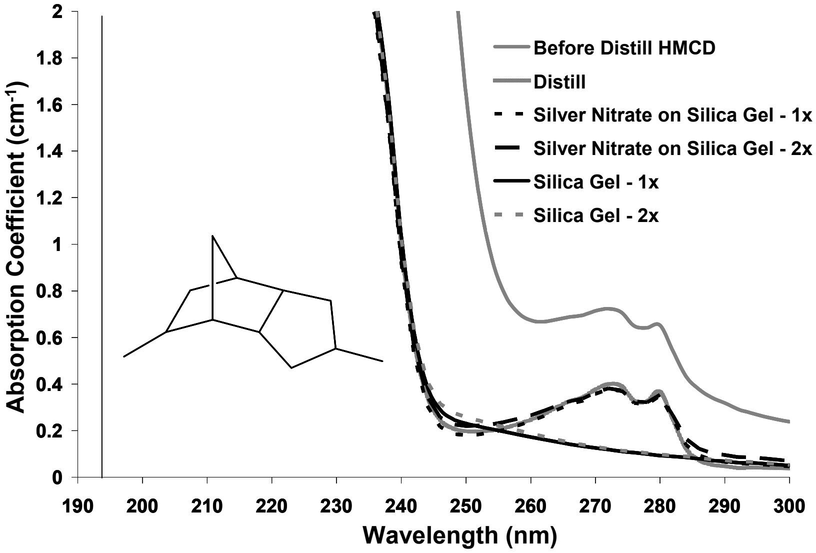

Figure A.38: UV-Vis absorbance spectra following the purification of HMCD when the methylcyclopentadiene dimer was distilled prior to hydrogenation

A.5.11 Cyano-tricyclo[4.2.1.0^{2,5}]nonane

The reaction scheme for the synthesis of cyano-tricyclo[4.2.1.0^{2,5}]nonane (CTN) is given in Scheme A.1. Quadricyclane, 10 g, was combined with hydroquinone, 60 mg, and acrylonitrile, 60 mL, in a sealed Schlenk tube over nitrogen. The flask was placed in an oil bath and heated to 96 ˚C, while stirring, for 72 hours. The resulting solution was reduced in vacuo to remove excess solvent. The resulting fluid was dissolved in a 10% solution of methanol in ethyl acetate and hydrogenated over a palladium catalyst (10% on carbon). Approximately 2 g of catalyst (palladium, 10% on carbon) were added to the solution in a high pressure Parr reactor. The reactor was pressurized with 800 psi of hydrogen and stirred at room temperature. Once the hydrogen was consumed, the reactor was re-pressurized to 800 psi of hydrogen. This process was repeated until the consumption of hydrogen gas ceased. The solution was then filtered through a celite pad and reduced in vacuo. The resulting fluid was distilled at 50 – 54 °C (0.16 torr). The fluid was purified using columns of both silica gel and silver nitrate on silica gel. A summary of these purification results is given in Figure A.39.

This fluid has a strong absorbance to wavelengths > 300 nm. Cyano groups are weakly absorbing at 193 nm. Acetonitrile, for example, has a weak absorbance maximum at 167 nm.[1] This strong absorbance is likely not due to the cyano group. Even though residual impurities could be causing the strong absorbance observed in Figure A.39, CTN contains a highly strained four-carbon ring group. High strain energy and "destabilizes" the HOMO to increases the absorbance (red-shift the absorbance edge). Thus, the strong absorbance of CTN is expected based on the structure. Even though the absorbance of CTN might be lower at some wavelengths, the absorbance at 193 nm is likely high. The index of refraction of CTN at 193 nm is 1.6801.

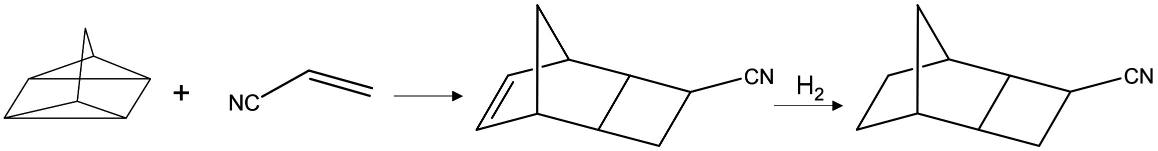

Scheme A.1: Synthesis of cyano-tricyclo[4.2.1.0^{2,5}]nonane (CTN)

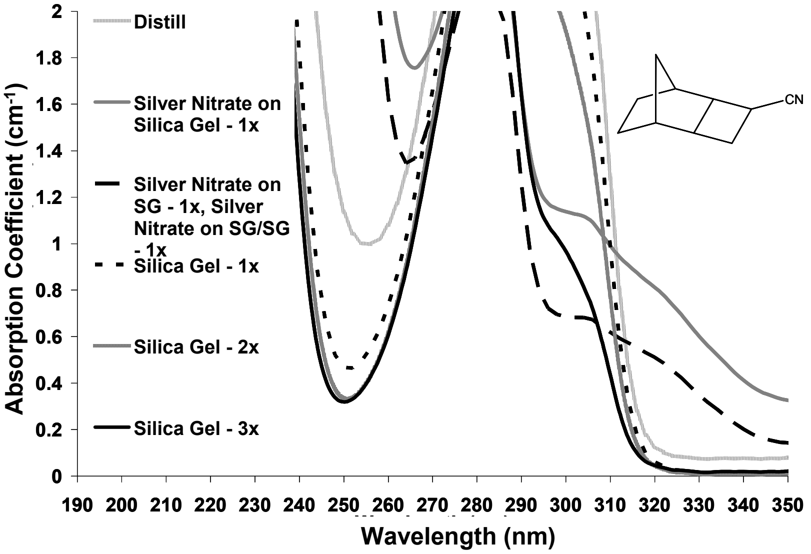

Figure A.39: UV-Vis absorbance spectra following the purification of CTN

A.6 REFERENCES

1. Yadav, L. D. S., *Organic Spectroscopy*. 2005, Boston: Kluwer Academic Publishers. pp. 324.

Appendix B: Salt Synthesis and Purification

The synthesis and purification of the two types of salts discussed in Chapter 4 will be described. These salts were studied in an attempt to identify an aqueous additive with an incorporated hydrocarbon group. The first salts consist of a metal cation and sulfonate anion with a large (> five carbon) hydrocarbon attached to the sulfonate. The second group includes quaternary ammonium methylsulfonate salts.

B.1 SULFONATE SALTS

The structures of the salts studied, that have a hydrocarbon group attached to a sulfonate anion, are given in Table 4.1. Sodium cyclohexylsulfonate (NaCy) was purchased from Fluka and used as received. The remaining salts were synthesized by Kazuya Matsumoto, a visiting graduate student from the Tokyo Institute of Technology.

B.1.1 Sodium Decahydronaphthalene-2-sulfonate (NaDc)

The synthesis of NaDc is shown in Scheme B.1. Chlorotrimethylsilane was first added to a solution of lithium bromide in dry acetonitrile, under nitrogen. Decahydro-2-naphthol was then added, and the reaction mixture was heated under reflux for 24 h. After cooling to room temperature, water was added to the mixture, and the mixture was extracted with ethyl acetate, washed with $NaHCO_3(aq)$ and water and concentrated in vacuo. A solution of the resulting liquid and sodium sulfite in water and ethanol was refluxed for 48 h. The solvent was evaporated, and the resulting solid was dissolved in hot ethanol and filtered. The ethanol solution was evaporated, and the resulting solid was recrystallized from water and ethanol.

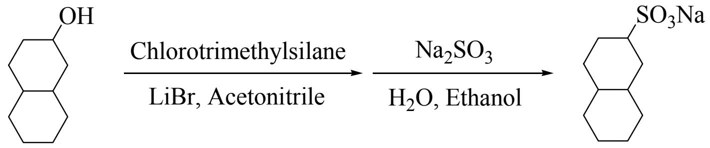

Scheme B.1: Synthesis of sodium decahydronaphthalene-2-sulfonate (NaDc)

B.1.2 Potassium 1-Adamantanesulfonate (KAd)

The reaction steps to synthesize KAd are given in Scheme B.2. To first synthesize 1-adamantanethiol, a mixture of 1-adamantanol, thiourea, 48% HBr, and glacial acetic acid was refluxed overnight under nitrogen. After cooling to room temperature, the reaction mixture was refluxed with 30% aqueous NaOH containing ethanol for 3 h. After removal of ethanol, the solution was cooled with an ice bath. The precipitate was filtered and dispersed into water, then acidified with conc. HCl. The crude product, 1-adamantanethiol, was filtered, washed with water, dried in vacuo, and used without further purification. To a stirred solution of 1-adamantanethiol in glacial acetic acid were added dropwise H_2O_2 and glacial acetic acid at 30 ^{o}C. The reaction mixture was stirred at 70 ^{o}C for 2 h. After cooling to room temperature, the reaction mixture was neutralized with a KOH solution and concentrated in vacuo. The resulting solid was recrystallized from ethanol and water.

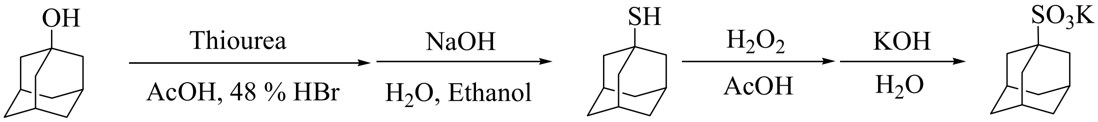

Scheme B.2: Synthesis of potassium 1-adamantanesulfonate (KAd)

B.1.3 Sodium Cyclohexylmethanesulfonate (NaCyMs)

NaCyMs was synthesized according to Scheme B.3. A mixture of bromomethylcyclohexane and sodium sulfite in water was refluxed for 24 h, the reaction mixture was filtered, and the resulting solid was recrystallized from water.

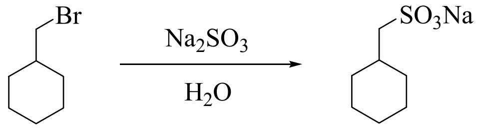

Scheme B.3: Synthesis of sodium cyclohexylmethanesulfonate (NaCyMs)

B.1.4 Potassium 1-Adamantanemethanesulfonate (KAdMs)

KAdMs was synthesized through the multi-step procedure shown in Scheme B.4. *p*-Toluenesulfonyl chloride was added to a stirred solution of 1-adamantanemethanol in pyridine, and the solution was stirred at room temperature for 24 h. Water was added to the reaction mixture, and the mixture was filtered. The resulting solid was washed with NaOH*(aq)* and water and used without further purification. A mixture of this solid (*p*-(1-adamantyl methyl)toluenesulfonate) and potassium thioacetate in DMF was stirred at 100 °C for 10 h under nitrogen. After cooling to room temperature, the reaction mixture was poured into water and filtered. The resulting solid was washed with water to yield S-adamantylmethyl ethanethioate. S-Adamantylmethyl ethanethioate in dry THF was added dropwise to a stirred solution of $LiAlH_4$ in dry THF at 0 °C under nitrogen. After the mixture was stirred at room temperature for 6 h, water, and then 1N HCl solution, were added dropwise at 0 °C. The product, adamantyl-1-methanethiol, was extracted with ethylacetate, washed with water, dried over $MgSO_4$, and concentrated in vacuo. The sulfonate salt was synthesized from the thiol according to the same procedure described for the synthesis of KAd from 1-adamantanethiol.

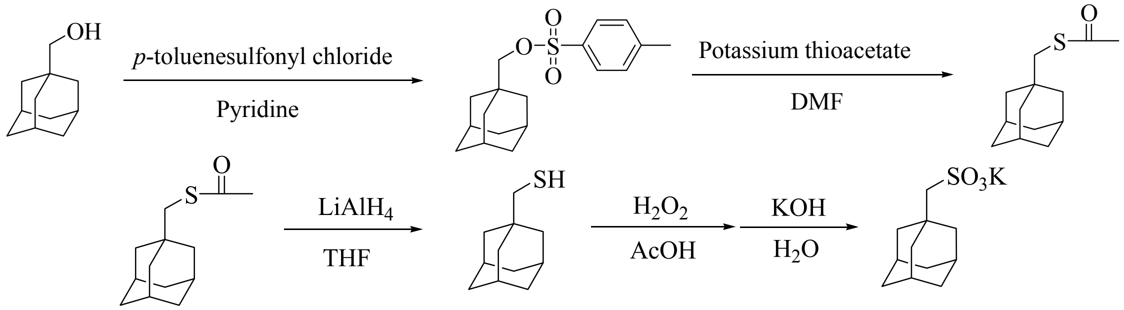

Scheme B.4: Synthesis of potassium 1-adamantanemethanesulfonate (KAdMs)

B.2 QUATERNARY AMMONIUM SALTS

Quaternary ammonium methylsulfonate salts were also studied. The structures of these salts are given in Table 4.2.

B.2.1 Decyl (DMS) and Hexadecyl (HDMS)

These salts were prepared by an acid-base reaction, shown in Scheme B.5. The ammonium base was received from SACHEM, Inc. (Austin, TX) and used as received. Methanesulfonic acid was added dropwise in a 1:1 molar ratio to a stirred solution of the ammonium base in water at 0 ˚C. The mixture was reduced in vacuo, and the solid dried overnight under vacuum. The resulting solid was then recrystallized from acetonitrile.

$$RN(CH_3)_3OH + HOSO_2CH_3 \longrightarrow RN(CH_3)_3OSO_2CH_3 + H_2O$$

Scheme B.5: Reaction scheme for the acid-base reaction to form the decyl (DMS) and hexadecyl (HDMS) salts

B.2.2 Cyclohexyl (CyMS)

The general reaction scheme for the synthesis of a trimethylalkylammonium methylsulfonate salt is shown in Scheme B.6. Methylmethanesulfonate was used to methylate an amine containing the target hydrocarbon group. Methylation of this amine forms the desired quaternary ammonium methylsulfonate salt. To synthesize CyMS, dimethylcyclohexylamine was used. A flask was evacuated, dried, and filled with nitrogen. Methylmethanesulfonate was then added, dropwise under nitrogen, to a stirred solution of the amine in a 1.2:1 molar ratio in an excess of dry THF at 0 ˚C. After the reaction stirred for approximately 1 h at 0 ˚C, the reaction was stirred at room temperature overnight. The resulting solid was washed with hexanes and reduced in vacuo.

The absorbance of 1 M solutions of CyMS in water was tested to determine which purification method provided the lowest absorbance at 193 nm. These absorbance spectra following the various purification methods are given in Figure B.1. First, the salt was tested without any purification. Secondly, the absorbance of a solution of salt recrystallized from acetonitrile was tested. Finally, prior to reaction with methylmethanesulfonate, dimethylcyclohexylamine was distilled over zinc dust. The product from the reaction using this amine was recrystallized from acetonitrile. The salt made using the distilled amine and recrystallized from acetonitrile provided the solution with the lowest absorbance (see Figure B.1).

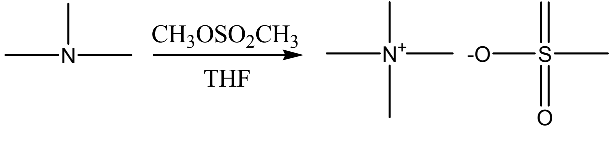

Scheme B.6: Methylation of an amine with methylmethane sulfonate to synthesize a quaternary ammonium methylsulfonate salt

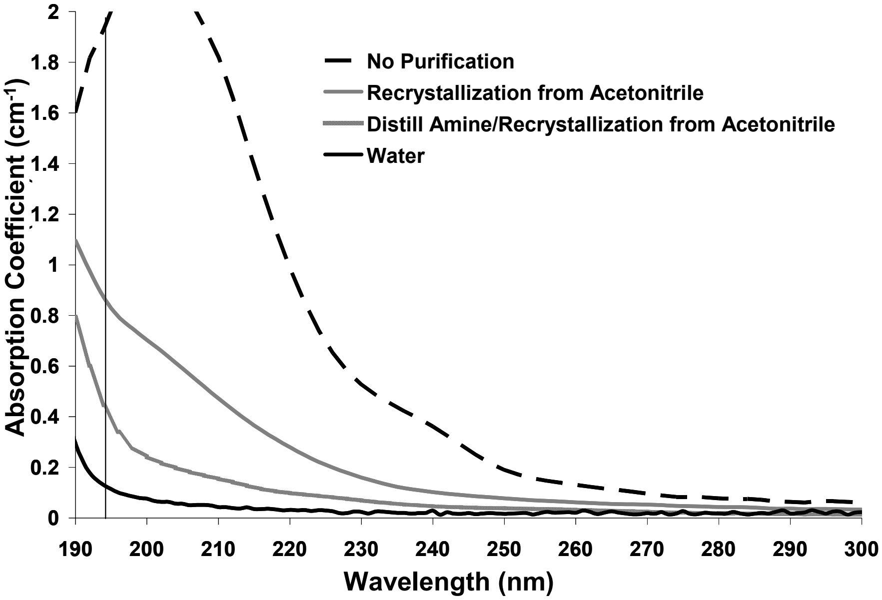

Figure B.1: Absorbance of 1 M CyMS following various purification methods

B.2.3 Cycloheptyl (ChpMS)

Cycloheptylamine was methylated using the Eschweiler-Clarke reaction to form dimethylcycloheptylamine through the reaction shown in Scheme B.7.[1] To methylate this amine, 3 molar equivalents of formaldehyde (37 wt% in water) were added to 1 molar equivalent of the amine while stirring at 0 ˚C. Three molar equivalents of formic acid (88 wt% in water) were then added dropwise while stirring at 0 ˚C. The reaction vessel was sealed and vented with a syringe needle, and heated to 80 ˚C for 24 h. After cooling the solution to room temperature, a solution of 50 wt% KOH*(aq)* was added to the reaction mixture until the mixture reached pH > 7. The product was extracted three times with diethylether, washed with water, dried over $MgSO_4$, and concentrated in vacuo. The methylated amine product, dimethylcycloheptylamine in this case, was then methylated further to make the methylsulfonate salt (ChpMS) using the reaction shown in

Scheme B.6 and procedure given in B.2.2. The salt was then recrystallized from acetonitrile. The absorbance spectrum of a 1 M solution of this salt is shown in Figure B.2. To further purify the salt, the amine product from the Eschweiler-Clarke reaction, dimethylcycloheptylamine, was distilled over zinc dust at 81 ˚C (45 torr) prior to the reaction with methylmethanesulfonate. The absorbance spectrum of a 1 M solution of this salt is also shown in Figure B.2. Distilling the methylated amine (following the Eschweiler-Clarke reaction) significantly reduces the absorbance of the salt solution.

$$\mathrm{RNH_2 + CH_2{=}O \xrightarrow{HCOOH} RN(CH_3)_2 + H_2O}$$

Scheme B.7: Eschweiler-Clarke reaction to methylate an amine

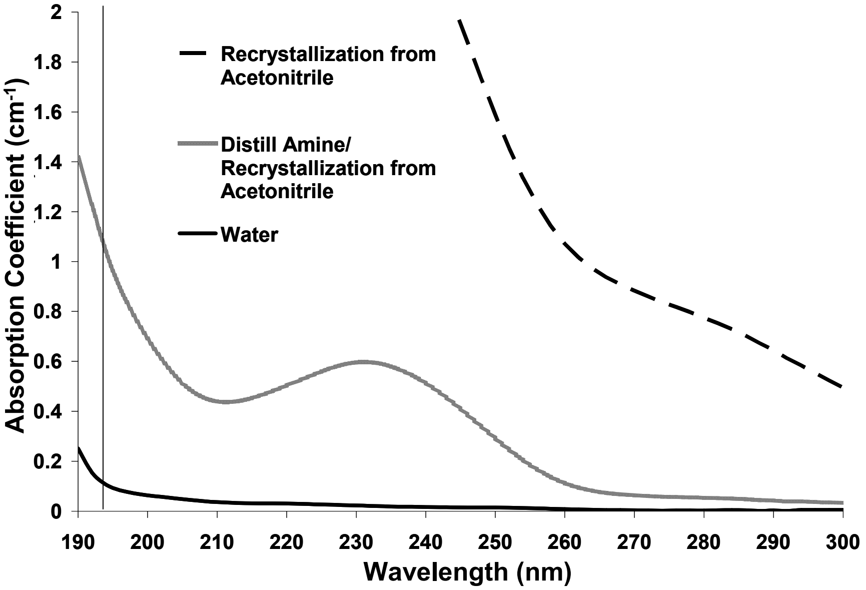

Figure B.2: Absorbance spectra of 1 M ChpMS with varying purification methods

B.2.4 Adamantyl (AdMS and AdHMS)

AdMS was synthesized by first methylating adamantylamine using the Eschweiler-Clarke reaction shown in Scheme B.7, following the procedure described in B.2.3. To make the methylsulfonate salt from dimethyladamantylamine, the procedure described in B.2.2 and reaction shown in Scheme B.6 was followed with the mixture at room temperature for the entire reaction. NMR results verify that none of the initial starting material is present in the final salt and that the amine methylation takes place as expected based on the reaction. Based on these results, the Eschweiler-Clarke methylation procedure was used when amine methylation was needed. ^{1}H NMR (DMSO-d6, ppm): 2.933 (bs, 9H), 2.295 (s, 3H), 2.191 (bs, 3H), 1.969 (s, 6H), 1.602 (s, 6H).

AdHMS was synthesized through the reaction scheme shown in Scheme B.8. Methanesulfonic acid was added dropwise to a stirred solution of adamantylamine in dichloromethane at 0 ˚C. The resulting solid was rinsed with hexanes and recrystallized from methanol.

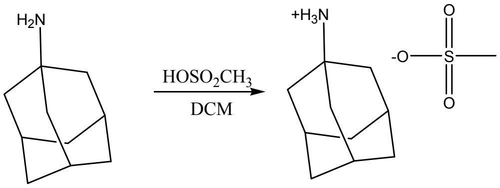

Scheme B.8: Synthesis of AdHMS

B.2.5 Dicyclohexyl (dCyMS)

dCyMS was synthesized by first methylating dicyclohexylamine using the Eschweiler-Clarke reaction shown in Scheme B.7, following the procedure described in B.2.3. The resulting amine, methyldicyclohexylamine, was distilled over zinc dust at 116 ˚C (14 torr). To make the methylsulfonate salt from methylcyclohexylamine, the procedure described in B.2.2 and reaction shown in Scheme B.6 was followed. However, the salt was recrystallized from tetrahydrofuran, rather than acetonitrile.

In addition to the method previously described (Method A), alternative procedures were also attempted to minimize the absorbance of the solution. First (Method B), a commercially available sample of methyldicyclohexylamine (MCA) was distilled at 116 ˚C (14 torr) prior to methylating to make the methylsulfonate salt. The salt was recrystallized from tetrahydrofuran. Also (Method C), MCA was dissolved in diethylether and extracted three times with 1 N HCl. A solution of approximately 50 wt% KOH*(aq)* was then added to the acid solution until the pH > 7. The amine was then extracted three times with diethylether, washed with brine, dried over $MgSO_4$, and concentrated in vacuo. The amine was then distilled over zinc dust at 116 ˚C (14 torr) and used to make the methylsulfonate salt following the procedure described in B.2.2. The absorbance spectra of 1 M solutions of the salts purified with these methods are given in Figure B.3. Methods A and B provide a lower absorbance than Method C. Since Method A has the lowest absorbance at the shorter wavelengths, Method A is assumed to be the best of these purification methods.

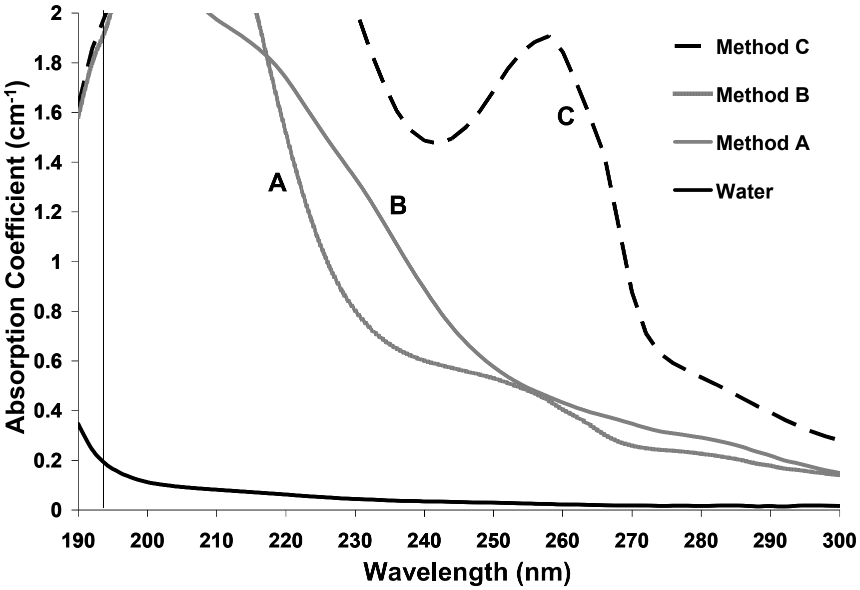

Figure B.3: Absorbance spectra of 1 M dCyMS, varying purification methods

B.2.6 Piperidine (PdMS)

Methylpiperidine was used to synthesize PdMS according to the procedure given in B.2.2 and reaction shown in Scheme B.6. Two different purification methods were used to minimize the absorbance of the salt solution. First, the salt was recrystallized from acetonitrile. Secondly, according to the procedure described in B.2.5 (Method C), methylpiperidine was purified and distilled over zinc dust at 106 ˚C prior to the reaction with methylmethanesulfonate. The absorbance spectra of 1 M solutions of the salts purified with each of these methods are given in Figure B.4. The lowest absorbance is obtained following the extraction (Method C), distillation, and recrystallization from acetonitrile.

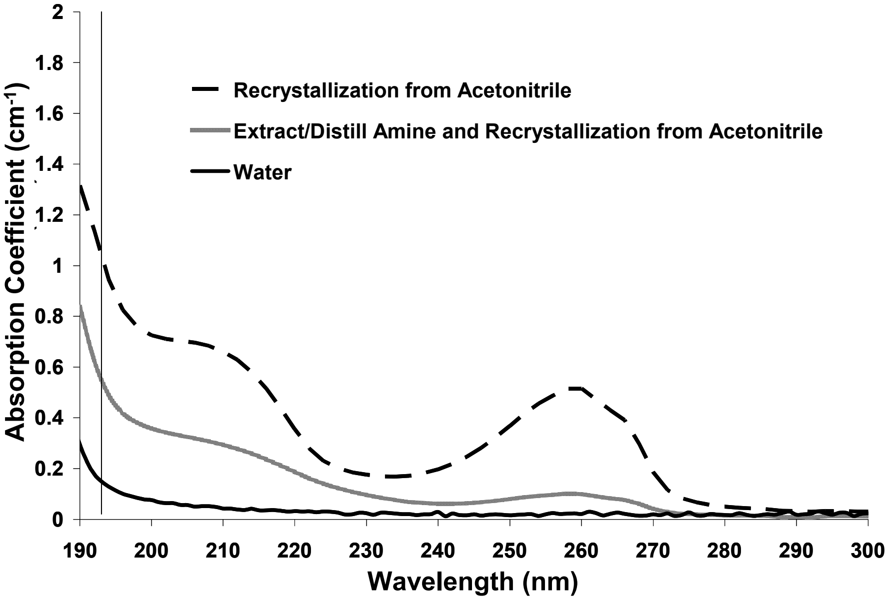

Figure B.4: Absorbance spectra of 1 M PdMS using various purification methods

B.2.7 Decahydroquinoline (DHQMS)

Decahydroquinoline was first methylated using the Eschweiler-Clarke reaction, shown in Scheme B.7, according the procedure described in B.2.3. DHQMS was then synthesized by further methylating the amine with methylmethanesulfonate, following the procedure described in B.2.2 and shown in Scheme B.6, and recrystallizing the salt from acetonitrile. In an attempt to minimize the absorbance the amine was also distilled over zinc dust at 75 ˚C (20 torr) after the Eschweiler-Clarke reaction. The absorbance spectra of 1 M solutions of salts prepared both with and without distillation of the amine are given in Figure B.5. Distillation of the amine provides the salt solution with the lowest absorbance.

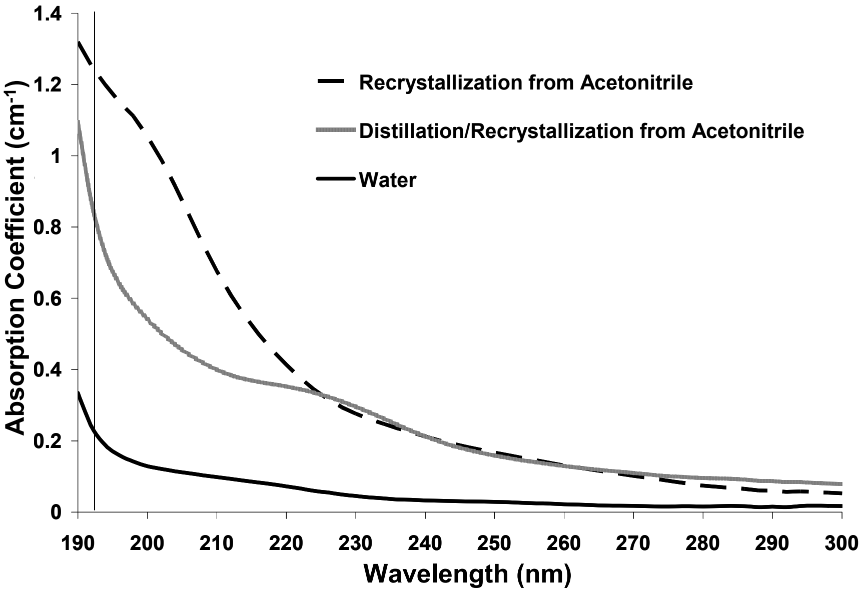

Figure B.5: Absorbance spectra of 1 M DHQMS, varying purification methods

B.2.8 Quinuclidine (QuinMS)

QuinMS was synthesized from quinuclidine using the procedure described in B.2.2 and shown in Scheme B.6. The resulting salt was recrystallized from acetonitrile.

B.2.9 Dimethylpiperazine (PzMS)

The reaction scheme shown in Scheme B.6 was used to make PzMS. To encourage methylation on both of the nitrogens in dimethylpiperazine, the amine was added slowly to a stirred solution of methylmethanesulfonate in a 1:2.4 molar ratio in an excess of dry THF at 0 ˚C under nitrogen. After the reaction stirred for approximately 1 h at 0 ˚C, the reaction was stirred at room temperature overnight. The product was washed with hexanes and reduced in vacuo. The salt was recrystallized from methanol.

B.2.10 1,4-Diazabicyclo[2.2.2]octane (DabMS)

DabMS was synthesized according to the reaction scheme shown in Scheme B.6. Since 1,4-diazabicyclo[2.2.2]octane contains two nitrogens, like dimethylpiperazine, the procedure described in B.2.9 was followed to encourage methylation at both nitrogens. The resulting salt was recrystallized from methanol. To reduce the absorbance the amine was also recrystallized from acetonitrile prior to the methylation reaction with methylmethanesulfonate. The absorbance spectra of 1 M solutions of both of these salts are given in Figure B.6. Recrystallizing the amine leads to the lowest absorbance in the salt solution.

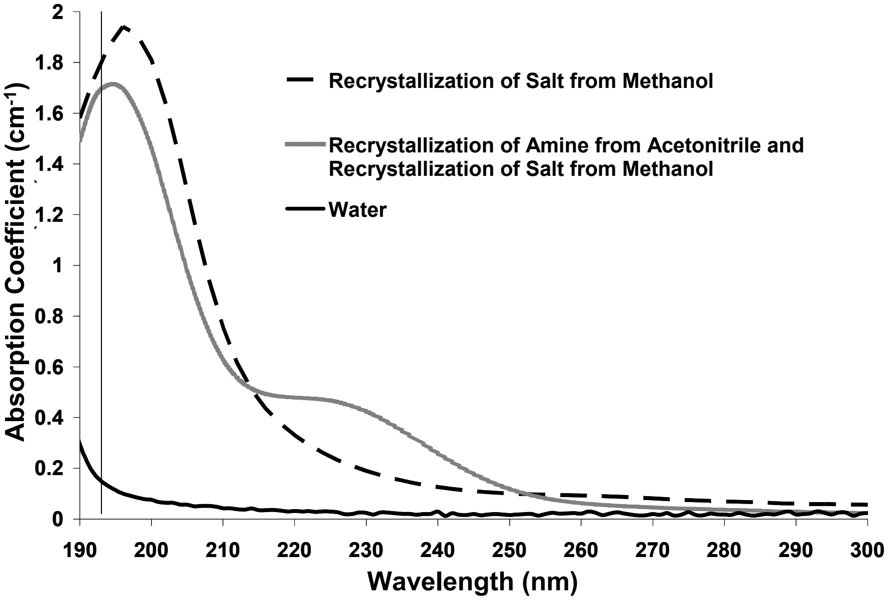

Figure B.6: Absorbance spectra of 1 M DabMS solutions with varying purification methods

B.3 REFERENCES

1. Pine, S. H. and Sanchez, B. L., Formic acid-formaldehyde methylation of amines. J. Org. Chem., 1971 36(6): p. 829-32.

Appendix C: MATLAB Code for Immersion Fluid Modeling Program

C.1 NUMERICAL SOLUTIONS TO THE KRAMERS-KRONIG INTEGRAL

Two numerical methods have been derived by Ohta and Ishida[1] to solve the integral:

$$I(\nu_i) = \frac{2}{\pi} P \int_{\nu_1}^{\nu_m} \frac{\nu k(\nu)}{\nu^2 - \nu_i^2} d\nu \qquad \text{(C.1)}$$

in which P is the Cauchy principal value of the integral. Assuming that all values of k(ν) outside the interval (ν_1, ν_m) are zero, Equation C.1 is analogous to the Kramers-Kronig integral for calculation of the index from the absorbance. In these solution methods, the values of the spectrum k(ν) are given by *m* digitized discrete values k_j at *m* wavenumber (cm^{-1}) values ν_j with equal intervals as

$$\nu_1, \nu_2, \nu_3, \ldots, \nu_j, \ldots, \nu_{m-1}, \nu_m \qquad \text{(C.2)}$$

$$k_1, k_2, k_3, \ldots, k_j, \ldots, k_{m-1}, k_m \qquad \text{(C.3)}$$

The interval *h* is designated as

$$h = \nu_{j+1} - \nu_j \quad (j = 1, 2, \ldots, m-1). \qquad \text{(C.4)}$$

C.1.1 Maclaurin's Formula

To solve Equation C.1 using Maclaurin's Formula, the following summation is calculated using every other data point

$$I_i = \frac{2}{\pi} \times 2h \times \left\{ \sum_j {}' f_j \right\} \qquad \text{(C.5)}$$

where

$$f_j = \frac{\nu_j k_j}{\nu_j^2 - \nu_i^2} = \frac{1}{2} \left\{ \frac{k_j}{\nu_j - \nu_i} + \frac{k_j}{\nu_j + \nu_i} \right\} \qquad \text{(C.6)}$$

In Equation C.5, the sign $\sum'$ denotes the summation using every other data point. The starting point depends on whether *i* is even or odd to avoid direct calculation of the point at $i = j$. When *i* is odd,

$$j = 2, 4, 6, \ldots, i-1, i+1, \ldots$$

When *i* is even

$$j = 1, 3, 5, \ldots, i-1, i+1, \ldots$$

This method allows for the calculation of the integral in Equation C.1 without special treatment of the pole at $i = j$.[1] The MATLAB code written for this solution method is given by:

maclaurin.m

```
function [real, delta_n] = maclaurin(wavelength,imag,n_inf)

%Inputs:  ‘wavelength’ - array in cm-1, constant interval
%         ‘imag’ - array containing the absorbance or imaginary part of
%         the complex dielectric constant
%         ‘n_inf’ - n_offset value
%Outputs: ‘real’ - solution to the integral + n_inf
%         ‘delta_n’ - solution to the integral
%Written from the method described in Ohta et al.  Appl Spectr. 1988

j = length(wavelength);
i = length(wavelength);
h = wavelength(j - 1) - wavelength(j);

for g = 1:i
   fj_odd_g(g) = 0;
   fj_even_g(g) = 0;
   if rem(g,2) == 1 % when i is odd
        fj_odd = 0;
        for k = 1:j
           if rem(k,2) == 0  % even j values
           fj_odd_sum = fj_odd + (1/2) * ((imag(k) / (wavelength(k)…
           - wavelength(g))) + (imag(k) / (wavelength(k)…
           + wavelength(g))));
               fj_odd_g(g) = fj_odd_sum;
               fj_odd = fj_odd_sum;
           end
       end
    else  % when i is even
       fj_even = 0;
       for k = 1:j
           if rem(k,2) == 1  % odd j values
           fj_even_sum = fj_even + (1/2) * ((imag(k) / (wavelength(k)…
                         - wavelength(g))) + (imag(k) / (wavelength(k)…
```

```
                         + wavelength(g))));
               fj_even_g(g) = fj_even_sum;
               fj_even = fj_even_sum;
           end
       end
   end
sum(g) = fj_odd_g(g) + fj_even_g(g);
delta_n(g) = (2 / pi) * 2 * h * sum(g);
end
real = delta_n + n_inf;
```

C.1.2 Trapezium Sum

The Trapezium sum method solves Equation C.1 with a summation[1] which is given by

$$I_i = \frac{2}{\pi} \times h \times \left\{ \sum_{j=1}^{m} f_j \right\} \tag{C.7}$$

where f_j is defined by Equation C.6. To make an approximation for the pole at $j = i$, Equation C.7 is divided into

$$I_i = I_{i(c)} + I_{i(p)} + I_{i(m)} \tag{C.8}$$

where

$$I_{i(c)} = \frac{2}{\pi} \times h \times \left\{ \sum_{j=1, j \neq i}^{m} f_j \right\} \tag{C.9}$$

$$I_{i(c)} = \frac{1}{\pi} \times h \times \frac{k_i}{2\nu_i} \tag{C.10}$$

$$I_{i(m)} = \frac{1}{\pi} P \int_{\nu_i - h/2}^{\nu_i + h/2} \frac{k(\nu)}{\nu - \nu_i} d\nu \tag{C.11}$$

$I_{i(c)}$ is the summation (as in Equation C.7) with the pole at $j = i$ omitted. $I_{i(p)}$ is the second term of Equation C.6 at $j = i$. $I_{i(m)}$ corresponds to the first term of Equation C.6, which contains the pole at $j = i$. A Taylor series expansion of k(ν) around $\nu = \nu_i$ is made to solve the integral in Equation C.11 so that $I_{i(m)}$ becomes

$$I_{i(m)} = \frac{1}{\pi} \times h \times k'(\nu_i) \tag{C.12}$$

when the higher order derivative terms are ignored. To obtain the first derivative (k’(ν)) from the discrete data array, the following formula are used for *i* = 1 and *m*:

$$k'(\nu_1) = \frac{\{4(k_2 - k_1) - (k_3 - k_1)\}}{2h} \tag{C.13}$$

and

$$k'(\nu_m) = \frac{\{4(k_m - k_{m-1}) - (k_m - k_{m-2})\}}{2h}. \tag{C.14}$$

For the all other values of *i*,

$$k'(\nu_i) = \frac{k_{i+1} - k_{i-1}}{2h}, \tag{C.15}$$

$$k'(\nu_i) = \frac{\{8(k_{i+1} - k_{i-1}) - (k_{i+2} - k_{i-2})\}}{12h}, \tag{C.16}$$

and

$$k'(\nu_i) = \frac{\{45(k_{i+1} - k_{i-1}) - 9(k_{i+2} - k_{i-2}) + (k_{i+3} - k_{i-3})\}}{60h}. \tag{C.17}$$

Equation C.15 is used for *i* = 2 and *m* – 1. Equation C.16 is used for *i* = 3 and *m* – 2, and Equation C.17 is used for the remaining values of *i*. The MATLAB code written to solve Equation C.1 with this solution method is given by:

trapezium_B3.m

```
function [real, delta_n] = trapezium_B3(wavelength,imag,n_inf)


%Inputs:  ‘wavelength’ - array in cm-1, constant interval required
%         ‘imag’ - array containing the absorance or imaginary part of
%         the complex dielectric constant
%         ‘n_inf’ - n_offset value
%Outputs: ‘real’ - solution to the integral + n_inf
%         ‘delta_n’ - solution to the integral
%Written from the method described in Ohta et al.  Appl Spectr. 1988

j = length(wavelength);
i = length(wavelength);
h = wavelength(j - 1) - wavelength(j);

for g = 1:i % Ii(c)
    fj(g) = 0;
    for k = 1:j
    if g ~= k
        fj(g) = fj(g) + (1 / 2) * ((imag(k) / (wavelength(k)…
                - wavelength(g))) + (imag(k) / (wavelength(k)…
```

```
                + wavelength(g))));
        end
    end
I_c(g) = (2 / pi) * h * fj(g);
end

for g = 1:i % Ii(p)
    I_p(g) = (1 / pi) * h * (imag(g) / (2 * wavelength(g)));
end

for g = 1:i % Ii(m)
    k_prime(g) = 0;
    if g == 1  % i = 1
        k_prime(g) = ((4 * (imag(g + 1) - imag(g)) - (imag(g + 2) -…
                     imag(g))) / (2 * h));
    elseif g == i  % i = m
        k_prime(g) = ((4 * (imag(g) - imag(g - 1)) - (imag(g)…
                     - imag(g - 2))) / (2 * h));
    elseif g == 2 || g == i - 1  % i = 2, m - 1
        k_prime(g) = (imag(g + 1) - imag(g - 1)) / (2 * h);
    elseif g == 3 || g == i - 2  % i = 3, m - 2
        k_prime(g) = (8 * (imag(g + 1) - imag(g - 1)) - (imag(g + 2)…
                     - imag(g - 2))) / (12 * h);
    else
        k_prime(g) = (45 * (imag(g + 1) - imag(g - 1)) - 9 *…
                     (imag(g + 2) - imag(g - 2)) + (imag(g + 3) -…
                     imag(g - 3))) / (60 * h);
    end
I_m(g) = (1 / pi) * h * k_prime(g);
end

delta_n = I_c + I_p + I_m;
real = delta_n + n_inf;
```

C.2 SIMULATED ANNEALING PROGRAM

A simulated annealing algorithm with the Metropolis criterion was written to identify absorbance spectra composed of Gaussian peaks that provide target index and absorbance values at 193 nm and 589 nm. A program using the simulated annealing algorithm was written in MATLAB R2006a by Saul Lee. The Signal Processing Toolbox (Version 6.5) is required to calculate the Hilbert transform. This program is given by:

immersion_fit_guassian.m

```
function [ntest,ktest,lambdarange,nmin,kmin,Ehatminerror,Einfatmin,
          An1atmin,En1atmin,Brn1atmin,An2atmin,En2atmin,Brn2atmin,
          An3atmin,En3atmin,Brn3atmin,Tfinal,Tatmin,stepmin,Tinitial] =
          immersion_fit_gaussian(N,Tinitial,Tincrement,Tmax,Tmin,
```

```
        accept_rate)

%   Subfunctions:   'realpart' - calculates epsilon1 given the
%                    parameters
%                   'imaginarypart' - calculates epsilon2 given the
%                    parameters
%                   'calcn' - calculates n from epsilon1 and epsilon2
%                   'calck' - calculates k from epsilon1 and epsilon1
%                   'find_error' - calculates the error used in the
%                    metropolis comparison
%   Inputs:         'N'- the number of trials
%                   'Tinitial' - the initial "temperature" of annealing
%                   'Tincrement' - the temperature increment change at
%                    each step of the annealing schedule
%                   'Tmax' - the maximum temperature in the schedule
%                   'Tmin' - the minimum temperature in the schedule
%                   'accept_rate' is the rate of acceptances to the
%                    metropolis condition before the incremental change
%                    is applied to the temperature
%   Outputs:        'n_test' - a vector containing the index of
%                    refraction at the end of the run
%                   'k_test' - a vector containing the absorptivities
%                    at the end of the run
%                   'lambdarange' - the range of wavelengths used in
%                    the calculations of n and k
%                   'nmin' - a matrix containing the index of
%                    refraction at each minimum error encountered
%                   'kmin' - a matrix containing the absorptivities
%                    at each minimum error encountered
%                   'Ehatminerror' - a vector containing the error
%                    to the target Ehat at each minimum error
%                    encountered
%                   'Einfatmin' - a vector containing the values for
%                    eoffset at each minimum error encountered
%                   'Aniatmin' - a vector containing the values for Ani
%                    at each minimum error encountered
%                   'Eniatmin' - a vector containing the values for Eni
%                    at each minimum error encountered
%                   'Brniatmin' - a vector containing the values for
%                    Brni at each minimum error encountered
%                   'Tfinal' - the final temperature at the end of the
%                    run
%                   'Tatmin' - a vector containing the values for T
%                    at each minimum error encountered
%                   'stepmin' - a vector containing the values for the
%                    step at each minimum error encountered
%                   'Tinitial' - the initial temperature

%==================================
%       Constants Section
%==================================

% define the ranges for the equations
EinfMIN = 1;
EinfMAX = 1.8;
An1MIN = 0.2;
An1MAX = 0.7;
En1MIN = 7.5;
En1MAX = 8;
Brn1MIN = 0.3;
```

```
Brn1MAX = 0.7;
An2MIN = 0.35;
An2MAX = 0.8;
En2MIN = 8;
En2MAX = 9.5;
Brn2MIN = 0.401;
Brn2MAX = 1;
An3MIN = 0.51;
An3MAX = 1;
En3MIN = 9.5;
En3MAX = 11;
Brn3MIN = 0.71;
Brn3MAX = 1;

lambdaMIN = 10;
lambdaMAX = 2000;
ntarget_193 = 1.475;
ktarget_193 = 3.62e-7;
ntarget_589 = 1.333;
ktarget_589 = 9.63e-9;

numberofpoints = 995;
lambdarange = linspace(lambdaMIN,lambdaMAX,numberofpoints);

global eps2 eps1
eps2 = zeros(1,numberofpoints);
eps1 = zeros(1,numberofpoints);

%==================================
%   Initialization Section
%==================================

% initialize the test values to generate the base case

Einf = EinfMIN;
An1 = An1MIN;
En1 = En1MIN;
Brn1 = Brn1MIN;
An2 = An2MIN;
En2 = En2MIN;
Brn2 = Brn2MIN;
An3 = An3MIN;
En3 = En3MIN;
Brn3 = Brn3MIN;
T = Tinitial;

% initialize min values

Einfatmin = Einf;
An1atmin = An1;
En1atmin = En1;
Brn1atmin = Brn1;
An2atmin = An2;
En2atmin = En2;
Brn2atmin = Brn2;
An3atmin = An3;
En3atmin = En3;
Brn3atmin = Brn3;
Tatmin = Tinitial;
```

```
% calculate initial values
eps1 = realpart(Einf,An1,En1,Brn1,An2,En2,Brn2,An3,En3,Brn3);
eps2 = imaginarypart(An1,En1,Brn1,An2,En2,Brn2,An3,En3,Brn3);
eps1_193 = eps1(1,91); % eps1 value at 193
eps2_193 = eps2(1,91); % eps2 values at 193
eps1_589 = eps1(1,296); % eps1 value at 589
eps2_589 = eps2(1,296); % eps2 value at 589
n_193 = calcn(eps1_193, eps2_193); % calculate n at 193 nm
k_193 = calck(eps1_193, eps2_193); % calculate k at 193 nm
n_589 = calcn(eps1_589, eps2_589); % calculate n at 589 nm
k_589 = calck(eps1_589, eps2_589); % calculate k at 589 nm

Ehaterror = find_error(n_193, k_193, n_589, k_589, ntarget_193,
ktarget_193, ntarget_589, ktarget_589);
Ehatminerror(1) = Ehaterror;

% initialize counters
totalaccepts = 0;   % keep track of the total acceptances
current_trials = 0; % keep track of the number of trials at a current
                    % temperature
current_rate = 0;   % keep track of the rate of acceptance at a current
                    % temperature
min_count = 1;      % index for the number of minimum cases encountered
accept_count = 0;   % keep track of acceptances at a current
                    % temperature

%===================================
%   Monte Carlo Section
%===================================

for m=1:N

    % setup/reset trial data
    Ehattrial = 0;
    Einftrial = Einf;
    An1trial = An1;
    En1trial = En1;
    Brn1trial = Brn1;
    An2trial = An2;
    En2trial = En2;
    Brn2trial = Brn2;
    An3trial = An3;
    En3trial = En3;
    Brn3trial = Brn3;

    % randomly pick and vary parameter
    p1 = rand;  % generate random number, the first number determines
                % which parameter will be varied
    p2 = rand;  % generate random number, the second number generates
                % the value

    if (p1 < 0.1)
        Einftrial = p2 * (EinfMAX - EinfMIN) + EinfMIN;
    elseif (p1 < 0.2)
        An1trial = p2 * (An1MAX - An1MIN) + An1MIN;
    elseif (p1 < 0.3)
        En1trial = p2 * (En1MAX - En1MIN) + En1MIN;
    elseif (p1 < 0.4)
        Brn1trial = p2 * (Brn1MAX - Brn1MIN) + Brn1MIN;
    elseif (p1 < 0.5)
```

```
    An2trial = p2 * (An2MAX - An2MIN) + An2MIN;
elseif (p1 < 0.6)
    En2trial = p2 * (En2MAX - En2MIN) + En2MIN;
elseif (p1 < 0.7)
    Brn2trial = p2 * (Brn2MAX - Brn2MIN) + Brn2MIN;
elseif (p1 < 0.8)
    An3trial = p2 * (An3MAX - An3MIN) + An3MIN;
elseif (p1 < 0.9)
    En3trial = p2 * (En3MAX - En3MIN) + En3MIN;
else
    Brn3trial = p2 * (Brn3MAX - Brn3MIN) + Brn3MIN;
end

% calculate the trial epsilon values based on the new set of
% parameters

eps1trial = realpart(Einftrial,An1trial,En1trial,Brn1trial,
An2trial,En2trial,Brn2trial,An3trial,En3trial,Brn3trial);
eps2trial = imaginarypart(An1trial,En1trial,Brn1trial,An2trial,
En2trial,Brn2trial,An3trial,En3trial,Brn3trial);
eps1trial_193 = eps1trial(1,91); % eps1 value at 193
eps2trial_193 = eps2trial(1,91); % eps2 value at 193
eps1trial_589 = eps1trial(1,296); % eps1 value at 589
eps2trial_589 = eps2trial(1,296); % eps2 value at 589
ntrial_193 = calcn(eps1trial_193, eps2trial_193); % calc n at 193
ktrial_193 = calck(eps1trial_193, eps2trial_193); % calc k at 193
ntrial_589 = calcn(eps1trial_589, eps2trial_589); % calc n at 589
ktrial_589 = calck(eps1trial_589, eps2trial_589); % calc k at 193

% calculate the error of the base on the new set of parameters

Ehattrialerror = find_error(ntrial_193, ktrial_193, ntrial_589,
ktrial_589, ntarget_193, ktarget_193, ntarget_589, ktarget_589);
delta = Ehattrialerror - Ehaterror;  % calculate the change in
                                     % error

% apply the metropolis criteria

 if (delta <= 0)
    % if the change is negative, then the move is accepted and the
    % current set of parameters is updated to the trial parameters
    Einf = Einftrial;
    An1 = An1trial;
    En1 = En1trial;
    Brn1 = Brn1trial;
    An2 = An2trial;
    En2 = En2trial;
    Brn2 = Brn2trial;
    An3 = An3trial;
    En3 = En3trial;
    Brn3 = Brn3trial;

    Ehaterror = Ehattrialerror;
    accept_count = accept_count + 1;
    totalaccepts = totalaccepts + 1;

 else
    % else a probability of acceptance is calculated and the
```

```
        % acceptance
        % is determined by a random number

        prob = exp(-delta / T);
        q = rand;
        if (q <= prob)
            % if the random number q is less than or equal to the
            % probability, then the move is accepted

            Einf = Einftrial;
            An1 = An1trial;
            En1 = En1trial;
            Brn1 = Brn1trial;
            An2 = An2trial;
            En2 = En2trial;
            Brn2 = Brn2trial;
            An3 = An3trial;
            En3 = En3trial;
            Brn3 = Brn3trial;

            Ehaterror = Ehattrialerror;
            accept_count = accept_count + 1;
            totalaccepts = totalaccepts + 1;
        end
    end

    current_trials = current_trials + 1;
    current_rate = accept_count / current_trials;

    if (mod(m,100) == 0)
        % checks the rate at a set number of steps to see if the rate
        % is above or below the target acceptance rate.  If it is
        % below, then the T will be raised by Tincrement, and if it is
        % above then the T
        % will be decreased by Tincrement

        if (current_rate < accept_rate)
            accept_count = 0;   % reset the counts
            current_trials = 0;
            T = T + Tincrement;
            if (T > Tmax)
                T = Tmax;
            end
        else
            accept_count = 0;
            current_trials = 0;
            T = T - Tincrement;
            if (T < Tmin)
                T = Tmin;
            end
        end
    end

    if (Ehaterror < Ehatminerror(min_count))
        % check if the error is the minimum, if so the set of
        % parameters will be outputed

        Ehatminerror(min_count) = Ehaterror;
        Einfatmin(min_count) = Einf;
        An1atmin(min_count) = An1;
```

```
        En1atmin(min_count) = En1;
        Brn1atmin(min_count) = Brn1;
        An2atmin(min_count) = An2;
        En2atmin(min_count) = En2;
        Brn2atmin(min_count) = Brn2;
        An3atmin(min_count) = An3;
        En3atmin(min_count) = En3;
        Brn3atmin(min_count) = Brn3;
        Tatmin(min_count) = T;

        eps1 = realpart(Einf,An1,En1,Brn1,An2,En2,Brn2,An3,En3,Brn3);
        eps2 = imaginarypart(An1,En1,Brn1,An2,En2,Brn2,An3,En3,Brn3);
        nmin = zeros(min_count, numberofpoints);
        kmin = zeros(min_count, numberofpoints);


        for j = 1:numberofpoints
            nmin(min_count,j) = calcn(eps1(1,j), eps2(1,j));
            kmin(min_count,j) = calck(eps1(1,j), eps2(1,j));
        end

        min_count = min_count + 1;
        Ehatminerror(min_count) = Ehaterror;    % set up the error for
                                                % the next check
    end
end

        Ehatminerror(min_count) = ''; % remove the last line from the
                                      % Ehatminerror

        % outputs the final set of parameters

        eps1 = realpart(Einf,An1,En1,Brn1,An2,En2,Brn2,An3,En3,Brn3);
        eps2 = imaginarypart(An1,En1,Brn1,An2,En2,Brn2,An3,En3,Brn3);
        ntest = zeros(1, numberofpoints);
        ktest = zeros(1, numberofpoints);

        for j = 1:numberofpoints
            ntest([j]) = calcn(eps1(1,j), eps2(1,j));
            ktest([j]) = calck(eps1(1,j), eps2(1,j));
        end

        Tfinal = T;
end

function [eps1] = realpart(Einf,An1,En1,Brn1,An2,En2,Brn2,An3,En3,Brn3)
% calculates epsilon1 term with the Hilbert transform of the Gaussian
% epislon2 term

global eps1 eps2
lambdaMIN = 10;
lambdaMAX = 2000;
numberofpoints = 995;   % number of points to use when plotting
lambda = linspace(lambdaMIN,lambdaMAX,numberofpoints);
E = 1240 ./ lambda;
eps2 = zeros(1, numberofpoints);

    for j = 1:numberofpoints
        eps2([j]) = An1*exp(-((E(j) - En1)/(Brn1))^2) - An1*exp(-((E(j)
                    + En1)/(Brn1))^2) + An2*exp(-((E(j) - En2)…
```

```
                    /(Brn2))^2) - An2*exp(-((E(j) + En2)/(Brn2))^2) +…
                    An3*exp(-((E(j) - En3)/(Brn3))^2) - An3*exp(-…
                    ((E(j)+ En3)/(Brn3))^2);
    end

    e = hilbert(eps2);
    eps1 = imag(e) + Einf;
end



function [eps2] = imaginarypart(An1,En1,Brn1,An2,En2,Brn2,An3,En3,Brn3)
% calculates the epsilon2 term using a Gaussian function

global eps1 eps2
lambdaMIN = 10;
lambdaMAX = 2000;
numberofpoints = 995;   % number of points to use when plotting
lambda = linspace(lambdaMIN,lambdaMAX,numberofpoints);
E = 1240 ./ lambda;
eps2 = zeros(1, numberofpoints);

    for j = 1:numberofpoints
        eps2([j]) = An1*exp(-((E(j) - En1)/(Brn1))^2) - An1*exp(-((E(j)
                    + En1)/(Brn1))^2) + An2*exp(-((E(j) - En2)…
                    /(Brn2))^2) - An2*exp(-((E(j) + En2)/(Brn2))^2) +…
                    An3*exp(-((E(j) - En3)/(Brn3))^2) - An3*exp(-…
                    ((E(j)+ En3)/(Brn3))^2);
    end
end

function [n] = calcn(epsilon1, epsilon2)
%calculates n from epsilon1 and epsilon2

    n = (0.5*((epsilon1^2 + epsilon2^2)^0.5 + epsilon1))^0.5;
end

function [k] = calck(epsilon1, epsilon2)
%calculates k from epsilon1 and epsilon2

    k = (0.5*((epsilon1^2 + epsilon2^2)^0.5 - epsilon1))^0.5;
end

function [overallerror] =  find_error(n_193,k_193,n_589,k_589,
          ntarget_193,ktarget_193, ntarget_589, ktarget_589)
% error calculation between the target and calculated n and k at 193
% and 589

overallerror = ((n_193 - ntarget_193) / ntarget_193) ^2 + ((k_193 -…
               ktarget_193) / ktarget_193) ^ 2 + ((n_589 -…
               ntarget_589) / ntarget_589) ^ 2 + abs((k_589 -…
               ktarget_589));
end
```

C.3 CONSTRAINT SUBROUTINES

Additional constraints were added to the simulated annealing program to try to limit the acceptance of cases to physically realistic solutions. These constraints were developed based on the Handbook of Optical Constants data for the index and absorbance of water.[2] The first program restricts the λ_{max} value to wavelengths lower than 100 nm, in the region of the spectrum which contains the ionization peaks. Based on the value returned by this program, the trial spectra would be either rejected or subject to the simulated annealing schedule. This code was written in MATLAB and is given by:

find_max.m

```
function [max_e2] = find_max(An1,En1,Brn1,An2,En2,Brn2,An3,En3,Brn3)
% checks to make sure the trial peaks are not larger than the
% ionization peaks

lambdaMIN = 10;
lambdaMAX = 2000;
numberofpoints = 995;   % number of points to use when plotting
lambda = linspace(lambdaMIN,lambdaMAX,numberofpoints);

E = 1240 ./ lambda;
An_IP_A = 1.5083;
En_IP_A = 13.015;
Brn_IP_A = 1.74;
An_IP = 1.1047;
En_IP = 15.906;
Brn_IP = 2.17;
An_IP_1 = 0.4908;
En_IP_1 = 18.649;
Brn_IP_1 = 1.715;
An_IP_2 = 0.53114;
En_IP_2 = 21.527;
Brn_IP_2 = 3.59;
An_IP_3 = 0.31039;
En_IP_3 = 27.01;
Brn_IP_3 = 4.174;

eps2_IP = zeros(1, numberofpoints);
eps2_trial = zeros(1, numberofpoints);

    for j = 1:numberofpoints

        eps2_IP([j]) = An_IP_A*exp(-((E(j) - En_IP_A)/(Brn_IP_A))^2) -…
                       An_IP_A*exp(-((E(j) + En_IP_A)/(Brn_IP_A))^2) +…
                       An_IP_1*exp(-((E(j) - En_IP_1)/(Brn_IP_1))^2) -…
                       An_IP_1*exp(-((E(j) + En_IP_1)/(Brn_IP_1))^2) +…
                       An_IP*exp(-((E(j) - En_IP)/(Brn_IP))^2) -An_IP*…
                       exp(-((E(j) + En_IP)/(Brn_IP))^2) + An_IP_2*…
                       exp(-((E(j) - En_IP_2)/(Brn_IP_2))^2) -An_IP_2*…
```

```
                      exp(-((E(j) + En_IP_2)/(Brn_IP_2))^2) +An_IP_3*…
                      exp(-((E(j) - En_IP_3)/(Brn_IP_3))^2) -An_IP_3*…
                      exp(-((E(j) + En_IP_3)/(Brn_IP_3))^2);

        eps2_trial([j]) = An1*exp(-((E(j) - En1)/(Brn1))^2) -An1*exp(-…
                          ((E(j) + En1)/(Brn1))^2) + An2*exp(-((E(j) -…
                          En2)/(Brn2))^2) - An2*exp(-((E(j) + En2)/…
                          (Brn2))^2) + An3*exp(-((E(j) - En3)/(Brn3))…
                          ^2) - An3*exp(-((E(j) + En3)/(Brn3))^2);
    end

IP = max(eps2_IP); % maximum e2 value for the ionization peaks
trial = max(eps2_trial); % maximum e2 value for the trial spectra

if IP >= trial
    max_e2 = 1; % accept for simulated annealing
else
    max_e2 = -1; % reject trial spectrum
end

end
```

An additional MATLAB program was written to further restrict the trial peak sizes and positions. The minimum separation between each parameter is based on the Handbook of Optical Constants data for water.[2] The MATLAB subroutine written to evaluate the trial spectrum for these characteristics is given by:

sep_peak.m

```
function [sep_num_trial] = sep_peak(An1,An2,An3,En1,En2,En3,Brn1,Brn2,
Brn3)
% Calculates differences in peak positions to try to make a more
% continuous spectrum
% An and Brn must increase with decreasing wavelength
% minimum peak separation distances are also required based on En

% minimum values based on literature data for water
deltaAn_min = 0.12;
deltaEn_min12 = 0.5;
deltaEn_min23 = 1;
deltaBrn_min12 = 0.1;
deltaBrn_min23 = 0.3;

% differences between each parameter
deltaAn12 = An2 - An1;
deltaAn23 = An3 - An2;
deltaEn12 = En2 - En1;
deltaEn23 = En3 - En2;
deltaBrn12 = Brn2 - Brn1;
deltaBrn23 = Brn3 - Brn2;
deltaAn = [deltaAn12, deltaAn23];

% An
```

```
z = min(deltaAn);
if (z >= deltaAn_min)
    valAn = 0.5;
else
    valAn = 0;
end

% En
if (deltaEn12 >= deltaEn_min12) && (deltaEn23 >= deltaEn_min23)
    valEn = 0.5;
else
    valEn = 0;
end

% Brn
if (deltaBrn12 >= deltaBrn_min12) && (deltaBrn23 >= deltaBrn_min23)
    valBrn = 0.5;
else
    valBrn = 0;
end

sep_num_trial = valAn + valEn + valBrn; % reject trial solution if <1.5

end
```

C.4 REFERENCES

1. Ohta, K. and Ishida, H., *Comparison among several numerical integration methods for Kramers-Kronig transformation.* Appl. Spectrosc., 1988. **42**(6): p. 952-7.

2. Querry, M. R., Wieliczka, D. M. and Segelstein, D. J., *Water (H2O).* Handbook of Optical Constants of Solids II, Palick, E. D. 1991, New York: Academic Press, Inc. pp. 1059 - 1077.

Appendix D: Transport Characteristics of Varying Molecular Weight Poly(ethylene glycol) diacrylate Hydrogels

D.1 INTRODUCTION

Hydrogels are three dimensional polymeric networks which contain a fluid, such as water, within the polymer matrix. Hydrogels typically possess biocompatibility, easily manipulable physical properties, and tunable mass transport characteristics.[1, 2] Hydrogels are used as ophthalmic[3] and vascular prostheses,[4] controlled release systems,[2] and soft tissue replacements and scaffolds.[5] Hydrogels can also be used as biochip sensors since probe DNA molecules can diffuse into these hydrogels and can be used for rapid detection of DNA defects.[6] The material properties of a hydrogel can be manipulated by changing the nature and molecular weight of the monomer, adjusting the mass percent of monomer in the pre-polymer solution,[7] or incorporating porogens during polymerization.[8] The transport of ions and solutes within the liquid phase (solvent that is dispersed within the polymer matrix) of these gels is of interest for many applications. For hydrogels used as drug delivery systems or as biosensors, the mass transport characteristics of species into and out of the gel determine the drug release or sensor detection time scale.

This project was designed to understand mass transport in a hydrogel for a biochip sensor application.[6] The analysis time of the biochip sensor array is determined by the diffusion rates of different species of probe DNA molecules into and out of the hydrogels. The efficacy of the biochip sensor array depends on the response time of the sensor and thus mass transport of the target species into the gel. This experiment studied the tradeoff between strong material properties in a lower molecular weight gel and fast mass transport in a higher molecular weight gel to help identify the ideal biochip material. This study quantifies the mass transport characteristics of various molecular weight and water content hydrogels. The hydrogels studied in this project were made of various molecular weight and water content poly(ethylene glycol) diacrylate (PEG-da). The hydrogels are formed by crosslinking the PEG monomers at the acrylate groups using UV light. PEG-da is the hydrogel material used for many applications, including tissue engineering,[9] drug delivery,[2] and biosensor arrays.[6]

The objective of this work was to fully characterize the relationship between the structure of the hydrogel and its transport properties. Scanning electrochemical microscopy (SECM) was used to measure the diffusion coefficient of an electroactive species, ferrocene methanol (FcMeOH), in the hydrogel. These diffusion characteristics can be used to understand the effect of structure and formulation changes on the transport characteristics of species within the hydrogel.

D.2 SCANNING ELECTROCHEMICAL MICROSCOPY

A number of different techniques have been used to study diffusion in hydrogels. Diffusion coefficients can generally be determined by creating a concentration gradient across a sample of known area and measuring the change in concentration of diffusing species after a specific time. For a hydrogel, classical techniques are challenging since hydrogels can swell over time such that the thickness is not constant. The diffusing species can get trapped within the pores of the polymer matrix or adsorb to the gel, distorting the final concentration measurement. SECM[10] is an alternative method that has been used to measure the diffusion coefficient in a hydrogel.[11, 12] This method is particularly advantageous since swelling of the gel and the concentration of the diffusing species does not affect the measurement.

A schematic of the setup used in SECM is given in Figure D.1. To perform the measurement, a potential is applied across a microelectrode (known as the working electrode) that has been inserted within the gel. The application of this potential causes a reduction, as in the Figure D.1 example, (or oxidation) reaction at the surface of the working electrode. Thus, as the species at the working electrode surface is reduced (or oxidized), the concentration of that species at the electrode surface is depleted, creating a concentration gradient between the oxidized (or reduced) species at the electrode surface and in the bulk gel. As diffusion takes place from the bulk gel to the working electrode surface, the transient current (i_T) due to the reduction (or oxidation) reaction is measured.

The SECM diffusion measurement is independent of both the size of the hydrogel and the concentration of the diffusing species and requires only knowledge of the radius of the microelectrode.[13] Since the hydrogel can swell and crack over time and due to the uncertainty in determining exact concentrations and lengths in these systems, SECM is an attractive method for measuring the diffusion characteristics of the gel. The shortcoming is that the diffusing species must be electroactive.

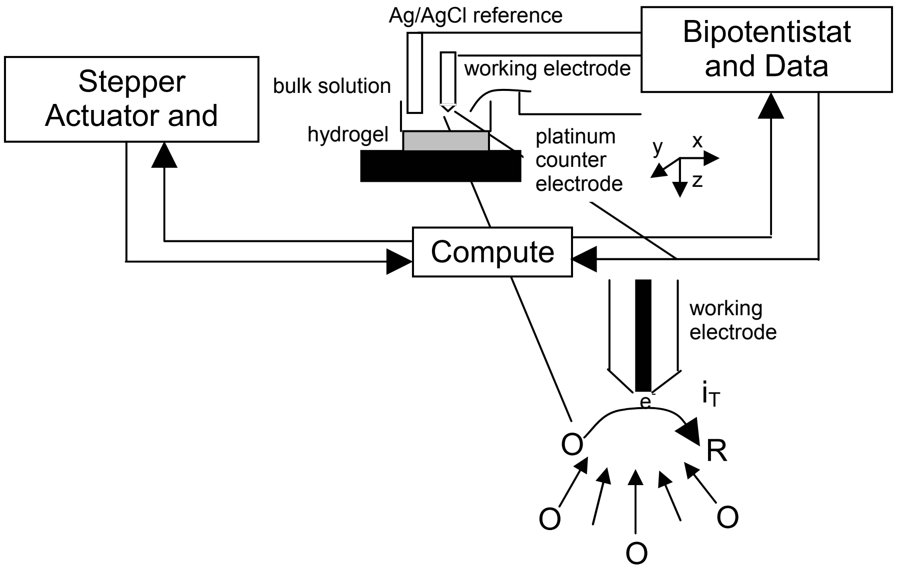

Figure D.1: Diagram of SECM diffusion measurement

D.3 EXPERIMENTAL DETAILS

D.3.1 Hydrogels

PEG-da polymers of different molecular weights (MW) were used to make the hydrogels. PEG-da with weight-average MWs 575 and 700 were purchased from Aldrich (Milwaukee, WI), MW 2000 and 4000 from Monomer-Polymer and Dajac Labs (Feasterville, PA), and MW 10000 from Sunbio Labs (Orinda, CA). The photoinitiator, 1-hydroxy-2-methyl-1-phenyl-1-propanone, (Darocur 1173), was obtained from Ciba Specialty Chemicals (Tarrytown, NY).

A pre-polymer solution of 1 vol % initiator, 30 to 70 vol % water, and the remainder polymer was prepared. The pre-polymer was exposed to broadband ultraviolet (UV) radiation from a 200-W high pressure mercury arc lamp from Newport Corporation – Oriel Instruments (Stratford, CT) until the hydrogel was fully polymerized. The bulb was housed in an Oriel shutter enclosure that collimated the radiation to approximately a 15 cm diameter area and filtered out wavelengths below 365 nm. An Oriel 68810 arc lamp power supply, coupled with an Oriel 68705 igniter, was used to power the bulb. The shutter was controlled by an Oriel 8160 timer. The minimum cure time to form the gel was determined empirically for each MW PEG-da. The exposure time required to form a stable gel ranged from 20 – 100 s for 500 – 1000 μL of pre-polymer solution using molds of 1500 μm thickness. To remove excess photoinitator or unreacted polymer, the gels were soaked in 5000 μL of water for at least 24 hours prior to diffusion measurements. Each of the gels had an approximate thickness of 1500 μm, with variations due primarily to different degrees of swelling based on MW.

The hydrogels were soaked in 40 mL of an aqueous solution of 1 mM FcMeOH and 0.1 M potassium chloride for approximately 24 hours prior to the diffusion coefficient measurement. During this 24 hour soak, the FcMeOH solution diffuses into the hydrogel. Argon was bubbled through the solution during this 24 time to prevent oxidation of FcMeOH.

D.3.2 Electrochemical Measurement

A CHInstruments 832C potentiostat was used for all electrochemical diffusion measurements. A stepper motor was used to control the position of the electrode relative to the hydrogel so that it could be inserted into the gel at the same depth for each measurement (ca. 100 µm into the gel). The hydrogel was immersed in an aqueous solution of 1 mM FcMeOH and 0.1 M potassium chloride throughout the experiment. The working electrode was a 25 µm diameter platinum microelectrode. The glass surrounding the platinum wire was polished to a conical shape with an electrode radius to glass radius ratio, RG = a/r_{glass}, of approximately 5 (determined optically). The reference electrode and counter electrode were an Ag/AgCl electrode and a platinum wire respectively.

Two electrochemical methods were used to characterize this system. The first is cyclic voltammetry (CV). This is a potential sweep method, in which the potential is first changed in the forward direction and then reversed to the starting potential, to obtain current versus potential data. The change in potential for the forward scan causes a reduction (oxidation) reaction and in the reverse direction causes the opposite, oxidation (reduction) reaction. The data obtained provide a measure of the hysteresis of the system and an understanding of how quickly the system returns to equilibrium. Chronoamperometry (CA) was also used. In CA a potential step is applied to the system to initiate a reduction (oxidation) reaction for 20 seconds. After the initial, sharp change in current, when the oxidized (reduced) species close to the working electrode surface is reduced (oxidized), a concentration gradient between the electrode surface and bulk develops so that the reaction at the electrode is controlled by diffusion, and the current becomes essentially constant. Once the reaction is controlled by diffusion, the current versus time data can be used to calculate the diffusion coefficient.[14] Examples of CA and CV data for the FcMeOH solution and a MW 700 hydrogel are given in Figure D.2. For both the CV and CA, the absolute current obtained at the highest potential is higher in the solution than in the hydrogel. Since the polymer matrix of the hydrogel blocks diffusion of FcMeOH, this result is expected.

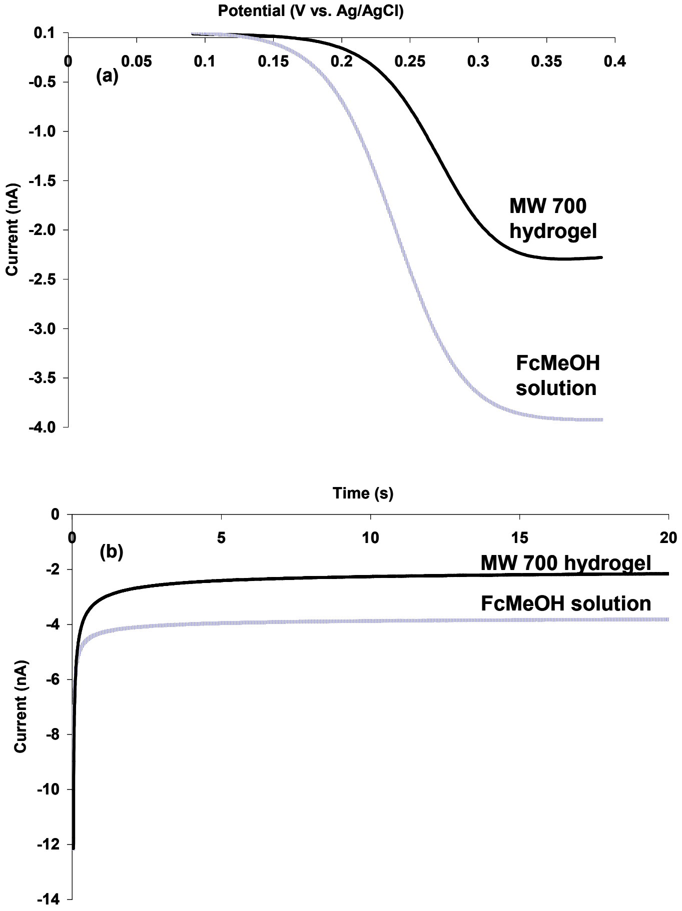

Figure D.2: Example CV (a) data for the forward direction potential sweep and CA (b) data for calculating the diffusion coefficient

D.3.2.1 Diffusion Coefficient Measurement and Calculation

CA data were collected approximately 100 μm within the hydrogel to calculate the diffusion coefficient. To prevent cracking of the hydrogel during the electrode insertion procedure, the electrode was inserted at a velocity of 1 μm/s. Bulk solution CA data were collected both before and after the hydrogel portion of the experiment at a sufficient distance above the hydrogel to avoid any influence of the hydrogel on the electrode response.

The diffusion coefficient can be calculated from the equation for the normalized diffusion-controlled current to an electrode of radius *a*,

$$i_d(t)/i_{d,ss} = (\pi^{1/2}/4)a(Dt)^{-1/2} + 1. \tag{D.1}$$

The steady state current ($i_{d,ss}$) is given by

$$i_{d,ss} = 4nFDCa. \tag{D.2}$$

Thus, the diffusion coefficient (D) is

$$D = \frac{\pi a^2}{16m^2} \tag{D.3}$$

In Equations D.1 – D.3, $i_d(t)$ is the transient current from the CA data, *a* is the radius of the electrode, *t* is time, *F* is the Faraday constant, *C* is the concentration of the diffusing species, and m is slope of line given by $i_d(t)/i_{d,ss}$ vs $t^{-1/2}$.[11, 13] Thus, the diffusion coefficient was calculated from the slope of $i_d(t)/i_{d,ss}$ vs $t^{-1/2}$, using the CA data.

Choosing an appropriate step time for chronoamperometry measurements depends upon the electrode radius and the diffusion coefficient of the electroactive species. At short times, the Faradaic current is complicated by charging current, making a quantitative analysis of this region of the chronoamperogram difficult. The long-time limit is governed primarily by thermal or density gradients that add a convective component to the current at the electrode.[15] For a 12.1 μm radius electrode, a step time of 20 seconds for CA measurements within a hydrogel falls into the intermediate time regime as defined by[13]

$$[10^{-4} < \frac{Dt}{a^2} < 10^2]. \tag{D.4}$$

For these intermediate times, Equation D.1 is not the most accurate method for predicting the diffusion coefficient. A more precise description of the current to a microdisk has been suggested by Shoup and Szabo and is given by[16]

$$\frac{i_d(t)}{i_{d,ss}} = 0.785 + 0.443\tau^{-1/2} + 0.215\exp(-0.391\tau^{-1/2}) \tag{D.5}$$

where $\tau = Dt/a^2$. However, if the $i_{d,ss}$ parameter is used as an adjustable parameter such that the intercept of the $i_d(t)/i_{d,ss}$ vs $t^{-1/2}$ plot is equal to 1 and the area determination procedure described previously is followed, the diffusion coefficients obtained from Equations D.1 and D.4 compare favorably. Thus, Equation D.1 was used to calculate the diffusion coefficient using an $i_{d,ss}$ value obtained by fitting the intercept to 1 with a linear regression analysis. Since the measurement at very short times is complicated by charging current, the first 75 data points collected (from time = 0 to time = 370 ms) in the CA experiment were not included in the analysis. After this time period, mass transfer in the system is controlled purely by diffusion.

D.3.2.2 Electrode Area

To calculate the diffusion coefficient accurately, an accurate measurement of the working electrode area is needed. The nominal radius of the working electrode is 12.5 µm, but dirt and other impurities can block some of the electrode surface area. The working electrode was polished using Buehler Micropolish Alumina (0.3 µm and 0.05 µm) on a Buehler 2-7/8 Microcloth PSA and then rinsed and sonicated to remove any residual alumina particles prior to each experiment. While this polishing technique removes dirt, an electrochemical radius measurement technique was also used to precisely calculate the electrode radius prior to each diffusion measurement. A 4 mM potassium ferrocyanide, 1 M potassium chloride aqueous solution was used as a standard.[17-19] The oxidation of this solution was used to calculate a diffusion coefficient, according to the procedure described in D.3.3.1, which was then compared to the literature value of this solution (6.32×10^{-6} cm^2/s)[20] and used to determine the electrode radius. With this method, averaging the data obtained for each experiment, an electrochemical area corresponding to an electrode radius of 12.1 ± 0.7 µm was obtained.

D.3.3 Equilibrium Water Content

The degree of swelling was characterized by measuring the equilibrium water content (EWC) of each gel. The swollen mass was measured after soaking for at least 24 h in water at ambient temperature. The gels were then dried in a vacuum oven at 50 ˚C for 24 h and reweighed. The EWC of each gel was calculated according to the equation

$$EWC = \frac{m_s - m_d}{m_s} \tag{D.6}$$

where m_s is the mass of the swollen gel and m_d is the mass of the dried gel.

D.4 RESULTS AND DISCUSSION

D.4.1 Diffusion Coefficient

The diffusion coefficient of FcMeOH in PEG-da hydrogels of varying molecular weight was measured. At least four hydrogels were tested for each MW, and CA and CV data were collected at three different spots (ca. 100 µm into the hydrogel) for each gel. The average value for the diffusion coefficient of FcMeOH in PEG-da hydrogels of varying molecular weight is given in Figure D.3 and Table D.1. The diffusion coefficient increases sharply between MW 700 and 2000 and then is relatively constant from MW 2000 to 10000, suggesting that a critical MW exists above which the diffusion coefficient is constant. To understand the relationship between the void spaces in the gel and MW, the equilibrium water content (EWC) was measured; this data is given in Table D.1. Like the diffusion coefficient, the EWC also increases sharply between the MW 700 and 2000 hydrogels and then remains essentially constant with increasing MW. The similar trends in the diffusion coefficient and EWC data indicate that material transport occurs through the solution contained within the polymer matrix of the hydrogel. Hydrogels with higher porosity, or water content, have higher diffusion coefficients up to a critical MW; for the system of PEGs measured, $MW_{crit} = 2000$.

The diffusion coefficient in MW 2000 hydrogels with different vol % of water in the pre-polymer solution was also measured. At least three hydrogels were measured for each vol%, and both CA and CV data were obtained at three different spots approximately 100 μm within the hydrogel. The average data are given in Figure D.4 and Table D.2. The diffusion coefficient increases linearly with increasing vol % of water. With decreased water content in the pre-polymer solution, the hydrogel forms a tighter, denser polymer network, as indicated by the EWC in each of these gels, Table D.2. The denser the polymer network, the lower the diffusion coefficient.

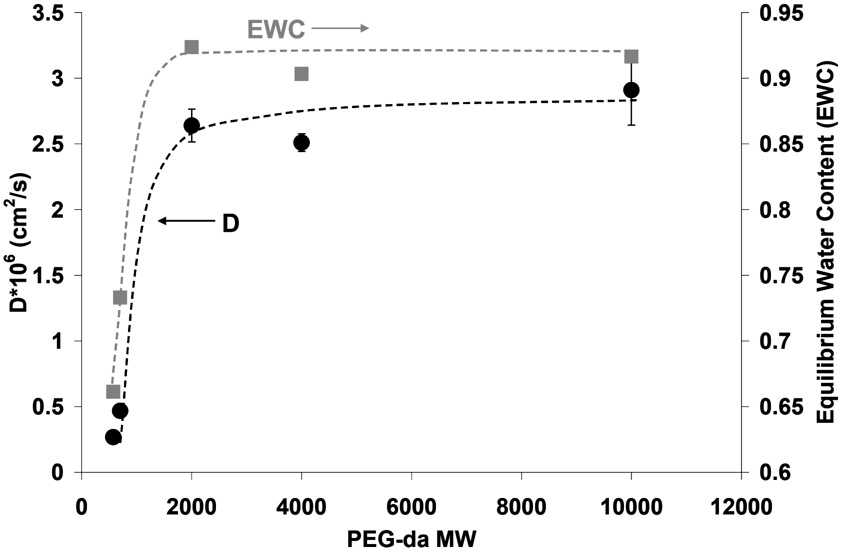

Figure D.3: Diffusion coefficient of FcMeOH (black circles) and equilibrium water content (gray squares) dependence on the MW of a PEG-da hydrogel

Table D.1: Diffusion coefficient and equilibrium water content (EWC) values of FcMeOH in varying MW PEG hydrogels

PEG MW (g/mol)	Dx10^6 (cm^{2}s^{-1}) ± 95% confidence limits	Equilibrium Water Content (EWC)	# of gels
575	0.267 ± 0.0353	0.661	4
700	0.467 ± 0.0456	0.733	5
2000	2.64 ± 0.125	0.924	5
4000	2.51 ± 0.067	0.903	5
10000	2.91 ± 0.267	0.917	5
D$_{solution}$x10^6 average* = 5.68 ± 0.174 cm^{2}s^{-1}			

*Literature values of the diffusion of FcMeOH solutions have been reported: 7.8x10^{-6} cm^2/s,[18] 6.1x10^{-6} cm^2/s,[21] and 6.7x10^{-6} cm^2/s.[22]

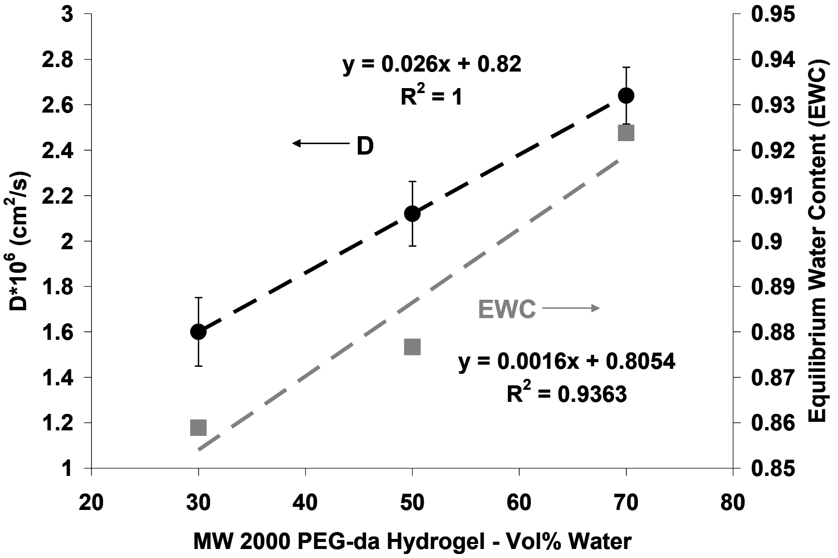

Figure D.4: Diffusion coefficient (black circles) and EWC (gray squares) dependence on vol% water in the pre-polymer for a MW 2000 PEG-da hydrogel

Table D.2: Diffusion coefficient of FcMeOH in MW 2000 hydrogels with varying vol % water in the pre-polymer

Vol % Water in MW 2000 PEG hydrogels	Dx10^6 (cm^2/s) ± 95% confidence limits	Equilibrium Water Content (EWC)	# of gels
30%	1.60 ± 0.151	0.924	3
50%	2.12 ± 0.142	0.877	3
70%	2.64 ± 0.125	0.959	5
$D_{solution}$x10^6 average = 5.50 ± 0.439 cm^2s^{-1}			

D.4.2 Electrochemical Procedure

The current as a function of distance data collected during the insertion and retraction of the electrode tip can be used to verify that this procedure is a viable measurement of the current within a hydrogel. These data show that the structure of the gel is unaffected by insertion of the microelectrode tip and that the electrode is not fouled during the experiment.

Examples of the insertion and retraction curves for a MW 700 hydrogel are given in Figure D.5. The current drops significantly just before entering the gel and decreases with increasing depth into the hydrogel. A decrease in current as the electrode is about to enter the hydrogel is expected since the hydrogel blocks diffusion to the electrode. The current decreases with increasing distance into the hydrogel simply because the insertion curve is obtained under non-steady state conditions. This behavior indicates that the electrode is penetrating the gel rather than creating a hole at the surface. Additionally, the current measurement within the hydrogel does not vary significantly between the insertion and retraction curves, indicating that the gel is unaffected by the microelectrode tip insertion. There is a slight difference between the position at which the electrode is removed from the hydrogel and at which it enters. As the microelectrode tip is removed from the hydrogel, the spot slowly fills with solution, creating a slight discrepancy in the current.

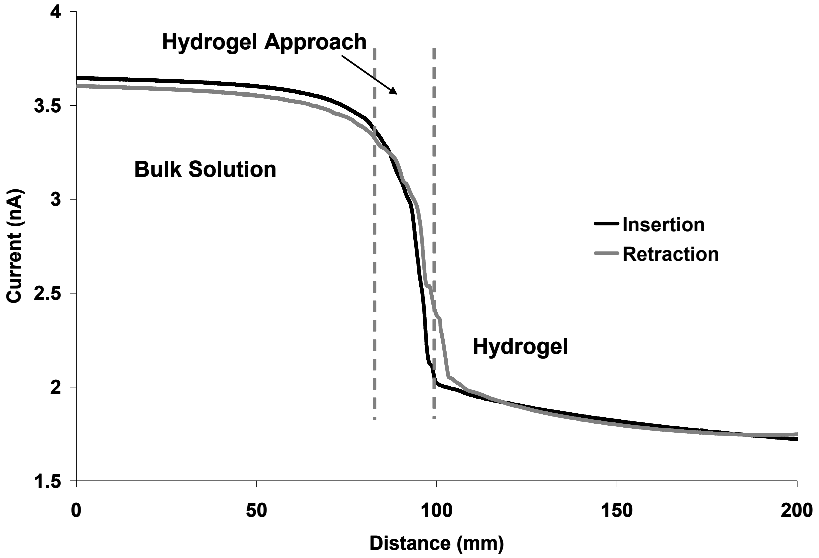

Figure D.5: Insertion and retraction curves for a MW 700 hydrogel

D.5 CONCLUSIONS

The diffusion coefficient of FcMeOH in PEG-da hydrogels of varying MW and water content has been measured. The diffusion of FcMeOH increases with increasing MW until a MW_{crit} at which further increases in MW do not significantly affect the transport characteristics and increase the diffusion coefficient. MW_{crit} for this system is 2000 g/mol. This behavior is also observed in the EWC of the gels. The diffusion coefficient is directly related to the amount of water contained in the dispersed phase of the hydrogel. A linear increase in the diffusion coefficient and EWC with vol % water in the pre-polymer solution was also observed. This electrochemical technique has been demonstrated previously for diffusion coefficient measurement in a gel and has also been used in this system to quickly and accurately evaluate the transport properties of a PEG-da hydrogel. These data can be used to qualitatively predict the diffusion of additional species within a PEG-da hydrogel. Increasing the molecular weight and water content in the pre-polymer solution should increase diffusion within the hydrogel. Diffusion decreases with lower molecular weight hydrogels with a decreased amount of water in the pre-polymer solution.

D.6 REFERENCES

1. Cruise, G. M., Scharp, D. S. and Hubbell, J. A., *Characterization of permeability and network structure of interfacially photopolymerized poly(ethylene glycol) diacrylate hydrogels.* Biomaterials, 1998. **19**(14): p. 1287-94.

2. Peppas, N. A., Keys, K. B., Torres-Lugo, M. and Lowman, A. M., *Poly(ethylene glycol)-containing hydrogels in drug delivery.* J. Control. Release, 1999. **62**(1-2): p. 81-87.

3. Goda, T., Watanabe, J., Takai, M. and Ishihara, K., *Water structure and improved mechanical properties of phospholipid polymer hydrogel with phosphorylcholine centered intermolecular cross-linker.* Polymer, 2006. **47**(4): p. 1390-1396.

4. Karrer, L., Duwe, J., Zisch, A. H., Khabiri, E., Cikirikcioglu, M., Napoli, A., Goessl, A., Schaffner, T., Hess, O. M., Carrel, T., Kalangos, A., Hubbell, J. A. and Walpoth, B. H., *PPS-PEG surface coating to reduce thrombogenicity of small diameter ePTFE vascular grafts.* Int. J. Artif. Organs, 2005. **28**(10): p. 993-1002.

5. Yang, F. W., C.G.; Wang, D.; Lee, H.; Manson, P.M.; Elisseeff, J., *The Effect of Incorporating RGD Adhesive Peptide in Polyethylene Glycol Diacrylate Hydrogel on Osteogenesis of Bone Marrow Stromal Cells.* Biomaterials, 2005. **26**(30): p. 5991-5998.

6. Meiring, J. E., Schmid, M. J., Grayson, S. M., Rathsack, B. M., Johnson, D. M., Kirby, R., Kannappan, R., Manthiram, K., Hsia, B., Hogan, Z. L., Ellington, A. D., Pishko, M. V. and Willson, C. G., *Hydrogel Biosensor Array Platform Indexed by Shape.* Chem. Mater., 2004. **16**(26): p. 5574-5580.

7. Lin-Gibson, S., Jones, R. L., Washburn, N. R. and Horkay, F., *Structure-property relationships of photopolymerizable poly(ethylene glycol) dimethacrylate hydrogels.* Macromolecules, 2005. **38**(7): p. 2897-2902.

8. Zhang, X.-Z., Chu, C.-C. and Zhuo, R.-X., *Using hydrophobic additive as pore-forming agent to prepare macroporous PNIPAAm hydrogels.* J. Polym. Sci. Pol. Chem., 2005. **43**(22): p. 5490-5497.

9. Nguyen, K. T. and West, J. L., *Photopolymerizable hydrogels for tissue engineering applications.* Biomaterials, 2002. **23**(22): p. 4307-4314.

10. Bard, A. J., Fan, F. R. F., Kwak, J. and Lev, O., *Scanning electrochemical microscopy. Introduction and principles.* Anal. Chem., 1989. **61**(2): p. 132-8.

11. Fan, F.-R., *Electrochemical Studies on Ion Transport in Gels with Scanning Electrochemical Microscopy.* J. Phys. Chem. B, 1998. **102**: p. 9777-9782.

12. Pyo, M. and Bard, A. J., *Scanning electrochemical microscopy. 35. Determination of diffusion coefficients and concentrations of Ru(NH3)63+ and methylene blue in polyacrylamide films by chronoamperometry at ultramicrodisk electrodes.* Electrochim. Acta, 1997. **42**(20-22): p. 3077-3083.

13. Denuault, G. M., M.V.; Bard, A.J., *Direct Determination of Diffusion Coefficients by Chronoamperometry at Microdisk Electrodes.* J. Electroanal. Chem., 1991. **308**: p. 27-38.

14. Bard, A. J. F., Larry R., *Electrochemical Methods.* 1980, New York: John Wiley and Sons. pp. 718.

15. Fisher, A. C., *Electrode Dynamics.* 1996, New York: Oxford University Press. pp. 83.

16. Shoup, D. and Szabo, A., *Chronoamperometric current at finite disk electrodes.* J. Electroanal. Chem., 1982. **140**(2): p. 237-45.

17. Collinson, M. M., Zambrano, P. J., Wang, H. and Taussig, J. S., *Diffusion Coefficients of Redox Probes Encapsulated within Sol-Gel Derived Silica Monoliths Measured with Ultramicroelectrodes.* Langmuir, 1999. **15**(3): p. 662-668.

18. Miao, W., Ding, Z. and Bard, A. J., *Solution Viscosity Effects on the Heterogeneous Electron Transfer Kinetics of Ferrocenemethanol in Dimethyl Sulfoxide-Water Mixtures.* J. Phys. Chem. B, 2002. **106**(6): p. 1392-1398.

19. Unwin, P. R. and Bard, A. J., *Scanning electrochemical microscopy. 9. Theory and application of the feedback mode to the measurement of following chemical reaction rates in electrode processes.* J. Phys. Chem., 1991. **95**(20): p. 7814-24.

20. Adams, R. N., *Electrochemistry at Solid Electrodes.* 1969, New York: Marcel Dekker. pp. 402.

21. Liljeroth, P., Johans, C., Slevin, C. J., Quinn, B. M. and Kontturi, K., *Micro ring-disk electrode probes for scanning electrochemical microscopy.* Electrochem. Commun., 2002. **4**(1): p. 67-71.

22. Anicet, N., Bourdillon, C., Moiroux, J. and Saveant, J.-M., *Electron Transfer in Organized Assemblies of Biomolecules. Step-by-Step Avidin/Biotin Construction and Dynamic Characteristics of a Spatially Ordered Multilayer Enzyme Electrode.* J. Phys. Chem. B, 1998. **102**(49): p. 9844-9849.

Bibliography

Adams, R. N., *Electrochemistry at Solid Electrodes.* 1969, New York: Marcel Dekker. pp. 402.

Anicet, N., Bourdillon, C., Moiroux, J. and Saveant, J.-M., *Electron Transfer in Organized Assemblies of Biomolecules. Step-by-Step Avidin/Biotin Construction and Dynamic Characteristics of a Spatially Ordered Multilayer Enzyme Electrode.* J. Phys. Chem. B, 1998. **102**(49): p. 9844-9849.

Ando, S., Fujigaya, T. and Ueda, M., *DFT calculations of photoabsorption spectra in the VUV region for design of photoresist materials for 157 nm lithography.* J. Photopolym. Sci. Technol., 2002. **15**(4): p. 559-568.

Ando, S. and Ueda, M., *DFT calculations of photoabsorption spectra for alicyclic and heterocyclic compounds in the VUV region.* J. Photopolym. Sci. Technol., 2003. **16**(4): p. 537-544.

Au, J. W., Cooper, G., Burton, G. R., Olney, T. N. and Brion, C. E., *The valence shell photoabsorption of the linear alkanes, CnH2n+2 (n = 1-8): absolute oscillator strengths (7-220 eV).* Chem. Phys., 1993. **173**(2): p. 209-39.

Baek, S. Y., Wei, A., Cole, D., Nellis, G., Yeung, M., Abdo, A. and Engelstad, R., *Simulation of the coupled thermal/optical effects for liquid immersion micro-/nanolithography.* Proc. SPIE Int. Soc. Opt. Eng., 2004. **5377**(Pt. 1, Optical Microlithography XVII): p. 415-427.

Bailey, G. E. and Adam, K., *Polarization influences through the optical path.* Proc. SPIE Int. Soc. Opt. Eng., 2005. **5754**(Optical Microlithography XVIII): p. 1102-1112.

Basch, H., Robin, M. B., Kuebler, N. A., Baker, C. and Turner, D. W., *Optical and photoelectron spectra of small rings. III. The saturated three-membered rings.* J. Chem. Phys., 1969. **51**(1): p. 52-66.

Bassett, D. W. and Bonnecaze, R. T., *Immersion lithography for laser mask writing.* J. Vac. Sci. Technol., B, 2006. **24**(6): p. 2659-2667.

Bard, A. J., Fan, F. R. F., Kwak, J. and Lev, O., *Scanning electrochemical microscopy. Introduction and principles.* Anal. Chem., 1989. **61**(2): p. 132-8.

Bard, A. J. F., Larry R., *Electrochemical Methods.* 1980, New York: John Wiley and Sons. pp. 718.

Blandamer, M. J. and Fox, M. F., *Theory and applications of charge-transfer-to-solvent spectra.* Chem. Rev., 1970. **70**(1): p. 59-93.

Block, E., Corey, E. R., Penn, R. E., Renken, T. L., Sherwin, P. F., Bock, H., Hirabayashi, T., Mohmand, S. and Solouki, B., *Flash vacuum pyrolysis studies. 9. Photoelectron spectra and molecular properties. 101. Synthesis and thermal decomposition of 1,3-dithietane and its S-oxides.* J. Am. Chem. Soc., 1982. **104**(11): p. 3119-30.

Bodor, N., Dewar, M. J. S. and Worley, S. D., *Photoelectron spectra of molecules. III. Ionization potentials of some cyclic hydrocarbons and their derivatives, and heats of formation and ionization potentials calculated by the MINDO[minimum neglect of differential overlap]SCF MO method.* J. Am. Chem. Soc., 1970. **92**(1): p. 19-24.

Bohren, C. F. and Huffman, D. R., *Absorption and Scattering of Light by Small Particles*. 1983, Weinheim: WILEY-VCH Verlag GmbH & Co. KGaA. pp. 530.

Born, M. and Wolf, E., *Principles of Optics*. 2nd. 1964, New York: Pergamon Press. pp. 808.

Bourov, A., Fan, Y., Cropanese, F. C., Lafferty, N. V., Zavyalova, L., Kang, H. and Smith, B. W., *Immersion microlithography at 193 nm with a Talbot prism interferometer.* Proc. SPIE, 2004. **5377**(Pt. 3, Optical Microlithography XVII): p. 1573-1578.

Bottcher, C. J. F., *Theory of Electric Polarisation*. 1952, London: Elsevier Publishing Company. pp. 492.

Bradbury, S., *The Evolution of the Microscope*. 1st. 1967, New York: Pergamon Press. pp. 357.

Burnett, J. H. and Kaplan, S. G., *Measurement of the refractive index and thermo-optic coefficient of water near 193 nm.* J. Microlith. Microfab. Microsys., 2004. **3**(1): p. 68-72.

Chumanov, G., Evanoff, D. D., Jr., Luzinov, I., Klep, V., Zdryko, B., Conley, W. and Zimmerman, P., *Nanocomposite liquids for 193 nm immersion lithography: a progress report.* Proc. SPIE Int. Soc. Opt. Eng., 2005. **5753**(Pt. 2, Advances in Resist Technology and Processing XXII): p. 847-850.

Collinson, M. M., Zambrano, P. J., Wang, H. and Taussig, J. S., *Diffusion Coefficients of Redox Probes Encapsulated within Sol-Gel Derived Silica Monoliths Measured with Ultramicroelectrodes.* Langmuir, 1999. **15**(3): p. 662-668.

Cruise, G. M., Scharp, D. S. and Hubbell, J. A., *Characterization of permeability and network structure of interfacially photopolymerized poly(ethylene glycol) diacrylate hydrogels.* Biomaterials, 1998. **19**(14): p. 1287-94.

Dammel, R. R., Houlihan, F. M., Sakamuri, R., Rentkiewicz, D. and Romano, A., *193 nm immersion lithography - Taking the plunge.* J. Photopolym. Sci. Technol., 2004. **17**(4): p. 587-602.

Denuault, G. M., M.V.; Bard, A.J., *Direct Determination of Diffusion Coefficients by Chronoamperometry at Microdisk Electrodes.* J. Electroanal. Chem., 1991. **308**: p. 27-38.

Dewar, M. J. S. and Worley, S. D., *Photoelectron spectra of molecules. I. Ionization potentials of some organic molecules and their interpretation.* J. Chem. Phys., 1969. **50**(2): p. 654-67.

Djurisic, A. B. and Li, E. H., *Modeling the index of refraction of insulating solids with a modified Lorentz oscillator model.* Appl. Opt., 1998. **37**(22): p. 5291-5297.

Enthalpy of Solution of Electrolytes. CRC Handbook of Chemistry and Physics, 89th Edition (Internet Version 2009), Lide, D. R., ed., Boca Raton, FL: CRC Press/Taylor and Francis.

Estroff, A., Fan, Y., Bourov, A. and Smith, B., *Mask-induced polarization effects at high numerical aperture.* J. Microlith. Microfab. Microsyst., 2005. **4**(3): p. 031107/1-8.-031107/8.

Fan, F.-R., *Electrochemical Studies on Ion Transport in Gels with Scanning Electrochemical Microscopy.* J. Phys. Chem. B, 1998. **102**: p. 9777-9782.

Feuer, M. D. and Prober, D. E., *Projection photolithography-liftoff techniques for production of 0.2-micron metal patterns.* IEEE Trans. Electron Devices, 1981. **ED-28**(11): p. 1375-8.

Fisher, A. C., *Electrode Dynamics.* 1996, New York: Oxford University Press. pp. 83.

Fox, M. F. and Hunter, T. F., *Charge-transfer-to-solvent spectra.* Nature, 1969. **223**(5202): p. 177-8.

French, R. H., Sewell, H., Yang, M. K., Peng, S. P., McCafferty, D., Qiu, W., Wheland, R. C., Lemon, M. F., Markoya, L. and Crawford, M. K., *Imaging of 32-nm 1:1 lines and spaces using 193-nm immersion interference lithography with second-generation immersion fluids to achieve a numerical aperture of 1.5 and a k1 of 0.25.* J. Microlith. Microfab. Microsyst., 2005. **4**(3): p. 031103-1 - 031103-14.

French, R. H., Tran, H. V., Adelman, D. J., Rogado, N. S., Kaku, M., Mocella, M., Chen, C. Y., Hendrickx, E., Van Roey, F., Bernfeld, A. S. and Derryberry, R. A., *High-index immersion fluids enabling cost-effective single-exposure lithography for 32 nm half pitches.* Proc. SPIE Int. Soc. Opt. Eng., 2008. **6924**(Pt. 1, Optical Microlithography XXI): p. 692417/1-692417/8.

French, R. H., Yang, M. K., Lemon, M. F., Synowicki, R. A., Pribil, G. K., Cooney, G. T., Herzinger, C. M., Green, S. E., Burnett, J. H. and Kaplan, S. G., *Immersion fluid refractive indices using prism minimum deviation techniques.* Proc. SPIE, 2004. **5377**(Pt. 3, Optical Microlithography XVII): p. 1689-1694.

Furukawa, T., Kishida, T., Yasuda, K., Shimokawa, T., Liu, Z., Slezak, M. and Hieda, K., *High refractive index materials design for the next generation ArF immersion lithography.* Proc. SPIE Int. Soc. Opt. Eng., 2008. **6924**(Pt. 1, Optical Microlithography XXI): p. 692412/1-692412/8.

French, R. H., Peng, S. and Wheland, R. C. 2005. *USA Patent No. 2005119371*

Furukawa, T., Kishida, T., Miyamatsu, T., Kawaguchi, K., Yamada, K., Tominaga, T., Slezak, M. and Hieda, K., *High-refractive index material design for ArF immersion lithography.* Proc. SPIE Int. Soc. Opt. Eng., 2007. **6519**(Pt. 1, Advances in Resist Materials and Processing Technology XXIV): p. 65190B/1-65190B/10.

Gil, D., Brunner, T. A., Fonseca, C., Seong, N., Streefkerk, B., Wagner, C. and Stavenga, M., *Immersion lithography: New opportunities for semiconductor manufacturing.* J. Vac. Sci. Technol., B, 2004. **22**(6): p. 3431-8.

Goda, T., Watanabe, J., Takai, M. and Ishihara, K., *Water structure and improved mechanical properties of phospholipid polymer hydrogel with phosphorylcholine centered intermolecular cross-linker.* Polymer, 2006. **47**(4): p. 1390-1396.

Griffiths, T. R. and Wijayanayake, R. H., *Effects of cations upon absorption spectra. 5. Charge-transfer-to-solvent spectrum of iodide and ion-pair formation.* Trans. Faraday Soc., 1970. **66**(7): p. 1563-73.

Gronheid, R., Hendrickx, E., Wiaux, V., Maenhoudt, M., Goethals, M., Vandenberghe, G. and Ronse, K., *Lithography options for the 32nm half pitch node and their implications on resist and material technology.* Proc. SPIE Int. Soc. Opt. Eng., 2008. **6827**(Quantum Optics, Optical Data Storage, and Advanced Microlithography): p. 68271V/1-68271V/10.

Harder, P. M. and Shedd, T. A., *Contact angles and liquid loss behavior of high index fluids.* Proc. SPIE Int. Soc. Opt. Eng., 2007. **6533**(European Mask and Lithography Conference, 2007): p. 653305/1-653305/12.

Hazelton, A. J., Wuest, A., Hughes, G. and Lercel, M., *Predicting lithography costs - guidance for < 32 nm patterning solutions.* Proc. SPIE Int. Soc. Opt. Eng., 2008. **7028**: p. 70283N/1 - 70283N/10.

Heath, B. A., Kuebler, N. A. and Robin, M. B., *Multiphoton ionization spectra of polycyclic alkanes.* J. Chem. Phys., 1979. **70**(7): p. 3362-8.

Hecht, E., *Optics*. 4th. 2002, San Francisco: Addison Welsey. pp. 698.

Heilbronner, E., Honegger, E., Zambach, W., Schmitt, P. and Guenther, H., *The equivalent bond orbital model revisited. II. The persistence of ribbon orbitals in polycyclic alkanes.* Helv. Chim. Acta, 1984. **67**(7): p. 1681-90.

Heller, W., *Remarks on refractive index mixture rules.* J. Phys. Chem., 1965. **69**(4): p. 1123-9.

Hibbs, M. S., *System Overview of Optical Steppers and Scanners*. 2nd. Microlithography: Science and Technology, Suzuki, K. and Smith, B. W. 2007, Boca Raton: CRC Press. pp. 96.

Hinsberg, W., Wallraff, G. M., Larson, C. E., Davis, B. W., Deline, V., Raoux, S., Miller, D., Houle, F. A., Hoffnagle, J., Sanchez, M. I., Rettner, C., Sundberg, L. K., Medeiros, D. R., Dammel, R. R. and Conley, W. E., *Liquid immersion lithography - Evaluation of resist issues.* Proc. SPIE Int. Soc. Opt. Eng., 2004. **5376**(Pt. 1, Advances in Resist Technology and Processing XXI): p. 21-33.

Hoffnagle, J. A., Hinsberg, W. D., Sanchez, M. and Houle, F. A., *Liquid immersion deep-ultraviolet interferometric lithography.* J. Vac. Sci. Technol., B, 1999. **17**(6): p. 3306-3309.

Holmes, J. L. and Lossing, F. P., *Ionization energies of homologous organic compounds and correlation with molecular size.* Org. Mass Spectr., 1991. **26**(6): p. 537-41.

Honig, R. E., *Ionization potentials of some hydrocarbon series.* J. Chem. Phys., 1948. **16**: p. 105-12.

Hua, F., Sun, Y., Gaur, A., Meitl, M. A., Bilhaut, L., Rotkina, L., Wang, J., Geil, P., Shim, M., Rogers, J. A. and Shim, A., *Polymer Imprint Lithography with Molecular-Scale Resolution.* Nano Lett., 2004. **4**(12): p. 2467-2471.

http://en.wikipedia.org/wiki/Polarization, 2009.

Jellison, G. E., Jr. and Modine, F. A., *Parameterization of the optical functions of amorphous materials in the interband region.* Appl. Phys. Lett., 1996. **69**(3): p. 371-373.

Jellison, G. E., Jr. and Modine, F. A., *Parameterization of the optical functions of amorphous materials in the interband region. [Erratum to document cited in CA125:207104].* Appl. Phys. Lett., 1996. **69**(14): p. 2137.

Kawata, H., Matsumura, I., Yoshida, H. and Murata, K., *Fabrication of 0.2 micro m fine patterns using optical projection lithography with an oil immersion lens.* Jpn. J. Appl. Phys., Part 1, 1992. **31**(12B): p. 4174-7.

Kameta, K., Kouchi, N., Ukai, M. and Hatano, Y., *Photoabsorption, photoionization, and neutral-dissociation cross sections of simple hydrocarbons in the vacuum ultraviolet range.* J. Electron Spectrosc., 2002. **123**(2-3): p. 225-238.

Karrer, L., Duwe, J., Zisch, A. H., Khabiri, E., Cikirikcioglu, M., Napoli, A., Goessl, A., Schaffner, T., Hess, O. M., Carrel, T., Kalangos, A., Hubbell, J. A. and Walpoth, B. H., *PPS-PEG surface coating to reduce thrombogenicity of small diameter ePTFE vascular grafts.* Int. J. Artif. Organs, 2005. **28**(10): p. 993-1002.

Kaye, W. I., *Far ultraviolet spectroscopy. II. Analytical applications.* Appl. Spectrosc., 1961. **15**: p. 130-44.

King, F. W., *Efficient numerical approach to the evaluation of Kramers-Kronig transforms.* J. Opt. Soc. Am. B: Opt. Phys., 2002. **19**(10): p. 2427-2436.

Kingslake, R., *Optical System Design*. 1983, New York: Academic Press. pp. 323.

Kirkpatrick, S., Gelatt, C. D. and Vecchi, M. P., *Optimization by Simulated Annealing.* Science, 1983. **220**(4598): p. 671-680.

Klevens, H. B. and Platt, J. R., *Ultraviolet-transmission limits of some liquids and solids.* J. Am. Chem. Soc., 1947. **69**: p. 3055-62.

Korff, S. A. and Breit, G., *Optical Dispersion.* Rev. Mod. Phys., 1932. **4**(3): p. 471-504.

Kramers, H. A., *La diffusion de la luniere par les atoms.* Atti Cong. Intern. Fisica, 1927. **2**: p. 545-557.

Kramers, H. A., *The law of dispersion and Bohr's theory of spectra.* Nature, 1924. **113**: p. 673-4.

Kronig, R. d. L., *The theory of dispersion of x-rays.* J. Opt. Soc. Am., 1926. **12**: p. 547-57.

La Fontaine, B., Deng, Y., Kim, R.-h., Levinson, H. J., Okoroanyanwu, U., Sandberg, R., Wallow, T. and Wood, O., *Extreme ultraviolet lithography: From research to manufacturing.* J. Vac. Sci. Technol., B, 2007. **25**(6): p. 2089-2093.

Lagesson, V., Lagesson-Andrasko, L., Andrasko, J. and Baco, F., *Identification of compounds and specific functional groups in the wavelength region 168-330 nm using gas chromatography with UV detection.* J. Chromatogr., A, 2000. **867**(1 + 2): p. 187-206.

Lee, K., Kunjappu, J., Jockusch, S., Turro, N. J., Widerschpan, T., Zhou, J., Smith, B. W., Zimmerman, P. and Conley, W., *Amplification of the index of refraction of aqueous immersion fluids by ionic surfactants.* Proc. SPIE Int. Soc. Opt. Eng., 2005. **5753**(Pt. 1, Advances in Resist Technology and Processing XXII): p. 537-553.

Lee, S., Byers, J., Jen, K., Zimmerman, P., Rice, B., Turro, N. J. and Willson, C. G., *An analysis of double exposure lithography options.* Proc. SPIE Int. Soc. Opt. Eng., 2008. **6924**(Pt. 1): p. 69242A-69242A-12.

Liberman, V., Rothschild, M., Palmacci, S. T., Bristol, R., Byers, J., Turro, N. J., Lei, X., O'Connor, N. and Zimmerman, P. A., *High-index immersion lithography: preventing lens photocontamination and identifying optical behavior of LuAG.* Proc. SPIE Int. Soc. Opt. Eng., 2008. **6924**(Pt. 1, Optical Microlithography XXI): p. 692416/1-692416/11.

Liberman, V., Rothschild, M., Palmacci, S. T., Zimmerman, P. A. and Grenville, A., *Laser durability studies of high index immersion fluids: fluid degradation and optics contamination effects.* Proc. SPIE Int. Soc. Opt. Eng., 2007. **6520**(Pt. 3, Optical Microlithography XX): p. 652035/1-652035/10.

Liljeroth, P., Johans, C., Slevin, C. J., Quinn, B. M. and Kontturi, K., *Micro ring-disk electrode probes for scanning electrochemical microscopy.* Electrochem. Commun., 2002. **4**(1): p. 67-71.

Lin, B. J., *Depth of focus in multilayered media - a long-neglected phenomenon aroused by immersion lithography.* J. Microlith. Microfab. Microsys., 2004. **3**(1): p. 21-27.

Lin, B. J., *Immersion lithography and its impact on semiconductor manufacturing.* J. Microlith. Microfab. Microsys., 2004. **3**(3): p. 377-395.

Lin, B. J., *Optical lithography-present and future challenges.* C. R. Phys., 2006. **7**(8): p. 858-874.

Lin, B. J., *The ending of optical lithography and the prospects of its successors.* Micro. Eng., 2006. **83**(4-9): p. 604-613.

Lin, B. J., *The k3 coefficient in nonparaxial l/NA scaling equations for resolution, depth of focus, and immersion lithography.* J. Microlith. Microfab. Microsys., 2002. **1**(1): p. 7-12.

Lin-Gibson, S., Jones, R. L., Washburn, N. R. and Horkay, F., *Structure-property relationships of photopolymerizable poly(ethylene glycol) dimethacrylate hydrogels.* Macromolecules, 2005. **38**(7): p. 2897-2902.

Lombos, B. A., Sauvageau, P. and Sandorfy, C., *Electronic spectra of n-alkanes.* J. Mol. Spectrosc., 1967. **24**(3): p. 253-69.

Lopez-Gejo, J., Kunjappu, J. T., Turro, N. J. and Conley, W., *Amplification of the index of refraction of aqueous immersion fluids with crown ethers.* J. Micro/Nanolithogr. MEMS MOEMS, 2007. **6**(1): p. 013002/1-013002/5.

Lopez-Gejo, J., Kunjappu, J. T., Conley, W., Zimmerman, P. and Turro, N. J., *Methods for the synthesis and purification of polycycloalkane candidates for photolithography immersion fluids at 193 nm: requirements for removal of oxygen.* J. Micro/Nanolithogr. MEMS MOEMS, 2007. **6**(3): p. 033003/1-033003/7.

Lopez-Gejo, J., Kunjappu, J. T., Zhou, J., Smith, B. W., Zimmerman, P., Conley, W. and Turro, N. J., *Polycycloalkanes as Potential Third-Generation Immersion Fluids for Photolithography at 193 nm.* Chem. Mater., 2007. **19**(15): p. 3641-3647.

Lucarini, V., Saarinen,J.J., Peiponen,K.-E. and Vartiainen,E.M., *Kramers-Kronig Relations in Optical Materials Research.* 2005, Germany: Springer. pp. 160.

Matsumoto, K., Costner, E. A., Nishimura, I., Ueda, M. and Willson, C. G., *High Index Resist for 193 nm Immersion Lithography.* Macromolecules, 2008. **41**(15): p. 5674-5680.

McCallum, M., Kameyama, M. and Owa, S., *Practical development and implementation of 193nm immersion lithography.* Micro. Eng., 2006. **83**(4-9): p. 640-642.

Meiring, J. E., Schmid, M. J., Grayson, S. M., Rathsack, B. M., Johnson, D. M., Kirby, R., Kannappan, R., Manthiram, K., Hsia, B., Hogan, Z. L., Ellington, A. D., Pishko, M. V. and Willson, C. G., *Hydrogel Biosensor Array Platform Indexed by Shape.* Chem. Mater., 2004. **16**(26): p. 5574-5580.

Metropolis, N., Rosenbluth, A. W., Rosenbluth, M. N., Teller, A. H. and Teller, E., *Equation-of-state calculations by fast computing machines.* J. Chem. Phys., 1953. **21**: p. 1087-92.

Miao, W., Ding, Z. and Bard, A. J., *Solution Viscosity Effects on the Heterogeneous Electron Transfer Kinetics of Ferrocenemethanol in Dimethyl Sulfoxide-Water Mixtures.* J. Phys. Chem. B, 2002. **106**(6): p. 1392-1398.

Moore, G. E., *Cramming more components onto integrated circuits.* Electronics Magazine, 1965. **38**(8).

Mulkens, J., Flagello, D. G., Streefkerk, B. and Graeupner, P., *Benefits and limitations of immersion lithography.* J. Microlith. Microfab. Microsys., 2004. **3**(1): p. 104-114.

Mulliken, R. S., *Electronic structures of polyatomic molecules. IX. Methane, ethane, ethylene, acetylene.* J. Chem. Phys., 1935. **3**: p. 517-28.

Murray, E. C. and Keller, R. N., *Purification of hydrocarbon solvents with a silver nitrate column.* J. Org. Chem., 1969. **34**(7): p. 2234-5.

NIST Chemistry WebBook. http://webbook.nist.gov/, 2009.

Nesselrodt, D. R., Potts, A. R. and Baer, T., *Stereochemical Analysis of Methyl-Substituted Cyclohexanes Using 2 + 1 Resonance-Enhanced Multiphoton Ionization Spectroscopy.* Anal. Chem., 1995. **67**(23): p. 4322-9.

Nguyen, K. T. and West, J. L., *Photopolymerizable hydrogels for tissue engineering applications.* Biomaterials, 2002. **23**(22): p. 4307-4314.

Nitsche, R. and Fritz, T., *Determination of model-free Kramers-Kronig consistent optical constants of thin absorbing films from just one spectral measurement: application to organic semiconductors.* Phys. Rev. B: Condens. Matter, 2004. **70**(19): p. 195432/1-195432/14.

Nussenzveig, H. M., *Causality and dispersion relations.* 1972, New York: Academic Press. pp. 435.

O'Connor, N. A., Liberman, V., Lei, X., Lopez-Gejo, J., Turro, N. J. and Zimmerman, P. A., *Degradation of hydrocarbon fluids in the immersion lithography at 193 nm.* J. Photopolym. Sci. Technol., 2008. **21**(5): p. 607-611.

Ohmura, Y., Nakashima, T., Nagasaka, H., Sukegawa, A., Ishiyama, S., Kamijo, K., Shinkai, M. and Owa, S., *Current status of high-index immersion lithography development.* Proc. SPIE Int. Soc. Opt. Eng., 2007. **6520**(Pt. 1, Optical Microlithography XX): p. 652006/1-652006/9.

Ohta, K. and Ishida, H., *Comparison among several numerical integration methods for Kramers-Kronig transformation.* Appl. Spectrosc., 1988. **42**(6): p. 952-7.

Owa, S. and Nagasaka, H., *Advantage and feasibility of immersion lithography.* J. Microlith. Microfab. Microsys., 2004. **3**(1): p. 97-103.

Owa, S. and Umatate, T., *High index lithography (HIL) progress and plans.* 2008 SEMATECH Litho Forum, 2008. (Conference Presentation).

Owen, G., Pease, R. F. W., Markle, D. A., Grenville, A., Hsieh, R. L., Von Bunau, R. and Maluf, N. I., *1/8 micron optical lithography.* J. Vac. Sci. Technol., B, 1992. **10**(6): p. 3032-6.

Parsons, B. F. and Chandler, D. W., *On the Dissociation of van der Waals Clusters of X2-Cyclohexane (X = O, Cl) Following Charge-Transfer Excitation in the Ultraviolet.* J. Phys. Chem. A, 2003. **107**(49): p. 10544-10553.

Peiponen, K.-E., Vartianinen, E. M. and Asakura, T., *Dispersion, Complex Analysis and Optical Spectroscopy.* 1999, New York: Springer. pp. 130.

Peppas, N. A., Keys, K. B., Torres-Lugo, M. and Lowman, A. M., *Poly(ethylene glycol)-containing hydrogels in drug delivery.* J. Control. Release, 1999. **62**(1-2): p. 81-7.

Pickett, L. W., Muntz, M. and McPherson, E. M., *Vacuum ultraviolet absorption spectra of cyclic compounds. I. Cyclohexane, cyclohexene, cyclopentane, cyclopentene, and benzene.* J. Am. Chem. Soc., 1951. **73**: p. 4862-5.

Potts, A. W. and Streets, D. G., *Photoelectron spectra of linear valence shells. 1. Saturated hydrocarbons.* J. Chem. Soc., Faraday Trans. 2, 1974. **70**(5): p. 875-84.

Press, W. H., Teukolsky, S. A., Vetterling, W. T. and Flannery, B. P., *Numerical recipes: The art of scientific computing.* 3rd. 2007: Cambridge University Press. pp. 1235.

Pyo, M. and Bard, A. J., *Scanning electrochemical microscopy. 35. Determination of diffusion coefficients and concentrations of Ru(NH3)63+ and methylene blue in polyacrylamide films by chronoamperometry at ultramicrodisk electrodes.* Electrochim. Acta, 1997. **42**(20-22): p. 3077-3083.

Querry, M. R., Wieliczka, D. M. and Segelstein, D. J., *Water (H2O).* Handbook of Optical Constants of Solids II, Palick, E. D. 1991, New York: Academic Press, Inc. p. 1059 - 1077.

Rabinowitch, E., *Electron-transfer spectra and their photochemical effects.* Rev. Mod. Phys., 1942. **14**: p. 112-31.

Rao, C. N. R., *Ultra-Violet and Visible Spectroscopy.* 3rd. 1975, England: Butterworth and Co. Ltd. pp. 242.

Raymonda, J. W. and Simpson, W. T., *Experimental and theoretical study of sigma-bond electronic transitions in alkanes.* J. Chem. Phys., 1967. **47**(2): p. 430-48.

Raymonda, J. W., *Rydberg states in cyclic alkanes.* J. Chem. Phys., 1972. **56**(8): p. 3912-20.

Rice, B. J., *High-index materials research key to extending immersion lithography.* Solid State Technol., 2008. **51**(2): p. 28-30, 32-33.

Robin, M. B., *Higher Excited States of Polyatomic Molecules*. 1. 1974, New York: Academic Press. pp. 374.

Rothschild, M., Bloomstein, T. M., Kunz, R. R., Liberman, V., Switkes, M., Palmacci, S. T., Sedlacek, J. H. C., Hardy, D. and Grenville, A., *Liquid immersion lithography: Why, how, and when?* J. Vac. Sci. Technol., B, 2004. **22**(6): p. 2877-2881.

Sakai, K., Iwasaki, Y., Mori, S., Yamada, A., Ogusu, M., Yamashita, K., Nishikawara, T., Hara, S.-i. and Watanabe, Y., *Feasibility study on immersion system using high-index materials.* Jpn. J. Appl. Phys., 2008. **47**(6, Pt. 2): p. 4853-4861.

Sakai, K., Mori, S., Sakamoto, E., Iwasaki, Y., Yamashita, K., Hara, S.-i., Watanabe, Y. and Suzuki, A., *Progress of high-index immersion exposure system.* 5th International Symposium on Immersion Lithography Extensions, 2008. (Conference Presentation).

Sanders, D. P., Sundberg, L. K., Brock, P. J., Ito, H., Truong, H. D., Allen, R. D., McIntyre, G. R. and Goldfarb, D. L., *Self-segregating materials for immersion lithography.* Proc. SPIE Int. Soc. Opt. Eng., 2008. **6923**(Pt. 1, Advances in Resist Materials and Processing Technology XXV): p. 692309/1-692309/12.

Schoen, R. I., *Absorption, ionization, and ion-fragmentation cross sections of hydrocarbon vapors under vacuum-ultraviolet radiation.* J. Chem. Phys., 1962. **37**: p. 2032-40.

Schleyer, P. v. R., Williams, J. E., Jr. and Blanchard, K. R., *Evaluation of strain in hydrocarbons. The strain in adamantane and its origin.* J. Am. Chem. Soc., 1970. **92**(8): p. 2377-86.

Sewell, H., McCafferty, D., Markoya, L., Hendrickx, E., Hermans, J. and Ronse, K., *32nm node technology development using interference immersion lithography.* Proc. SPIE Int. Soc. Opt. Eng., 2005. **5753**(Pt. 1, Advances in Resist Technology and Processing XXII): p. 491-501.

Sewell, H., Mulkens, J., Graeupner, P., McCafferty, D., Markoya, L., Donders, S., Cortie, R., Meijers, R., Evangelista, F. and Samarakone, N., *High-n immersion lithography.* Proc. SPIE Int. Soc. Opt. Eng., 2008. **6924**(Pt. 1, Optical Microlithography XXI): p. 692415/1-692415/12.

Shang, Q. Y. and Bernstein, E. R., *(s3s) Rydberg states of cyclohexane, bicyclo[2.2.2]octane, and adamantane.* J. Chem. Phys., 1994. **100**(12): p. 8625-32.

Shoup, D. and Szabo, A., *Chronoamperometric current at finite disk electrodes.* J. Electroanal. Chem., 1982. **140**(2): p. 237-45.

Smith, B. W., Bourov, A., Fan, Y., Zavyalova, L. V., Lafferty, N. V. and Cropanese, F. C., *Approaching the numerical aperture of water - Immersion lithography at 193 nm.* Proc. SPIE Int. Soc. Opt. Eng., 2004. **5377**(Pt. 1, Optical Microlithography XVII): p. 273-284.

Smith, B. W., Bourov, A., Kang, H., Cropanese, F., Fan, Y., Lafferty, N. and Zavyalova, L., *Water immersion optical lithography at 193 nm.* J. Microlith. Microfab. Microsys., 2004. **3**(1): p. 44-51.

Smith, D. Y., *Dispersion Theory, Sum Rules, and Their Application to the Analysis of Optical Data.* Handbook of Optical Constants of Solids, Palick, E. D. 1985, New York: Academic Press, Inc. pp. 35-68.

Smith, M. and Symons, M. C. R., *Solvation spectra. I. Effect of environmental changes upon the ultraviolet absorption of solvated iodide ions.* Trans. Faraday Soc., 1958. **54**: p. 338-45.

Smith, M. and Symons, M. C. R., *Solvation spectra. II. Nature of the electronically excited state of solvated iodide ions.* Trans. Faraday Soc., 1958. **54**: p. 346-52.

Solomons, T. W. G. and Fryhle, C. B., *Organic Chemistry*. 7th. 2000, New York: John Wiley and Sons, Inc. pp. 1258.

Sowers, B. L., Arakawa, E. T. and Birkhoff, R. D., *Optical properties of six-member carbon ring organic liquids in the vacuum ultraviolet.* J. Chem. Phys., 1971. **54**(6): p. 2319-24.

Sreenivasan, S. V., Willson, C. G., Schumaker, N. E. and Resnick, D. J., *Low-cost nanostructure patterning using step and flash imprint lithography.* Proc. SPIE Int. Soc. Opt. Eng., 2002. **4608**(Nanostructure Science, Metrology, and Technology): p. 187-194.

Stein, G. and Treinin, A., *Absorption spectra of anions in solution. III. Ionic effects.* Trans. Faraday Soc., 1960. **56**(1): p. 1393-403.

Stewart, M. D., Johnson, S. C., Sreenivasan, S. V., Resnick, D. J. and Willson, C. G., *Nanofabrication with step and flash imprint lithography.* J. Microlith. Microfab. Microsyst., 2005. **4**(1): p. 011002/1-011002/6.

Stewart, M. D., Patterson, K., Somervell, M. H. and Willson, C. G., *Organic imaging materials: a view of the future.* J. Phys. Org. Chem., 2000. **13**(12): p. 767-774.

Switkes, M., Kunz, R. R., Rothschild, M., Sinta, R. F., Yeung, M. and Baek, S. Y., *Extending optics to 50 nm and beyond with immersion lithography.* J. Vac. Sci. Technol., B, 2003. **21**(6): p. 2794-2799.

Switkes, M. and Rothschild, M., *Immersion lithography at 157 nm.* J. Vac. Sci. Technol., B, 2001. **19**(6): p. 2353-2356.

Switkes, M., Rothschild, M., Kunz, R. R., Baek, S. Y., Cole, D. and Yeung, M., *Immersion lithography: beyond the 65 nm node with optics.* Microlithography World, 2003. **12**(2): p. 4-6, 18, 20.

Switkes, M., Kunz, R. R., Sinta, R. F., Rothschild, M., Gallagher-Wetmore, P. M., Krukonis, V. J. and Williams, K., *Immersion liquids for lithography in the deep ultraviolet.* Proc. SPIE Int. Soc. Opt. Eng., 2003. **5040**(Pt. 2, Optical Microlithography XVI): p. 690-699.

Synowicki, R. A., Pribil, G. K., Cooney, G., Herzinger, C. M., Green, S. E., French, R. H., Yang, M. K., Burnett, J. H. and Kaplan, S., *Fluid refractive index measurements using rough surface and prism minimum deviation techniques.* J. Vac. Sci. Technol., B, 2004. **22**(6): p. 3450-3453.

Tabarelli, W. and Loebach, E. W. 1982. *USA Patent No. 4346164*

Taylor, J. C., Costner, E. A., Goh, S., Wojtczak, W., Dewulf, D. and Willson, C. G., *The effect of added salts on the optical properties of water for high index immersion lithography fluids.* J. Vac. Sci. Technol., B, 2008. **26**(2): p. 506-513.

Taylor, J. C., LeSuer, R. J., Chambers, C. R., Fan, F.-R. F., Bard, A. J., Conley, W. E. and Willson, C. G., *Experimental Techniques for Detection of Components Extracted from Model 193 nm Immersion Lithography Photoresists.* Chem. Mater., 2005. **17**(16): p. 4194-4203.

The International Technology Roadmap for Semiconductors. http://public.itrs.net, 2008.

Thompson, L. F., Willson, C. G. and Bowden, M. J., *Introduction to Microlithography*. 2nd. 1994, Washington, D.C.: An American Chemical Society Publication. pp. 540.

Tompkins, H. G. and McGahan, W. A., *Spectroscopic Ellipsometry and Reflectometry: A User's Guide.* 1999, New York: John Wiley and Sons, Inc. pp. 228.

Turro, N. J., *Modern Molecular Photochemistry.* 1978, Menlo Park: The Benjamin/Cummings Publishing Company, Inc. pp. 628.

Unwin, P. R. and Bard, A. J., *Scanning electrochemical microscopy. 9. Theory and application of the feedback mode to the measurement of following chemical reaction rates in electrode processes.* J. Phys. Chem., 1991. **95**(20): p. 7814-24.

Volkmann, H., *Ernst Abbe and His Work.* Appl. Opt., 1966. **5**(11): p. 1720-1731.

Weideman, J. A. C., *Computing the Hilbert Transform on the Real Line. Mathematics of* Mack, C. A. and Byers, J. D., *Exploring the capabilities of immersion lithography through simulation.* Proc. SPIE Int. Soc. Opt. Eng., 2004. **5377**(Pt. 1, Optical Microlithography XVII): p. 428-441.

Wooten, F., *Optical Properties of Solids*. 1972, New York: Academic Press. pp. 260.

Yadav, L. D. S., *Organic Spectroscopy*. 2005, Boston: Kluwer Academic Publishers. pp. 324.

Yang, F. W., C.G.; Wang, D.; Lee, H.; Manson, P.M.; Elisseeff, J., *The effect of incorporating RGD adhesive peptide in PEG-da hydrogel on osteogenesis of bone marrow stromal cells.* Biomaterials, 2005. **26**(30): p. 5991-5998.

Young, D., *Computational Chemistry: A Practical Guide for Applying Techniques to Real World Problems.* 2001, New York: Wiley-Interscience. pp. 381.

Zhang, X.-Z., Chu, C.-C. and Zhuo, R.-X., *Using hydrophobic additive as pore-forming agent to prepare macroporous PNIPAAm hydrogels.* J. Polym. Sci. Pol. Chem., 2005. **43**(22): p. 5490-5497.

Zhou, J., Fan, Y., Bourov, A., Lafferty, N., Cropanese, F., Zavyalova, L., Estroff, A. and Smith, B. W., *Immersion lithography fluids for high NA 193 nm lithography.* Proc. SPIE Int. Soc. Opt. Eng., 2005. **5754**(Pt. 2, Opt Microlith XVIII): p. 630-7.

Zhou, J., Fan, Y., Bourov, A. and Smith, B. W., *Inorganic immersion fluids for ultrahigh numerical aperture 193 nm lithography.* Appl. Opt., 2006. **45**(13): p. 3077-3082.

Zimmerman, P. A., Byers, J., Rice, B., Ober, C. K., Giannelis, E. P., Rodriguez, R., Wang, D., O'Connor, N., Lei, X., Turro, N. J., Liberman, V., Palmacci, S., Rothschild, M., Lafferty, N. and Smith, B. W., *Development and evaluation of a 193nm immersion generation-three fluid candidates.* Proc. SPIE Int. Soc. Opt. Eng., 2008. **6923**(Pt. 1, Advances in Resist Materials and Processing Technology XXV): p. 69230A/1-69230A/10.

Zimmerman, P. A., van Peski, C., Rice, B., Byers, J., Turro, N. J., Lei, X., Gejo, J. L., Liberman, V., Palmacci, S., Rothschild, M., Whittaker, A., Blakey, I., Chen, L., Dargaville, B. and Liu, H., *Status of high-index materials for generation-three 193nm immersion lithography.* J. Photopolym. Sci. Technol., 2007. **20**(5): p. 643-650.

Vita

Elizabeth A. Costner graduated from Dunwoody High School in Atlanta, GA in May 2000. She enrolled at the Georgia Institute of Technology in August 2000 and received the Bachelors of Science in Chemical Engineering with highest honors in July 2004. In August 2004, Elizabeth enrolled in the graduate chemical engineering program at The University of Texas at Austin. She received the Master's Degree in Chemical Engineering in December 2007 and hopes to receive a Doctor of Philosophy in Chemical Engineering in May 2009.

Permanent Address: 303 W 35th St Apt 202, Austin, TX 78705

This manuscript was typed by the author.